INFORMATION TO USERS

This manuscript has been reproduced from the microfilm master. UMI films the text directly from the original or copy submitted. Thus, some thesis and dissertation copies are in typewriter face, while others may be from any type of computer printer.

The quality of this reproduction is dependent upon the quality of the copy submitted. Broken or indistinct print, colored or poor quality illustrations and photographs, print bleedthrough, substandard margins, and improper alignment can adversely affect reproduction.

In the unlikely event that the author did not send UMI a complete manuscript and there are missing pages, these will be noted. Also, if unauthorized copyright material had to be removed, a note will indicate the deletion.

Oversize materials (e.g., maps, drawings, charts) are reproduced by sectioning the original, beginning at the upper left-hand corner and continuing from left to right in equal sections with small overlaps. Each original is also photographed in one exposure and is included in reduced form at the back of the book.

Photographs included in the original manuscript have been reproduced xerographically in this copy. Higher quality 6" x 9" black and white photographic prints are available for any photographs or illustrations appearing in this copy for an additional charge. Contact UMI directly to order.

UMI

A Bell & Howell Information Company
300 North Zeeb Road, Ann Arbor MI 48106-1346 USA
313/761-4700 800/521-0600

The Harmonically Forced Complex Ginzburg-Landau Equation

by

D.J. Wielaard

A dissertation submitted to the Graduate Faculty in Physics in partial fulfillment of the requirements for the degree of Doctor of Philosophy, The City University of New York.

1996

This manuscript has been read and accepted by the Graduate Faculty in Physics in satisfaction of the dissertation requirements for the degree of Doctor of Philosophy.

11/27/95
Date

Prof. J. Koplik
(Chair of Examining Committee)

1/20/96
Date

Prof. J. Krieger (Executive Officer)

Supervisory Committee:

Prof. N. P. Chang
Prof. E. M. Chudnovsky
Prof. D. Papageorgiou
Prof. G. Triantafyllou

THE CITY UNIVERSITY OF NEW YORK

Abstract

The harmonically forced complex Ginzburg-Landau equation

by

D. J. Wielaard

Adviser: Prof. George Triantafyllou

The complex Ginzburg-Landau equation $\partial_t \Psi - \sigma \Psi + \lambda \partial_x^2 \Psi + \beta |\Psi|^2 \Psi = F(x,t)$ is studied as a model equation regarding the accomplishment of spatio-temporal order in extended systems (systems of infinite length) as a result of a harmonic external forcing $F(x,t) = F(x)e^{i\omega t}$. Two types of spatial behaviour of the forcing are considered: a spatially localized forcing of Gaussian shape, $F(x) = F_0 e^{-K^2 x^2}$, and a spatially extended forcing in the form of a plane wave, $F(x) = F_0 e^{iKt}$.

For the spatially independent case the lock-in region in the phase diagram in F_0-ω space is obtained analytically. Stable locked-in states ($\sim e^{i\omega t}$) become possible for sufficiently large forcing strength. The only other stable state observed is a quasi-periodic state. Coexistence of two locked states as well as a locked and a quasi-periodic state is possible.

For a spatially dependent linear growth rate of the form $Re\sigma(x) = \sigma_\infty + \sigma_0 e^{-Q^2x^2}$, where $\sigma_0 > -\sigma_\infty > 0$, the system size is effectively determined by the width of the growth rate (Q). In small systems the behaviour shows great similarity with the spatially independent case, although some differences are observed as function of the location. As the system size is increased, the similarity with the spatially independent case remains present for where it concerns phase-locked states. For the other states the behaviour depends strongly on the location in the system. Local organization becomes possible with a small forcing (around resonance). States occur which show phase-locked, quasi-periodic and chaotic behaviour in different spatial regions of the system.

For the sitation with constant coefficients ($Re\beta > 0$ and $Re\sigma > 0$) and a plane wave forcing, the region of stability for phase-locked states (plane waves) is constructed in the F_0-ω-K space. Stability requires in all cases $Re\lambda > 0$. In the Benjamin-Feir unstable regime for the unforced equation, stable forced plane wave states become possible for sufficiently strong forcing with $K^2_{min}(F_0) < K^2 < K^2_{max}(F_0)$, where $K^2_{min} = 0$ for most parameter choices. It is found that the classification of the different spatio-temporal chaotic states in the forced system in terms of amplitude chaos and phase chaos is insufficient, a more elaborate description is needed.

This work was performed at the Physics Department and the Benjamin Levich Institute of the City College of the City University of New York. I would like to thank my advisor professor George Triantafyllou. The financial support of the Office of Naval Research Grant No. N00014-93-1-0932 is gratefully acknowledged.

Contents

List of Tables

List of Figures

Chapter 1

Introduction.

This work consists of a study of solutions of the complex Ginzburg-Landau equation (CGLE) in the presence of an external forcing. The CGLE appears in many problems in physics. In its general form, for one spatial dimension, the equation reads

$$\frac{\partial}{\partial t}\Psi - \sigma\Psi - \lambda\frac{\partial^2}{\partial x^2}\Psi + \beta|\Psi|^2\Psi \cdots\cdots = F(x,t). \tag{1.1}$$

The complex function $\Psi(x,t)$ may be related to an order parameter, for instance the magnetization in a magnetic substance. In fluid mechanics $\Psi(x,t)$ may represent an amplitude function or potential related to specific properties of the original flow. The complex function $F(x,t)$ represents the external

field or forcing. The coefficients σ , λ , and β are in general complex and may be functions of space (x) and time (t). The ellipses on the left hand side symbolize higher order terms such as $|\Psi|^4\Psi$ and higher order derivatives, these will however not be considered here. Also, situations for more than one spatial dimension will not be considered here. The CGLE is known to be a generic equation for two classes of problems.

The first class of problems in which the equation arises and from which it actually derives its name, are problems in statistical mechanics concerning critical phenomena and phase transitions. The equation in its stationary form (no time dependence) was first obtained by Ginzburg and Landau in their phenomenological theory of superconductivity [1] and was found later on to be of much more universal character in the following sence. To study phase transitions one tries to write the effective action as a functional of an order parameter field Ψ (related to a physical property of the system) and its conjugate field F (external field, forcing). It can be shown that based on quite general considerations, the effective action close to a critical point may always be written in the so called Ginzburg-Landau form, which in the mean field approximation then precisely leads to the CGLE (real coefficients). In that sense the equation is a universal equation for an order parameter for

a large class of physically distinct systems close to criticality, their different physical properties being reflected merely in the interpretations of Ψ, F, σ, λ, β etc.. Comprehensive discussions of critical phenomena and phase transitions are given in [2],[3].

Being a mean field equation, the equation gives a description in terms of "hydrodynamic" quantities, that is the order parameter Ψ, external field F and the other parameters are to be considered as being averaged over their microscopic equivalents, thereby eliminating fluctuations on the short space and time scales. In the general theory however the treatment of the microscopic fluctuations is of fundamental importance. A way to simulate them in some sense on the Ginzburg-Landau level is to add small stochastic terms in the equation to F, and possibly the various other parameters dependent on the specific physical problem under consideration.

The second class of problems in which the equation plays a fundamental role are problems in fluid mechanics. There the equation appears as a generic amplitude equation close to a bifurcation in a variety of problems such as Rayleigh-Bénard convection, Taylor-Couette flow, shear flow, deep water waves, thin film flows and reaction-diffusion problems . Typically one performs a perturbation analysis near the critical wave number k_c and critical

bifurcation parameter value $R = R_c$ where the first Fourier mode becomes unstable. In general this results in an amplitude equation which is of a Ginzburg-Landau form. The equation in this case governs the evolution of the instability in the original problem on its long space and time scales close to criticality. The instability, and hence the stability of the original physical system may then further be analyzed on the basis of the CGLE. An extension of these concepts away from near criticality was given in [8]. The CGLE is thus again a universal equation, describing the stability close to a bifurcation for a variety of problems in fluid mechanics, their specific physics again being contained merely in the interpretation of Ψ, F, σ, λ and β.

For fluid mechanical systems, the external field or forcing does not appear quite as natural as in problems concerning phase transitions. It is perhaps therefore that far more is known about the unforced CGLE than about the forced equation. On the other hand, for problems related to phase transitions and critical phenomena, the equation appears almost without exception with real coefficients.

Besides the already quite impressive universality of the equation it has yet another useful property. This is that the qualitative features present in the Navier-Stokes equation believed to be significant in the problem of turbulence

are also present in the CGLE. The equation serves therefore also as a model in many studies in relation to turbulence. More in general the CGLE serves as a model equation concerning the chaotic behaviour of spatially distributed systems with many degrees of freedom. It has been suggested [9] that chaotic behaviour in the limit of an infinite system, i.e. extensive chaos, might be understood in terms of concepts derived from statistical mechanics and critical phenomena. Another idea, which goes back many years [9], is that it seems to be a general property of continuum mechanical systems that their assymptotic states are effectively of a finite or even low dimensional nature. By now this idea has received analytical, numerical as well as experimental support. In relation to this the CGLE is also frequently used as a model equation, see for instance [11] or [12].

We will in this work mostly consider the situation in which the bifurcation is supercritical and the bifurcation parameter is above the critical value ($R > R_c$). This means that we take $Re(\beta) > 0$ and $Re(\sigma) > 0$ in general. The subcritical case is sometimes studied with inclusion of a stabilizing fifth order term $|\Psi|^4\Psi$, for which case a considerable amount of analytic results are obtained in reference [13]. The cubic subcritical unforced CGLE has also been studied quite extensively, see for instance references [14] and [15]. A

confinement to the supercritical case is not a severe limitation, since for applications in fluid mechanics as well as statistical mechanics it is usually the physically most relevant case.

Before making our discussion more concrete, it is useful to rescale the equation. The rescaled versions vary somewhat in the literature, in this work we will use

$$\begin{aligned} t &= |Re(\sigma)|t', \\ \Psi &= \left|\frac{Re(\sigma)}{Re(\beta)}\right|^{1/2}\Psi', \\ F &= \left|\frac{Re(\sigma)}{Re(\beta)}\right|^{3/2}F', \\ \Lambda &= \frac{(2\pi)^2}{l^2}\cdot\frac{Re(\lambda)}{|Re(\sigma)|}. \end{aligned} \tag{1.2}$$

The parameter Λ functions in an actual simulation as a cut-off parameter. In general, the length l may be taken to be the system length (simulation, experiment) or any other significant length in the problem. The equation then becomes

$$\left[\frac{\partial}{\partial t} - \mu_1(1+ic_1) - \Lambda(1+ic_2)\frac{\partial^2}{\partial x^2} + \mu_2(1+ic_3)|\Psi|^2\right]\Psi\cdots = F(x,t). \tag{1.3}$$

where the primes are left out and

$$c_1 = \frac{Im(\sigma)}{Re(\sigma)},$$

$$c_2 = \frac{Im(\lambda)}{Re(\lambda)} ,$$

$$c_3 = \frac{Im(\beta)}{Re(\beta)} ,$$

$$\mu_1 = sign(Re(\sigma)) ,$$

$$\mu_2 = sign(Re(\beta)) . \tag{1.4}$$

For the supercritical case $\mu_1 = \mu_2 = +1$.

Of course these transformations strictly speaking only make sense when the coefficients are constants. If the coefficients are not constant, the same transformation may be used in principle if one can distinguish characteristic values for the parameters, such as for instance $Re(\sigma(x \to \infty))$ or $Im(\sigma(t = 0))$ etc.. We will see an example of this in chapter 4.

We will exclusively consider the case that the forcing varies harmonically in time;

$$F(x,t) = F(x)e^{i\omega t}. \tag{1.5}$$

In this case the parameter c_1 may be incorporated in the forcing frequency ω or vice versa. Also in the unforced equation the parameter c_1 may be eliminated by a simple transformation. It therefore suffices to consider the equation with either $c_1 = 0$ or $\omega = 0$.

We will first discuss a selection of published results for the CGLE which are related to it's role as a model for the study of spatio-temporal chaos, or which concern the forced equation. After that an outline of this thesis will be given.

1.1 A selection of other work.

A considerable amount of analytic results were obtained concerning uniformly translating solutions of the unforced equation with constant coefficients [16,17,18,19]. The results usually are valid for (or necessarily involve) more complicated versions of the equation, by inclusion of higher order nonlinear terms and derivatives. Uniformly translating solutions are obtained from the ansatz

$$\Psi(x,t) = A(\xi)e^{i\omega t},$$

$$\xi = x - vt,$$

$$A(\xi) = a(\xi)e^{i\phi(\xi)}, \tag{1.6}$$

and it turns out to be effective to transform the equation to a set of ode's in the pseudo-time variable ξ for the quantities

$$a(\xi)\,,$$

$$q(\xi) = \frac{\partial}{\partial \xi}\phi\,,$$

$$\kappa(\xi) = a^{-1}\frac{\partial}{\partial \xi}a\,. \tag{1.7}$$

Fixed points and trajectories in the phase space of this dynamical system correspond to different uniformly translating solutions of the CGLE. Fronts, pulses and domain boundaries may now be studied in terms of the heteroclinic orbits between fixed points of (1.6) [17,18]. Besides this more complicated trajectories such as limit cycles and chaotic orbits were also considered [16,19]. The method has the drawback that it has little to say about the stability of a solution of the original pde, but it is a powerful method for obtaining analytic results regarding the existence of solutions.

Unfortunately, when an external forcing is included in the equation this approach fails, even for the most simple case of a spatially uniform forcing. Infact, published results for the externally forced CGLE are scarce, certainly where it concerns the equation in its truly complex form.

An example of an application of the forced equation in the theory of phase transitions can be found in [20]. The equation appears here in highly simplified form with real coefficients and real constant forcing. The relaxation of front solutions describes the nucleation of a new phase near the critical point (first order phase transition). Additive noise is included to simulate a thermal ensemble. On the basis of this different dynamical properties of the nucleation process are computed.

Another example of the appearence of the forced equation may be found in [21]. Here the $\partial^2\Psi/\partial x^2$ term is treated in discretized form resulting in a set of globally coupled identical limit cycle oscillators. This set of equations can be interpreted as a "mean field" version of the original CGLE. The equations are numerically analyzed and a chaotic (in time) region is found, in which the (ordered) configuration of the oscillators is argued to be explained by the observation that in this region the set of equations may as a first approximation be replaced by a Landau equation (LE) (space independent CGLE) with a harmonic forcing.

Both results just mentioned however give a very small part of the picture for where it concerns solutions of equation (1.3), which is the object of study of this work. Apparently no systematic studies have been published of the

CGLE in it's truly complex form with a truly external forcing (forcing independent of solution). A reason may be that when the original system (the system for which the CGLE is valid around the instability threshold) is exposed to an external forcing, this usually gives rise to terms in the amplitude equation which are themselves a function of the amplitude.

An example of this is provided by electrohydrodynamic instabilities in nematic liquid crystals [22]. For nearly resonant forcing with forcing strength α and wavenumber $q_1 = \frac{n}{m} \cdot (q_0 + k)$, with k small and q_0 the wavenumber of the instability in the unforced system, the amplitude equation has besides the usual terms the extra term [23,24]

$$\alpha^m (\Psi^*)^{n-1} e^{inkx} . \tag{1.8}$$

The amplitude equation relevant here however has real coefficients, so that whatever is known for the $n = 1$ case in this context, is still negligible for what concerns the situation we wish to consider in this work.

The closest to a more or less systematic discussion of an equation of the form (1.3) are some results presented in reference [25]. This paper concerns the situation of strongly resonant forcing of systems with an oscillatory instability. For an external forcing in the original problem with forcing frequency

$\omega_e = \frac{n}{m}(\omega_0 - \nu)$, where ν is small and ω_0 is the frequency at which the instability occurs in the unforced system, the amplitude equation (now with complex coefficients) has the standard form with the extra term

$$\gamma_n(\Psi^*)^{n-1} . \tag{1.9}$$

The parameter γ_n is proportional to the m^{th} power of the forcing amplitude. For $n = 1$ the supercritical version of equation (1.3) ($c_1, c_2, c_3 \neq 0$) with a spatially uniform harmonic forcing is recovered. For as far as the results discussed in reference [25] concern the $n = 1$ case, they apply to situations with either a very large forcing amplitude or a very small forcing amplitude with $\gamma_1 \sim \epsilon^2$, close to the Benjamin-Feir instability (see below) $1 + c_1 c_2 \sim \epsilon$ and very close to resonance in the CGLE, $\nu - c_3 \sim \epsilon^3$. No results are presented for more realistic values of the forcing parameters. In the strong forcing limit the locked states are shown to be always stable. We will see in chapter 5 of this work that this is infact not completely correct for all parameter values. In the small forcing limit, the emergence of a spatially periodic pattern is derived on the basis of a phase equation.

Perhaps the most simple nontrivial and best studied solutions of the su-

percritical unforced equation are the plane waves

$$\Psi(x,t) = \Psi_0 e^{i\Omega t + iKx},$$

$$|\Psi_0|^2 = 1 - \Lambda K^2,$$

$$\Omega = -c_2 \Lambda K^2 - c_3(1 - \Lambda K^2). \tag{1.10}$$

They are sometime referred to as "rotating waves". Standing waves are also possible, they are however always unstable in the supercritical case.

The instability of the plane wave solutions is governed by the so called Benjamin-Feir (BF) instability [26], sometimes also refered to as the Eckhaus or modulational instability. This instability consists here in that a plane wave with wavenumber q and frequency ω becomes unstable by resonant excitation of sidebands with wavenumbers q_1 and q_2 and frequenties ω_1 and ω_2 satisfying

$$\frac{1}{2}(q_1 + q_2) = q\,,$$

$$\frac{1}{2}(\omega_1 + \omega_2) = \omega\,. \tag{1.11}$$

A detailed stability analyses was performed in reference [27] and [28]. Dependence on the parameters c_2 and c_3 of the stability criterion can be quite complicated, but it is always of the form $K^2 < K^2_{BF}(c_2, c_3)$. For $1 + c_2 c_3 = 0$

the band of stable wavenumbers shrinks to zero ($K_{BF}(c_2, c_3) = 0$), and for $1 + c_2 c_3 < 0$ all plane waves are unstable.

For the behaviour of solutions of the CGLE below the BF instability ($1 + c_2 c_3 < 0$), the system length is important. More precisely, following reference [9] and [29], the behaviour observed will depend on the length of the system l in comparision to the dissipation length l_D, the excitation length l_E and the correlation length l_C. The dissipation length is the characteristic length at which energy is dissipated. The excitation length is the characteristic length at which energy is injected into the system. The correlation length is more difficult to define since it requires a rather complete knowledge of the solutions. The simplest definition is in terms of a correlation function $C(r)$: if $C(r)$ decays exponentially for large r, $C(r) \sim e^{-r/\xi}$, $r \to \infty$, one may define $l_C = \xi$. For a spatially uniform state which becomes unstable for perturbations with wavenumber q_0 the excitation length $l_E \sim q_0^{-1}$, the dissipation length is typically of the same order of magnitude.

Small systems are then systems for which $l \approx l_D$. The number of excited modes will be severely restricted by the geometry. If a chaotic state arises it will be described by an attractor in a low dimensional phase space. The correlation length is also at least of order of the system length, so that the

spatial behaviour is dynamically irrelevant.

Large systems are systems for which the system length $l \gg l_D$. The system now has many degrees of freedom. If a chaotic state arises, any description of it must necessarily take this multiplicity into account, and the atractor dimension is expected to be correspondingly large.

Obviously, the simplest way to create a large system is to increase the system length at fixed controll parameter(s) (l_D, l_E fixed). Chaotic states obtained in this way are refered to as spatio-temporal chaos [29]. The other way to reach the large-system limit as explained in reference [29], is to effectively decrease the disipation length l_D (fix l, increase R). An example being strong turbulence in fluids with high Reynold's number.

As explained above, the dynamics of a small system is effectively low dimensional. An illustration of this for the (unforced) CGLE is given in [12]. Here the CGLE is considered in the near nonlinear Schrödinger regime for a system size for which the lowest fourier mode is just within the Benjamin-Feir stable region. For an expansion of the solution around the spatially uniform solution (Stokes wave) the CGLE is shown to reduce to a 3 dimensional Lorenz-like system of equations.

A numerical analyses of the fate of the uniform Stokes wave in the BF

unstable regime is given in [30]. Here the system size is varied, regulating the number of possible BF unstable fourier modes allowed to exist in the system. Two different routes to chaos of the Ruelle-Takens-Newhouse type are observed, involving a limit cycle and two and three frequency quasi-periodic motions in time.

For large unforced systems in the BF unstable regime the CGLE was shown to display two kinds of spatio-temporal chaos, known as amplitude (defect) chaos and phase chaos [31], [32]. The characteristic difference between the two is the absence of defects in the phase chaotic states. Defects,or space-time dislocations, are space-time points where $\Psi = 0$. The phase of the solution is not defined at a defect and it shows a discontinuity of π. As defects occur, a phase description of the solution is believed to break down, and the transition from phase chaos to amplitude chaos in the CGLE is a good example of this [33]. Phase chaos is characterized by small amplitude variations around the uniform solution, whereas defect chaos shows defects and large amplitude fluctuations.

The phase diagram of the unforced CGLE as function of the parameters c_2 and c_3, close to the BF instability, has been constructed in [32]. Further differences between the two chaotic states were here characterized by means

of the temporal and spatial correlations. It was shown that the temporal and spatial correlations decay exponentially for amplitude chaos, whereas for phase chaos, exponential decay was not observed. Finally, a bistable region in the phase diagram was obtained in which the two states coexist.

It is suggested in reference [34] that in this bistable region infact a state of spatio-temporal intermittency may exist. Being well established in reference [34] to exist in the BF stable regime, the existence of spatio-temporal intermittency in the BF unstable regime remains arguable. The spatio-temporal intermittency in the CGLE is characterized by laminar ("absorbing") patches consisting of linearly stable plane waves (BF stable regime), separated by turbulent ("active") regions made up of localized objects such as shocks, defects, holes etc., with a well defined dynamics. The simplest of these objects were shown to be members of a family of exact solutions obtained by Nozaki and Bekki [35], [36].

1.2 Outline of this thesis.

The objective of this work is to study the accomplishment of spatio-temporal order in spatially extended systems as a result of an external forcing. It has

been more than justified in the previous discussion that the CGLE may serve as a useful model for this purpose. We will discuss the behaviour of the CGLE in or close to the BF unstable regime in the presence of an external forcing. Since the little that has been published for this situation appears in a rather unorganized way, any systematic discussion of merely possible solutions is already useful.

The understanding of spatio-temporal chaos in general is still in a rather primitive stage. The situations where this behaviour is observed in the CGLE are in that respect of special interest. The CGLE provides a simple model which displays spatio-temporal chaos and which can be analyzed relatively easily. Regarding the forced equation, we will see that it provides a richer and broader spectrum of behaviour than the unforced equation, without hardly changing the simplicity of the model. Moreover, as discussed in the previous section, the forcing is of course besides this also of interest in real experimental situations. With this in mind, the parameter values will be kept as general as reasonably possible in this work.

The time dependence of the forcing will be taken to be harmonic, $F \sim e^{i\omega t}$, or put in an other way, one could say that we will consider a time independent forcing of equation (1.3) with $c_1 \neq 0$. For what concerns the spatial part of

the forcing, basically two situations will be considered; a localized forcing of Gaussian shape and a plane wave forcing. The motivation for this is the wish to study spatially localized as well as spatially extended solutions. The ultimate goal is to obtain phase diagrams as function of the forcing parameters (strength, frequency, and wavenumber or width) for different situations.

First we will demonstrate the derivation of the amplitude equation for Rayleigh-Bénard convection in chapter 2. This serves as an example of the derivation of a CGLE in general for a real experimental situation in fluid mechanics. In the derivation presented here we will closely follow reference [29].

In chapter 3 the phase diagram for the harmonically forced LE (CGLE without spatial dependence) will be constructed. The LE is for instance valid when only one unstable mode is excited in the original system. It appears also sometimes as a specific approximation of the CGLE, see for instance reference [21]. As for the CGLE, also for the much simpler LE apparently no systematic study has been performed of the behaviour in the presence of a harmonic external forcing. An exception is the case for $c_3 = 0$, for which the equation has been extensively analized in relation to van der Pol's equation,

see reference [37] and references there. In chapter 3 the region of stability for phase locked states as function of the forcing strength and frequency will be derived analytically for all c_3. The behaviour in regions of parameter space where phase locked states are unstable will be analyzed carefully by numerical integration of the equation and a fixed points analyses. Of interest as they stand, the results of chapter 3 will moreover prove to be useful in chapter 5.

In chapter 4 we will consider pulse solutions of the CGLE. With a pulse solution is meant a solution $\Psi(x,t)$ with the property that $\Psi(x \to \pm\infty, t) \to 0$. Unforced stable pulse solutions of the cubic CGLE have not been observed to exist, neither for the supercrirical nor for the subcrirical case. We will discuss the findings for the unforced as well as the forced system, the results will however be negative in both cases: no stable pulse solutions appear to be possible. The major part of chapter 4 will concern the situation where μ_1 is spatially dependent and of a Gaussian shape, such that $\mu_1 > 0$ locally and $\mu_1 < 0$ elsewhere. For this situation stable pulse solutions become possible. Other than the fact that it allows one to study pulse solutions of the cubic CGLE, a space dependent linear growth rate $\mu_1(x)$ has of course also a physical relevance. It will for instance apply to a situation where the controll

parameter is space dependent. Since no results were published for a linear growth rate of the form considered here, not even for the unforced system, a large part of chapter 4 will consist of an analyses of the solutions occurring in the unforced system for different growth rate parameters (amplitude, width). The width of the growth rate in effect determines the size of the system. The unforced behaviour as the amplitude of the growth rate is varied will be discussed for a small system, an intermediate size system and a large system. After having obtained an idea of the unforced behaviour, the forced system will be discussed. An example of a small system with a Gausian forcing will be analyzed as well as an intermediate size system with a Gaussian forcing and with a plane wave forcing. The phase diagram, or at least the outlines of it, will be discussed as a function of the forcing parameters.

In chapter 5 we will analyze the equation with a plane wave forcing. With use of the results of chapter 3, the stable region for phase locked states (plane waves) will be constructed as function of the forcing strength frequency and wavenumber, for the extended as well as for finite size systems. After this we will discuss the behaviour in the part of the forcing parameter space where the plane wave states are unstable. We will consider the situation where the unforced solution shows amplitude chaos. We will look at the behaviour for

various parameter choices around resonance (for forcing frequenties and wave numbers compatible with the free dispersion relation (1.10)), and well away from resonance.

Chapter 6 gives a summary of the results obtained in this work that deserve further study.

Chapter 2

A derivation of an amplitude equation.

In this chapter we will illustrate the derivation of an amplitude equation for the problem of Rayleigh-Bénard convection. Historically it was for Rayleigh-Bénard convection that amplitude equations were first derived by Newell and Whitehead [4]. A more important motivation for us however is that the basic equations describing the phenomenon are well known and there is in this case in fact a clear and unambiguous derivation of an amplitude equation possible. In presenting the derivation here we will closely follow reference [29].

Rayleigh-Bénard convection in its idealistic form involves a fluid placed

between two horizontal plates that are infinite in extend and are perfect heat conductors. The fluid is driven by maintaining the lower plate at a temperature ΔT above the upper plate temperature. For small driving the fluid remains at rest and a linear temperature profile is set up, this is the "conducting" or "uniform" solution. Due to the thermal expansion however, the fluid near the lower plate is less dense. Of course this layer of fluid can not rise as a whole, and we encounter an instability at finite wavelength. This instability occurs when the driving ΔT is strong enough to overcome the dissipative effects of thermal conduction and viscosity. The control parameter describing the instability, the Rayleigh number R, is the dimensionless ratio of the destabilizing buoyancy force $\rho_0 \alpha g \Delta T$ and the stabilizing dissipative force $\nu\kappa\rho_0/d^3$;

$$R = \frac{\alpha g \Delta T d^3}{\kappa \nu}, \tag{2.1}$$

where ρ_0 is the average mass density, α the thermal expansion coefficient, g the accelaration of gravity, ν the kinematic viscosity, κ the thermal diffusivity and d the plate separation. The wave vector q_0 of the instability is of the order of d^{-1} since d is the only length scale in the ideal problem. Thus one arrives at the picture of an instability towards a flow in which fluid rises

in some regions and falls in others, with a characteristic horizontal length scale d. For the Rayleigh number slightly above the critical value the growth of this flow is limited because convective flow transports part of the heat applied, decreasing thereby the temperature gradient and buoyancy force. In general the fluid settles down to a stationary flow regime near threshold. The simplest example of such a flow is the familiar convective roll pattern shown schematically in figure 2.1, but superposition of rolls forming hexagons and squares are also possible.

The "microscopic" equations describing Rayleigh-Bénard convection are the Navier-Stokes equation for the velocity field

$$(\partial_t + \vec{u} \cdot \nabla)(\rho \vec{u}) = -\nabla P + \nabla \cdot \sigma - \rho g \hat{z}, \tag{2.2}$$

with

$$\sigma_{ij} = \eta[\partial_i u_j + \partial_j u_i - \frac{2}{3}\delta_{ij}\partial_k u_k] + \xi \delta_{ij} \partial_k u_k, \tag{2.3}$$

the equation for mass conservation

$$\partial_t \rho + \nabla \cdot \rho \vec{u} = 0 \tag{2.4}$$

and the conservation law for heat

$$(\partial_t + \vec{u} \cdot \nabla)(c_p T) = \nabla \cdot (K \nabla T), \tag{2.5}$$

where the heat produced by the viscous dissipation is neglected in the last equation. The variables in these equations are the density $\rho(\vec{x},t)$, the velocity $\vec{u}(\vec{x},t) = (u,v,w)$, the pressure $P(\vec{x},t)$ and the temperature $T(\vec{x},t)$. The parameters are the shear viscosity η, the bulk viscosity ξ, the constant pressure specific heat c_p, the thermal conductivity K and the acceleration of gravity g. To close the equations the dependence of η, ξ, K on temperature and density and the equation of state $P(\rho,T)$ must be known. In the "Boussinesq approximation" one assumes temperature dependence only in the density $\rho = \bar{\rho}(1-\alpha(T-\bar{T})$, and otherwise an incompressible fluid. The Oberbeck-Boussinesq equations are

$$(\partial_t + \vec{u}\cdot\nabla)\vec{u} = -\nabla(P/\rho) + \nu\nabla^2\vec{u} + g\alpha T\hat{z}, \tag{2.6}$$

$$(\partial_t + \vec{u}\cdot\nabla)T = \kappa\nabla^2 T, \tag{2.7}$$

$$\nabla\cdot\vec{u} = 0, \tag{2.8}$$

where the bars have been dropped on ρ, ν and κ and some constants have been absorbed in the pressure term. The last equation effectively replaces the equation of state and the pressure may now be eliminated in favor of $\vec{u}$ and T.

In the ideal system the boundary conditions for the temperature are

$$\begin{aligned} T(z=0) &= T_u + \Delta T, \\ T(z=d) &= T_u. \end{aligned} \tag{2.9}$$

For the velocity we will take free-slip boundary conditions;

$$\partial_z \vec{u}_\perp = w = 0, \quad \text{at } z = 0, d\,, \tag{2.10}$$

where $\vec{u}_\perp$ is the horizontal 2D component of $\vec{u}$. In the absence of flow the conducting solution is given by $T = T_0(z) = T_u + \Delta T(1 - z/d)$ and also $P = P_0(z)$ to balance the buoyancy force. To study deviations from the conducting state it is useful to define $\theta = T - T_0(z)$ and $p = P - P_0(z)$.

The dimensionless variables are obtained by introduction of the thermal diffusion time accross the cell d^2/κ as the unit time, the cell width d as the unit length, the Rayleigh number R as the dimensionless temperature difference and the dissipative force per unit area $\rho\nu\kappa/d^2$ as the unit of pressure. The dimensionless equations then become

$$\sigma^{-1}(\partial_t + \vec{u}\cdot\nabla)\vec{u} = -\nabla p + \theta\hat{z} + \nabla^2\vec{u}, \tag{2.11}$$

$$(\partial_t + \vec{u}\cdot\nabla)\theta = Rw + \nabla^2\theta, \tag{2.12}$$

$$\partial_z \vec{u}_\perp = w = 0 \quad \text{at } z = 0, 1. \tag{2.13}$$

The equations now depend on just two dimensionless parameters, the Rayleigh number or driving strength R and the Prandtl number $\sigma = \nu/\kappa$.

To perform the actual derivation of the amplitude equation it is convenient to eliminate the pressure and write the equations in the form

$$\nabla^2\theta + Rw = \partial_t\theta + (\vec{u}_\perp \cdot \nabla_\perp)\theta + w\partial_z\theta, \tag{2.14}$$

$$\begin{aligned}\nabla_\perp^2\theta + \nabla^4 w &= \sigma^{-1}[\partial_t\nabla^2 w - \partial_z\nabla_\perp \cdot ((\vec{u}_\perp \cdot \nabla_\perp)\vec{u}_\perp + w\partial_z\vec{u}_\perp) \\ &\quad +\nabla_\perp^2((\vec{u}_\perp \cdot \nabla_\perp)w + w\partial_z w)].\end{aligned} \tag{2.15}$$

Besides these equations there is an equation for the vertical vorticity $\Omega_z = (\nabla \times \vec{u})_z$. Once w and Ω_z are known $\vec{u}$ may be calculated from the continuity equation $\nabla \cdot \vec{u} = 0$. The amplitude equation is now in principle derived by means of a multiple scales expansion of the equations around the conducting solution $\theta = \vec{u} = 0$. We will limit ourselves to $\sigma \to \infty$. This implies $\Omega_z \equiv 0$ and also eliminates the terms on the right hand side of (15). Keeping the Prandtl number finite would introduce some difficulties related to the fact that $\Omega_z \neq 0$ and it would take us too far from our main objective, which is simply to demonstrate a derivation of an amplitude equation. In the limit $\sigma \to \infty$ and the free-slip boundary conditions, the values of the parameters occurring in the derived amplitude equation can be obtained analytically.

First we solve the linear threshold problem and look for the neutrally stable mode (growth rate zero)

$$\begin{aligned} \theta(x,z) &= \bar{\theta}(q,z)e^{iqx} + c.c., \\ w(x,z) &= \bar{w}(q,z)e^{iqx} + c.c., \\ u(x,z) &= \bar{u}(q,z)e^{iqx} + c.c.. \end{aligned} \tag{2.16}$$

That is, we solve

$$\begin{bmatrix} (\partial_z^2 - q^2) & R_c(q) \\ q^2 & -(\partial_z^2 - q^2)^2 \end{bmatrix} \begin{bmatrix} \bar{\theta}(q,z) \\ \bar{w}(q,z) \end{bmatrix} = 0, \tag{2.17}$$

with the q-dependent Rayleigh number $R = R_c(q)$. Keeping in mind the free-slip boundary conditions we readily find (with an arbitrary overall normalization)

$$\begin{aligned} \bar{\theta}(q,z) &= (4\sqrt{2}/\pi^2)(q^2+\pi^2)^2 \sin \pi z, \\ \bar{w}(q,z) &= (4\sqrt{2}/\pi^2)q^2 \sin \pi z, \\ \bar{u}(q,z) &= (-4i\sqrt{2}/\pi)q \cos \pi z. \end{aligned} \tag{2.18}$$

The minimum $R_c(q) \equiv R_{c,0} = 27\pi^4/4$ occurs for $q = q_0 = \pi/\sqrt{2}$.

We write $\bar{\theta}(q_0, z) = \bar{\theta}_0$ etc. and expand in the small parameter

$$\epsilon = \frac{R_c - R_{c,0}}{R_{c,0}} \tag{2.19}$$

as follows

$$\begin{aligned} \theta &= \epsilon^{1/2}\theta_0 + \epsilon\theta_1 + \ldots, \\ w &= \epsilon^{1/2}w_0 + \epsilon w_1 + \ldots, \\ u &= \epsilon^{1/2}u_0 + \epsilon u_1 + \ldots, \end{aligned} \tag{2.20}$$

where

$$\begin{aligned} \theta_0 &= A_0(X,Y,T)e^{iq_0x}\bar{\theta}_0(z) + c.c., \\ w_0 &= A_0(X,Y,T)e^{iq_0x}\bar{w}_0(z) + c.c., \\ u_0 &= A_0(X,Y,T)e^{iq_0x}\bar{u}_0(z) + c.c.. \end{aligned} \tag{2.21}$$

The variables $X = \epsilon^{1/2}x$, $Y = \epsilon^{1/4}y$ and $T = \epsilon t$ are the slow varying variables. For the differential operators we must make the replacements $\partial_x \to \partial_x + \epsilon^{1/2}\partial_X$, $\partial_y \to \partial_y + \epsilon^{1/4}\partial_Y$ and $\partial_t \to \partial_t + \epsilon\partial_T$ etc.. The scaling of the slow variables with ϵ is formally determined by the ultimate consistency of the expansion. We rewrite the original equations ($\sigma \to \infty$) as

$$\mathcal{L}\begin{bmatrix} \theta \\ w \end{bmatrix} = \begin{bmatrix} \partial_t\theta + (u_\perp \cdot \nabla_\perp)\theta + w\partial_z\theta \\ 0 \end{bmatrix}, \tag{2.22}$$

where $\mathcal{L}$ has the expansion

$$\mathcal{L} = \mathcal{L}_0 + \epsilon^{1/2}\mathcal{L}_1 + \epsilon\mathcal{L}_2 + \ldots, \tag{2.23}$$

with

$$\begin{aligned}
\mathcal{L}_0 &= \begin{bmatrix} \partial_z^2+\partial_x^2 & R_{c,0} \\ -\partial_x^2 & -(\partial_z^2+\partial_x^2)^2 \end{bmatrix}, \\
\mathcal{L}_1 &= \begin{bmatrix} 1 & 0 \\ -1 & -2(\partial_x^2+\partial_z^2) \end{bmatrix} (2\partial_x\partial_X+\partial_Y^2), \\
\mathcal{L}_2 &= \begin{bmatrix} 1 & 0 \\ -1 & -2(\partial_x^2+\partial_z^2) \end{bmatrix} \partial_x^2 \\
&\quad + \begin{bmatrix} 0 & R_{c,0} \\ 0 & (2\partial_x\partial_X+\partial_Y^2)^2 \end{bmatrix}.
\end{aligned} \tag{2.24}$$

The r.h.s. has the expansion

$$\begin{aligned}
&\partial_t\theta + (\vec{u}_\perp\cdot\nabla_\perp)\theta + w\partial_z\theta = \epsilon[u_0\partial_x\theta_0 + w_0\partial_z\theta_0] \\
&+\epsilon^{3/2}[\partial_T\theta_0 + (u_1\partial_x\theta_0 + u_0\partial_x\theta_1) + (w_1\partial_z\theta_0 + w_0\partial_z\theta_1)] \\
&+\mathcal{O}(\epsilon^{3/2}) + \mathcal{O}(\epsilon^2),
\end{aligned} \tag{2.25}$$

where the terms $\mathcal{O}(\epsilon^{3/2})$ not displayed explicitely are not relevant in what follows.

Up to $\mathcal{O}(\epsilon)$ we have

$$\mathcal{L}_0 \begin{bmatrix} \theta_1 \\ w_1 \end{bmatrix} = -\mathcal{L}_1 \begin{bmatrix} \theta_0 \\ w_0 \end{bmatrix} + \begin{bmatrix} u_0\partial_x\theta_0 + w_0\partial_z\theta_0 \\ 0 \end{bmatrix}, \tag{2.26}$$

and we would like to invert this equation to obtain (θ_1, w_1). For this to be possible however we must require the r.h.s. to be orthogonal to all zero eigenvectors of $\mathcal{L}_0^\dagger$. The relevant eigenvector is precisely (θ_0, w_0) which depends on the fast variable x as $e^{\pm iq_0 x}$. The nonlinear terms on the r.h.s. depend on the fast variable x as $e^{\pm 2iq_0 x}$ or are independent of x, and they are automatically orthogonal to (θ_0, w_0). The linear terms do involve the dangerous exponential factors $e^{\pm iq_0 x}$ and we might expect a solvability condition at this order. Since we are expanding around the minimum q_0 of $R_c(q)$ however, this condition is identically satisfied. To see this we use the identity (obtained by differentiating (17) with respect to q)

$$\begin{bmatrix} \partial_z^2 - q_0^2 & R_{c,0} \\ q_0^2 & -(\partial_z - q_0^2)^2 \end{bmatrix} \begin{bmatrix} \bar{\theta}_0'(z) \\ \bar{w}_0'(z) \end{bmatrix} - 2q_0 \begin{bmatrix} 1 & 0 \\ -1 & -2(\partial_z^2 - q_0^2) \end{bmatrix} \begin{bmatrix} \bar{\theta}_0(z) \\ \bar{w}_0(z) \end{bmatrix} = 0, \tag{2.27}$$

where $\bar{\theta}_0' = \partial_q \bar{\theta}(q) \mid_{q=q_0}$ etc., and write

$$\begin{bmatrix} \theta_1 \\ w_1 \\ u_1 \end{bmatrix} = \begin{bmatrix} \tilde{\theta}_1 \\ \tilde{w}_1 \\ \tilde{u}_1 \end{bmatrix} + (2q_0)^{-1}(2\partial_x \partial_X + \partial_Y^2) A_0 \begin{bmatrix} \bar{\theta}_0'^{(z)} \\ \bar{w}_0'(z) \\ \bar{u}_0'(z) \end{bmatrix} + c.c.. \tag{2.28}$$

Then (26) reduces to

$$\mathcal{L}_0 \begin{bmatrix} \tilde{\theta}_1 \\ \tilde{w}_1 \end{bmatrix} = \begin{bmatrix} u_0\partial_x\theta_0 + w_0\partial_z\theta_0 \\ 0 \end{bmatrix} \tag{2.29}$$

which can now be inverted to give

$$\begin{bmatrix} \tilde{\theta}_1 \\ \tilde{w}_1 \end{bmatrix} = \left(A_0^2 e^{2iq_0x} \begin{bmatrix} f_1(z) \\ f_2(z) \end{bmatrix} + A_1 e^{iq_0x} \begin{bmatrix} \bar{\theta}_0(z) \\ \bar{w}_0(z) \end{bmatrix} + c.c. \right)$$
$$+|A_0|^2 \begin{bmatrix} f_3(z) \\ f_4(z) \end{bmatrix}. \tag{2.30}$$

We obtain $f_1 = f_2 = f_4 = 0$ and $f_3 = -18\pi\sin(2\pi z)$, the function A_1 depends on the slow variables and remains unknown at this stage.

We may now proceed with the next order $\mathcal{O}(\epsilon^{3/2})$, we obtain

$$\mathcal{L}_0 \begin{bmatrix} \theta_2 \\ w_2 \end{bmatrix} = G, \tag{2.31}$$

where G contains many terms. The requirement that G should not drive any zero-eigenvalue eigenvector of $\mathcal{L}_0$ yields at this order a nontrivial solvability condition, which in effect gives the amplitude equation. Again we need only collect terms proportional to $e^{\pm iq_0x}$, we obtain

$$G_{\pm q_0} = -\begin{bmatrix} -1 & 0 \\ -1 & -2(\partial_x^2 + \partial_z^2) \end{bmatrix} \begin{bmatrix} \bar{\theta}_0 \\ \bar{w}_0 \end{bmatrix} \left([(2\partial_x\partial_X + \partial_Y^2)A_1 + \partial_X^2 A_0]e^{iq_0x} + c.c. \right)$$

$$
-\begin{bmatrix} 1 & 0 \\ -1 & -2(\partial_x^2+\partial_z^2) \end{bmatrix}\begin{bmatrix} \bar{\theta}_0' \\ \bar{w}_0' \end{bmatrix}\frac{1}{2q_0}\left((2\partial_x\partial_X+\partial_Y^2)^2 A_0 e^{iq_0x}+c.c.\right)
$$

$$
-\left(\begin{bmatrix} \partial_T A_0 & R_{c,0}A_0 \\ 0 & (2\partial_x\partial_X+\partial_Y^2)^2 A_0 \end{bmatrix}\begin{bmatrix} \bar{\theta}_0 \\ \bar{w}_0 \end{bmatrix}e^{iq_0x}+c.c.\right)
$$

$$
+\begin{bmatrix} \tilde{u}_1\partial_x\theta_0+u_0\partial_x\tilde{\theta}_1+\tilde{w}_1\partial_z\theta_0+w_0\partial_z\tilde{\theta}_1 \\ 0 \end{bmatrix}_{\pm q_0}
$$

$$
+B_0+B_2e^{2iq_0x}+B_3e^{3iq_0x}+c.c.. \tag{2.32}
$$

The symbol $[\ldots]_{\pm q_0}$ means that we are only referring to the terms $\propto e^{\pm iq_0x}$. The first term in $G_{\pm q_0}$ may be eliminated using the same trick as we did for $\mathcal{O}(\epsilon)$. The operator $\mathcal{L}_0$ is self-adjoint under the following scalar product for the vectors $V_a=(\theta_a,w_a)$ and $V_b=(\theta_b,w_b)$:

$$
(V_a,V_b)=\int dx_\perp^2 dz\left((\nabla_\perp\theta_a^*)\cdot(\nabla_\perp\theta_b)+R_{c,0}w_a^*w_b\right). \tag{2.33}
$$

The solvability requires orthogonality of $G_{\pm q_0}$ under this definition of the scalar product to the zero eigenvalue mode (θ_0,w_0).

The 4^{th} term in $G_{\pm q_0}$ is readily evaluated to give

$$
\begin{bmatrix} -72\sqrt{2}\pi^2|A_0|^2A_0e^{iq_0x}+c.c. \\ 0 \end{bmatrix}, \tag{2.34}
$$

and further we have

$$\frac{1}{2q_0}\begin{bmatrix} \bar{\theta}_0'(z) \\ \bar{w}_0'(z) \end{bmatrix} = \frac{4\sqrt{2}}{\pi^2}\begin{bmatrix} 3\pi^2 \\ 1 \end{bmatrix} \sin \pi z. \tag{2.35}$$

Finally then, requiring the mentioned orthogonality yields the amplitude equation in the form

$$\frac{2}{3\pi^2}\partial_T A_0 = A_0 + \frac{8}{3\pi^2}\left(\partial_X + \frac{1}{2iq_0}\partial_Y^2\right)^2 A_0 - \frac{8}{3\pi^2}|A_0|^2 A_0. \tag{2.36}$$

If we rewrite the amplitude equation, which itself is of universal form, in the original variables with $A = \epsilon^{1/2} A_0$ etc., it becomes more obvious in which way the physical properties of the system enter in its coefficients. We obtain for the particular case of Rayleigh-Bénard convection discussed here

$$\partial_t A = \frac{3\pi}{2}\epsilon A + 4(\partial_x + \frac{1}{2iq_0}\partial_y^2)^2 A - 4|A|^2 A. \tag{2.37}$$

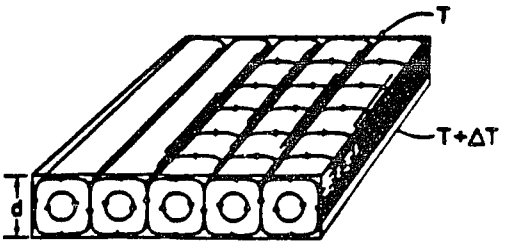

Figure 2.1: Schematic flow pattern for Rayleigh-Bénard convection in an ideal roll state. Shown are the stream lines, in parts of the cell the fluid rises while in others it falls. The figure is from reference [29].

Chapter 3

The harmonically forced Landau equation.

In this chapter we discuss the Landau equation (LE) with an external harmonic forcing. The most general form of this equation (up to cubic non linearity) is after elimination of irrelevant parameters and inclusion of the external forcing $F(t)$

$$\left[\frac{d}{dt} - (1 + ic_1) + (1 + ic_3)|\Psi|^2\right] \Psi = F(t). \tag{3.1}$$

The parameters c_1 and c_3 are real. We will exclusively consider the case that the forcing has the simple harmonic form

$$F(t) = F_0 e^{i\omega t}. \tag{3.2}$$

3.1 Phase-locked states.

When $F(t)$ has the harmonic form (3.2), the forcing strength F_0 may be taken to be real and positive without loss of generality. Furthermore, in this case the constant c_1 may be incorporated in ω or vice versa. The most general form of the LE with a harmonic forcing therefore becomes

$$\left[\frac{d}{dt} - 1 + (1 + ic_3)|\Psi|^2\right] \Psi = F_0 e^{i\omega t}. \tag{3.3}$$

For $F_0 = 0$ (unforced system) the solution of (3.3) will relax on the stable limit cycle $\Psi_\infty(t) = \exp(-ic_3 t + i\alpha)$, where α is determined by the initial condition. We are interested in phase-locked solutions of the form

$$\Psi_L(t) = A_L \exp(i\omega t + i\phi). \tag{3.4}$$

It is easy to see that such solutions exist for all c_3, F_0 and ω, and can be found from the following equations:

$$F_0^2 = \left[(-1 + A_L^2)^2 + (\omega + c_3 A_L^2)^2\right] A_L^2, \tag{3.5}$$

$$\phi = -\tan^{-1}\left(\frac{\omega + c_3 A_L^2}{-1 + A_L^2}\right). \tag{3.6}$$

To study the linear stability of these phase-locked states we add a small perturbation $\delta\Psi(t)$ to (3.4) and linearize the equation of motion for $\delta\Psi(t)$. The linearized equation of motion for $\delta\Psi(t)$ has solutions of the form

$$\delta\Psi(t) = (ae^{pt} + be^{p^* t})e^{i\omega t}. \tag{3.7}$$

For stability of the phase-locked states we have to require $Rep < 0$, this gives the stability criterion

$$-1 + 2A_L^2 > 0 \tag{3.8}$$

$$(\omega + 2c_3 A_L^2)^2 + (-1 + 2A_L^2)^2 - (1 + c_3^2)A_L^4 > 0. \tag{3.9}$$

The phase diagram, that is, a figure in the $F_0 - \omega$ plane which illustrates the different possible stable states, may be categorized into three different classes, the relevant parameter being the natural frequency c_3 of the unforced equation. The different classes are $c_3^2 < 1/3$, $1/3 < c_3^2 < 3$ and $c_3^2 > 3$. The proof of this involves some algebra.

First we observe that (3.5) may be interpreted as defining F_0 as function of A_L with parameters ω and c_3, let us denote this function by $f_{\omega,c_3}(A_L)$.

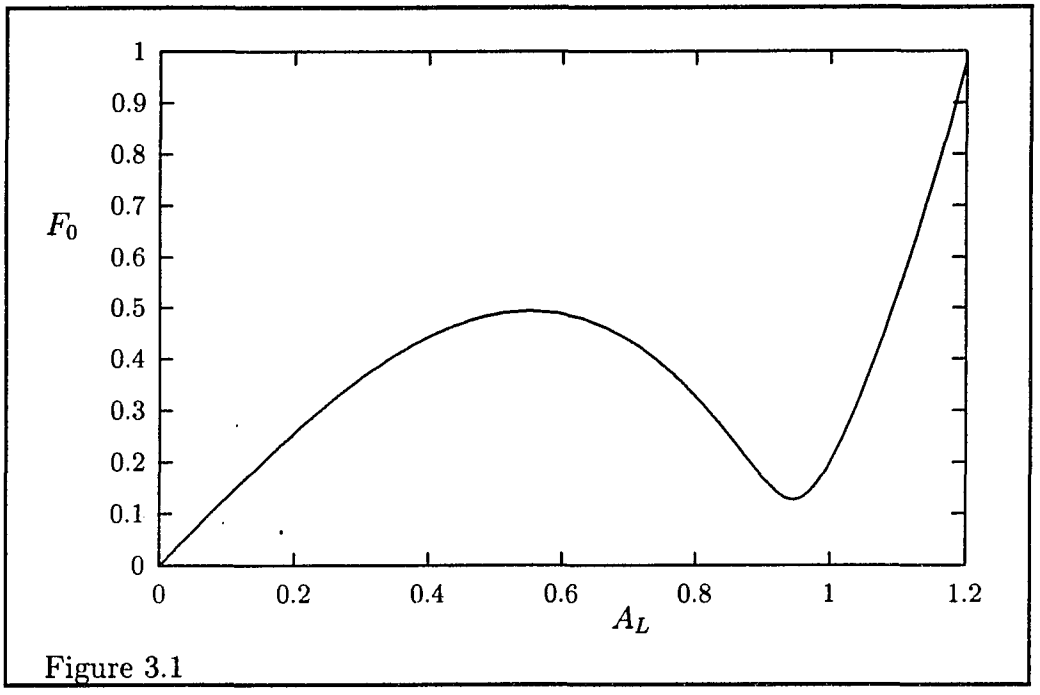

Figure 3.1: The function $f_{\omega,c_3}(A_L)$ for $c_3 = 1.1$, $\omega = -0.9$.

The function $f_{\omega,c_3}(A_L)$ has extrema in

$$A_{L\pm} = \left[\frac{2(1-c_3\omega) \pm \sqrt{4(1-c_3\omega)^2 - 3(1+c_3^2)(1+\omega^2)}}{3(1+c_3^2)}\right]^{1/2}. \qquad (3.10)$$

A plot of $f_{\omega,c_3}(A_L)$ for $c_3 = 1.1$, $\omega = -0.9$ is shown in figure 3.1. To make things not more confusing than necessary we asume for now that $c_3 > 0$.

The extrema of $f_{\omega,c_3}(A_L)$ exist only for $\omega'_- < \omega < \omega'_+$ and $c_3^2 < 3$, or for

$\omega < \omega'_+$ and $c_3^2 > 3$, where

$$\omega'_\pm = \frac{-4c_3 \pm \sqrt{3}(1+c_3^2)}{3-c_3^2}. \tag{3.11}$$

The stability criterion (3.9) implies $A_L^2 < A_{L-}^2$ or $A_L^2 > A_{L+}^2$. Further it is so that $A_{L+}^2 > 1/2$ for $\omega'_- < \omega < \omega'_+$ if $c_3 < 1/\sqrt{3}$, for $\omega'_- < \omega < \omega_+$ if $1/\sqrt{3} < c_3 < \sqrt{3}$ and for $\omega < \omega_+$ if $c_3 > \sqrt{3}$. Also, $A_{L-}^2 > 1/2$ for $\omega < \omega_-$ or $\omega > \omega_+$ if $c_3 < 1/\sqrt{3}$ and for $\omega < \omega_-$ if $c_3 > 1/\sqrt{3}$. The newly introduced frequenties $\omega_\pm$ are given by

$$\omega_\pm = -c_3 \pm \frac{1}{2}\sqrt{1+c_3^2}. \tag{3.12}$$

Finally, the following inequalities hold

$$\begin{aligned} \omega'_+ &> \omega_+ \quad \text{for all } c_3 \\ \omega'_- &< \omega_- \quad \text{for } c_3 < \sqrt{3}. \end{aligned} \tag{3.13}$$

Putting all the observations made above together we deduce that if $c_3 < 1/\sqrt{3}$ two closed bistable regions are present for $\omega'_- < \omega < \omega_-$, and $\omega_+ < \omega < \omega'_+$. Bistable regions being regions in the $F_0 - \omega$ plane in which there exist two different stable phase-locked states of the form (3.4). For $1/\sqrt{3} < c_3 < \sqrt{3}$ one closed bistable region is present for $\omega'_- < \omega < \omega_-$. If $c_3 > \sqrt{3}$ one open bistable region is present for $\omega < \omega_-$. We may, based on the bistable regions,

classify the phase diagram into three classes: $c_3 < 1/\sqrt{3}$, $1/\sqrt{3} < c_3 < \sqrt{3}$ and $c_3 > \sqrt{3}$.

The different classes of the phase diagram have in common that for $\omega \approx -c_3$ the line on which bifurcations involving a stable phase-locked state occur $F_+(\omega) = f_{\omega,c_3}(A_{L+}) \propto |\omega+c_3|$. For ω far away from $\omega_\pm$ and/or $\omega'_\pm$ bifurcations of the phase-locked state occurs on the line $F_{1/2}(\omega) = f_{\omega,c_3}(1/\sqrt{2}) \propto |\omega + \frac{1}{2}c_3|$.

Summerizing we can say that bifurcations involving the phase-locked states occur on the lines $F_+(\omega)$, $F_-(\omega)$ and $F_{1/2}(\omega)$, where F_+ and $F_{1/2}$ have been defined above and $F_-(\omega) = f_{\omega,c_3}(A_{L-})$. The relevant lines depend on the actual value of ω. The relevant ω ranges for the different lines are given in table 3.1. For some values of ω all three lines are present, forming the bistable regions.

Typical phase diagrams are shown in figure 3.2. In the regions marked **L** there is one and only one stable phase-locked state of the form (3.4). The regions marked **B** are the bistable regions. In the regions marked **P** stable phase-locked states of the form (3.4) do not exist.

So far, all our observations were made for $c_3 > 0$. The inclusion of the situation for $c_3 < 0$ can now simply be made by using symmetry ar-

Bifurcation	$c_3^2 < 1/3$	$1/3 < c_3^2 < 3$	$c_3^2 > 3$
$F_{1/2}(\omega)$	$\omega > \omega_+ , \omega < \omega_-$	$\omega > \omega_+ , \omega < \omega_-$	$\omega > \omega_+ , \omega < \omega_-$
$F_+(\omega)$	$\omega'_- < \omega < \omega'_+$	$\omega'_- < \omega < \omega_+$	$\omega < \omega_+$
$F_-(\omega)$	$\omega'_- < \omega < \omega_-$ $\omega_+ < \omega < \omega'_+$	$\omega'_- < \omega < \omega_-$	$\omega < \omega_-$

Table 3.1: Lines on which bifurcations occur (left column) and their relevant ω range for the three different classes of the phase diagram. The frequenties $\omega_\pm$ and $\omega'_\pm$ are given by $\omega_\pm = -c_3 \pm \frac{1}{2}\sqrt{1+c_3^2}$ and $\omega'_\pm = \frac{-4c_3 \pm \sqrt{3}(1+c_3^2)}{3-c_3^2}$. The table is for $c_3 > 0$, to obtain the results for $c_3 < 0$ one simply has to change $\omega_\pm \to \omega_\mp$ and $\omega'_\pm \to \omega'_\mp$.

guments. We observe that the equations on which we based our conclusions, equations (3.5), (3.8) and (3.9), are invariant under the transformation $(\omega, c_3) \rightarrow (-\omega, -c_3)$. Therefore our analyses for a $c_3 > 0$ is unaltered for $\tilde{c}_3 = -c_3$ provided we put $\tilde{\omega}_{\pm} = \omega_{\mp}$ and $\tilde{\omega}'_{\pm} = \omega'_{\mp}$. This implies that the phase diagram for a $\tilde{c}_3 < 0$ is obtained by reflection in $\omega = 0$ of the diagram belonging to $c_3 = -\tilde{c}_3$. The solution $\Psi_L(t)$ belonging to a certain $(-c_3, -\omega)$ pair is however not the same as the solution belonging to (c_3, ω) but undergoes a phase shift; $\phi(-c_3, -\omega) = -\phi(c_3, \omega)$. This property may infact be generelized to hold for any solution of the forced Landau equation and not just for the phase-locked states Ψ_L, provided $F(t)$ is of the simple form (3.2).

The property we have in mind is that if $\Psi_{L,+}(t)$ is a solution of the forced LE (3.3) belonging to the parameters (F_0, c_3, ω), then $\Psi_{L,-}(t)$ with

$$\begin{aligned} Re\, \Psi_{L,-}(t) &= Re\, \Psi_{L,+}(t) \\ Im\, \Psi_{L,-}(t) &= -Im\, \Psi_{L,+}(t) \end{aligned} \tag{3.14}$$

is a solution of the same equation belonging to the parameters $(F_0, -c_3, -\omega)$. From the stability conditions (3.8) and (3.9) it follows that $\Psi_{L,-}$ has the same stability properties as $\Psi_{L,+}$. We have already seen the implications of this

property for the phase-locked states Ψ_L. For the phase diagram in general it means that the bifurcations occurring for $c_3 < 0$ will be qualitatively the same as for $c_3 > 0$, with this difference that the trajectories (curves in the complex plane) will be reflected with respect to the real axis, clockwise oriented cycles becoming anti-clockwise oriented etc..

The property mentioned above is important for our further analyses of solutions of (3.3), which will follow in the next section and for which we almost entirely have to rely on numerical results. Thanks this property it suffices to analyze the behaviour for $c_3 > 0$.

3.2 The complete phase diagram.

Outside the regions **L** and **B**, that is in the region **P**, phase locked states Ψ_L do still exist they are however never stable. For a discussion of the phase diagram of (3.3) in general it is useful to make the transformation

$$u(t) = \Psi(t)e^{-i\omega t}. \tag{3.15}$$

The equation for u(t) is then autonomous:

$$\left[\frac{d}{dt} - 1 + i\omega + (1 + ic_3)|u|^2\right] u(t) = F_0, \tag{3.16}$$

and the phase locked states Ψ_L appear as critical points $u_L = A_L e^{i\phi}$ of this equation.

We have integrated (3.16) numerically using a Runge-Kutta method. In order to make the search for limit cycles and other possible stable solutions a responsible one, we have performed a complete analyses of the critical points of (3.16). The details are given in Appendix A. Our conclusions are as follows.

In the regions **L** and **B** the critical points that are positive attractors are either nodes or spirals, dependent on the parameters c_3, ω and F_0. The critical point with the property $A_{L-} < A_L < A_{L+}$ is a saddle point. Codimension

two bifurcations occur in the points $F_-(\omega_-)$ and $F_-(\omega_+)$ for $c_3^2 < 1/3$ and in $F_-(\omega_-)$ and $F_+(\omega_+)$ for $c_3^2 > 1/3$.

The response of the Landau equation in region **P** is a periodic state (limit cycle) $u_P(t)$ with a period that can be shown to reduce to $T_P \to \frac{2\pi}{|\omega+c_3|}$ in the $F_0 \to 0$ limit. The proof of this property is given in Appendix B.

Bistable regions **B1**, **B2** and **B3** occur, with structurally different flow patterns, in each of which a stable phase locked state u_L coexists with a stable limit cycle $u_P(t)$. The regions **B1** also occur for $c_3 = 0$, see []. The regions **B2** and **B3** exclusively occur for $c_3^2 > 1/3$. Two **B1** regions are present for $c_3^2 < 1/3$ and one **B1** region remains present for all $c_3^2 > 1/3$. Numerically we find that **B1** is bounded by $F_{1/2}(\omega)$ and $F_+(\omega)$ presisely as observed for $c_3 = 0$. For one of its boundaries however, we were not able to find an analytic expression, it is roughly indicated by a dashed line. Regions **B2** and **B3** (figure 1.f) are bounded by $F_\pm(\omega)$ and $F_{1/2}(\omega)$ partially. Point b is numerically found to coincide with $F_+(\omega_+)$, a point of codimension two bifurcation. The dashed lines shown as boundaries of **B2** and **B3** are obtained numerically.

Details of the various bifurcations occurring for $c_3^2 < 1/3$ are not different from the case that $c_3 = 0$, which is discussed in [37], and we will refrain from

further description here. Also the various bifurcations occurring for $c_3^2 > 1/3$ for as far as they do not involve **B2** or **B3**, do not qualitatively differ from the $c_3 = 0$ case and will not be further discussed here. Bifurcations involving the regions **B2** or **B3** do present new fearures not present for $c_3 = 0$ and we will discuss them in some detail.

Going from **L** to **B2** or **B3** (see figure 3.2.f) we observe a bifurcation from a situation with one sink (phase locked state) to a bistable situation with a sink and a limit cycle. On a-e-d a saddleloop occurs, on d-c a saddleloop and saddlenode occur simultaniously. See figure 3.4c and d respectively. In **B2** the region of attraction for the sink is formed by the heteroclinic orbits between the saddle and the source, figure 3.4f and figure 3.3b for a realistic plot. In **B3** the region of attraction for the sink is formed by a repelling closed orbit, figure 3.4g and figure 3.3a. Going from **B2** to **B3** a saddleloop occurs on b-e, forming the region of attraction for the sink in this case, figure 3.4e.

When entering **P** from **B2**, the sink is eliminated on a-b by a saddle-node bifurcation, leaving only a stable limit cylcle and a source in **P**. See figure 3.4h and j. The saddlenode does not lie on the limit cycle, contrary to the situation on F_+ left of a, where the saddlenode does lie on the limit cycle.

When entering **P** from **B3** the repelling closed orbit shrinks to a point on b-c, leaving in **P** in the region bounded by b-c-f a stable limit cycle, a saddle and two sources. See figure 3.4i and k. Saddle-node bifurcations occur on b-c-f, leaving the limit cycle and a source in **P** outside b-c-f. An ordinary Hopf bifurcation occurs on $F_{1/2}$ right of point c.

Returning to the original equation (3.3) for $\Psi(t)$, the existence of a unique periodic solution $u_P(t)$ in the regions **B1**, **B2**, **B3** and **P** implies that equation (3.3) has a unique quasi-periodic state $\Psi_{QP}(t) = u_P(t)e^{i\omega t}$ in these regions. The state $\Psi_{QP}(t)$ reduces to a periodic state with a period equal to $n \times$ (*period of the forcing*) whenever $n \frac{2\pi}{|\omega|} = m\, T_P$, where T_P is the period of the periodic state u_P and m and n are integers. Frequenty locking is however not expected to occur because of the following. The equation (3.16) for $u(t)$ is isotropic in time, a translation in time leaves the equation invariant. The "natural frequency" of the equation in region **P**, $\omega_P = 2\pi/T_P$ is therefore expected to vary continuously as function of ω, F_0 and c_3 ruling out the possibility of frequency locking. We have tested this hypothesis for various values of m and n and the result was positive; no frequency locking was observed within the numerical accuracy.

The situation changes if $F(t)$ is of a more general periodic form. In

that case it is not possible to transform (3.3) to an autonomous equation. So besides a "natural frequency" an external frequency will occur in the equation for $\Psi(t)$ or any transformation of it. Therefore frequency locking is likely to occur in this situation. We have analyzed (numerically) (3.1) for a forcing of the form

$$F(t) = F_0(c_0 + e^{i\omega t}). \tag{3.17}$$

The outlines of the phase diagram were obtained by using a Fast Fourier Transform, for details see Appendix C.2. The result for $c_0 = 0.1$, $c_1 = 0$, $c_3 = -1$ is shown in figure 3.5.a The shape of the phase locked region is not too different from the situation for $c_0 = 0$ because we have kept c_0 small. Close observation of the region **P** however shows that frequency locking now does occur, see figure 3.5.b for $m = 2$, $n = 3$.

Figure 3.2: (Next page) Typical phase diagrams for the forced Landau equation. The different panels are for different values of the natural frequency c_3 representative for the different classes, panels (a), (b), (c) $c_3 = 0.1$; panel (d) $c_3 = 1.1$; panel (e) $c_3 = 2.1$. The panels (b) and (c) show the two bistable regions present for $c_3 = 0.1$ in detail. Panel (f) shows the, in the global picture invisible, bistable regions **B2** and **B3** for $c_3 = 10.1$. The diagrams are for $c_3 > 0$, the corresponding diagrams for $c_3 < 0$ are obtained by reflection in $\omega = 0$, as explained in the text. In region **L** there is one stable state Ψ_L while in the bistable region **B** there are two different stable states Ψ_L. In the region labeled **P** the states Ψ_L are unstable, here there exists one stable periodic state (section 3.2). Analytic expressions for the lines $F_{1/2}$ and $F_{\pm}$ are given in the text (see also table 1). The existence of the stable periodic state extends slightly into region **L** forming bistable regions **B1**, **B2** and **B3** in which Ψ_L and Ψ_P are both stable. We find numerically that they are bounded by $F_{1/2}$, F_+, F_- and the dashed lines, for which we have no analytic expressions available.

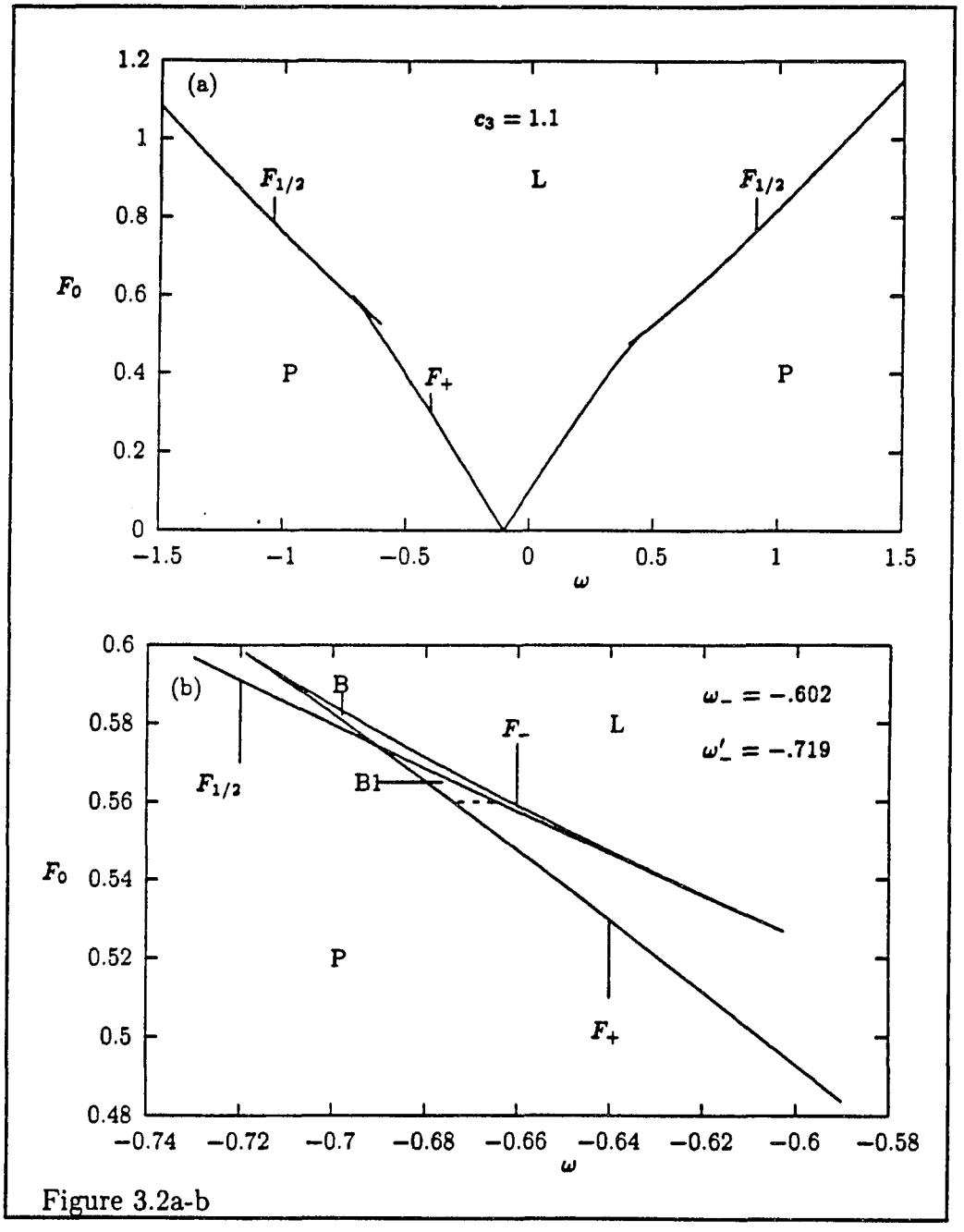
(a)
$c_3 = 1.1$
L
P
P
$F_{1/2}$
$F_{1/2}$
F_+
F_0
ω
1.2
1
0.8
0.6
0.4
0.2
0
−1.5
−1
−0.5
0
0.5
1
1.5
(b)
B
B1
F_-
L
P
$F_{1/2}$
F_+
$\omega_- = -.602$
$\omega'_- = -.719$
F_0
ω
0.6
0.58
0.56
0.54
0.52
0.5
0.48
−0.74
−0.72
−0.7
−0.68
−0.66
−0.64
−0.62
−0.6
−0.58

Figure 3.2a-b

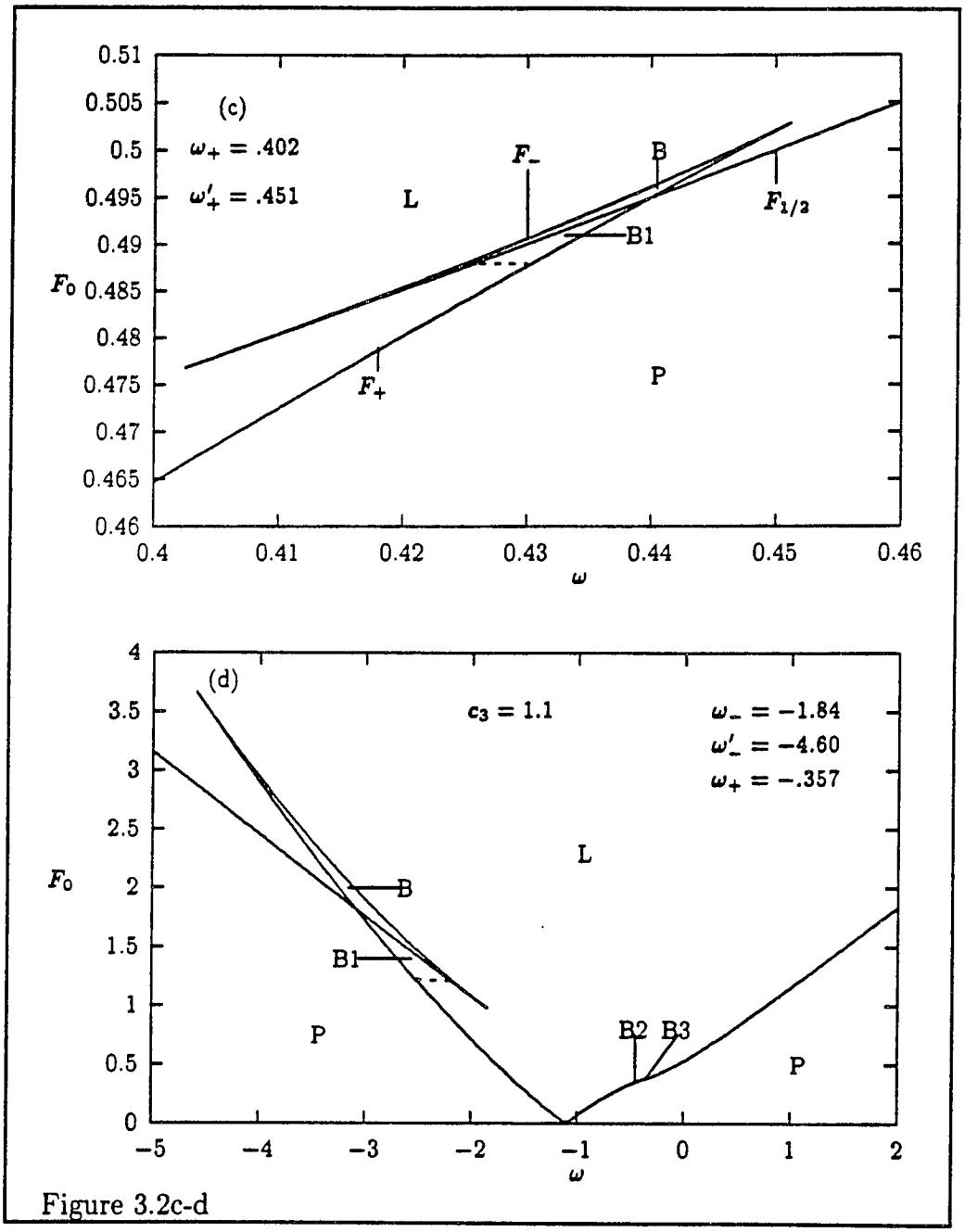
(c)
$\omega_+ = .402$
$\omega'_+ = .451$
L
F_-
B
$F_{1/2}$
B1
F_+
P
F_0
ω
(d)
$c_3 = 1.1$
$\omega_- = -1.84$
$\omega'_- = -4.60$
$\omega_+ = -.357$
L
B
B1
P
B2 B3
P
F_0
ω

Figure 3.2c-d

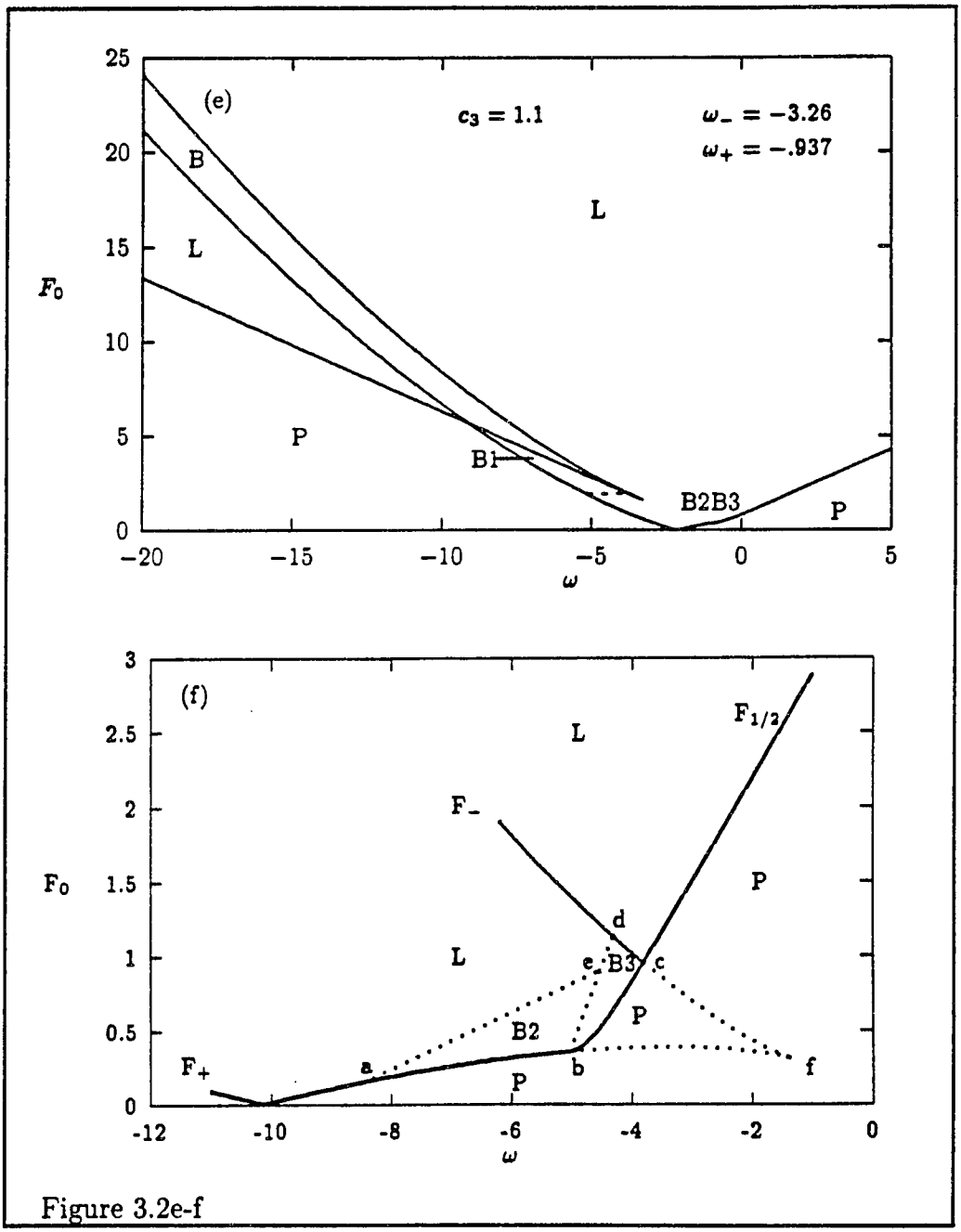
(e)
$c_3 = 1.1$
$\omega_- = -3.26$
$\omega_+ = -.937$
B
L
L
P
B1
B2B3
P
F_0
ω
(f)
L
$F_{1/2}$
F_-
P
d
L
e
B3
c
P
B2
F_+
a
b
f
P
F_0
ω

Figure 3.2e-f

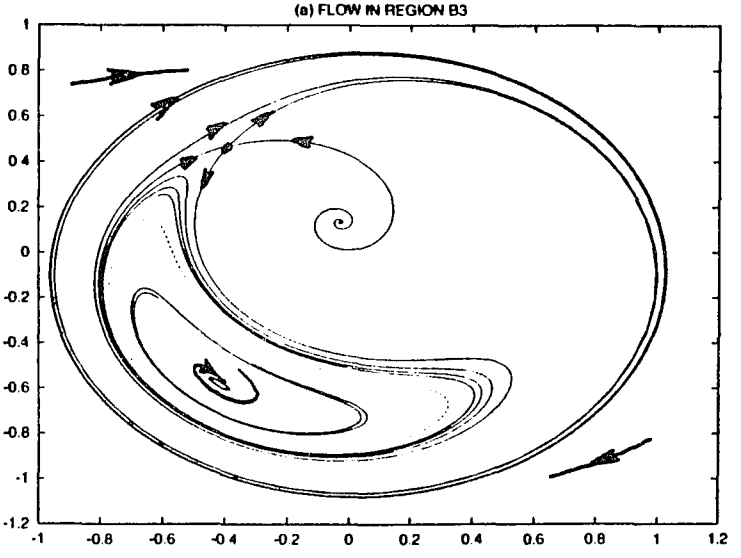

Figure 3.3a

Figure 3.3: Flow for the harmonically forced LE in the complex $u-$plane in region **B3** (panel a) and region **B2** (panel b) of the phase diagram (figure 3.2f). The repelling closed orbit occurring in region **B3** is represented by a dashed line.

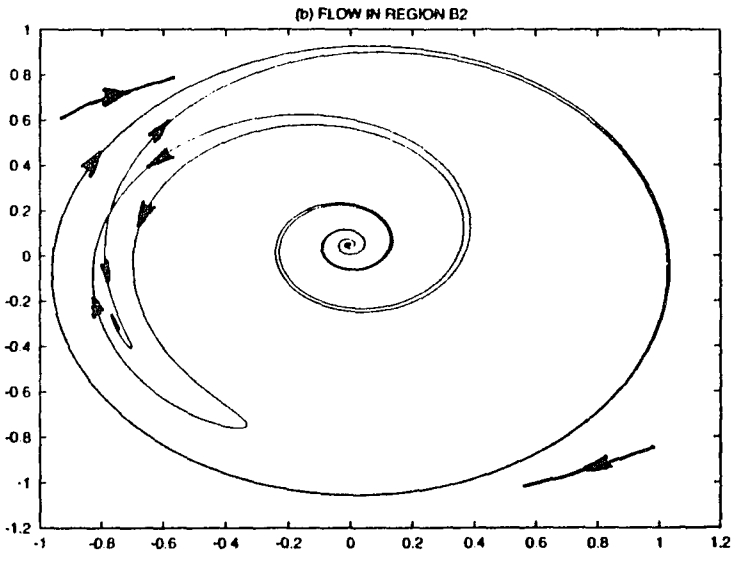
(b) FLOW IN REGION B2
1
0.8
0.6
0.4
0.2
0
-0.2
-0.4
-0.6
-0.8
-1
-1.2
-1
-0.8
-0.6
-0.4
-0.2
0
0.2
0.4
0.6
0.8
1
1.2

Figure 3.3b

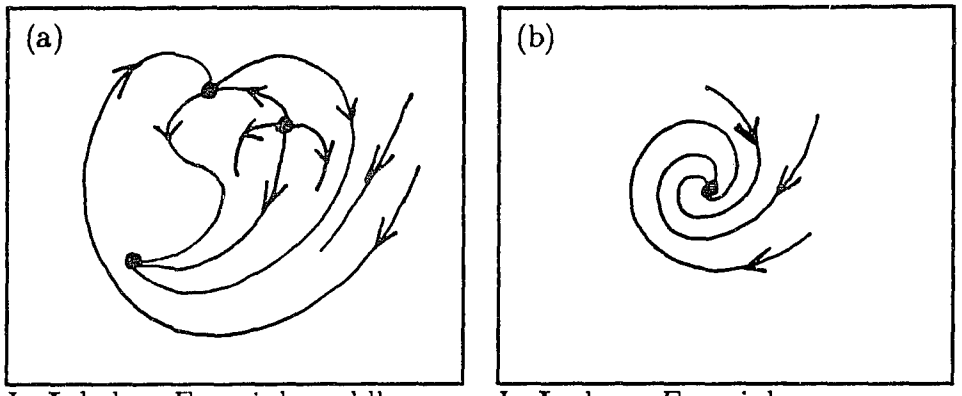

In **L** below F_- : sink, saddle, source.

In **L** above F_- : sink.

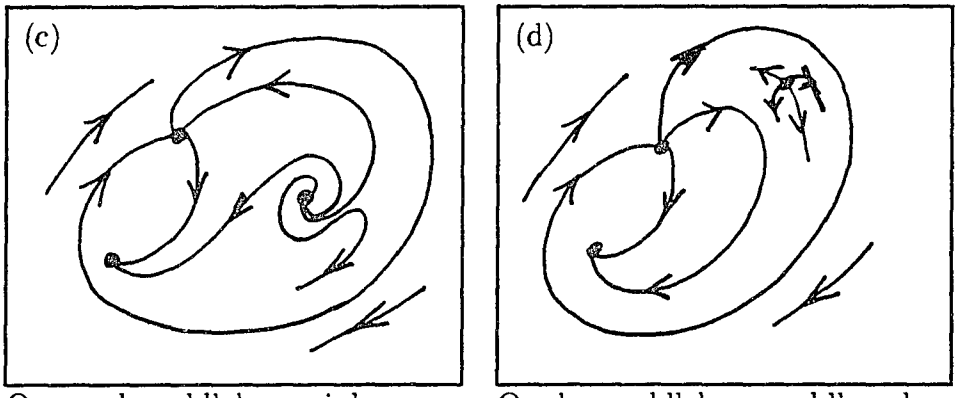

On a-e-d: saddleloop, sink ,source.

On d-c: saddleloop, saddlenode, sink, source.

Figure 3.4a-d

Figure 3.4: Schematic pictures of the flow in the complex $u-$plane for the harmonically forced LE going from a phase-locked state (fixed point) to a limit cycle, passing through regions **B2** and **B3** (figure 3.2f).

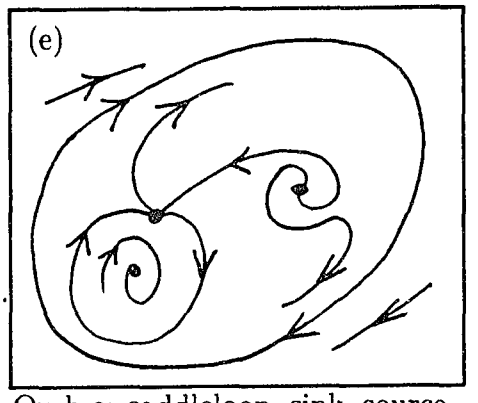

On b-e: saddleloop, sink, source, limit cycle.

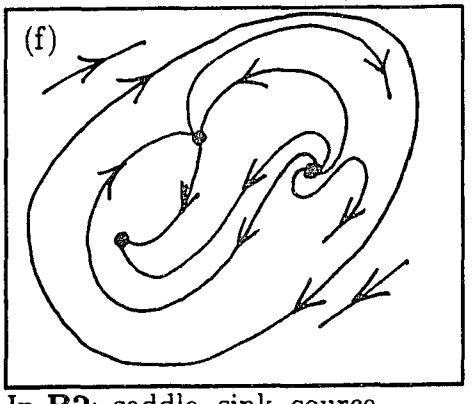

In **B2**: saddle, sink, source, limit cycle.

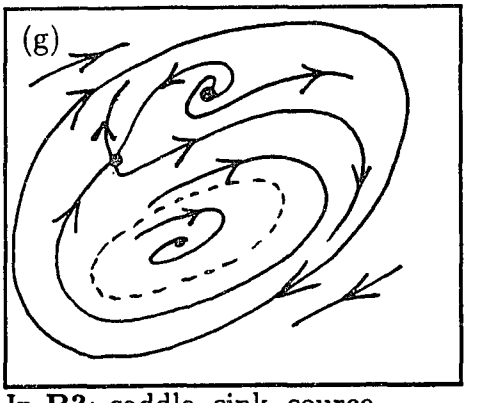

In **B3**: saddle, sink, source, limit cycle, repelling closed orbit.

Figure 3.4e-g

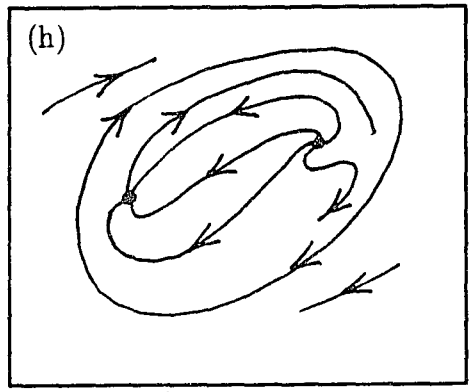

On a-b, saddlenode, source, limit cycle.

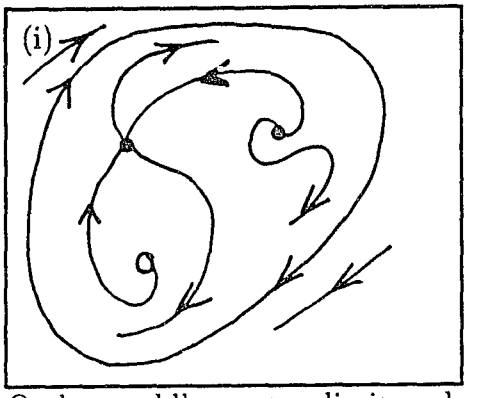

On b-c, saddle, centre, limit cycle, source.

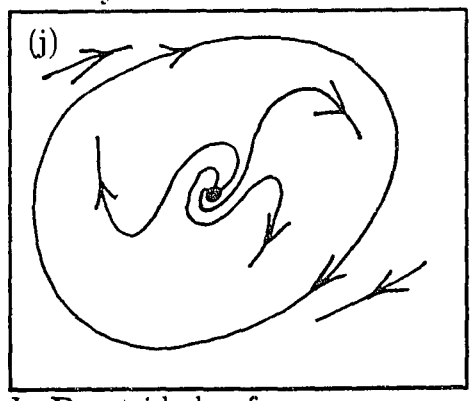

In **P** outside b-c-f, source, limit cycle.

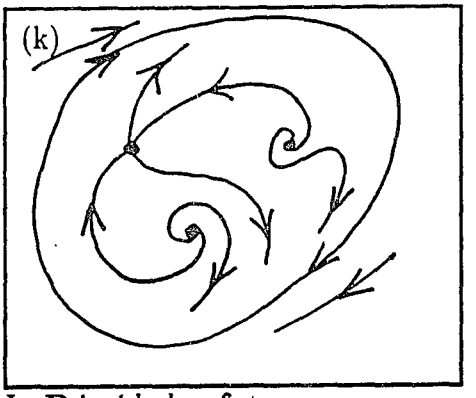

In **P** inside b-c-f, two sources, saddle, limit cycle.

Figure 3.4h-k

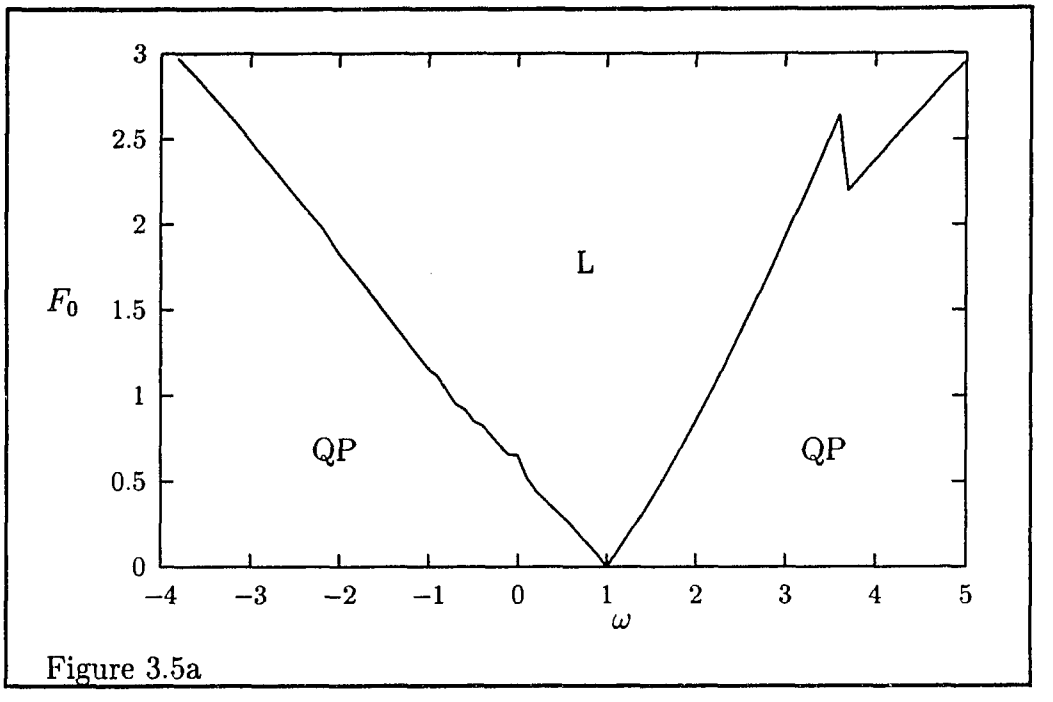

Figure 3.5a

Figure 3.5: The phase-locked region (region **L**) and frequency-locked region (region **FL**) of the forced LE with forcing $F(t) = F_0(c_0 + e^{i\omega t})$, for $c_0 = 0.1$, $c_1 = 0$, $c_3 = -1$. The shape of the phase-locked region is similar to the situation for $c_0 = 0$, i.e. the harmonically forced LE, figure 3.2d. In the region marked **QP** there is a quasi-periodic state.

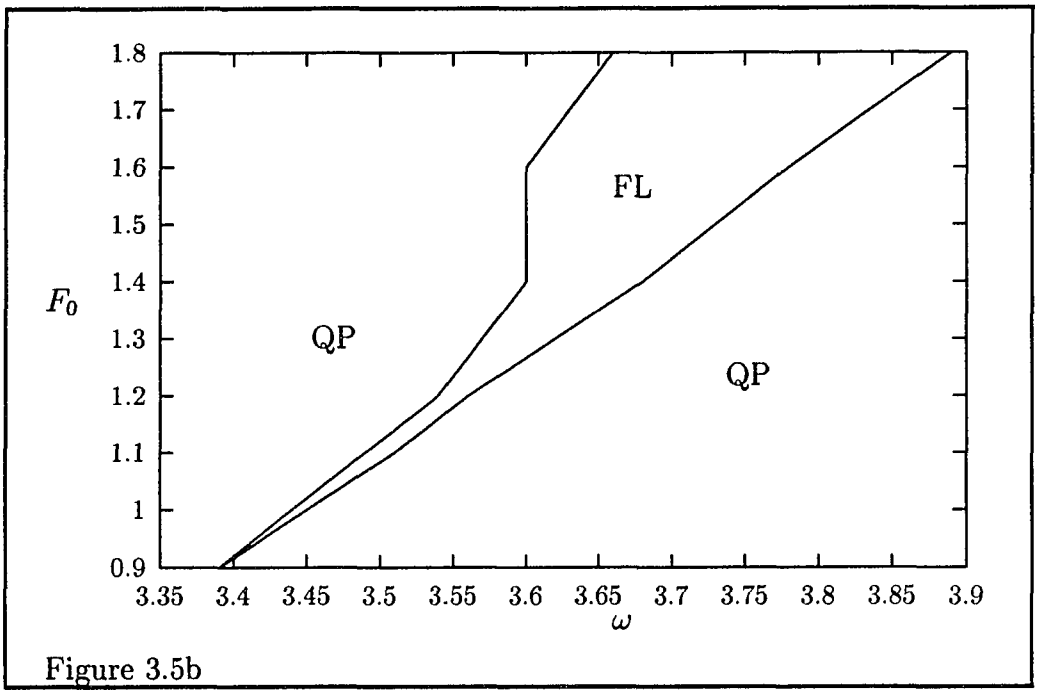
1.8
1.7
1.6
1.5
1.4
1.3
1.2
1.1
1
0.9
F_0
FL
QP
QP
3.35
3.4
3.45
3.5
3.55
3.6
3.65
3.7
3.75
3.8
3.85
3.9
ω

Figure 3.5b

Chapter 4

Harmonically forced pulse solutions.

In this chapter we will consider the CGLE for the situation where the forcing is localized in space and harmonic in time. We recall the general form, equation (1.1), in the presence of a harmonic forcing,

$$\left[\frac{\partial}{\partial t} - \sigma - \lambda\frac{\partial^2}{\partial x^2} + \beta|\Psi|^2\right]\Psi = F_0 e^{i\omega t}. \tag{4.1}$$

We will confine ourself to extended systems, which are systems with length $l \to \infty$. Unlike for the LE, where we could rely on analytic results obtained for the phase-locked states, the analyses of the CGLE presented in this chap-

ter will be, even for the phase-locked states, almost completely numerical. In a numerical simulation the system is at best an *approximated* extended system. Therefore to obtain results valid for the true extended system, one carefully has to verify their dependence on the system length l, or rather their *in*dependence of l as $l \to \infty$. For the analyses in space we will use a Fourier series expansion which implies periodic boundary condition on say the interval $[-l/2, l/2]$. If the results pass the previous test, it is likely but not however absolutely guaranteed that they do not change if one approaches the limit $l \to \infty$ with different (i.e. not periodic) boundary conditions. We will not dwell on this issue further in this work. Throughout periodic boundary conditions are assumed. In what follows the presented results have passed the previously mentioned test and in that sense may be assumed to be valid for extended systems.

Let us start the discussion in this chapter on a somewhat more general level and drop the confinement to the supercririal case. By introducing the parameters $\mu_1 = sign(Re\sigma)$ and $\mu_2 = sign(Re\beta)$ the CGLE may be written after appropriate rescaling ($x = \left(\frac{l}{2\pi}\right) x'$, $t = |Re\sigma|^{-1} t'$, $\Psi = |Re\sigma / Re\beta|^{1/2} \Psi'$)

as

$$\left[\frac{\partial}{\partial t} - \mu_1 - \Lambda(1+ic_2)\frac{\partial^2}{\partial x^2} + \mu_2(1+ic_3)|\Psi|^2\right]\Psi = F_0 e^{i\omega t}. \qquad (4.2)$$

Where the primes are left out and $c_2 = Im\lambda/Re\lambda$, $c_3 = Im\beta/Re\beta$, further $Im\sigma$ is omitted since it may be incorporated in the forcing frequency because the forcing is harmonic in time. The parameter Λ is the cut-off parameter

$$\Lambda = \frac{(2\pi)^2 Re\lambda}{l^2|Re\sigma|}. \qquad (4.3)$$

As mentioned already, in order to approximate the extended system, we have to make l sufficiently large (or equivalently Λ sufficiently small) so that the results do no longer depend on it. This implies in any case that he parameter l has to be several times larger than the largest typical length scale in the problem. This could for instance be an external length scale like the width of the forcing, but also, which is more difficult to evaluate, a dynamically established lenth scale in a particular parameter range.

In this chapter an ettempt will be made to give a description of the phase diagram belonging to (4.2). In section 4.1 we will discuss the impossibility of stationary pulse solutions, forced or unforced, of equation (4.2) when μ_1 and μ_2 are constants. In section 4.2 we will discuss the situation for a spatially dependent linear growth rate $Re\sigma$ and the unforced stationary pulse solutions

of (4.2) for that case. The forced solutions for this situation as well as the behaviour in the F_0-ω plane of the phase diagram will be discussed in section 4.3.

4.1 Stationary and phase-locked pulses for constant linear growth rate.

We will first discuss the unforced equation (4.2) and ask if there are any stationary pulse solutions, that is, solutions localized in space with a harmonic time dependence. Inspired by the solutions mentioned in reference [38] for the nonlinear Schrödinger equation, one finds that the stationary pulses

$$P(x,t) = A_0 \left[sech(Kx)\right]^{1+i\alpha} e^{i\Omega t} \tag{4.4}$$

satisfy the unforced CGLE when

$$K^2 = \Lambda^{-1}\mu_1(2\alpha c_2 - 1 + \alpha^2)^{-1}, \tag{4.5}$$

$$\Omega = \Lambda K^2(2\alpha + c_2(1-\alpha^2)), \tag{4.6}$$

$$A_0^2 = -K^2\mu_2 c_3 \Lambda(3\alpha + c_2(2-\alpha^2)), \tag{4.7}$$

$$\alpha = -\Delta \pm (2+\Delta^2)^{1/2} \tag{4.8}$$

and

$$\Delta = \frac{3(1 + c_2 c_3)}{2(c_3 - c_2)}. \tag{4.9}$$

Note that K scales as $\Lambda^{-1/2}$ which make Ω and A_0 independent of Λ, so that the criterion that he solution should not depend on l as $l \to \infty$ is trivially satisfied in this case. The existence of the pulse solutions (4.4) is not immediately clear however, because of their rather complicated dependence on the parameters. We will discuss this first and after that we will discuss their stability.

The solutions (4.4) are obviously guaranteed to exist whenever

$$\Lambda^{-1}\mu_1(2\alpha c_2 - 1 + \alpha^2)^{-1} > 0 \tag{4.10}$$

and

$$-\mu_2 c_3 \Lambda(3\alpha + c_2(2 - \alpha^2)) > 0. \tag{4.11}$$

Although these inequalities look rather cumbersome at this point because α depends on c_2 and c_3 in a not very trivial way, it turns out that things are not that bad. We observe that for validity of (4.10) and (4.11) the location of α with respect to the intervals (α'_-, α'_+) and (α''_-, α''_+) is of importance, where

$$\alpha'_\pm(c_2) = c_2 \pm \sqrt{c_2^2 + 1} \tag{4.12}$$

and

$$\alpha''_{\pm}(c_2) = \frac{3}{2c_2}\left[1 \pm \sqrt{1+\frac{8}{9}c_2^2}\right]. \tag{4.13}$$

Let's from now on refer to the α that actually solves the equation as $\alpha_{\pm}$, that is

$$\alpha_{\pm} = -\Delta \pm (2+\Delta^2)^{1/2}. \tag{4.14}$$

If we interpret the expressions (4.12), (4.13) and (4.14) as describing curves in the α-c_2 plane with c_3 as parameter, then it is possible to show that these curves never intersect if $|c_3| < 3$. If $c_3 > 3$ the curves α'_+ and α_- intersect in two points, say c'_{2+} and c'_{2-}, which are the solutions of

$$-\Delta - \sqrt{2+\Delta^2} = c_2 + \sqrt{1+c_2^2}. \tag{4.15}$$

If $c_3 < -3$ the curves α_- and α'_- intersect in two points, say c''_{2+} and c''_{2-} which are the solutions of

$$-\Delta - \sqrt{2+\Delta^2} = c_2 - \sqrt{1+c_2^2}. \tag{4.16}$$

One checks easily that $c'_{2\pm} = -c''_{2\mp}$. This symmetry property was not used in our reasoning above in order to make things not unnecessarily confusing. Typical curves $\alpha_{\pm}$, $\alpha'_{\pm}$ and $\alpha''_{\pm}$ are shown in figure 4.1 and 4.2 for $|c_3| < 3$ and $|c_3| > 3$ respectively.

$\mu_1\Lambda$	$\mu_2\Lambda$	$\lvert c_3\rvert < 3$	$\lvert c_3\rvert > 3$
+	+	all c_2	all c_2
+	−		$c'_{2-} < c_2 < c'_{2+}$ $(c_3 > 0)$ $c''_{2-} < c_2 < c''_{2+}$ $(c_3 < 0)$
−	+		
−	−	all c_2	$c_2 > c'_{2+}$ or $c_2 < c'_{2-}$ $(c_3 > 0)$ $c_2 > c''_{2+}$ or $c_2 < c''_{2-}$ $(c_3 < 0)$

Table 4.1: Existence of the stationary pulse solutions (4.4) as function of the parameters c_2, c_3, μ_1, μ_2 and Λ. Empty fields indicate that a solution of the form (4.4) does not exist, otherwise the range of existence in the c_2 parameter space is given.

Simple book keeping now allows us to derive the regions in parameter space for which the pulse solutions (4.4) exist. The results are shown in table (4.1). We see from table (4.1) that for $(\mu_1\Lambda, \mu_2\Lambda) = (-,+)$ no pulses of the form (4.4) exist, while for $(\mu_1\Lambda, \mu_2\Lambda) = (+,+)$ pulses of the form (4.4) exist for all parameter values c_2 and c_3. For other choices of $(\mu_1\Lambda, \mu_2\Lambda)$ their existence is limited to certain regions in (c_2, c_3) parameter space.

Next we will discuss the stability of the solutions (4.4). We linearize (4.2)

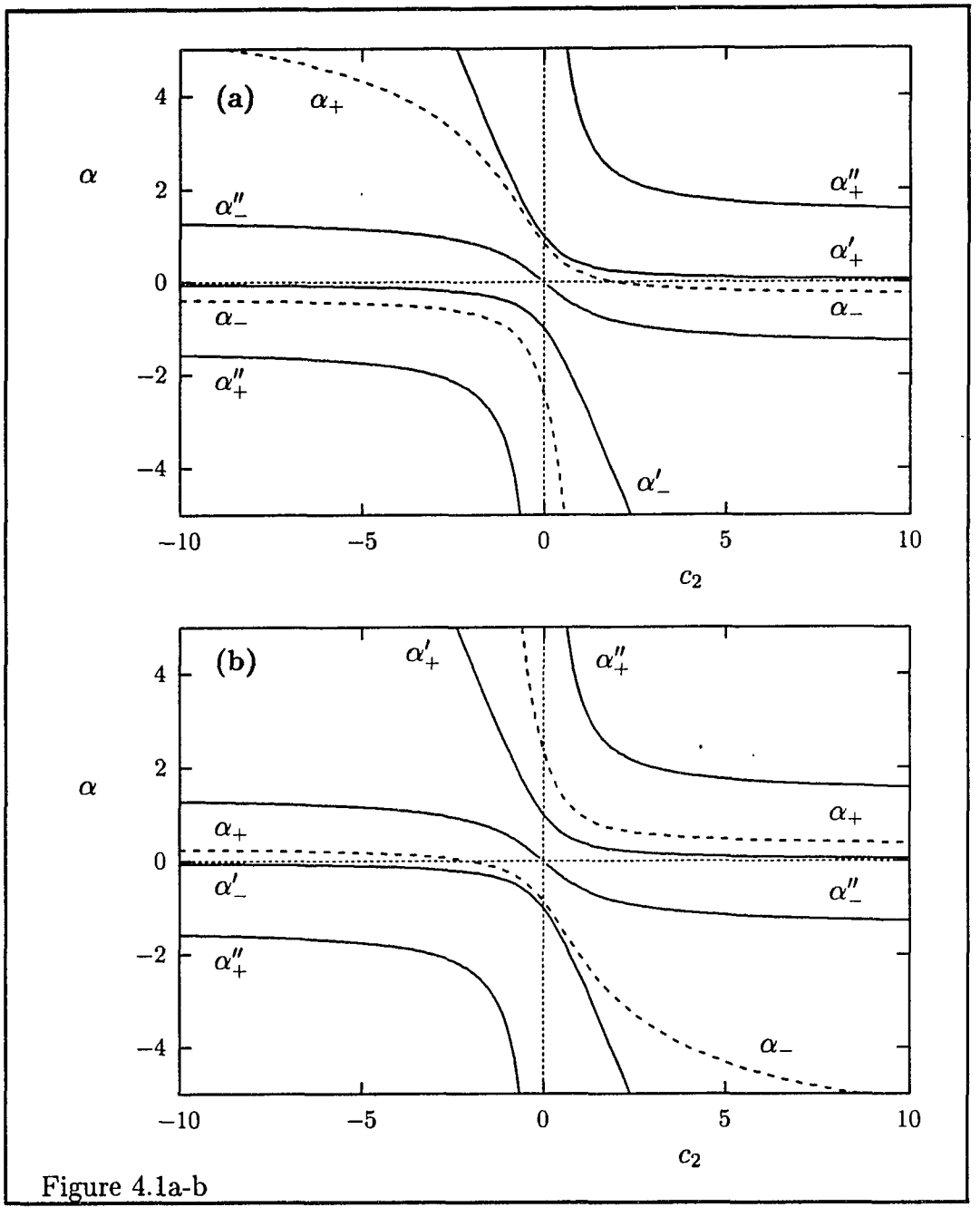

Figure 4.1a-b

Figure 4.1: The curves $\alpha_\pm$, $\alpha'_\pm$ and $\alpha''_\pm$ as function of c_2 for $c_3 = 2$ (panel a) and $c_3 = -2$ (panel b).

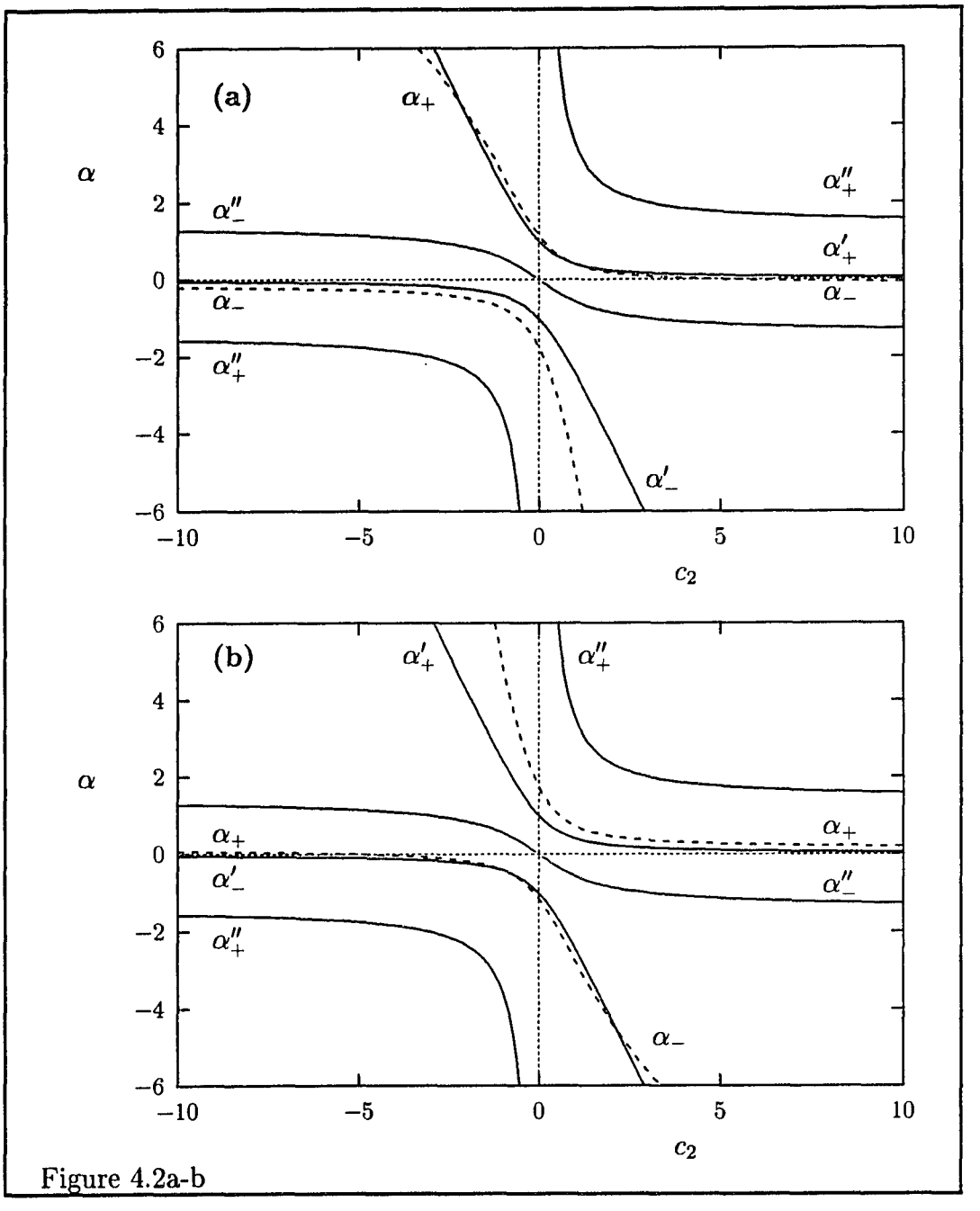

Figure 4.2a-b

Figure 4.2: The curves $\alpha_\pm$, $\alpha'_\pm$ and $\alpha''_\pm$ as function of c_2 for $c_3 = 5$ (panel a) and $c_3 = -5$ (panel b).

around the pulse solutions (4.4),

$$\Psi(x,t) = P(x,t) + \delta\Psi(x,t). \tag{4.17}$$

This yields the equation

$$\left[\frac{\partial}{\partial t} - \mu_1 - \Lambda(1+ic_2)\frac{\partial^2}{\partial x^2} + 2\mu_2(1+ic_3)|P|^2\right]\delta\Psi(x,t)$$

$$+\mu_2(1+ic_3)P^2\delta\Psi^*(x,t) = 0. \tag{4.18}$$

This equation may be solved by Fourier transformation via

$$\delta\Psi(x,t) = e^{i\Omega t}\sum_k \left(a(k)e^{p(k)t+ikx} + b(k)e^{p^*(k)t-ikx}\right). \tag{4.19}$$

The dispersion relation $p(k)$ follows from $det(S) = 0$, where

$$S_{k,k'} = \begin{bmatrix} (p(k) + i\Omega - \mu_1 + \Lambda k^2(1+ic_2))\delta_{k,k'} + 2\mu_2(1+ic_3)(|\tilde{P}|^2)_{k-k'} & \mu_2(1+ic_3)(\tilde{P}^2)_{k-k'} \\ \mu_2(1-ic_3)((\tilde{P}^*)^2)_{k-k'} & (p(k) - i\Omega - \mu_1 + \Lambda k^2(1-ic_2))\delta_{k,k'} + 2\mu_2(1-ic_3)(|\tilde{P}|^2)_{k-k'} \end{bmatrix}, \tag{4.20}$$

where $\tilde{P}(x) = P(x,t)e^{-i\Omega t}$. The requirement for stability is $\max(Rep(k)) < 0$. It is a simple matter to solve this numerically for the parameter values c_2, c_3, μ_1, μ_2 and Λ for which the pulses $P(x,t)$ exist. There are however a few things one has to be aware of. First, the degeneracy present in table

(4.1) with respect to Λ is not present in the actual solution. For instance, the parameter choices $(\mu_1, \mu_2, \Lambda) = (1, 1, -1)$ and $(\mu_1, \mu_2, \Lambda) = (-1, -1, 1)$ are represented by one field in table (4.1), although they actually correspond to two different solutions. Since this degeneracy is also not explicitely present in (4.20) one has to look at these solutions seperately to decide upon their stability. Second, one has to make sure that the dispersion relation $p(k)$ converges both when $\Lambda \to 0$ and when the number of Fourier components is increased. For most cases a convergence of at least six significant figures of $\max(Re(p(k)))$ is achieved when $|P(l/2)|/|P(0)| \approx 10^{-5}$ and the number of Fourier components is 64.

Testing the linear stabililty in the manner just described resulted in a negative answer in all cases. None of the existing pulses $P(x, t)$ were found to be stable. This is not too surprising for situations where $\mu_1 \Lambda > 0$ since the trivial solution ($\Psi = 0$) is unstable in such cases. However, there are also situations for which the trivial solution is stable and all pulses of the form (4.4) are still unstable, for instance when $\mu_1 = -1$ and $\Lambda > 0$.

Having been unable to find any analytic stationary pulse solutions that are stable, there remains the possibility to continue the search for them numerically. In order to minimize the size of the eigenvalue problem, a Fourier

transformation in space was used rather then a finite differences method. Anticipating to find at least phase-locked pulses we include the forcing again in the equation and write the solutions in the form $\Psi(x,t) = e^{i\omega t}\phi(x,t)$ with

$$\phi(x,t) = \sum_n \phi_n(t) e^{inx}, \tag{4.21}$$

and

$$\phi_n(t) = \frac{1}{2\pi}\int_{-\pi}^{\pi} \phi(x,t) e^{-inx} dx. \tag{4.22}$$

Equation (4.2) then becomes

$$[i\omega + \frac{\partial}{\partial t} - \mu_1 + n^2\Lambda(1+ic_2)]\phi_n(t) + \mu_2(1+ic_3)\sum_m (|\phi|^2)_{n-m}\phi_m(t) = F_n. \tag{4.23}$$

The phase-locked solutions are then the stationary solutions of this equation for which $\partial_t \phi_n = 0$. Their stability follows from $det(S) = 0$ where S is again given by (4.20) with $\tilde{P} \to \phi$, $\Omega \to \omega$.

Details of the numerical solution method for the phase-locked solutions of equation (4.23) are discussed in appendix C. The results of this numerical analyses are as follows. Other than the analtytic pulse solutions (4.4) for $F = 0$, stationary pulses were not found to exist. In particular, for the parameter regions where the pulses (4.4) do not exist, also unforced stationary pulse solutions were not found to exist numerically. When the forcing

is included the situation is somewhat different. In the numerical search for phase-locked pulses a Gaussian shaped forcing was used, given by

$$F(x) = F_0 e^{-Q^2|\Lambda|^{-1}x^2}. \tag{4.24}$$

The situation for $Q = 0$ (constant forcing) was also scrutinized. Phase-locked pulses were observed to exist for all values of μ_1, μ_2, c_2, c_3, ω ,Q and sufficiently large F_0. The result for their stability however was always negative; all puls solutions that were observed to exist were found to be linearly unstable. Since a rather extensive parameter range was scanned, we may with some confidence conclude that the CGLE contrary to the NLSE, has no stable puls solutions, be it stationary (unforced) or phase-locked (forced). Some (unstable) pulses are shown in figure (4.3).

The situation is not that extreme if a stabilizing fifth order nonlinearity is included. In this case stable stationary pulses exist for the subcritical case ($\mu_2 = -1$) below the bifurcation ($\mu_1 = -1$). There is usually a significant parameter range for which these pulses exist, see [13].

Rather than taking into account higher order terms in the CGLE, we will consider in the next section an other situation for which it allows for stable stationary and phase-locked pulses to exist.

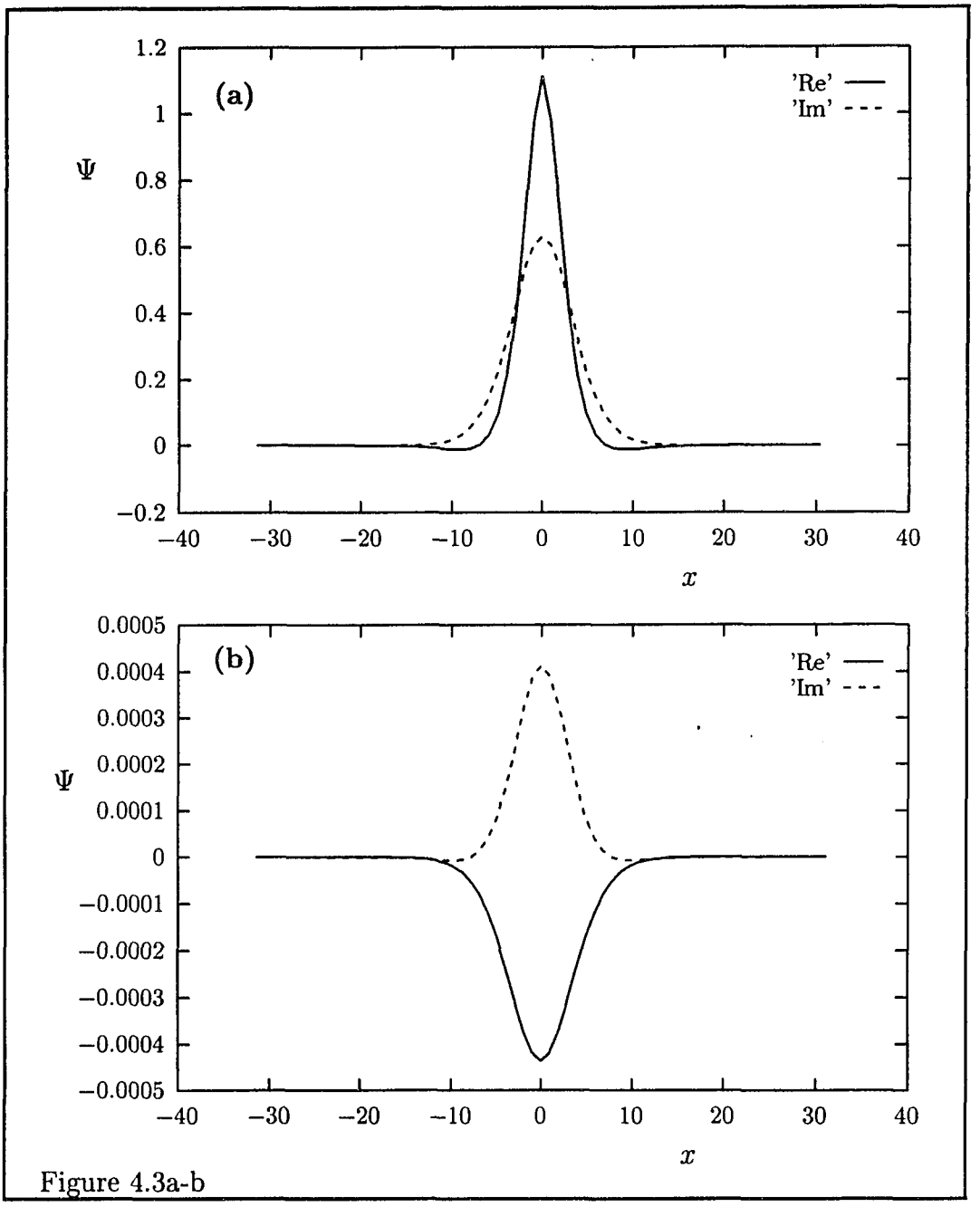

Figure 4.3a-b

Figure 4.3: Some (unstable) pulse solutions, unforced (panel a) with $c_2 = 4.5$, $c_3 = 1$, $\mu_1 = -1$, $\mu_2 = -1$ and $\Lambda = 0.01$, forced (panel b) with same c_3 and μ_2 and $\mu_1 = 1$, $\Lambda = -0.01$, $\omega = -0.69$, $Q = 0.3$ and $F_0 = 0.001$.

4.2 Space dependent linear growth rate, unforced pulses.

In this section we will discuss the situation when the linear growth rate $Re\sigma$ is space dependent, such that $Re\sigma > 0$ in a confined region of space and $Re\sigma < 0$ elsewhere. We will leave out the forcing and only discuss the unforced solutions in this section. The forced system will be discussed in the next section. We will take the growth rate to be of a Gaussian shape and we will exclusively consider the supercritical case ($\mu_2 = 1$). The most general form of μ_1 is then after proper rescaling

$$\mu_1(x) = -1 + \Sigma(x), \tag{4.25}$$

where

$$\Sigma(x) = \Sigma_0 e^{-K^2|\Lambda|^{-1}x^2}. \tag{4.26}$$

The dimensionless parameter K is the width of the growth rate in factors of $\left|\frac{Re\sigma(\infty)}{Re\lambda}\right|^{1/2}$, that is $K_{dim} = K\left|\frac{Re\sigma(\infty)}{Re\lambda}\right|^{1/2}$, where $\sigma(\infty) = \sigma(x \to \pm\infty)$. The parameter K thus defines an external length scale for energy injection in the system, $l_E \sim 1/K$.

The parameter K also defines in effect the size of the system. As discussed

in chapter 1, the system size may be defined in reference to the dissipation length l_D. Small, intermediate size and large systems are then respectively systems for which the system length $l \ll l_D$, $l \approx l_D$ and $l \gg l_D$. In our case one expects the length scale on which disorder could be present to be at most of the order of $1/K$, which will be also confirmed by the results we will discuss below. As we will see, the growth rate (4.25) admits pulse solutions with a width of the order of $1/K$ to exist. A proper measure to compare the correlation length with regarding the classification of size is therefore $1/K$ in this case and not the system length. From global inspection one finds that small systems are systems with $K \sim 10^0$, intermediate size have $K \sim 10^{-2}$ and for large systems $K \sim 10^{-3}$. This of course for reasonable (~ 1) values for the parameters c_2, c_3 and Σ_0. To get an impression of the behaviour for the different system sizes we will consider three different values of the parameter K; $K = 0.3$ (small), $K = 0.03$ (intermediate size) and $K = 0.003$ (large). One should not confuse the fact that we distinguish different sizes with the concept of the extended system. Our discussion is for extended systems, and the convergence of the results as $\Lambda \to 0$ has been verified. The fact that we in spite of this still need to make a classification into different sizes naturally arises because of the nonuniformity of the equation. This in

contrast to the situation where the equation has constant coefficients, when the extended system is identical to a large system.

The numerical integration of the CGLE with the growth rate (4.25) was performed with a predictor-corrector scheme in time. The spatial part was treated with a pseudo-spectral method combined with Fast Fourier transformation [39], see appendix C.3. As mentioned already, the Fourier transformation used implies periodic boundary conditions on a finite interval,

$$\Psi(x+l,t) = \Psi(x,t). \tag{4.27}$$

For each set of parameters considered the equation has been integrated twice, starting from two different initial conditions given by

$$\Psi(x,t=0) = \Psi_0 e^{-q^2|\Lambda|^{-1}x^2} + \Psi_1 e^{ix}, \tag{4.28}$$

where $\Psi_0 = 1$, $\Psi_1 = 0.2$ and $q = K$ or $q = 10K$. The motivation for these initial conditions is that starting from various initial conditions one usually finds that pulses with a width of the order $1/K$ exist. By integrating not only for $q = K$ but also for $q = 10K$ one gets some impression (albeit a severely limited one of course) of the region of attraction of the solution obtained for $q = K$. The long wavelenghth disturbance term $\Psi_1 e^{ix}$ is added in order to

avoid parity symmetry in the initial condition. Besides its practical insignificance, the presence of parity symmetry in the initial condition sometimes also unneccesarily introduces long-lived transients.

To analyze the spatio-temporal dynamics of the solutions their power spectrum [40] $\mathcal{P}(\omega)$ has been computed for various positions x. Another quantity that was computed when appropriate is the defect distribution function $d(x)$, the probability distribution for a defect occurrence at position x, see also chapter 1. Finally, information about the spatial and temporal correlations is obtained from computation of the following correlation functions,

$$D(x,x') = \frac{< \Psi^*(x,t)\Psi(x',t) > - < \Psi^*(x,t) >< \Psi(x',t) >}{< |\Psi(x,t)| >< |\Psi(x',t)| >} \qquad (4.29)$$

and

$$C(x,t,t') =< \Psi^*(x,t)\Psi(x,t') > - < \Psi^*(x,t) >< \Psi(x,t') > . \qquad (4.30)$$

The brackets $< \cdot >$ stand for averaging over time,

$$< f(t) >= \lim_{T\to\infty} \frac{1}{T} \int_0^T f(t+\tau)d\tau. \qquad (4.31)$$

The temporal correlation function $C(x,t,t')$ has the property that it depends on x because of the non-uniformity of the system and on $t-t'$ rather

than t and t' seperately because of the time isotropy. A more detailed discussion of this will be given in the next chapter. Further, $C(x,t,t')$ is quasi-periodic in $t-t'$ if $\Psi(x,t)$ is quasi-periodic in t and $|C(x,t,t')|$ is constant if $\Psi(x,t)$ is stationary with $\omega \neq 0$, finally $C(x,t,t') = 0$ if Ψ is time independent.

The spatial correlation function $D(x,x')$ does not depend on time because of the time isotropy. It does however depend on both x and x' and not just on $x-x'$ because of the non-uniformity of the system. The denominator in its definition is included to correct for any structure (decay) that might occur solely because of the spatial envelope of the solution. Defined as in (4.29), $|D(x,x')| = 1$ for stationary states with $\omega \neq 0$ and $D(x,x') = 0$ for time independent states. In this way it is assured that any structure (decay) occurring in $D(x,x')$ has to be a result from either quasi-periodic or chaotic behaviour in time or quasi-periodic or disorderded behaviour in space or both.

One final remark is in place concerning the definitions of the correlation functions C and D. When applying them to solutions $\Psi(x,t)$ of the forced system (4.2) the time isotropy is not present. However, by making the transformation $\Psi(x,t) = e^{i\omega t}\phi(x,t)$ the resulting equation for $\phi(x,t)$ is

again isotropic in time. Using this one easily checks that the properties of C and D mentioned above are valid for the forced solutions as well. It is here essential that one computes the correlation functions for Ψ rather than for ϕ.

We will now discuss the results of the numerical integration. We will discuss the bifurcations observed if we vary the growth rate Σ_0 while keeping the remaining parameters K, c_2 and c_3 fixed. In our discussion below $c_3 = 1$, $c_2 = -1$. As mentioned earlier, we will look at a small, intermediate size and a large system. Each system size leads to quite different behaviour and we will therefore look at them seperately.

4.2.1 Small systems.

As an example for the behaviour in an unforced small system with the Gaussian growth rate given by (4.25), (4.26) we will discuss the situation when the parameter $K = 0.3$. A schematic presentation of the bifurcations observed as Σ_0 is varied is shown figure 4.4. For $0 < \Sigma_0 < 1.4$ the trivial solution $\Psi = 0$ is obtained from both initial conditions. Between $\Sigma_0 = 1.4$ and $\Sigma_0 = 3.35$ a stable stationary pulse $\Psi(x,t) = \phi(x)e^{i\omega t}$ exists. The pulse has

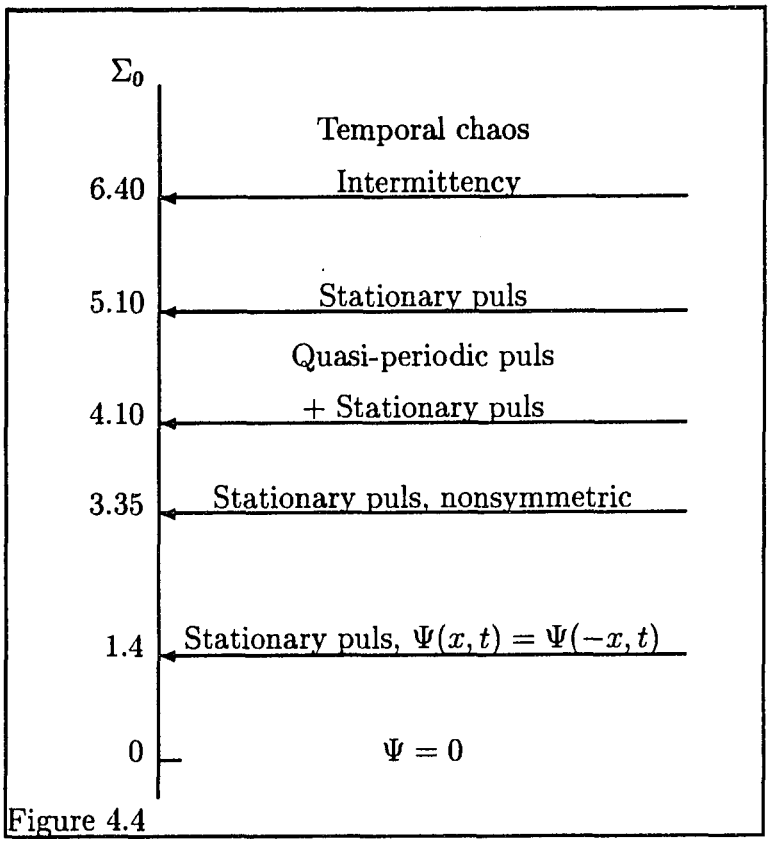

Figure 4.4

Figure 4.4: Bifurcation sequence of the CGLE with spatial dependent growth rate given by (4.25) and (4.26) in a small system with $K = 0.3$, $c_2 = -1$, $c_3 = 1$ as function of Σ_0, observed starting from the two different initial conditions given by (4.28).

inversion symmetry; $\phi(x) = \phi(-x)$. At $\Sigma_0 = 3.35$ the inversion symmetry is (spontaneously) broken, the solution remains however locked-in in time and is stable up to $\Sigma_0 = 6.4$ In the interval $4.1 < \Sigma_0 < 5.1$ a second solution exist. This solution is not symmetric in space and displays a two frequency quasi-periodic motion in time. Some typical plots of solutions obtained for $\Sigma_0 < 6.4$ are shown in figure 4.5.

For $\Sigma_0 > 6.4$ the stationary solution becomes unstable. A piece of the time series for $x = 0$ (center of system) and a snapshot of Ψ are shown in figure 4.6 for $\Sigma_0 = 7$. Figure 4.7 shows the power spectrum for different locations in the system, from their different appearence we may conclude that the motion is incoherent in space; $\Psi(x,t)$ displays a different time dependence for different x, disregarding any amplitude and phase differences.

An indication that the motion is however not disordered in space for $\Sigma_0 = 7$ is provided by the correlation function $D(x,x')$. A plot of $|D(x,x')|$ is shown in figure 4.8 for some positions x. Clearly $|D|$ does not display any significant decay on a scale comparable with the size of the pulse width. If we evaluate the correlation length based on exponential decay, $|D| \sim e^{-|x-x'|/\xi}$, we find $\xi = 6.5$ which is about half the size of the pulse width of the solution in this case.

Figure 4.9 shows the power spectrum at $x = 0$ as Σ_0 increases. We observe that the fundamental mode and its harmonics gradually vanish as Σ_0 becomes larger, indicating the transition to chaotic behaviour in time via the intermittency route. A stretch of regular behaviour in the intermittency region is visible in figure 4.6.

The correlation function $C(x,t,t')$ for $x = 0$ is shown in figure 4.10 for $\Sigma_0 = 7$ and $\Sigma_0 = 37$. The temporal correlations display a sharp decay for small $t - t'$ which eventually saturates. This behaviour is rather typical and is present for all $\Sigma_0 > 6.4$, not only in the chaotic region but also in the intermittency region. As the transition to chaos takes place the characteristic time for the initial decay of $C(x,t,t')$ strongly decreases. Assuming exponential decay, $|C| \sim e^{-|t-t'|/\tau}$, we find $\tau = 2$ for $\Sigma_0 = 17$ and $\tau = 0.2$ for $\Sigma_0 = 37$.

As discussed in the introduction, there are in general two ways in which spatio-temporal chaos can occur. One is by increasing the system length to larger and larger values until the correlation length is sufficiently smaller than the system size. The other way is to increase the controll parameter (for instance the Reynold's number in fluid mechanics) to larger and larger values to achieve the same effect. In our case at hand we may identify the

controll parameter with Σ_0. One would therefore expect a transition from temporal to spatio-temporal chaos as we increase Σ_0.

Figure 4.11 shows the spatial correlation function D as Σ_0 increases from 7 to 37. We clearly observe the transition to a correlation function which decays sharply for small $|x-x'|$ and then saturates, displaying flat shoulders for large $|x-x'|$. If we evaluate the characteristic length with which the initial decay takes place, assuming exponential decay, we obtain $\xi = 10$ for $\Sigma_0 = 37$. This is considerably smaller than the pulse width in this case, so that we may conclude that a transition to spatio-temporal chaos indeed takes place as Σ_0 increases.

We discussed in chapter 1 that as far as the behaviour of the ordinary supercritical CGLE ($\mu_1 = \mu_2 = 1$) is concerned, two different kinds of spatio-temporal chaos are observed: "amplitude chaos" and "phase-chaos". The difference between the two being the presence of defects; space-time events where $\Psi = 0$. Defects are not present in a state of phase-chaos. These classifications require a more or less disordered spatial behaviour. In the present situation the external length scale for energy injection is obviously not large enough to allow for spatial disorder for say $\Sigma_0 < 30$. Defects are however present as soon as the motion shows intermittency, that is for

$\Sigma_0 > 6.4$. They are infact also present in the quasi-periodic state observed for $4.1 < \Sigma_0 < 5.1$, but they do not occur in the stationary states.

Some defects are shown in figure 4.12, note the π phase jump at he location of the defect where $\Psi = 0$. A plot of the defect distribution function for $\Sigma_0 = 7$ is shown in figure 4.13. From this figure we see that the defects mainly occur in the region where the growth rate is positive as expected. The defect distribution function however displays a lot of structure and it is certainly not of a simple Gaussian shape. Defects gradually disappear as we move into the regions where the growthrate is negative. From the x-t plots of $Re(\Psi(x,t)) = 0$ and $Im(\Psi(x,t)) = 0$ shown in figure 4.14 we clearly see that in the tails of the solution where it decays exponentially, the defects are in fact size effects; they occur because of the boundaries of the system. Also the regular behaviour in the intermittency is clearly observable in the structure of the defect locations in the x-t plane (figure (4.14a).

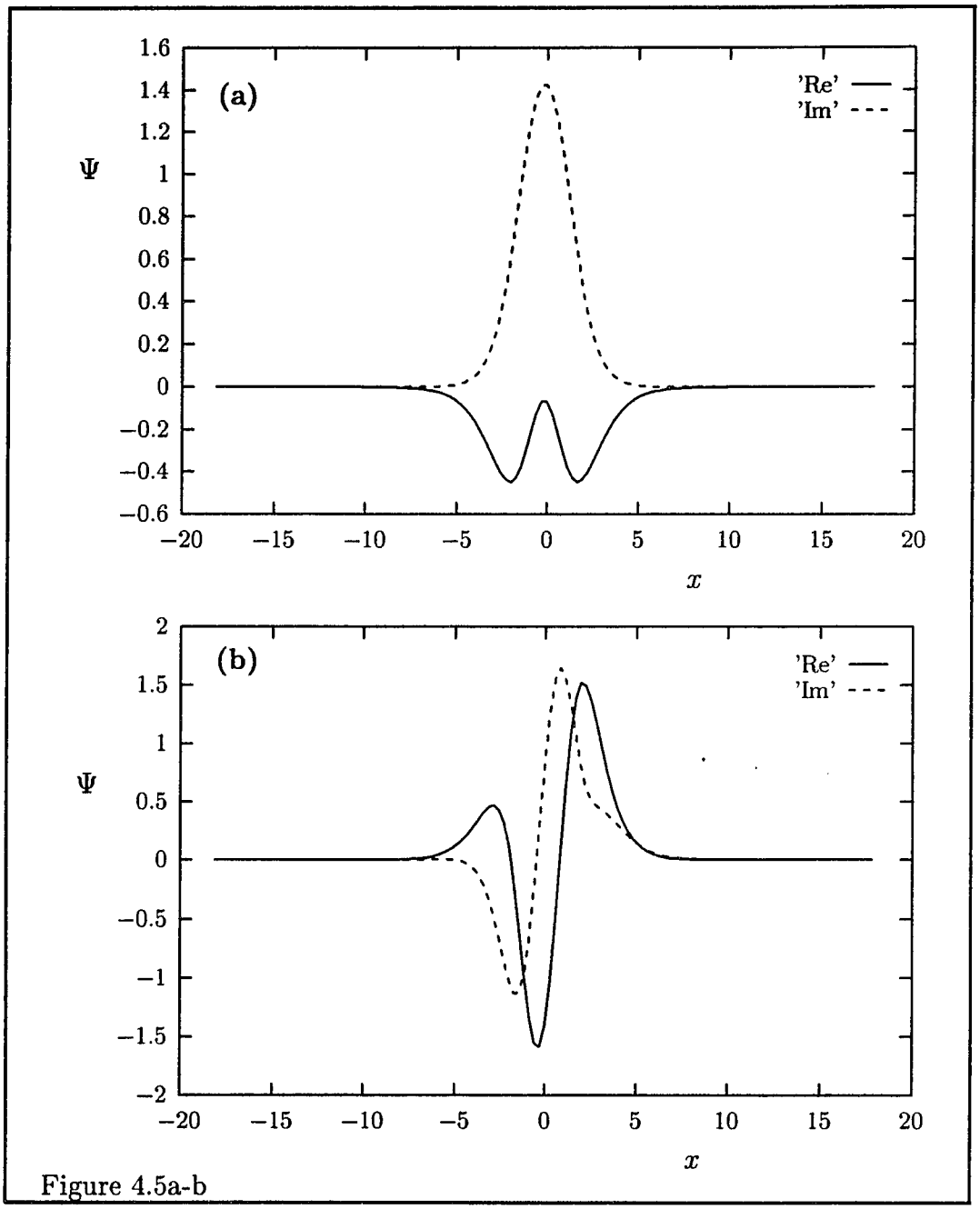

Figure 4.5a-b

Figure 4.5: Snapshots of two stationary solutions, $\Sigma_0 = 3$ (panel a) and $\Sigma_0 = 5.5$ (panel b). The frequenties of the solutions are respectively $\omega_0 = 1.05$ and $\omega_0 = 1.26$.

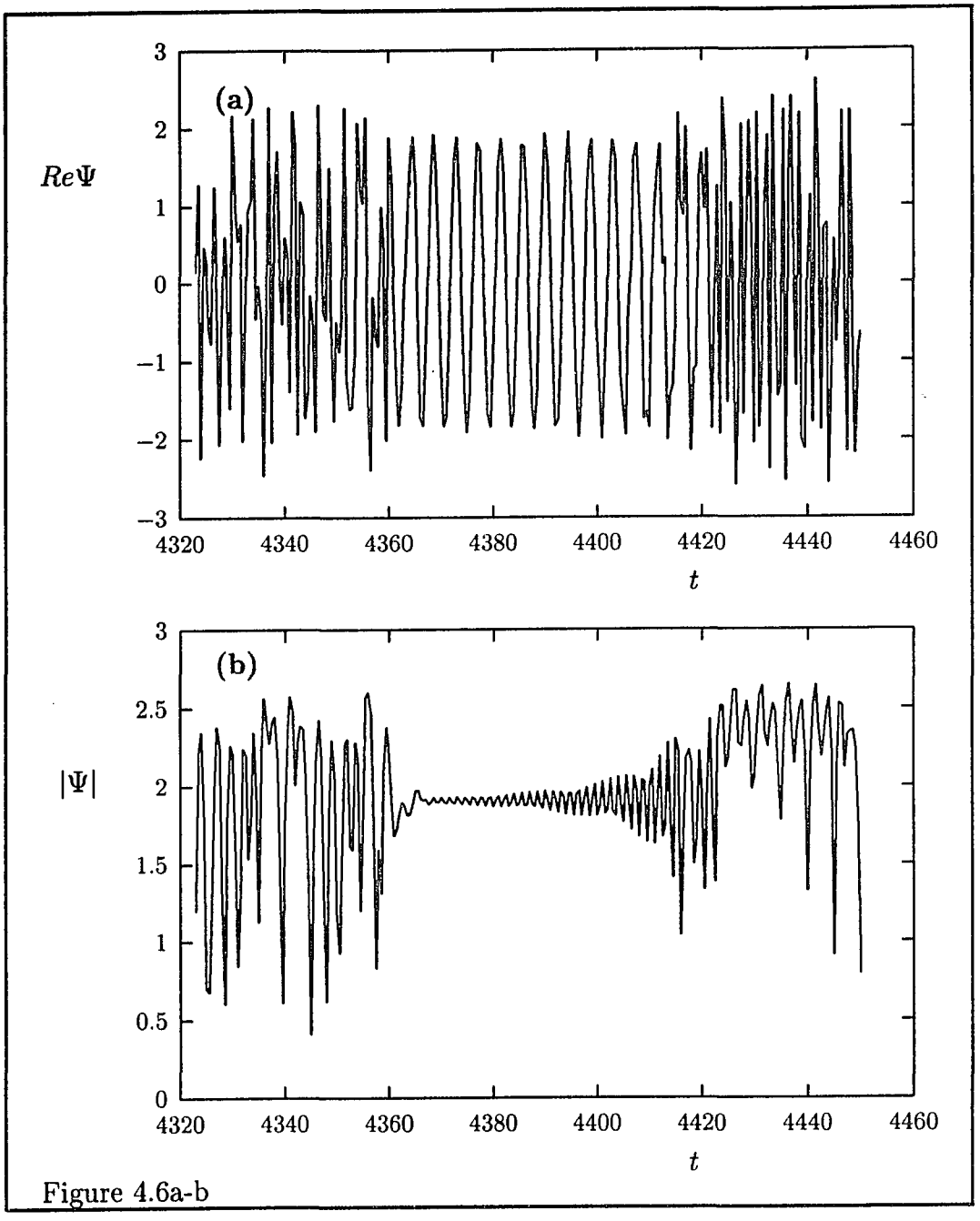

Figure 4.6: A typical period of regular motion in the otherwise chaotic time series of $\Psi(0,t)$ for $\Sigma_0 = 7$.

Figure 4.7: (Next page) Power spectra of $Re\Psi(x,t)$ at $x = 0$ (panel a) and $x = -3.8$ (panel b) for $\Sigma_0 = 7$. The corresponding temporal correlation functions $C(0,t,t')$ and $C(-3.8,t,t')$ are shown in panels c and d respectively.

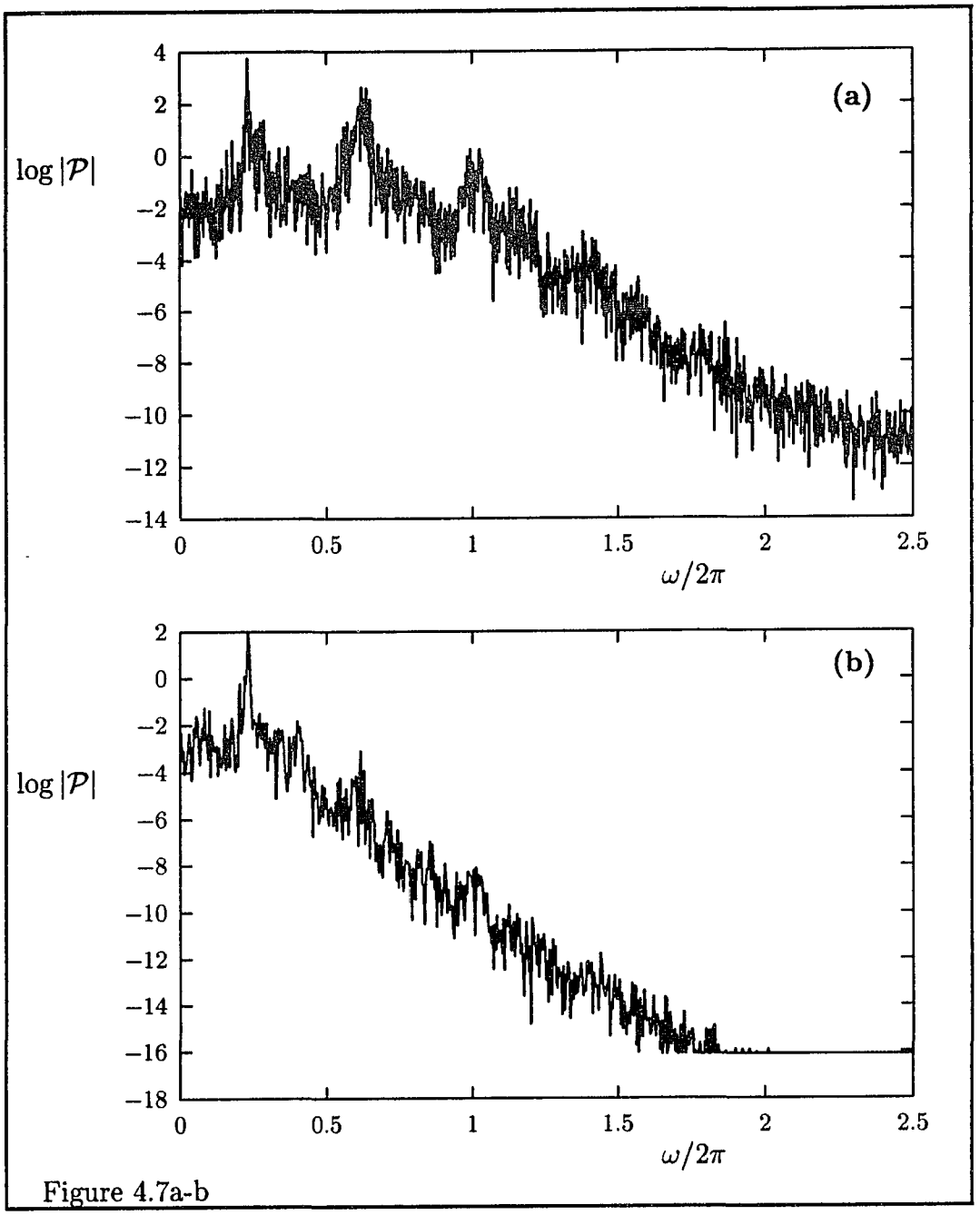
(a)
log |P|
4
2
0
−2
−4
−6
−8
−10
−12
−14
0
0.5
1
1.5
2
2.5
ω/2π
(b)
log |P|
2
0
−2
−4
−6
−8
−10
−12
−14
−16
−18
0
0.5
1
1.5
2
2.5
ω/2π

Figure 4.7a-b

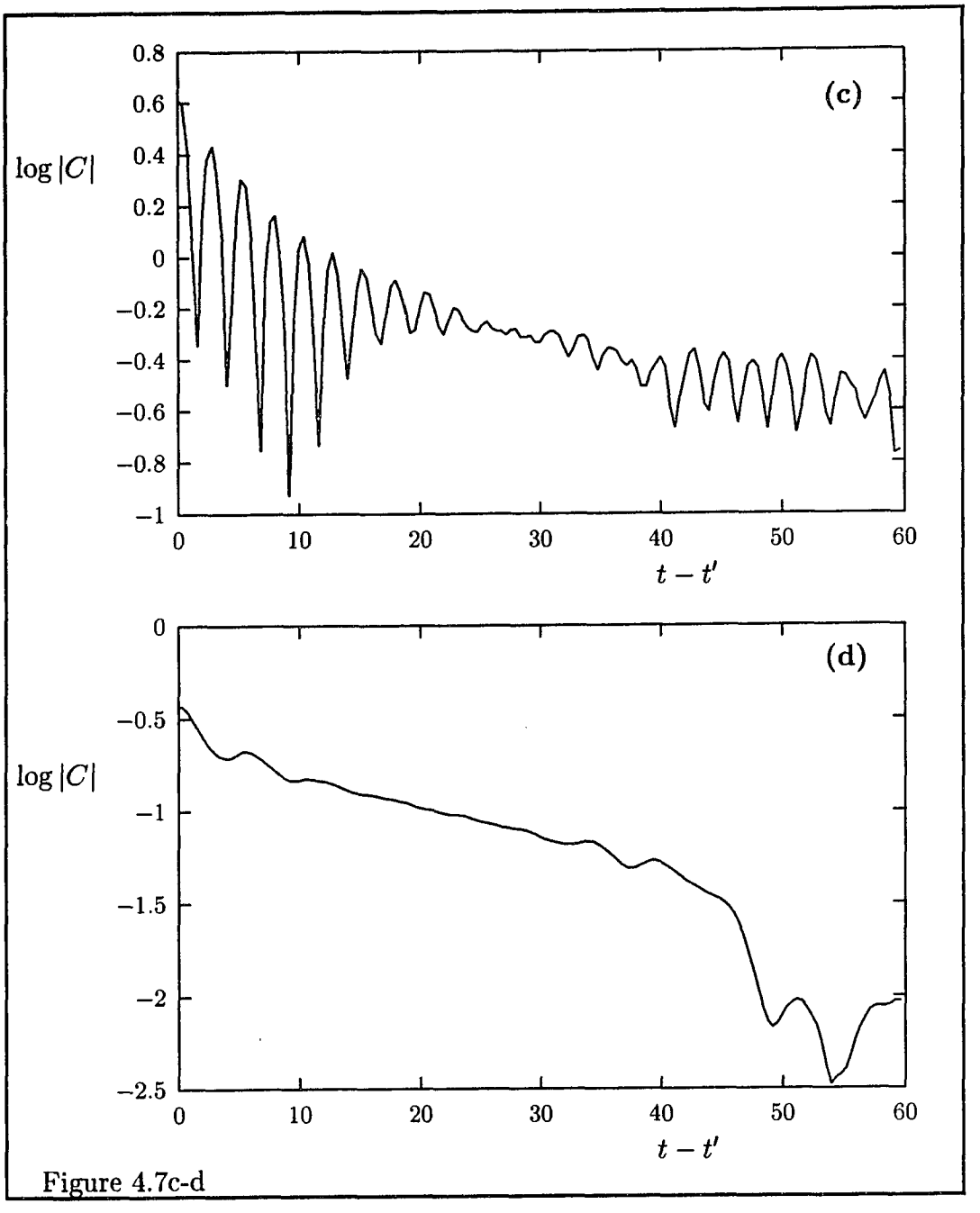
(c)
log |C|
0.8
0.6
0.4
0.2
0
−0.2
−0.4
−0.6
−0.8
−1
0
10
20
30
40
50
60
t − t′
(d)
log |C|
0
−0.5
−1
−1.5
−2
−2.5
0
10
20
30
40
50
60
t − t′

Figure 4.7c-d

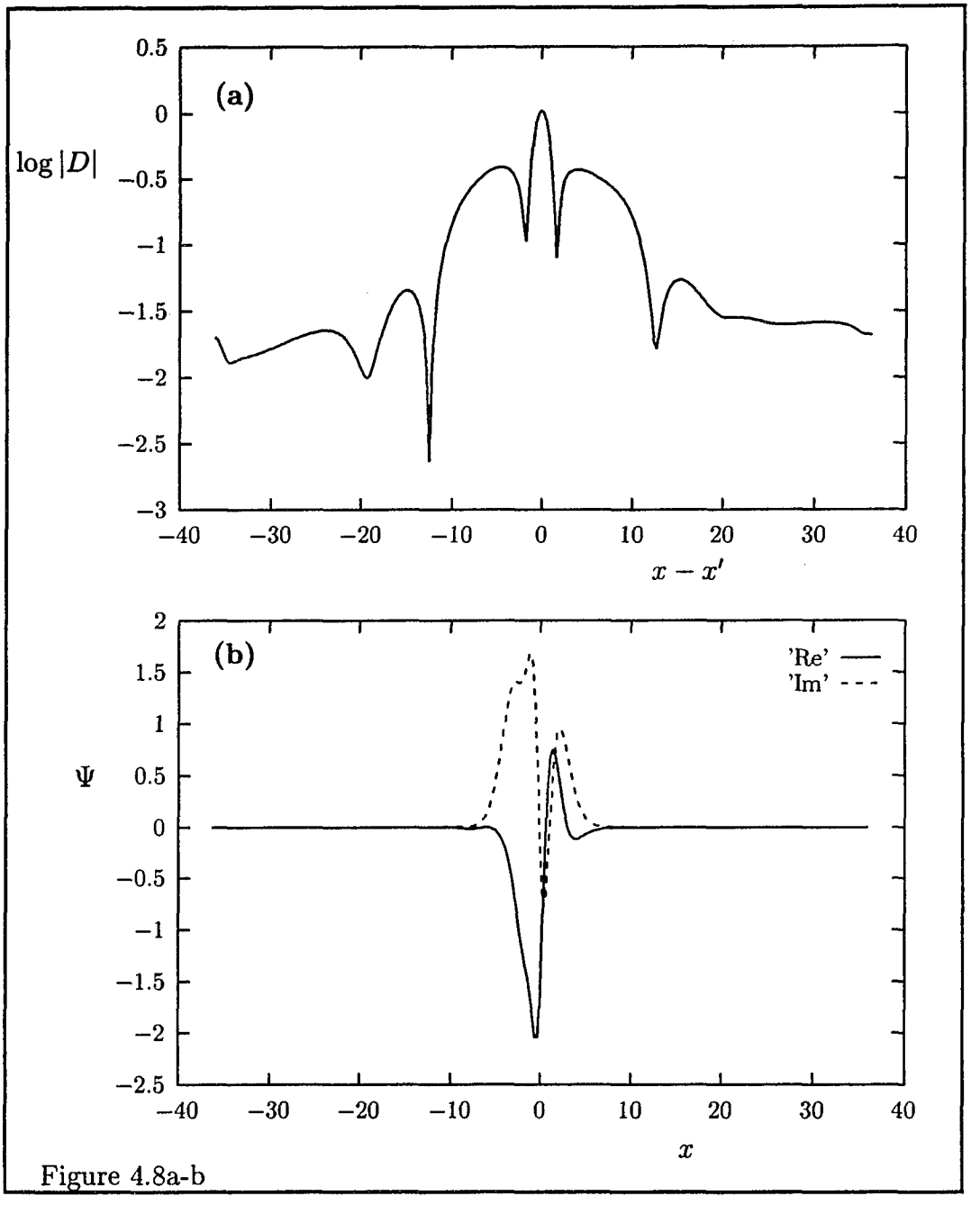

Figure 4.8a-b

Figure 4.8: The spatial correlation function $D(0, x')$ (panel a) and a snapshot of $\Psi(x, t)$ (panel b) for $\Sigma_0 = 7$.

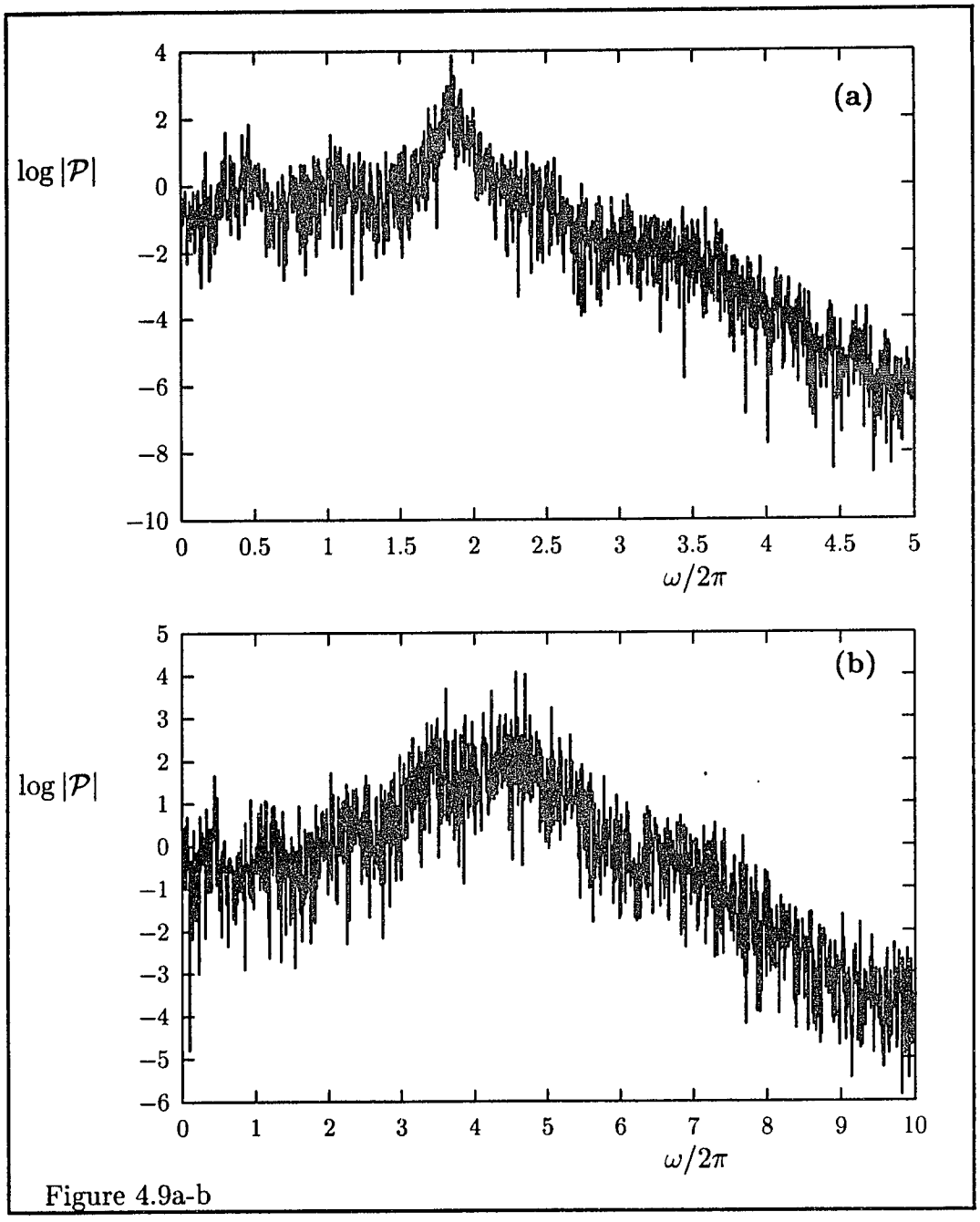

Figure 4.9: Power spectra of $Re\Psi$ at $x = 0$ for $\Sigma_0 = 17$ (panel a) and $\Sigma_0 = 37$ (panel b).

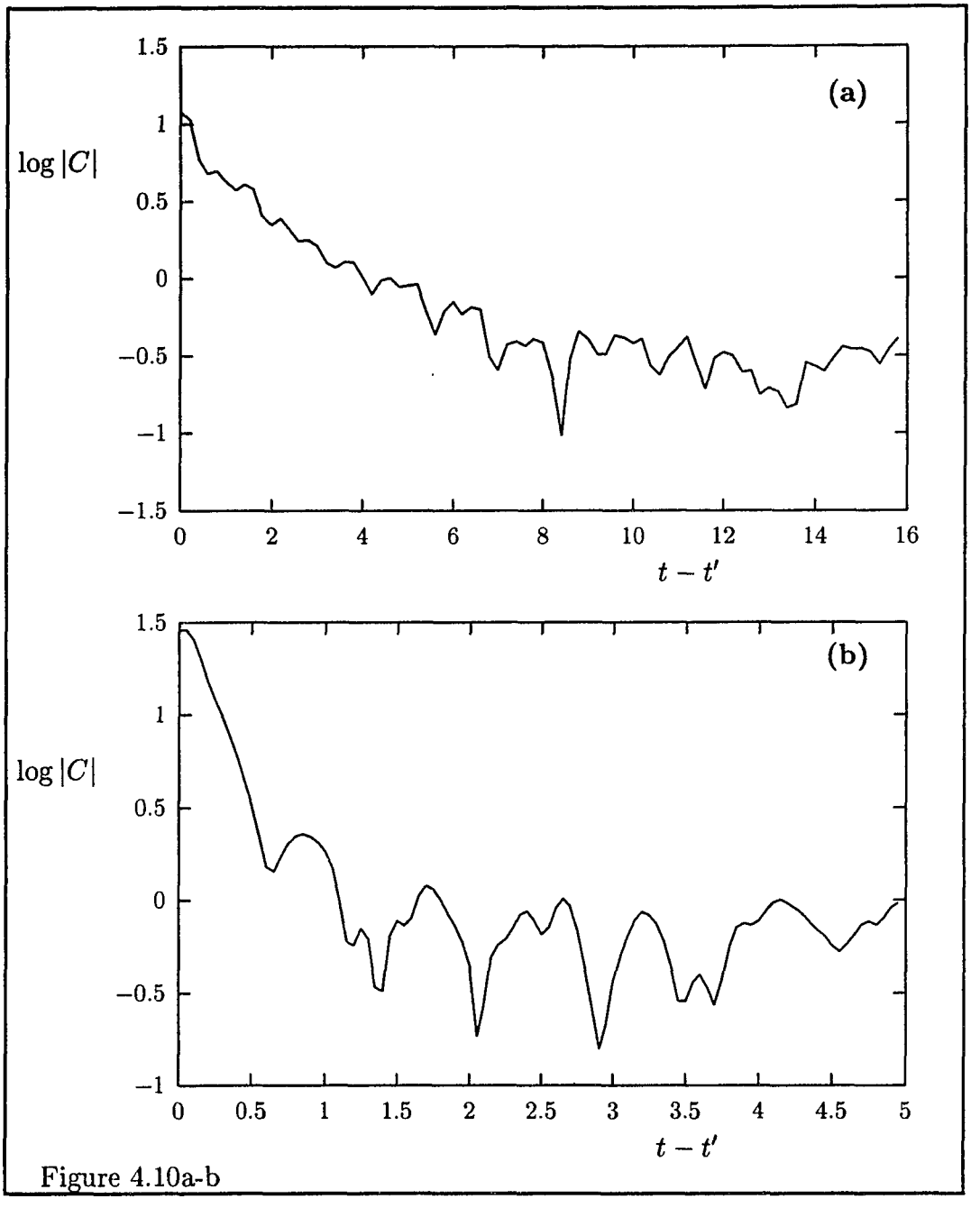

Figure 4.10a-b

Figure 4.10: The temporal correlation function $C(0, t, t')$ for $\Sigma_0 = 17$ (panel a) and $\Sigma_0 = 37$ (panel b).

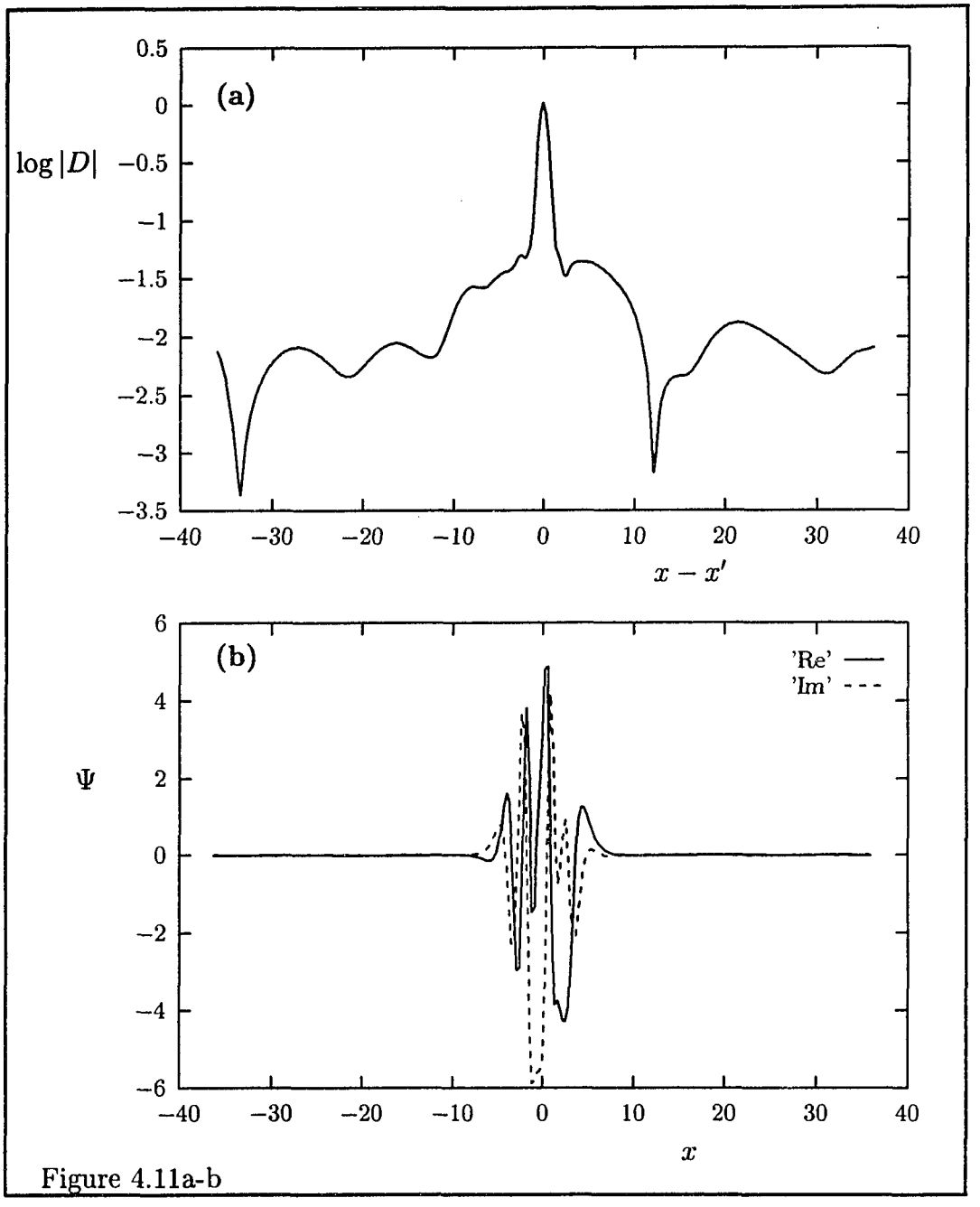

Figure 4.11: The spatial correlation function $D(0, x')$ (panel a) and a snapshot of $\Psi(x, t)$ (panel b) for $\Sigma_0 = 37$.

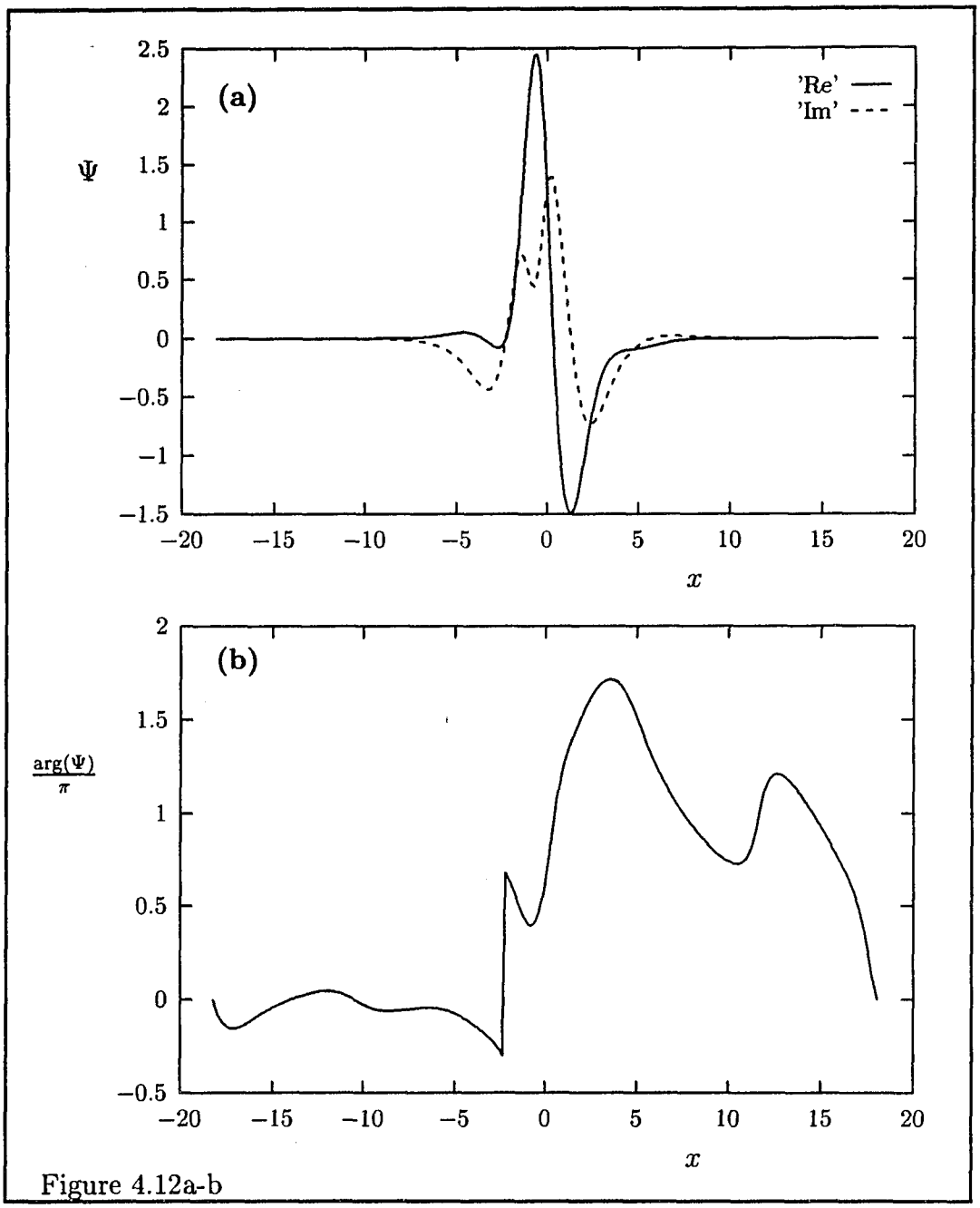

Figure 4.12a-b

Figure 4.12: Typical defects occurring for $\Sigma_0 = 7$, note the π phase jumps at the defect locations (panels b and d).

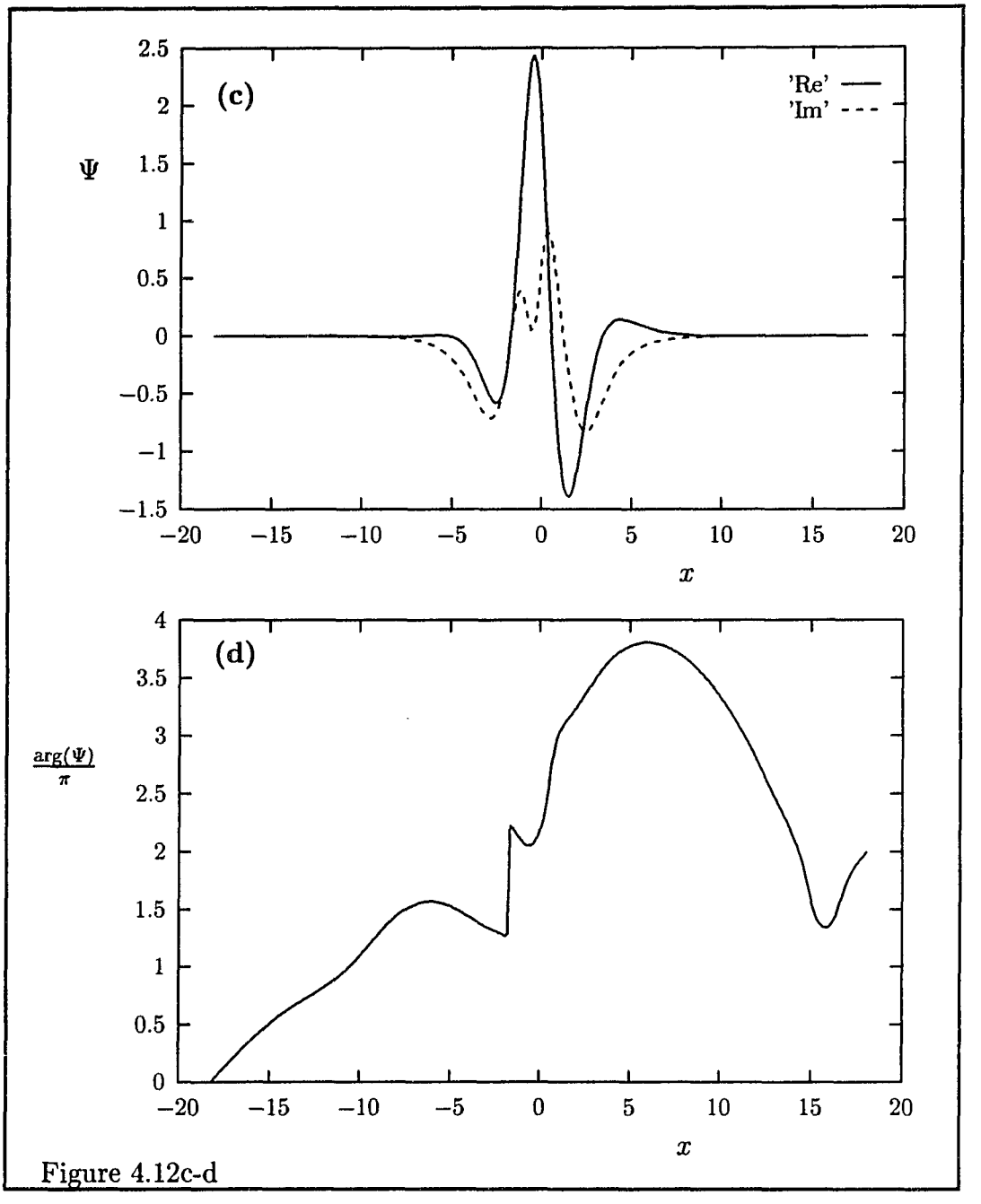

Figure 4.12c-d

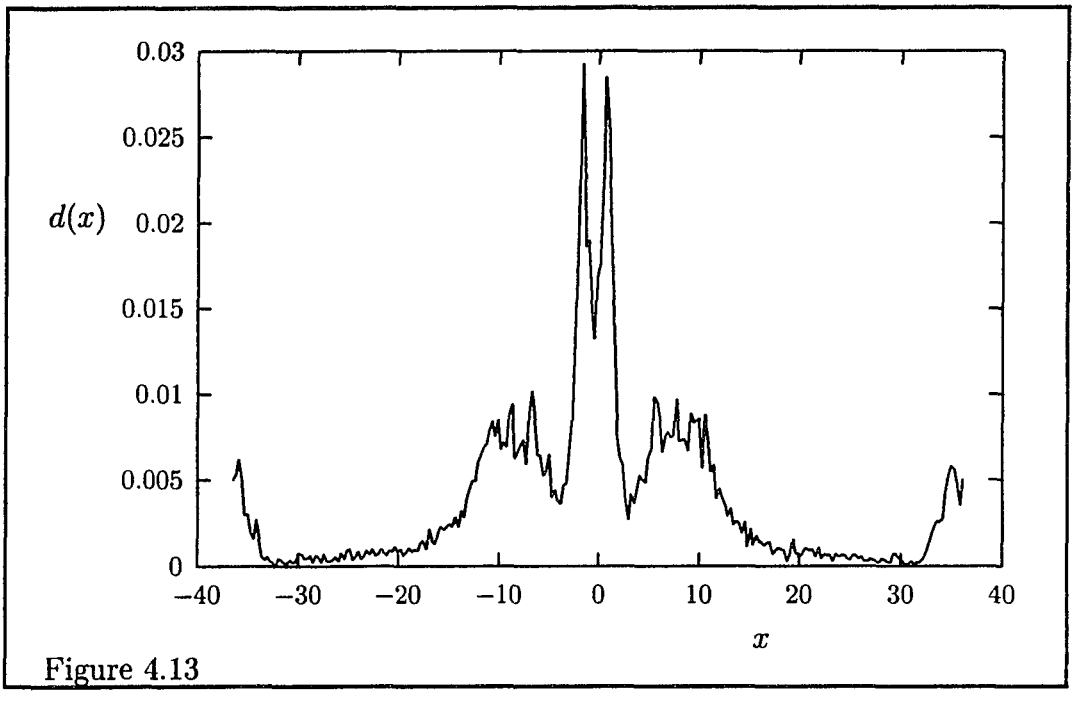

Figure 4.13: The defect distribution function $d(x)$ for $\Sigma_0 = 7$.

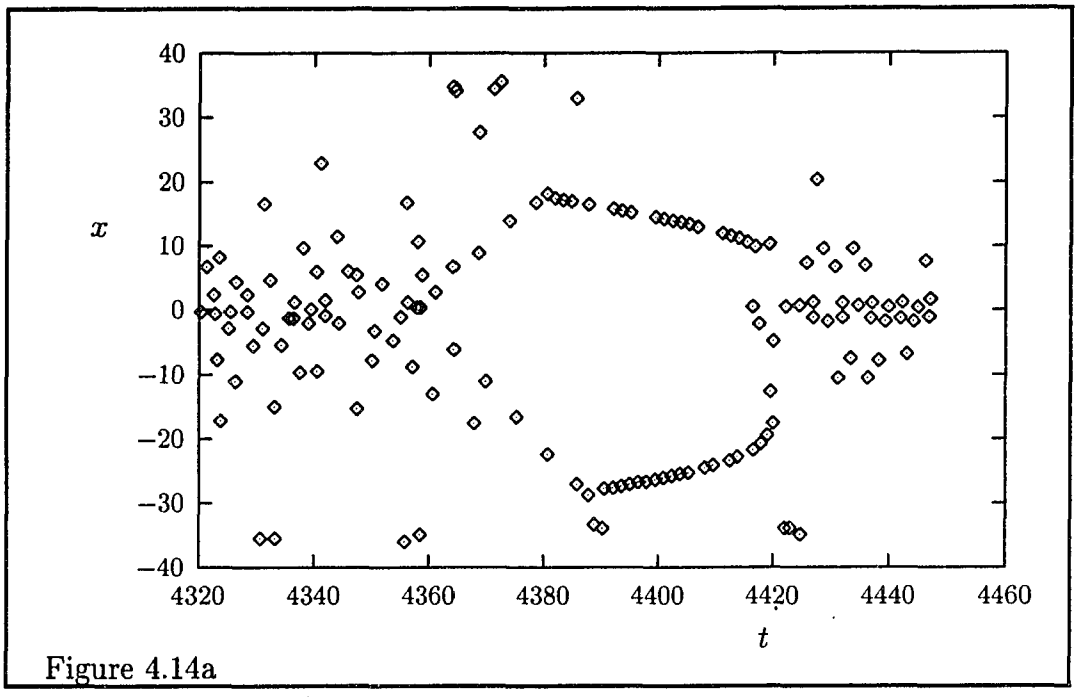

Figure 4.14a

Figure 4.14: Defects in the intermittency region for $\Sigma_0 = 7$. Note their structured appearence during an interval of regular motion, compare figure 4.6. Panels (b), (c) and (d) (next pages): The lines $Re\Psi = 0$ and $Im\Psi = 0$, defects occur at intersections. Compare panel (a) and figure 4.6. Defects located close to the system edges are size effects.

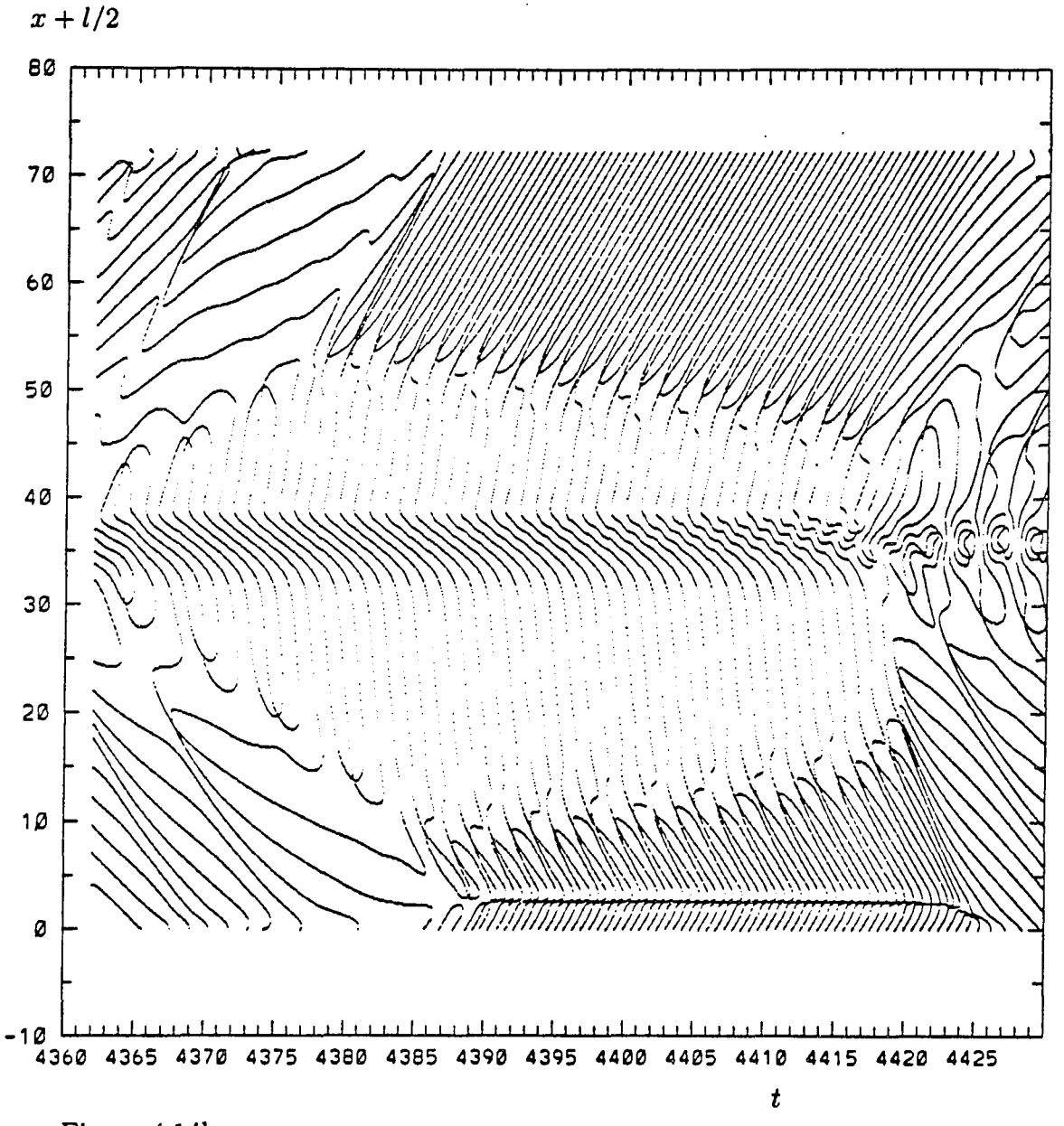
$x + l/2$
80
70
60
50
40
30
20
10
0
-10
4360 4365 4370 4375 4380 4385 4390 4395 4400 4405 4410 4415 4420 4425
t

Figure 4.14b

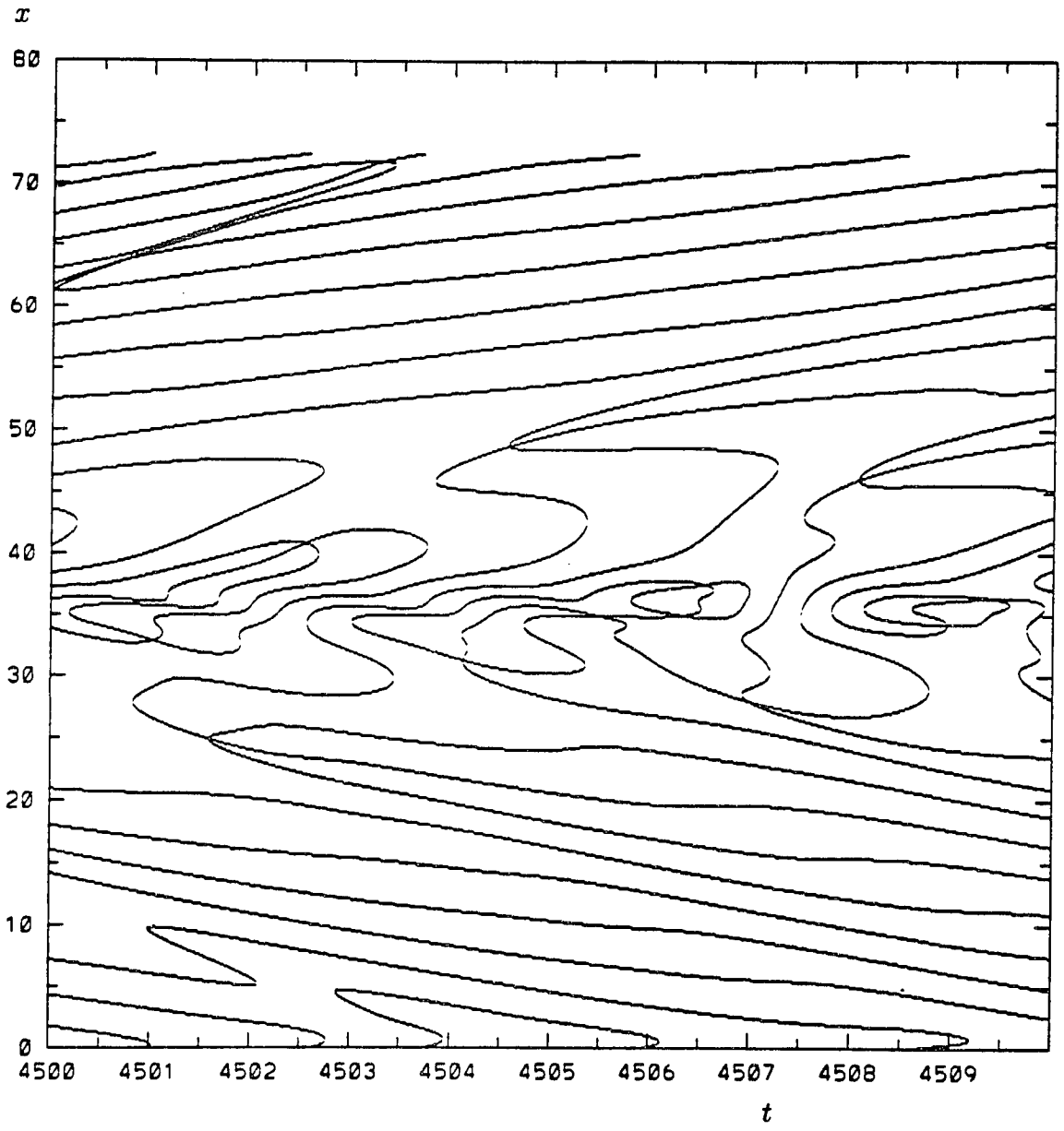
x
80
70
60
50
40
30
20
10
0
4500
4501
4502
4503
4504
4505
4506
4507
4508
4509
t

Figure 4.14c

4.2.2 Intermediate size systems.

As example of the behaviour in an intermediate size system we will discuss the situation where $K = 0.03$. The sequence of bifurcations observed as function of Σ_0 is schematically indicated in figure 4.15. Both initial conditions lead to the trivial solution $\Psi = 0$ for $0 < \Sigma_0 < 1.02$. For $1.02 < \Sigma_0 < 1.15$ a stationary pulse solution again exist which is symmetric, $\Psi(x,t) = \Psi(-x,t)$. The parity breaking occurs at $\Sigma_0 = 1.15$ and a stationary non symmetric pulse solution exist for $1.15 < \Sigma_0 < 1.32$. This state bifurcates into a two frequency quasi-periodic state which is of the form $\Psi_{QP}(x,t) = e^{i\omega t}\phi(x,t)$ where ϕ is periodic in time. It remains stable up to $\Sigma_0 = 1.38$. At $\Sigma_0 = 1.38$ intermittency sets in and the motion becomes fully chaotic at $\Sigma_0 = 1.4$. Some pictures of the behaviour for $\Sigma_0 < 1.38$ are shown in figure 4.16.

Defects are present in all states other than the stationary states. They occur as soon as the motion becomes quasi-periodic. The spatio-temporal behaviour of the chaotic states is quite different from what is observed in small systems ($K = 0.3$) as one would expect. Now there appear two distinct regions in space, each with its own characteristic behaviour.

In the central region where the growth rate is positive, defects are present

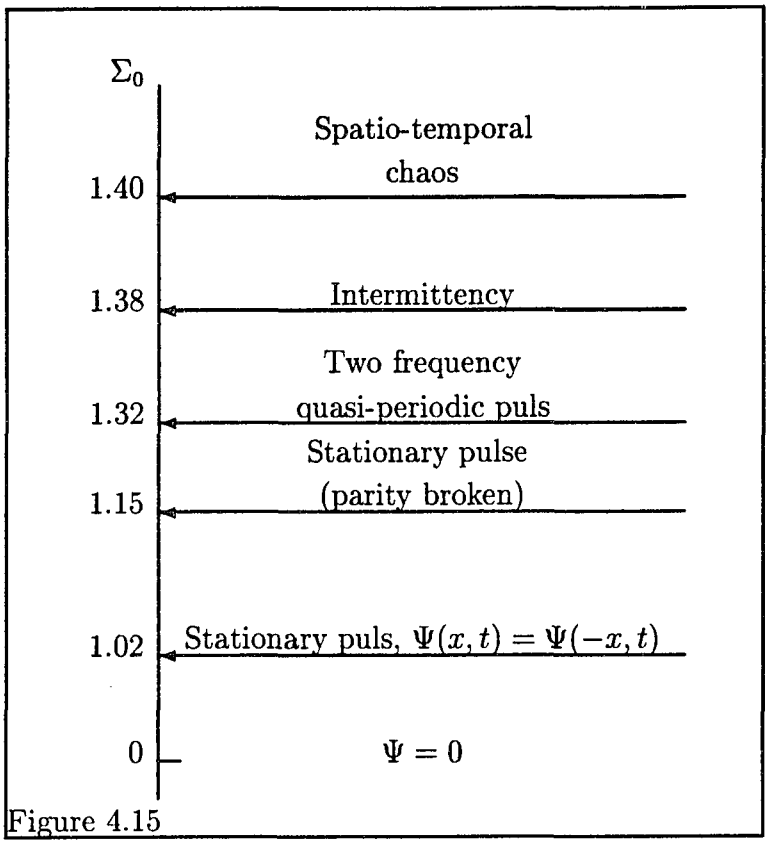

Figure 4.15

Figure 4.15: Bifurcation sequence of the CGLE with a spatially dependent growth rate given by (4.25) and (4.26) in an intermediate size system with $K = 0.03$, $c_2 = -1$, $c_3 = 1$ as function of Σ_0, observed starting from the two different initial conditions given by (4.28).

and the behaviour displays a transition to amplitude chaos via intermittency, see figure 4.17. It is obvious that this is not the so-called spatio-temporal intermittency mentioned in chapter 1. In the outer region where the growth rate is negative and eventually approaches -1 as $x \to \pm\infty$, the amplitude decays exponentiallly and becomes rapidly extremely small, $\approx 10^{-20}$ at the system boundaries in a typical simmulation. Defects occur here only because of size effects, that is they occur close to the boundaries and because of the boundary conditions.

Close to the boundaries between the two regions shoulders are present in the outher regions, in which the time behaviour of $|\Psi|$ for fixed x looks like $|\Psi(x,t)| = |\Psi_0(x)| + a(x,t)$ where $a(x,t)$ is small. See figure 4.18b. Obviously, defects do not occur in these shoulders which are of significant width, and this is therefore another observation suggesting that the defects occurring in the outer regions are indeed size effects. As we approach the boundaries between the central and outer regions from within the central region the behaviour also changes, we will discuss this a little further on.

The power spectrum of $Re\Psi(x,t)$ for x in the center of the system and in an outer region is shown in figure 4.19 for $\Sigma_0 = 3$. We clearly observe that the temporal behaviour at each position is very different. In the central

Figure 4.16: (Next page) Snapshots of a stationary and a quasi-periodic pulse for $\Sigma_0 = 1.3$ (a) and $\Sigma_0 = 1.37$ (b) repectively. Panels c and d (next page) show the power spectra of Ψ and $|\Psi|$ for $\Sigma_0 = 1.37$. The quasi-periodic pulse may be written as $\Psi_{QP}(x,t) = e^{i\omega t}\phi(x,t)$, where ϕ is periodic in t.

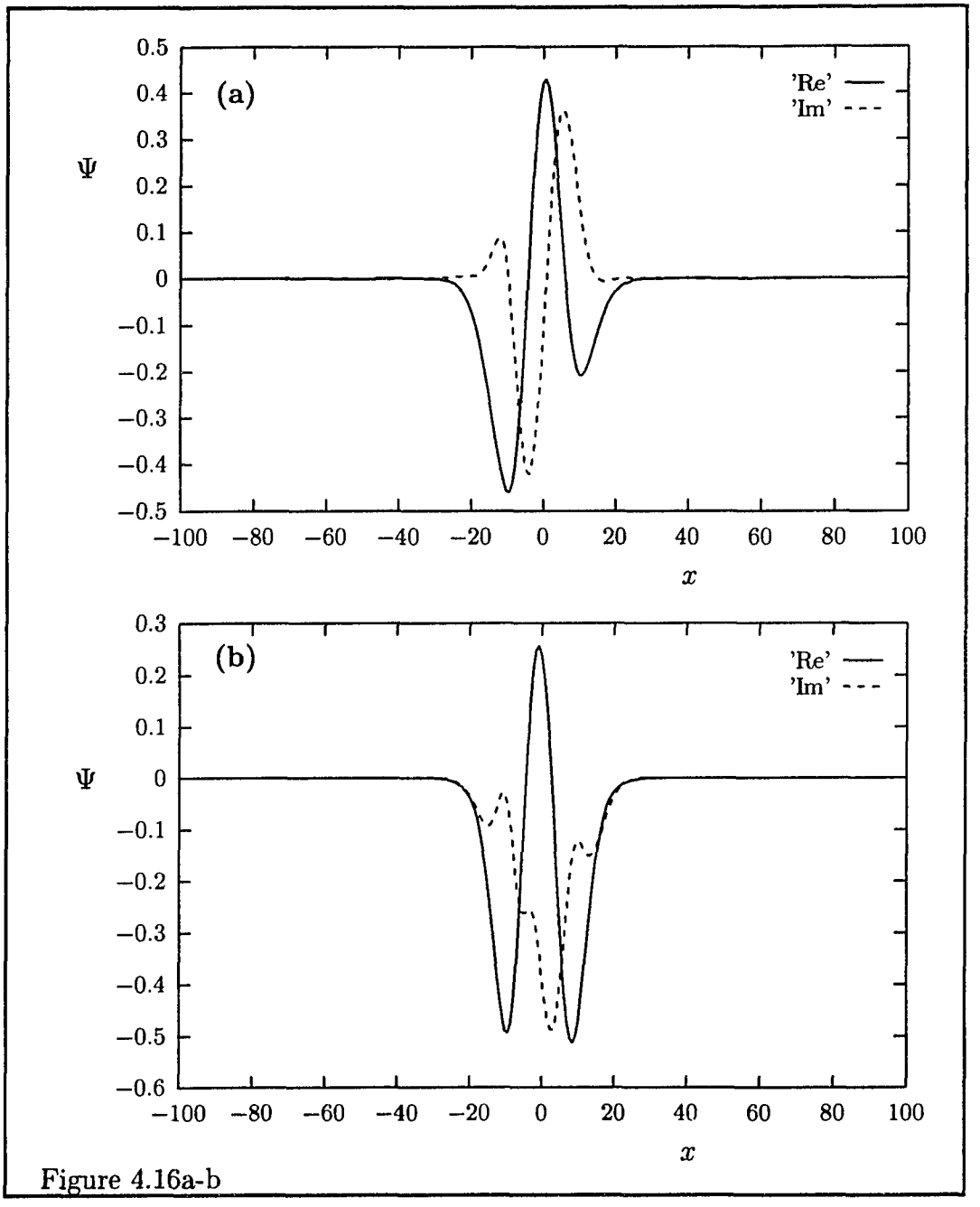

Figure 4.16a-b

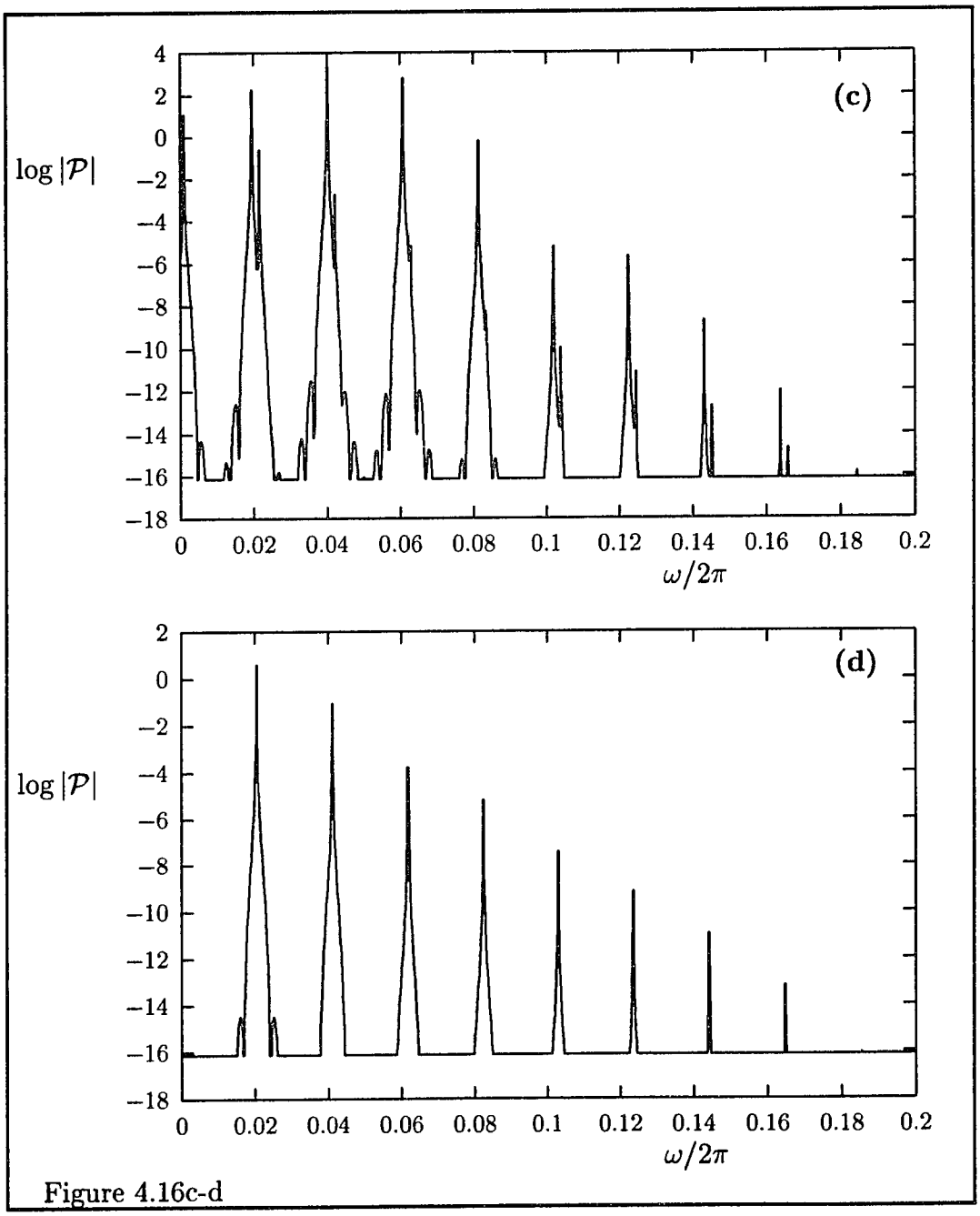

Figure 4.16c-d

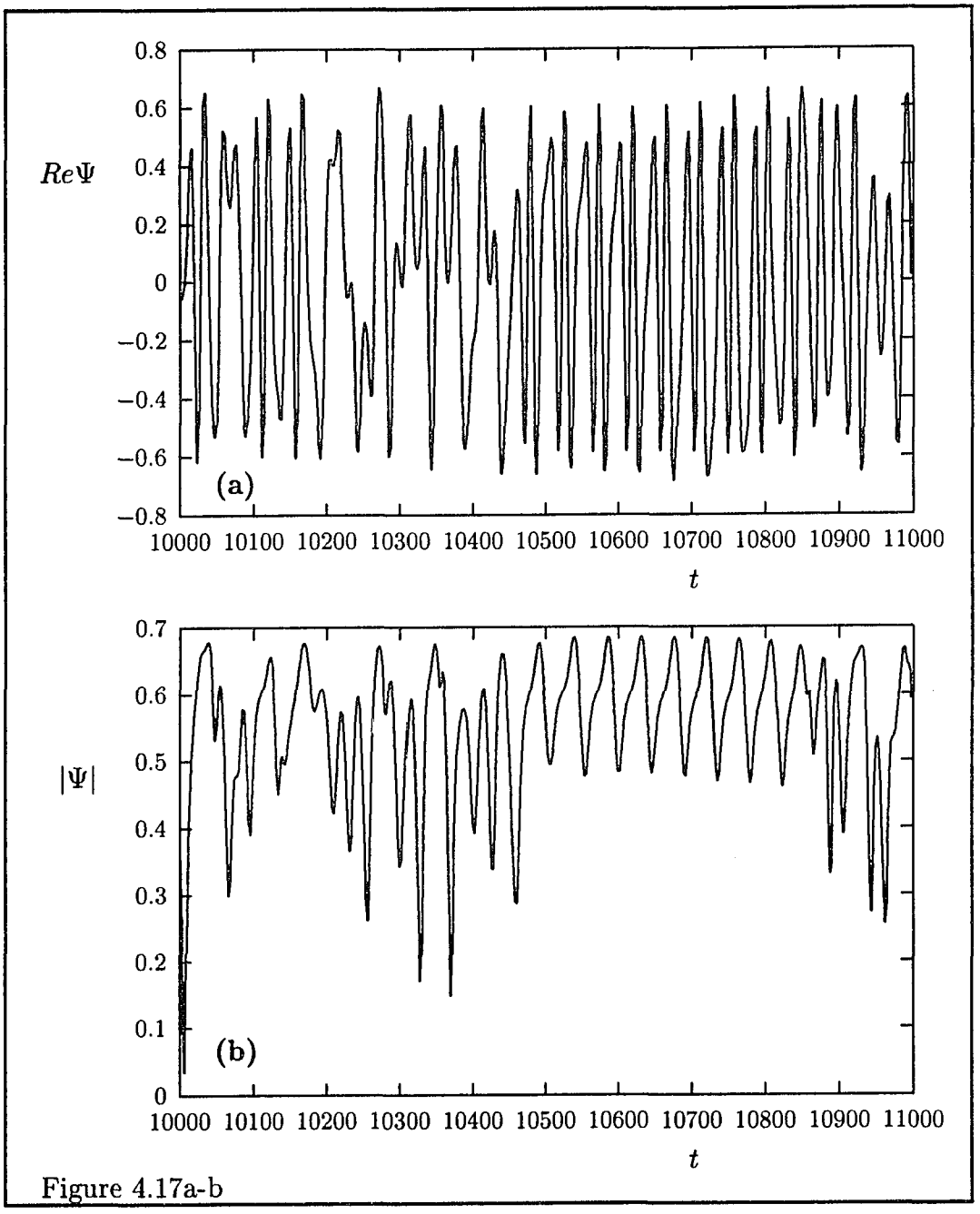

Figure 4.17a-b

Figure 4.17: Time series of $Re\Psi(0,t)$ and $|\Psi(0,t)|$ in the intermittency region for $\Sigma_0 = 1.39$.

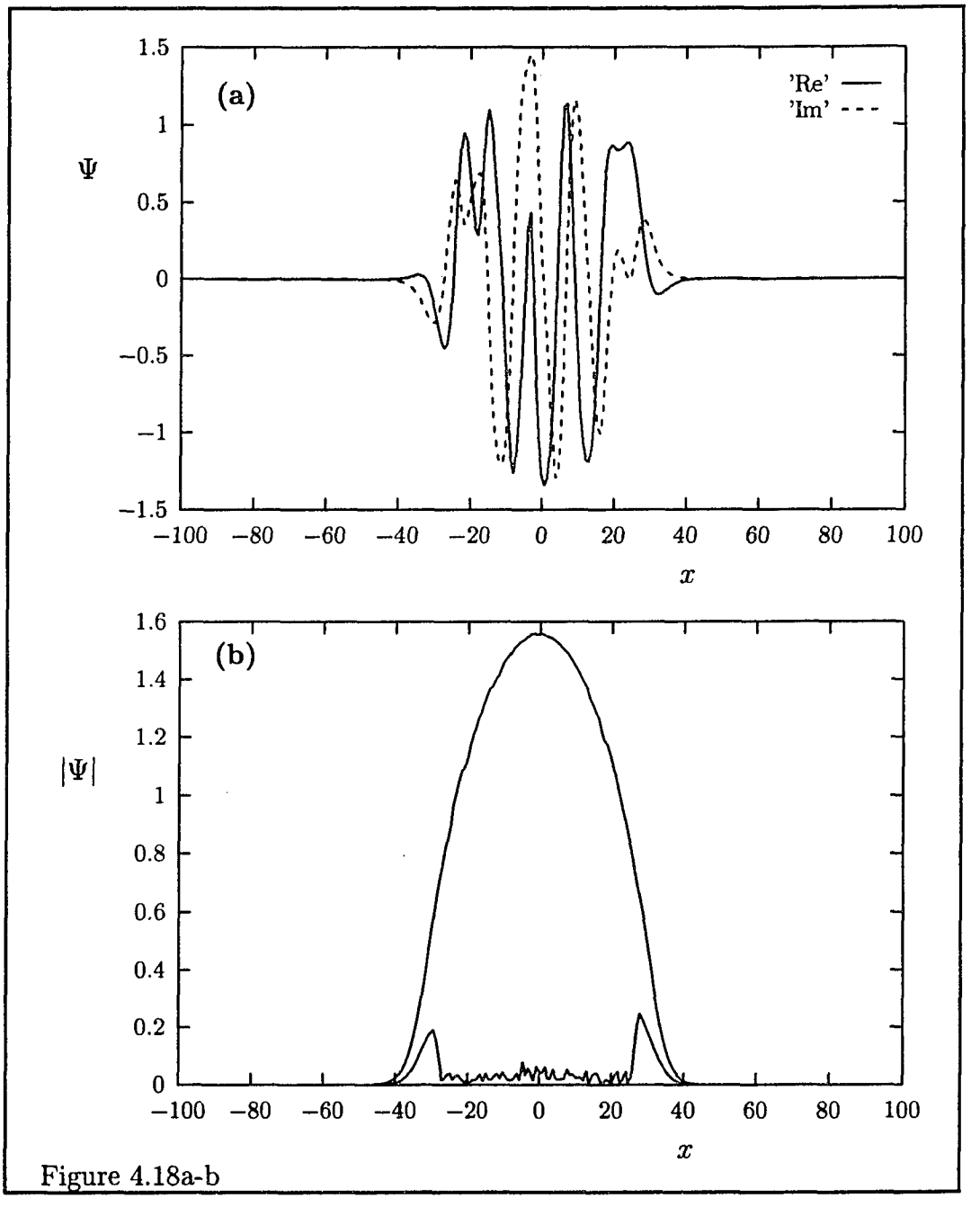

Figure 4.18a-b

Figure 4.18: Snapshot of the chaotic pulse solution (a) and the spatial envelope of $|\Psi(x,t)|$ (b) for $\Sigma_0 = 3$. Note the shoulders in $|\Psi|$ located at $x \approx [-40, -30]$ and $x \approx [30, 40]$.

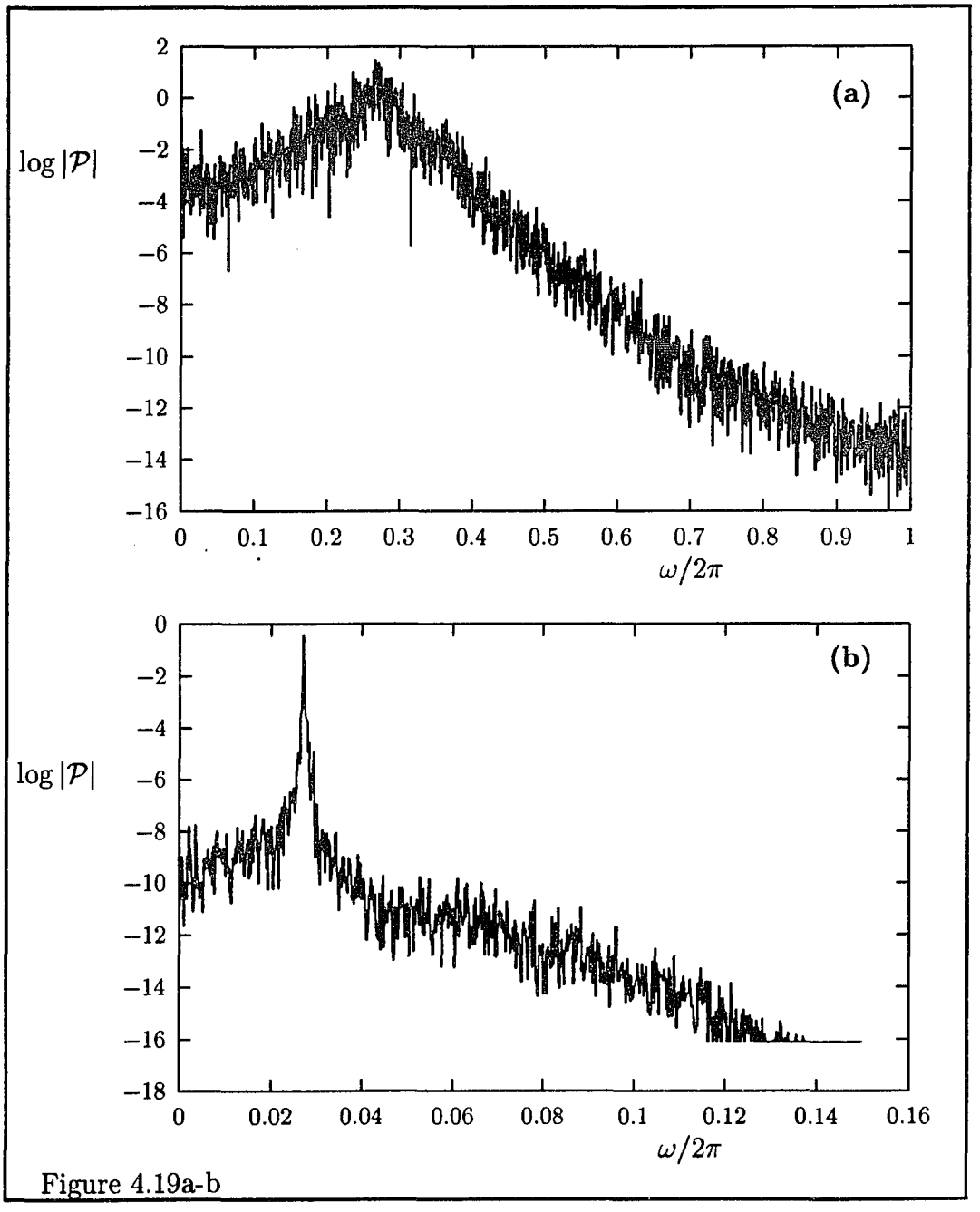

Figure 4.19a-b

Figure 4.19: Power spectra of $Re\Psi(0,t)$ (a) and $Re\Psi(-36,t)$ (b) for $\Sigma_0 = 3$.

region the power spectrum displays chaotic motion. In the outer region the power spectrum also illustrates chaotic motion with however the dominating presence of one particular frequency say ω_0. The temporal correlation function $C(x,t,t')$ for $\Sigma_0 = 3$ is shown in figure 4.20. For x in the central region we observe decay for small $t - t'$ and saturation for larger values. When x is in the outer region no significant decay is present, at least not on a time scale of the order of $2\pi/\omega_0$.

The spatial correlation function $D(x,x')$ is shown in figure 4.21 for some positions x and $\Sigma_0 = 3$. Also here the behaviour in the different spatial regions is obvious. The spatial correlations decay when x and x' are both in the central region. If we assume this decay to be exponential we find for the correlation length $\xi = 5$, which is about a factor 10 smaller than the pulse width in this case. In the outer regions the situation is completely different. When x and x' are both in the same outer region $D(x,x')$ doesn't show any decay. When x and x' are in different outer regions the spatial correlations show a little "jump" but also do not decay. Of course the boundary conditions will have a strong influence on the size of this jump. Infact, one would expect the behaviour in the left and right outer regions to be essentially uncorrelated because of the decay of correlations in the central region. The fact that we

don't observe this is most likely a consequence of the finite system size and the periodic boundary conditions.

The above observations lead us to the conclusions that in the central region a transition to amplitude chaos takes place at about $\Sigma_0 = 1.4$. The intermitent behaviour occurring between the states of amplitude chaos and quasi-periodic behaviour appears to be of a complicated nature. It can certainly not be classified as spatio-temporal intermittency [34], but on the other hand it is also not clear it is of a simular nature as the intermittency observed in low dimensional systems and mappings [41]. In the outer regions the behaviour shows a transition to temporal chaos via quasi-periodicity and intermittency. Here the intermittency appears to be more simular to what is observed in low dimensional systems. Also, here the behaviour appears to be coherent in space. In relation to this one should note that Ψ decays exponentially in the outer regions and in such a rapid manner that their actual size is limited by the smallest reliable value allowed for $|\Psi|$ in the simulation. In the simulations performed in this work, the size of the outer regions was too small to observe spatial disorder. We therefore can not make any clear prediction concerning the possiblity for phase-chaos in the outer regions, although it is certainly reasonable to expect that this behaviour might occur

under certain conditions.

The defect distribution function for $\Sigma_0 = 3$ is shown in figure 4.22. We see that he boundaries between the central and outer regions are sharp as far as the presence of defects is concerned. They are characterized by the sudden disapearence of defects as we leave the central region. The actual (analytical) defect distribution function therefore may be expected to have a non zero value at a boundary. Is the defect presence abruptly ended, other quantities may vary continuously as we pass it. For example, the correlation time increases sharply as we approach a boundary from within the central region (figure 4.20c), indicating a smooth transition to its value in the outer region, which is expected to be very high but finite. Also, the power spectrum clearly displays a superposition of the spectra characteristic for the two regions as we approach the boundary.

Figure 4.20: (Next page) The temporal correlation function $C(x, t, t')$ for $\Sigma_0 = 3$ at the positions $x = 0$ (a), $x = -9$ (b), $x = -22$ (c) and $x = -50$. For the location of these positions in the actual solution see figure 4.18, in particular figure 4.18b.

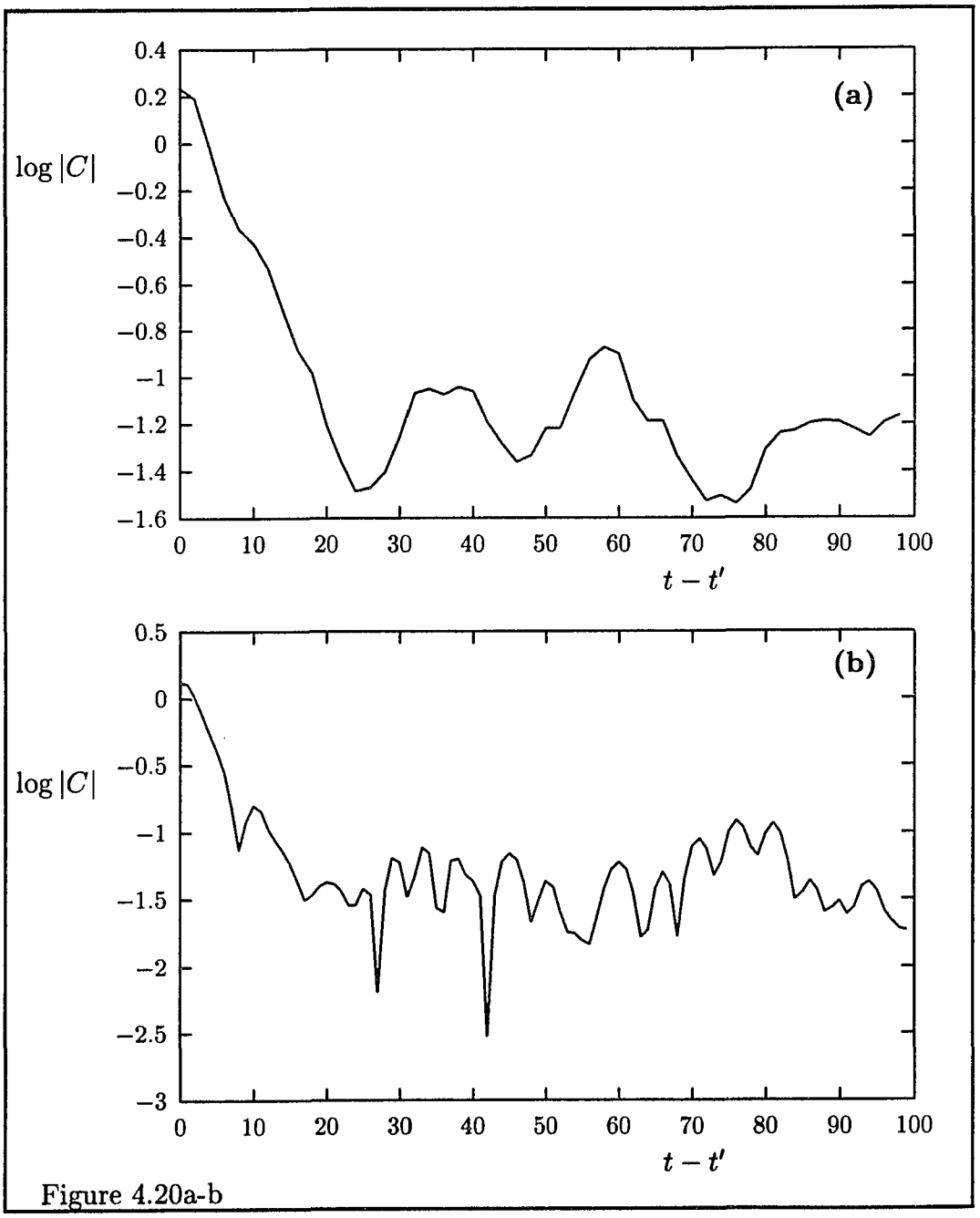

Figure 4.20a-b

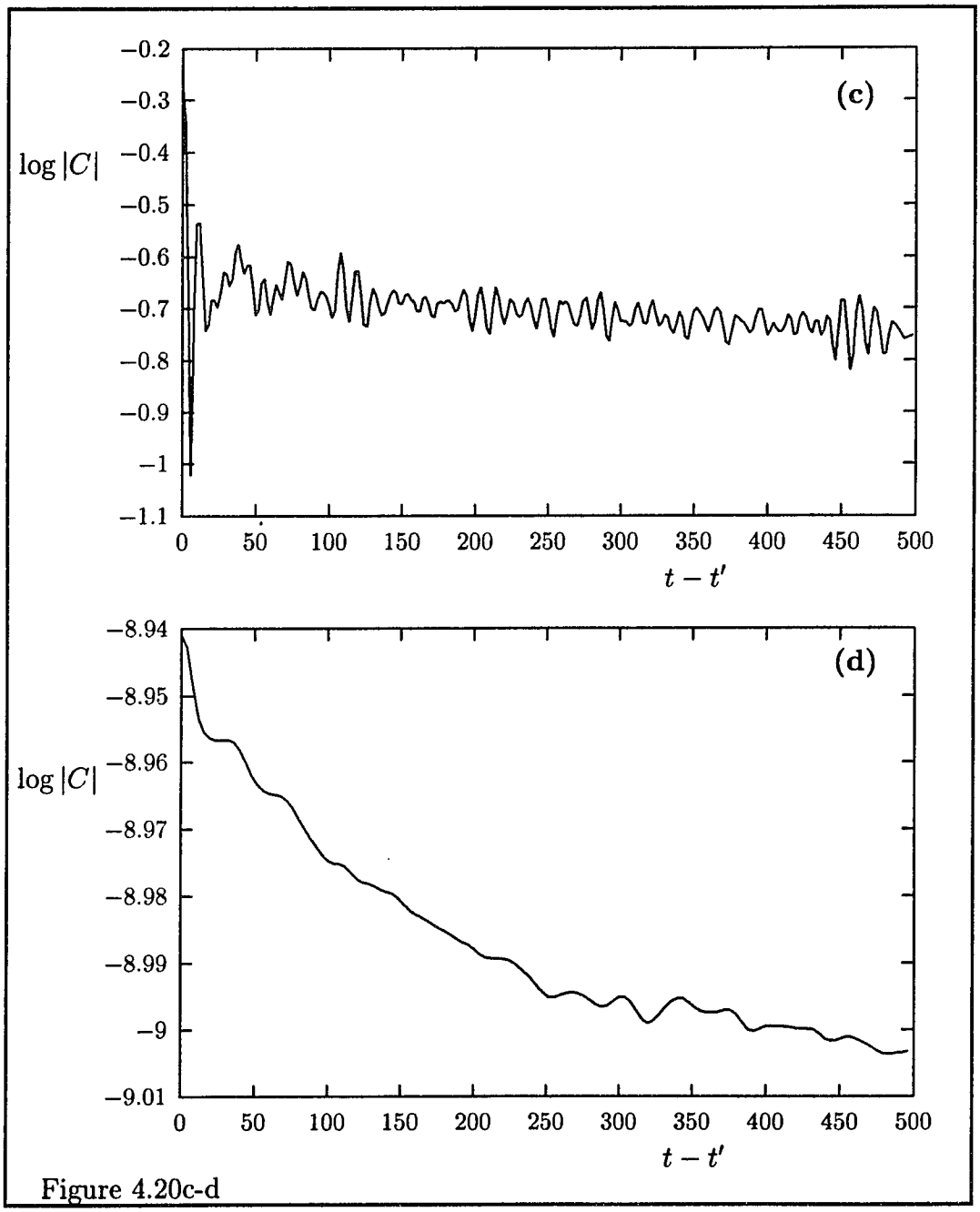

Figure 4.20c-d

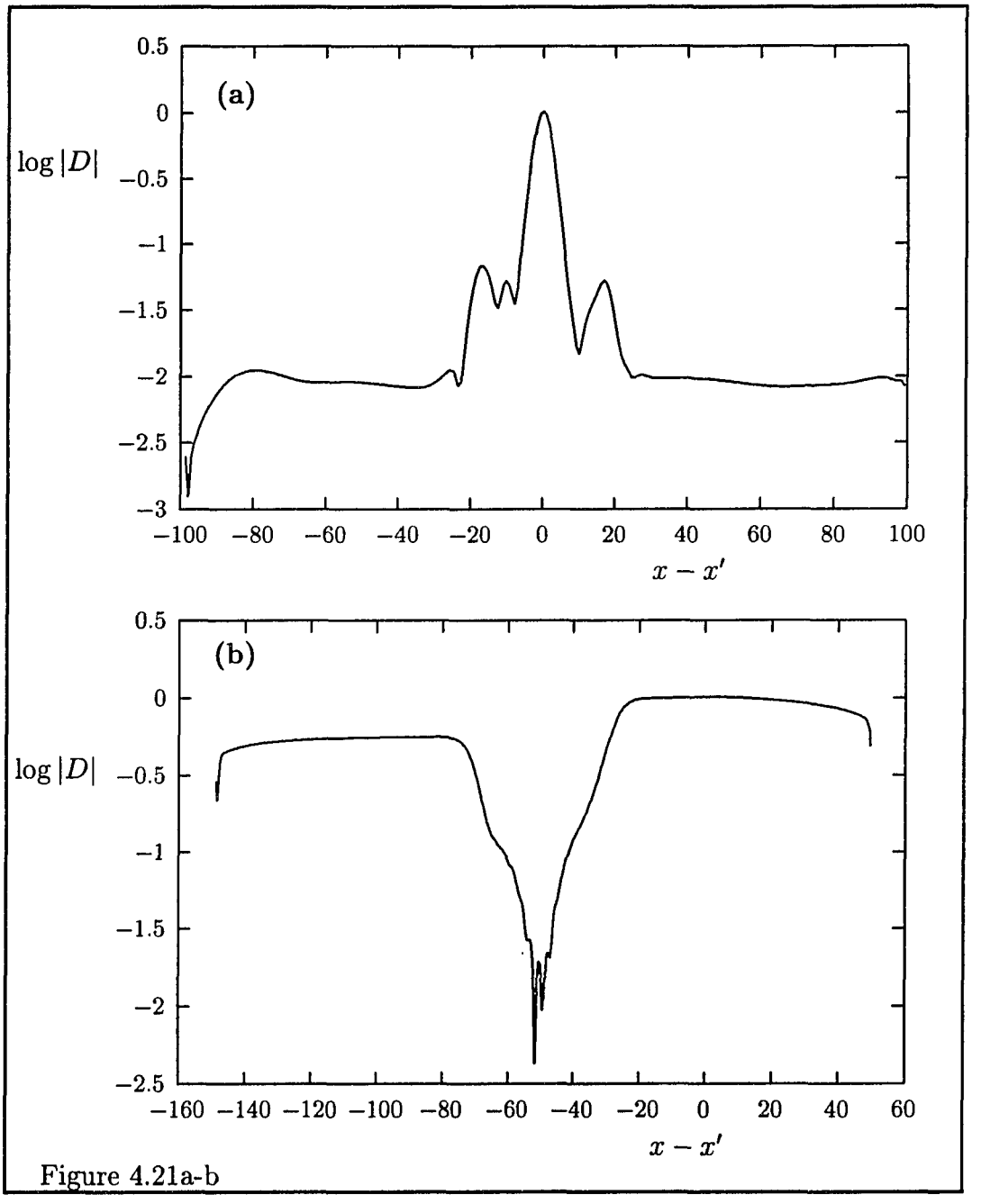

Figure 4.21a-b

Figure 4.21: The spatial correlation function $D(x, x')$ as function of $x - x'$ at $x = 0$ (a) and $x = -50$ (b) for $\Sigma_0 = 3$. For the location of these positions in the actual solution see figure 4.18, in particular figure 4.18b.

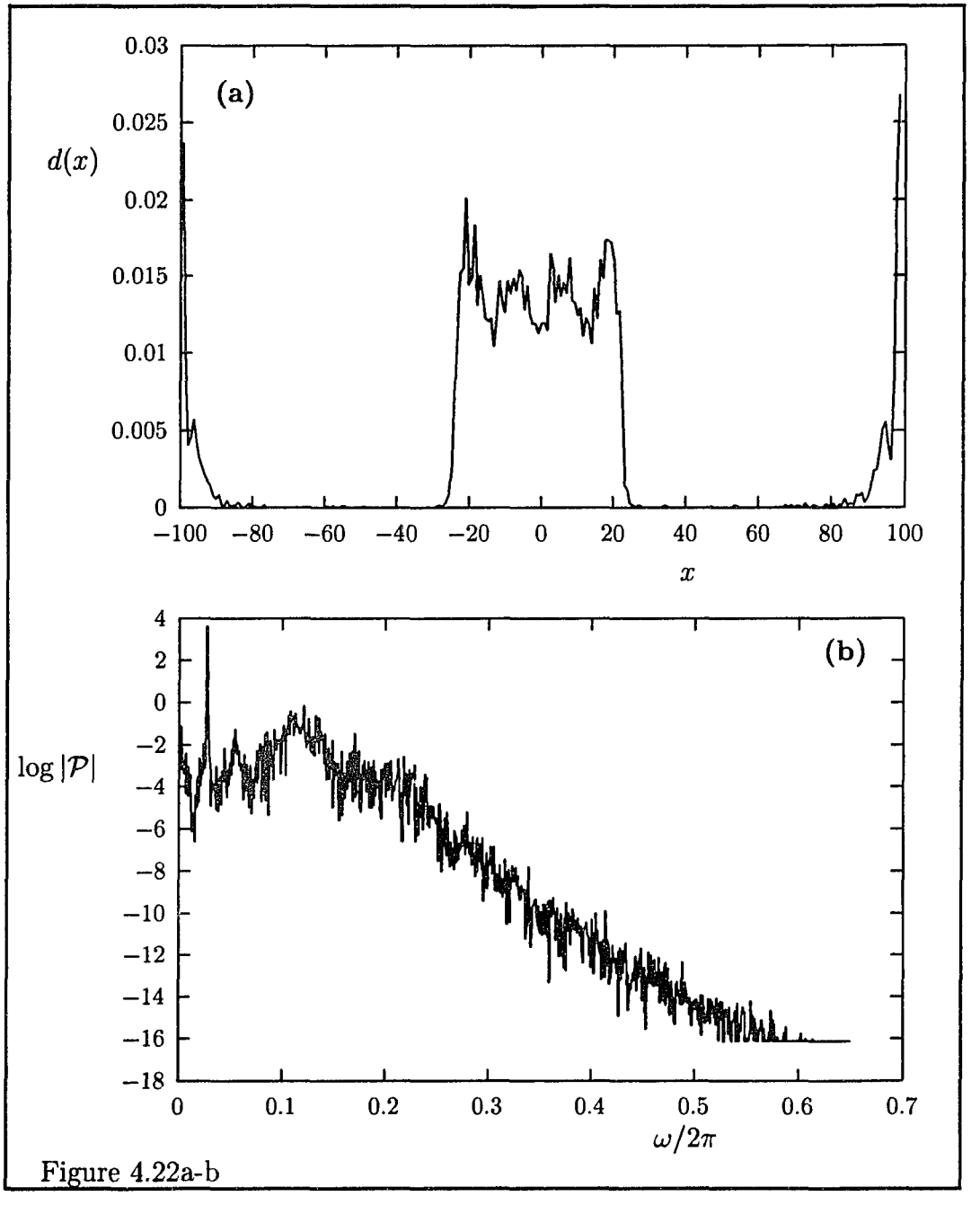

Figure 4.22: The defect distribution function $d(x)$ for $\Sigma_0 = 3$ (a) and the power spectrum of $Re\Psi(-23, t)$ (b) in the central region close to the left boundary, see figure 4.18b.

Figure 4.23: (Next page) The lines $Re\Psi = 0$ and $Im\Psi = 0$, defects occur at intersections. The plots are for $\Sigma_0 = 3$ (a) and $\Sigma_0 = 1.39$ (b),(c). In (a) the behaviour is chaotic in the central region. In (b) the behaviour shows intermittency.The change from a period of regular motion to chaotic behaviour similar to what is shown in figure 5.17a-b, occurs for instance at $t \approx 12400$. The picture continues in (c).

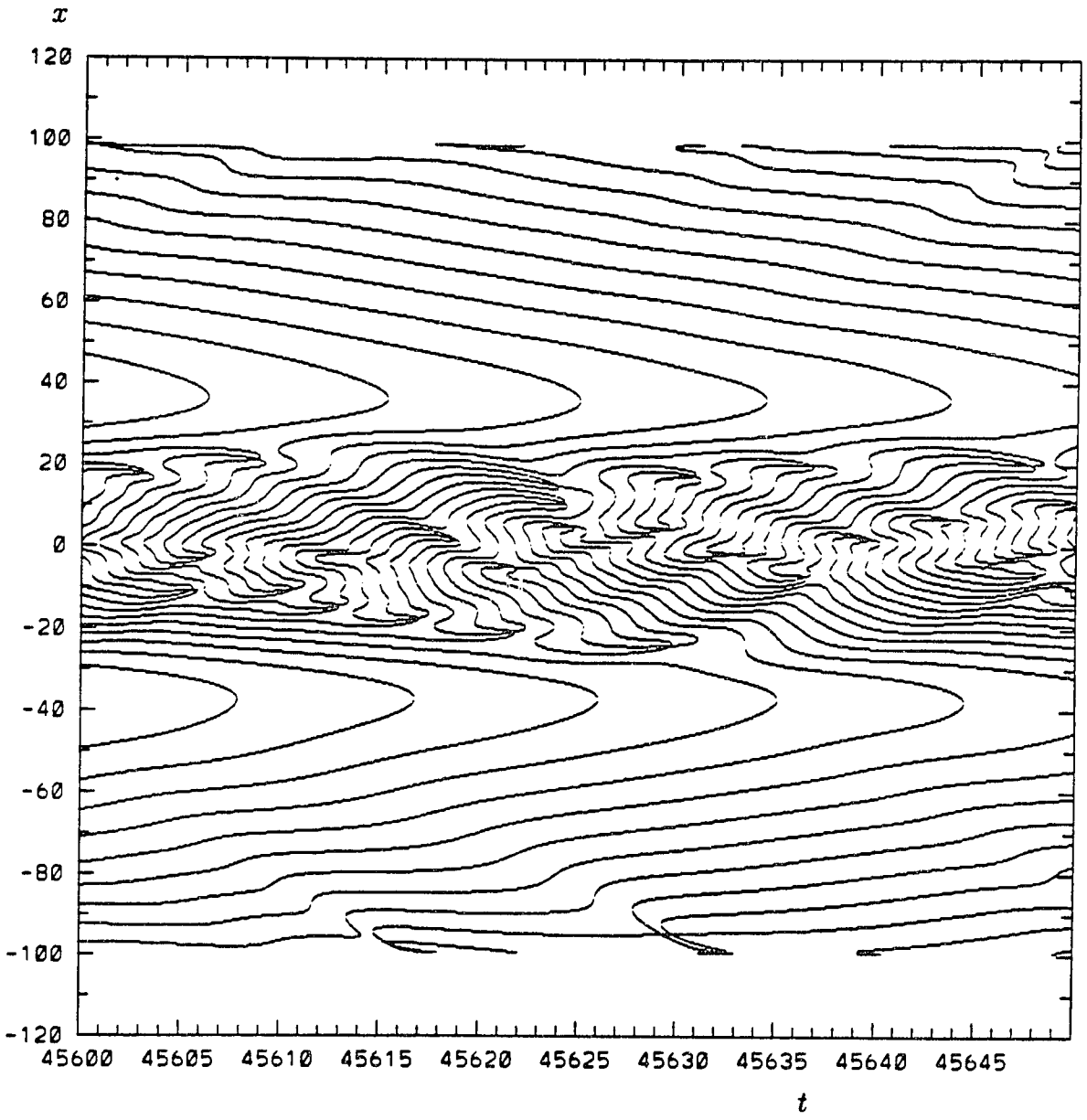
x
120
100
80
60
40
20
0
-20
-40
-60
-80
-100
-120
45600
45605
45610
45615
45620
45625
45630
45635
45640
45645
t

Figure 4.23a

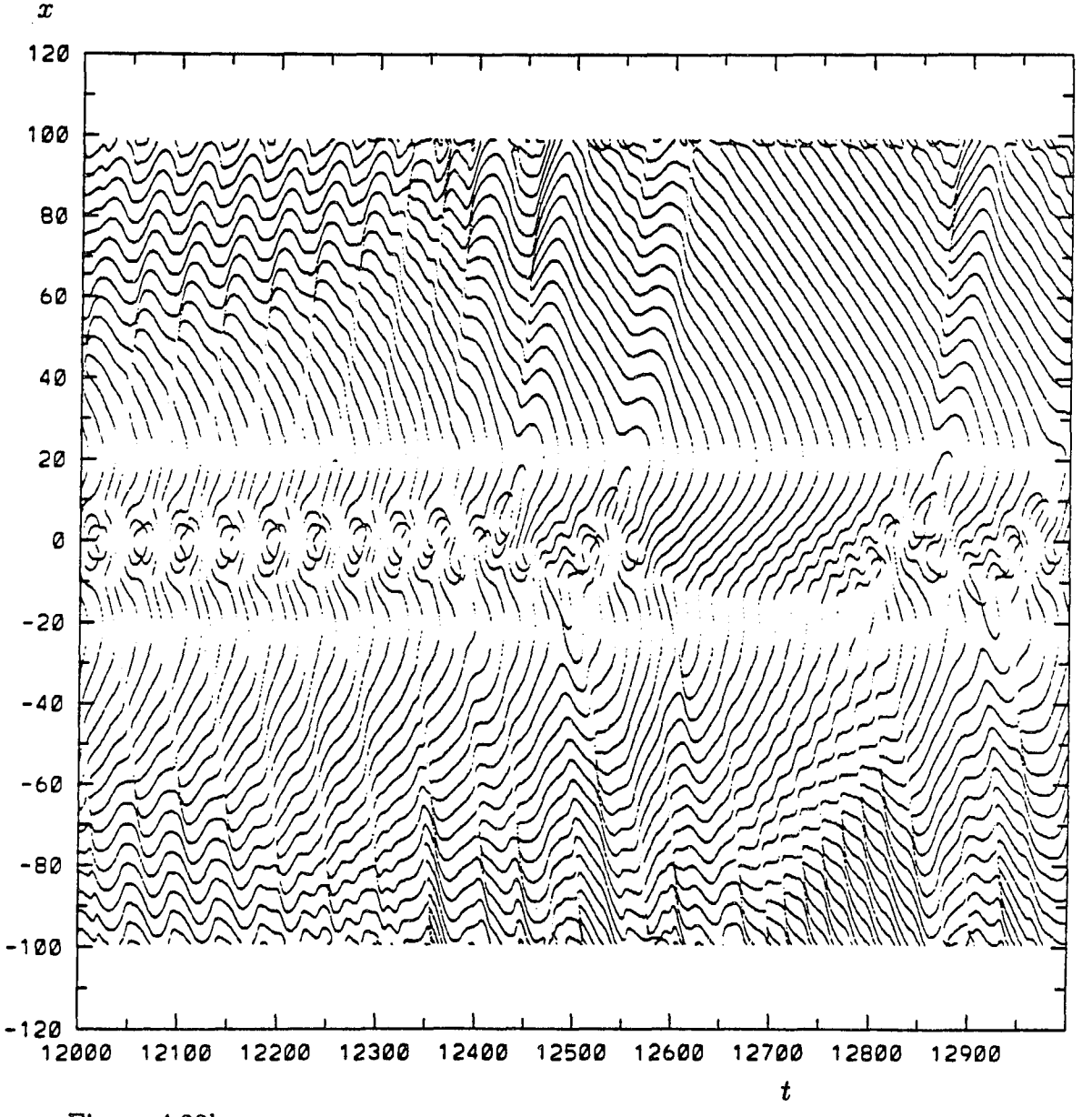
x
120
100
80
60
40
20
0
-20
-40
-60
-80
-100
-120
12000
12100
12200
12300
12400
12500
12600
12700
12800
12900
t

Figure 4.23b

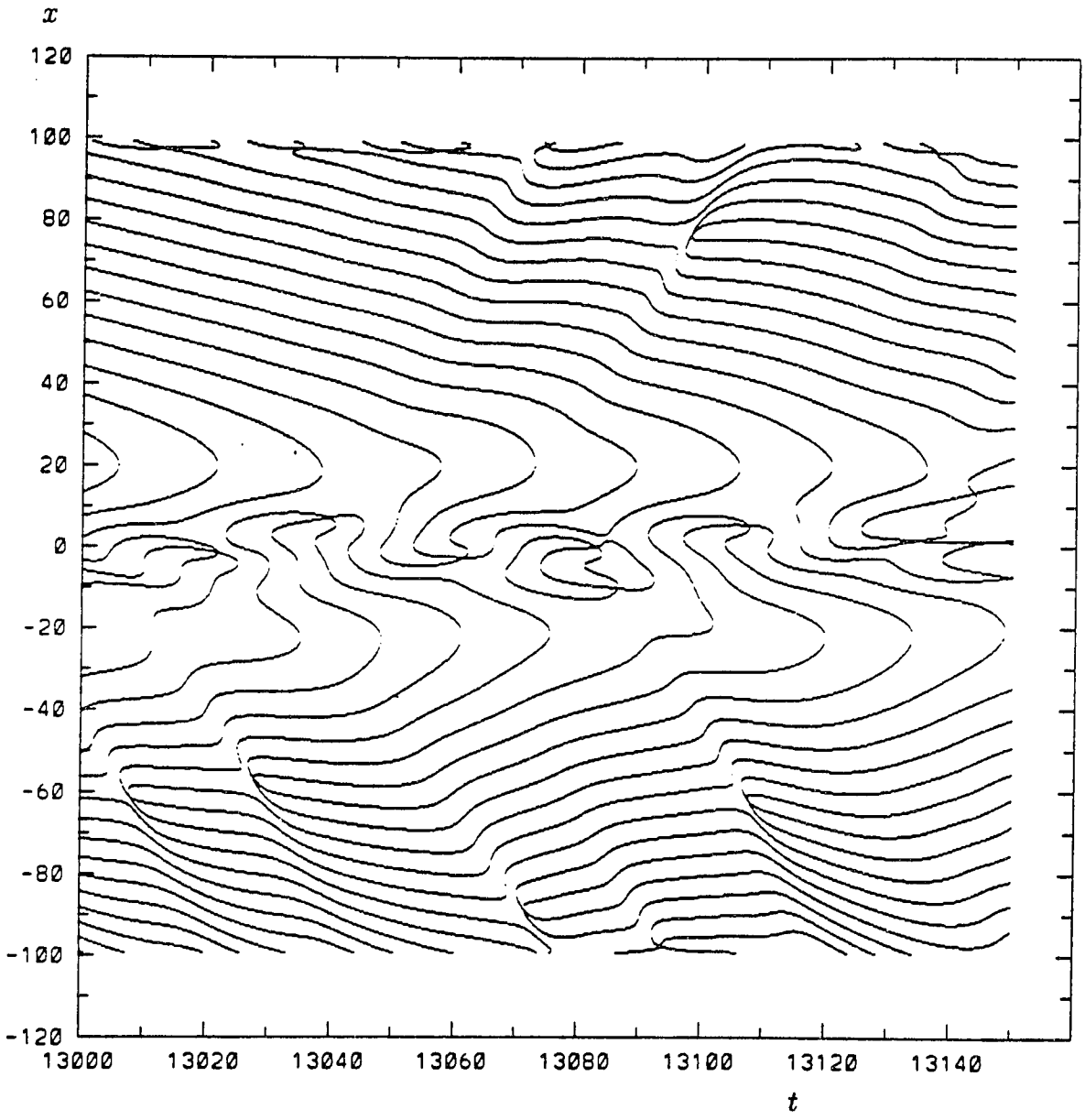
x
120
100
80
60
40
20
0
-20
-40
-60
-80
-100
-120
13000
13020
13040
13060
13080
13100
13120
13140
t

Figure 4.23c

4.2.3 Large systems.

As example of the behaviour in a large system we will discuss the situation where $K = 0.003$. The bifurcation sequence for this situation is shown in figure 4.24. The trivial solution is only stable for negative growth rate. As soon as $\mu_1(x)$ becomes positive locally $\Psi = 0$ becomes unstable and a stationary and symmetric pulse solution emerges. This solution is stable up to $\Sigma_0 = 1.015$, when parity breaking occurs. The new stable state is a stationary non symmetric pulse which is stable up to $\Sigma_0 = 1.035$. The behaviour for $\Sigma_0 > 1.035$ dispays features also observed in the previous cases as well as new phenomena. For Σ_0 just above 1.035 the behaviour looks similar to the chaotic behaviour observed for $K = 0.3$ and large Σ_0. The shoulders in $|\Psi|$ are not present and the decay of the spatial correlation function is not very convincing. The motion therefore, although not coherent over the length of the system, which is now of course much larger than for the $K = 0.3$ case, does not show any spatial disorder. See figure 4.25. For Σ_0 slightlly larger than 1.1 the spatial correlations show a more convincing decay and shoulders are present in $|\Psi|$, the behaviour looks similar to the chaotic state observed for $K = 0.03$. See figure 4.26.

If we increase Σ_0 further we observe spatio-temporal intermittency [34]. See figure 4.27. A snapshot of $|\Psi|$ shows a typical smooth behaviour with an overall pulse shaped structure interrupted by sharp localized irregularities, typical for spatio-temporal intermittency. The behaviour of $|\Psi|$ in time is of a similar nature, an overal constant (stationary) behaviour interrupted by periods of irregular motion. The shoulders in $|\Psi|$ however remain present and the spatio-temporal intermittency therefore is only present in a localized central region where the growth rate is positive. The behaviour in the outer regions is as discussed for $K = 0.03$.

As Σ_0 is further increased two different correlation lengths appear to be present, see figure 4.28. There is first a steep decay fore small $x - x'$ followed by a weaker deacy as $x - x'$ increases. This might indicate that the central part of the central region is in a state of ampolitude chaos while the remaining part is still in a state of spatio-temporal intermittency. I use the phrase "might indicate" because this behaviour is not obvious from snapshots of $\Psi(x, t)$. On the other hand, an other observation which is in favor of the above conclusion is that the correlation time, deduced from $C(x = 0, t, t')$ assuming exponential decay, shows a sharp decrease if Σ_0 increases from 1.035 to 1.3, then pauses up to $\Sigma_0 = 2$ after which it decreases again. See table

4.2.

Σ	τ
1.05	550
1.1	300
1.3	50
2	50
3	25

Table 4.2: The correlation time τ for $C(0,t,t')$ as function of Σ_0, the values are obtained assuming exponential decay of $|C|$.

Defects are not present in the stationary states but were observed to exist in all other states. Some plots of the lines $Re\Psi = 0$ and $Im\Psi = 0$ are shown in figure 4.29.

From the above results we see that there are many qualitative changes in the behaviour in the systems of different sizes as Σ_0 is varied. I have not extensively explored the change in behaviour as function of the parameters c_2 and c_3. However, the first impresions are that he bifurcation sequences do not change too much qualitatively. The trend is that the growth rate amplitude Σ_0 at which the bifurcations occur, shifts to somewhat higher values when

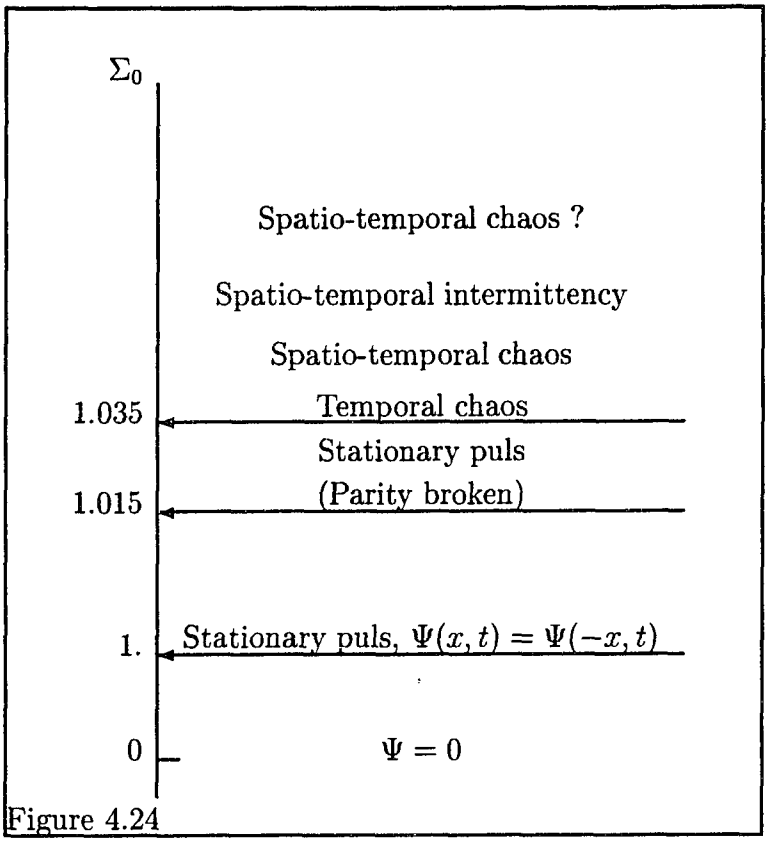

Figure 4.24: Bifurcation sequence of equation of the CGLE with a spatially dependent growth rate given by (4.25) and (4.26) in a large system with $K = 0.003$, $c_2 = -1$, $c_3 = 1$ as function of Σ_0, observed starting from the two different initial conditions given by (4.28).

the product c_2c_3 is larger (taking also its sign into account). In the next section we will discuss the situation in the presence of the forcing.

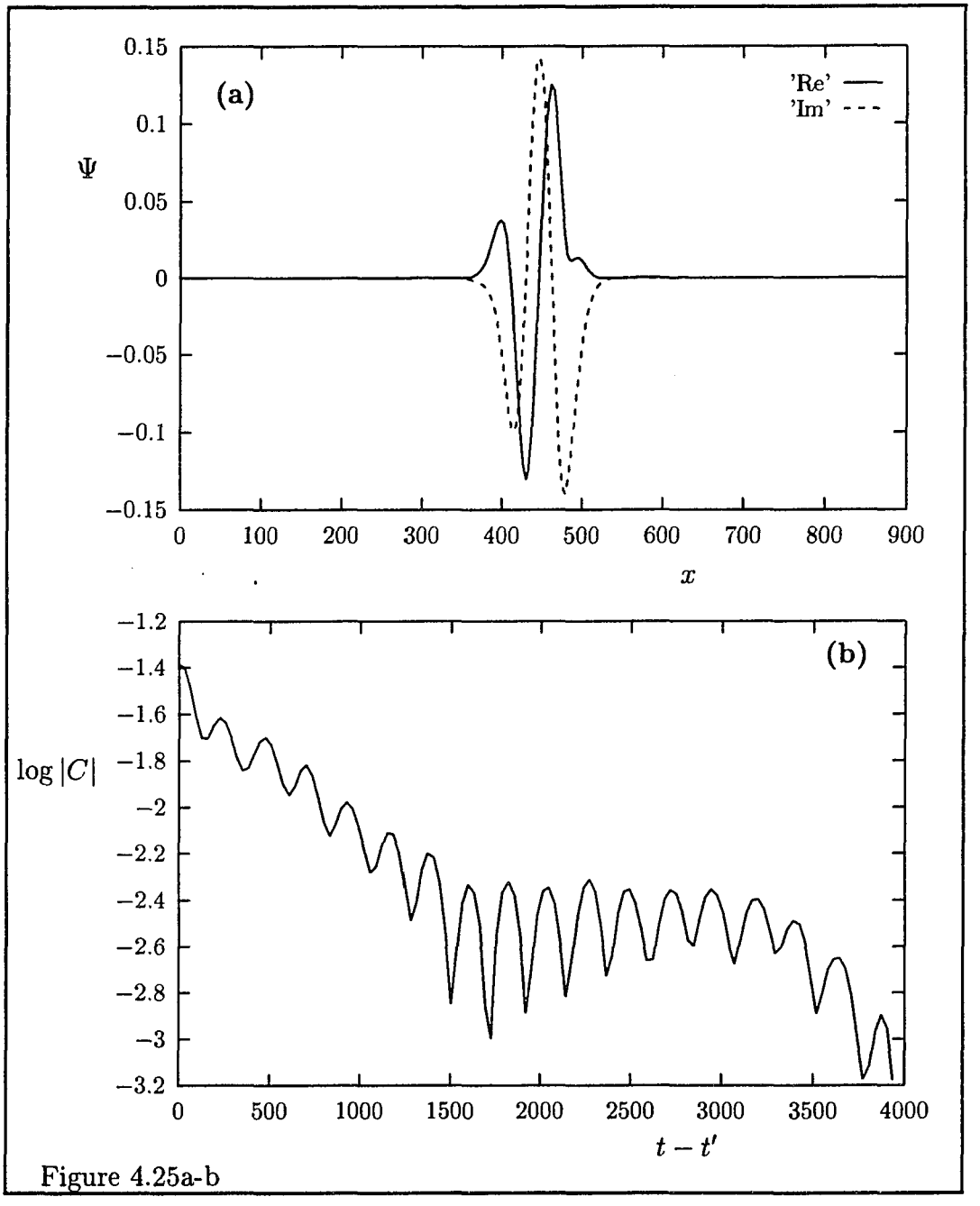

Figure 4.25a-b

Figure 4.25: Snapshot of $\Psi(x,t)$ (a) and plots of $C(0,t,t')$ (b), $D(0,x')$ (c) and the spatial envelope of $|\Psi(x,t)|$ (d), for $\Sigma_0 = 1.05$.

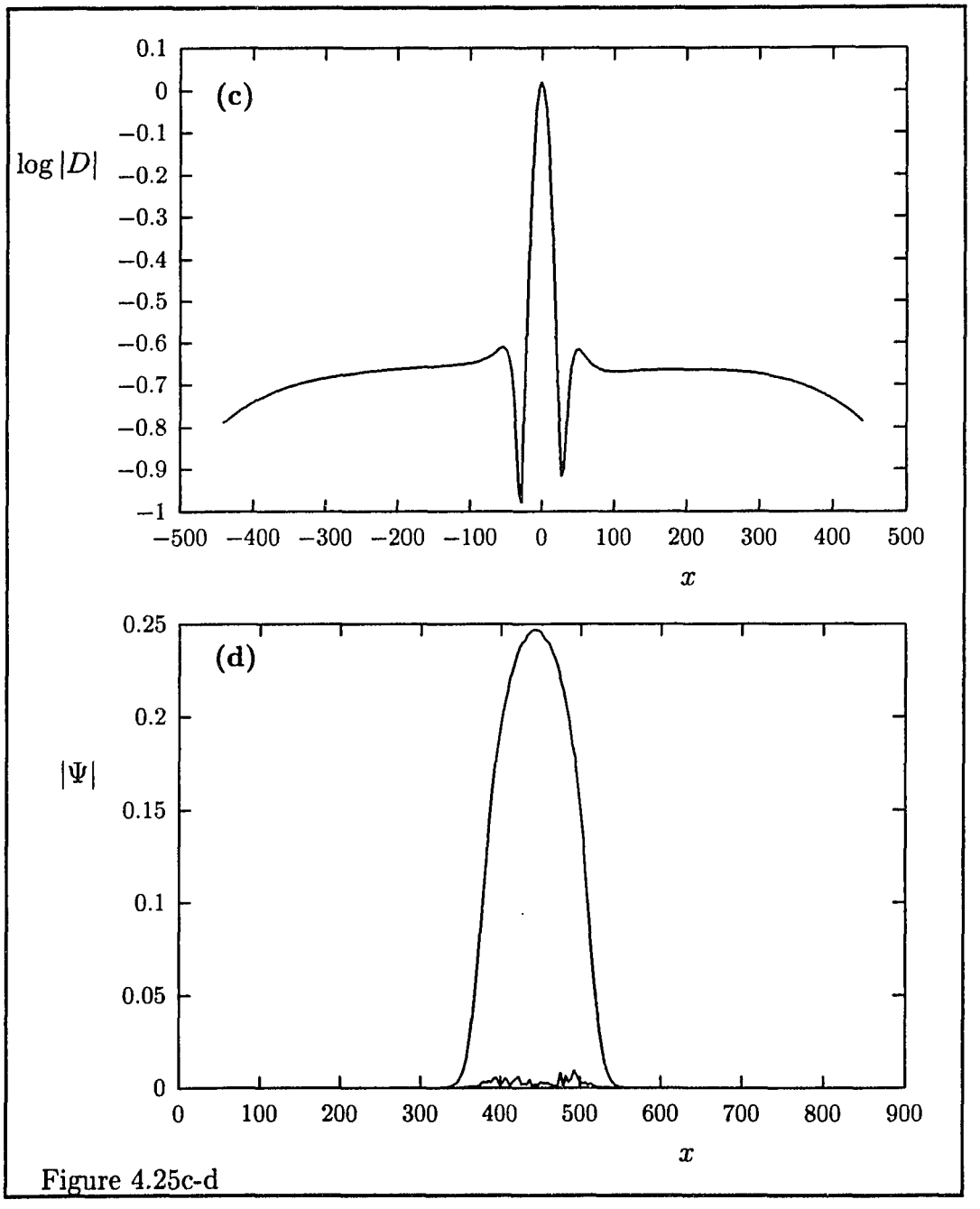

Figure 4.25c-d

Figure 4.26: (Next page) Snapshot of the chaotic pulse solution for $\Sigma_0 = 1.1$ (a) and the spatial envelope of $|\Psi(x,t)|$ (b) for this case. Panels (c) and (d) (next page) show respectively the temporal correlation function $C(0,t,t')$ and the spatial correlation function $D(0,x')$.

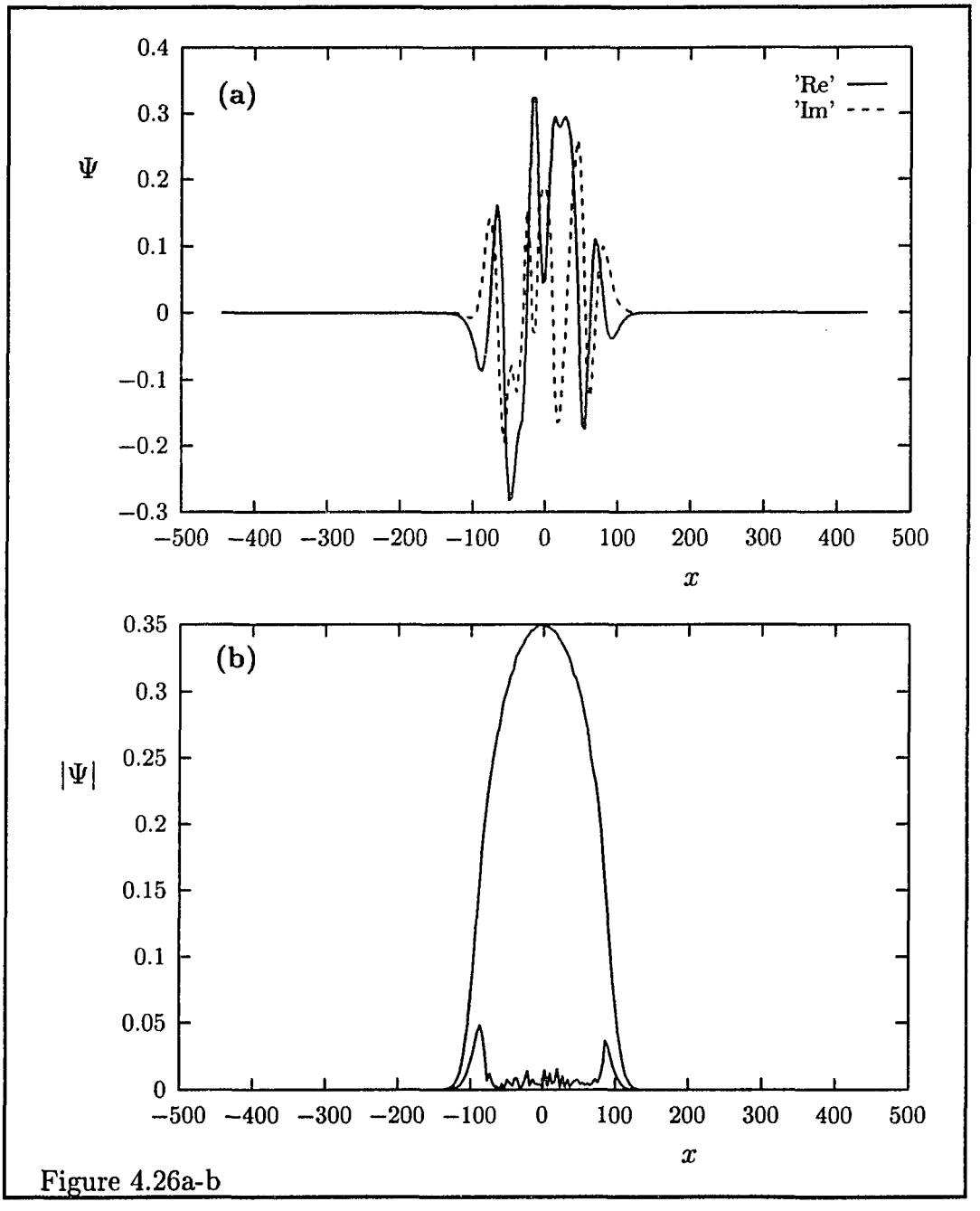

Figure 4.26a-b

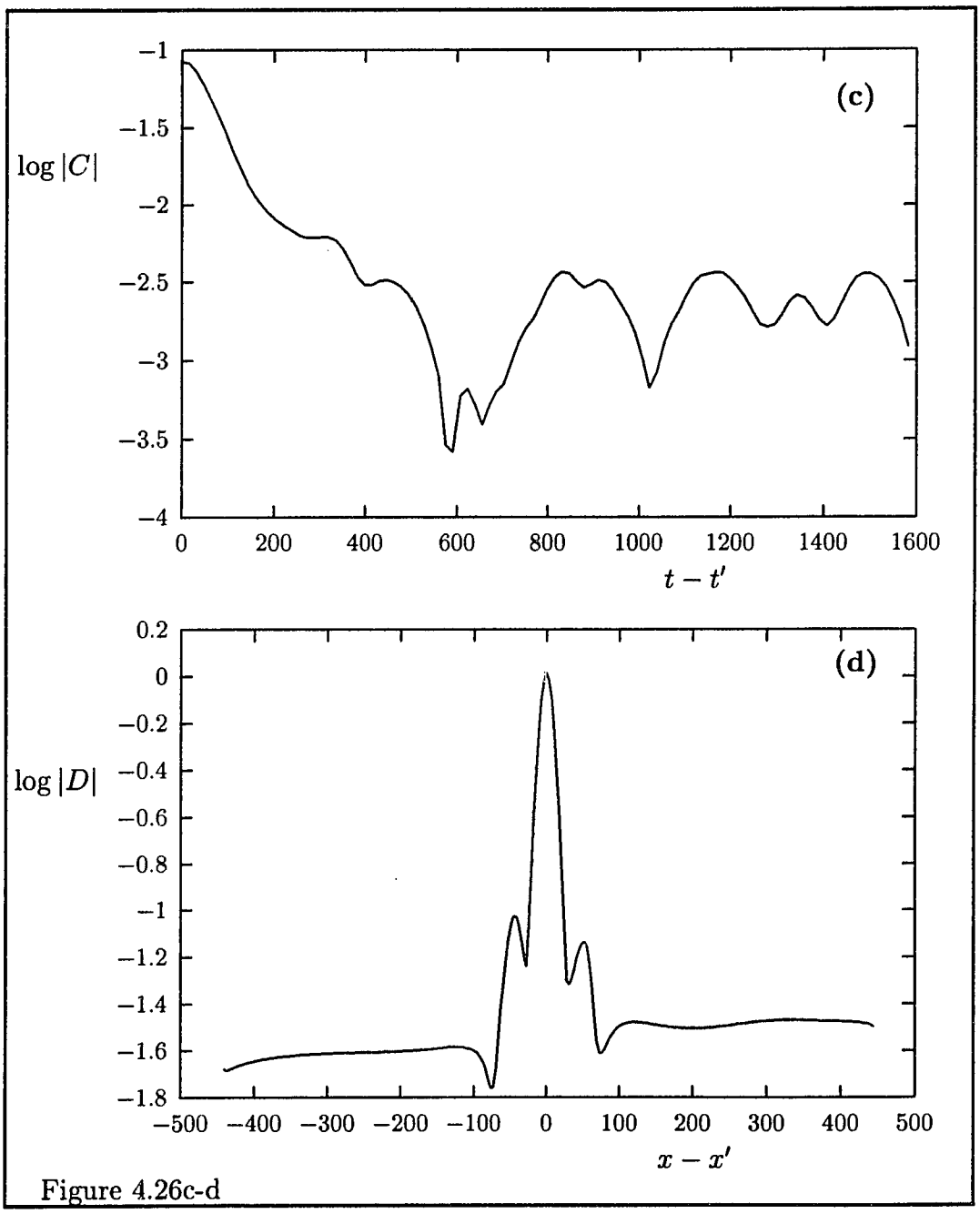

Figure 4.26c-d

Figure 4.27: (Next page) Snapshots of $Re\Psi$ (a), $Im\Psi$ (b), $|\Psi|$ (c) and the spatial envelope of $|\Psi|$ (d) for $\Sigma_0 = 2$. Note the typical spatial behaviour for spatio-temporal intermittency in panel (c). The correlation functions $C(0,t,t')$ and $D(0,x')$ are shown in panels (e) and (f).

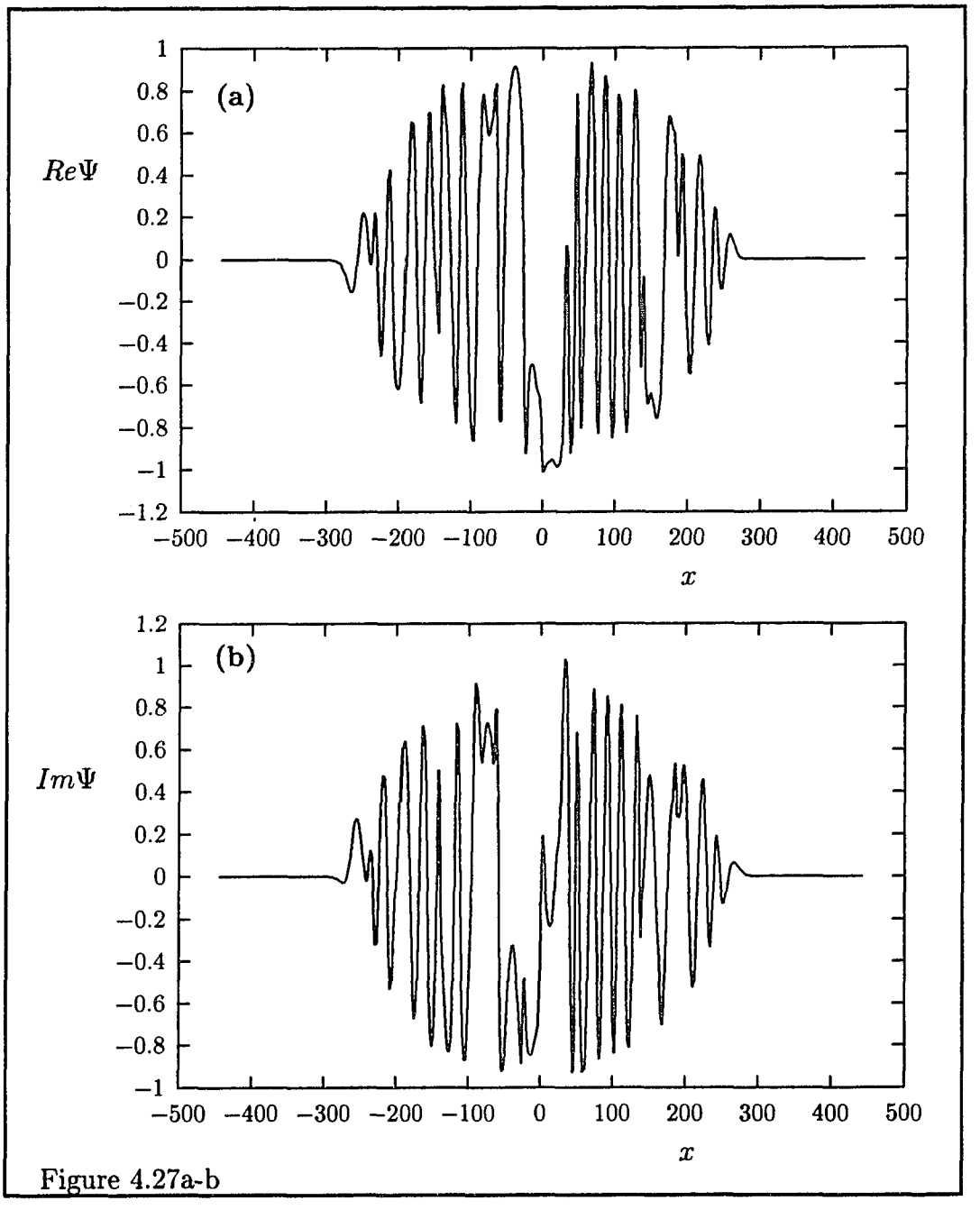

Figure 4.27a-b

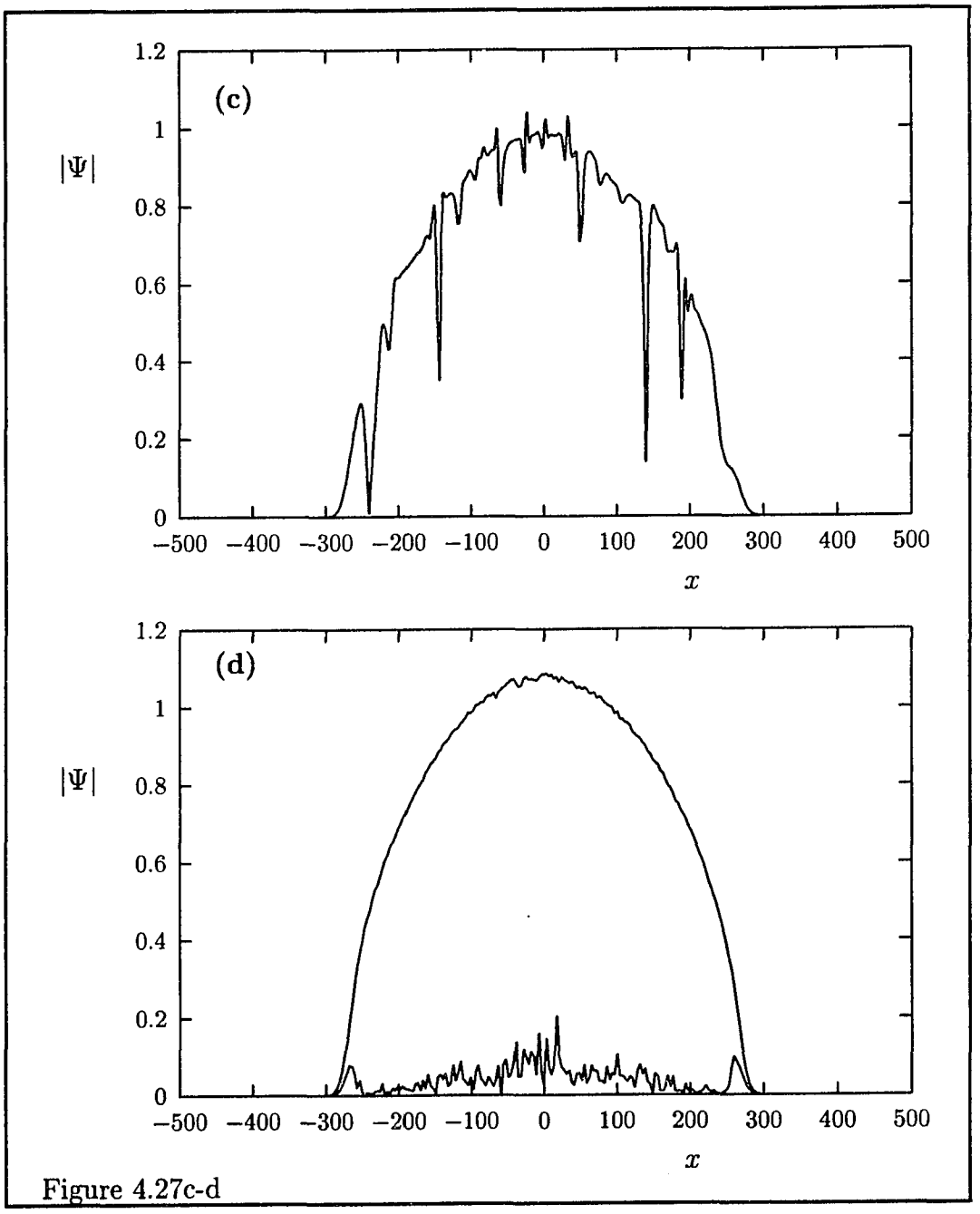

Figure 4.27c-d

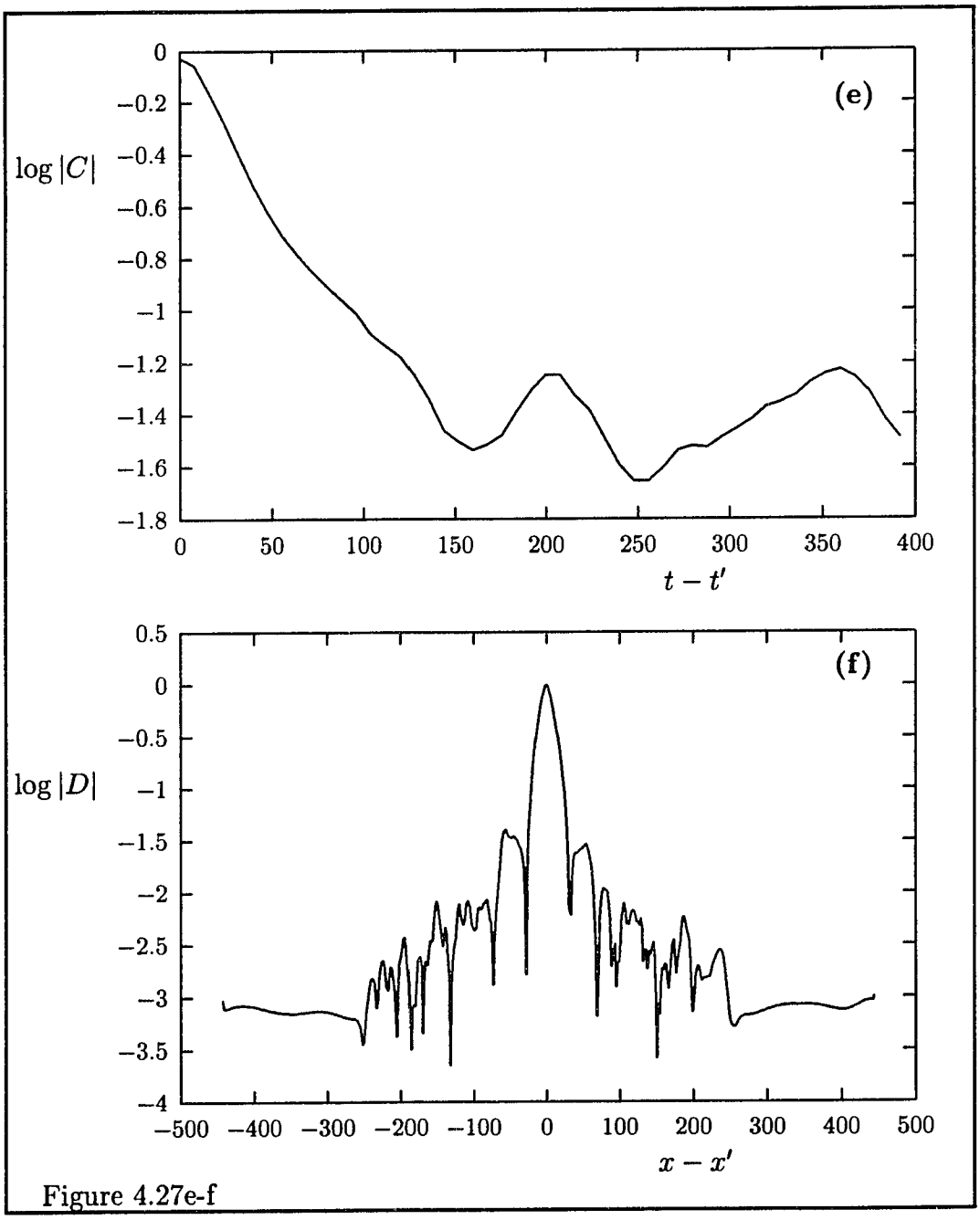

Figure 4.27e-f

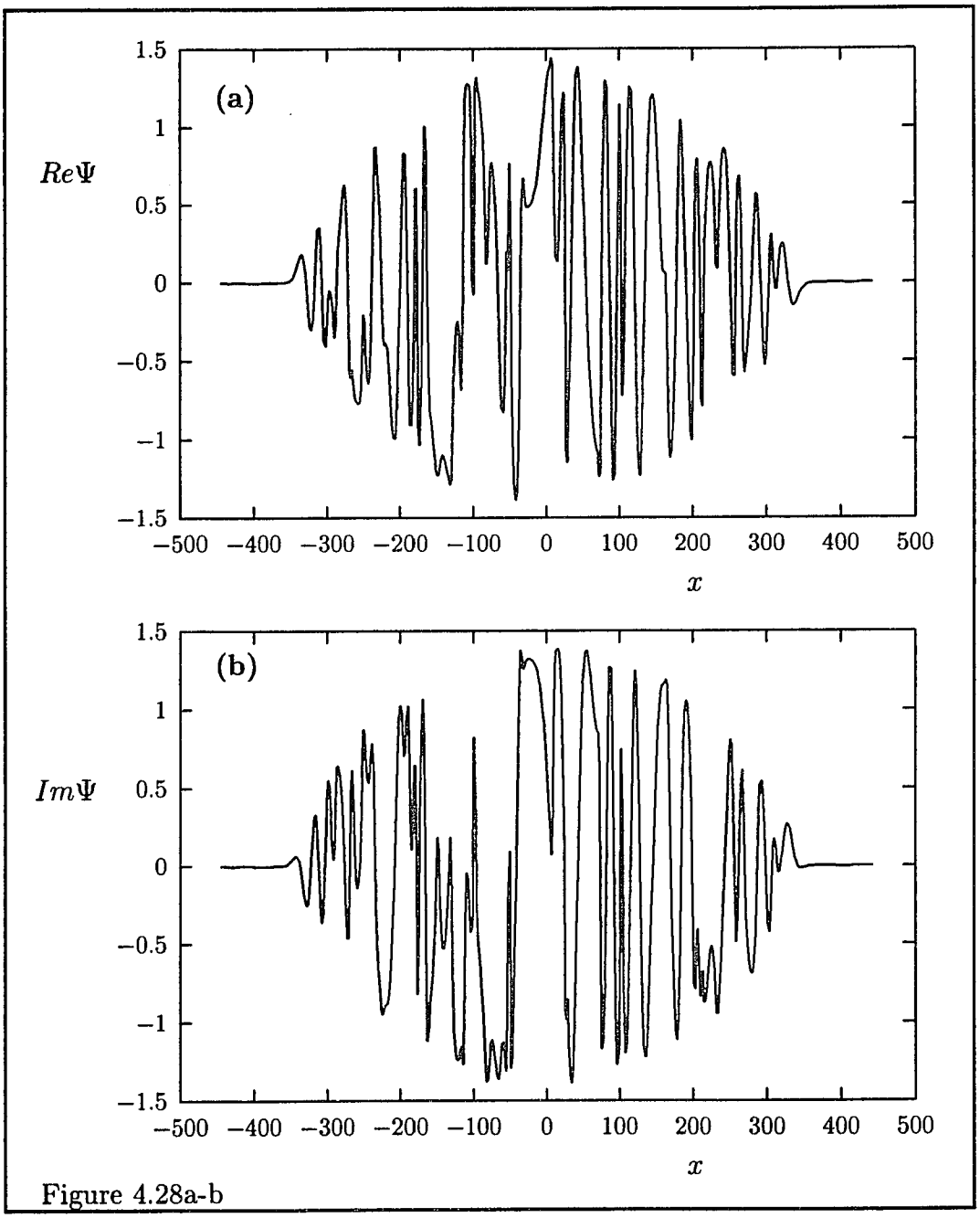

Figure 4.28a-b

Figure 4.28: Snapshots of $Re\Psi$ (a), $Im\Psi$ (b), $|\Psi|$ (c) and the spatial correlation function $D(0, x')$ (d), for $\Sigma_0 = 3$.

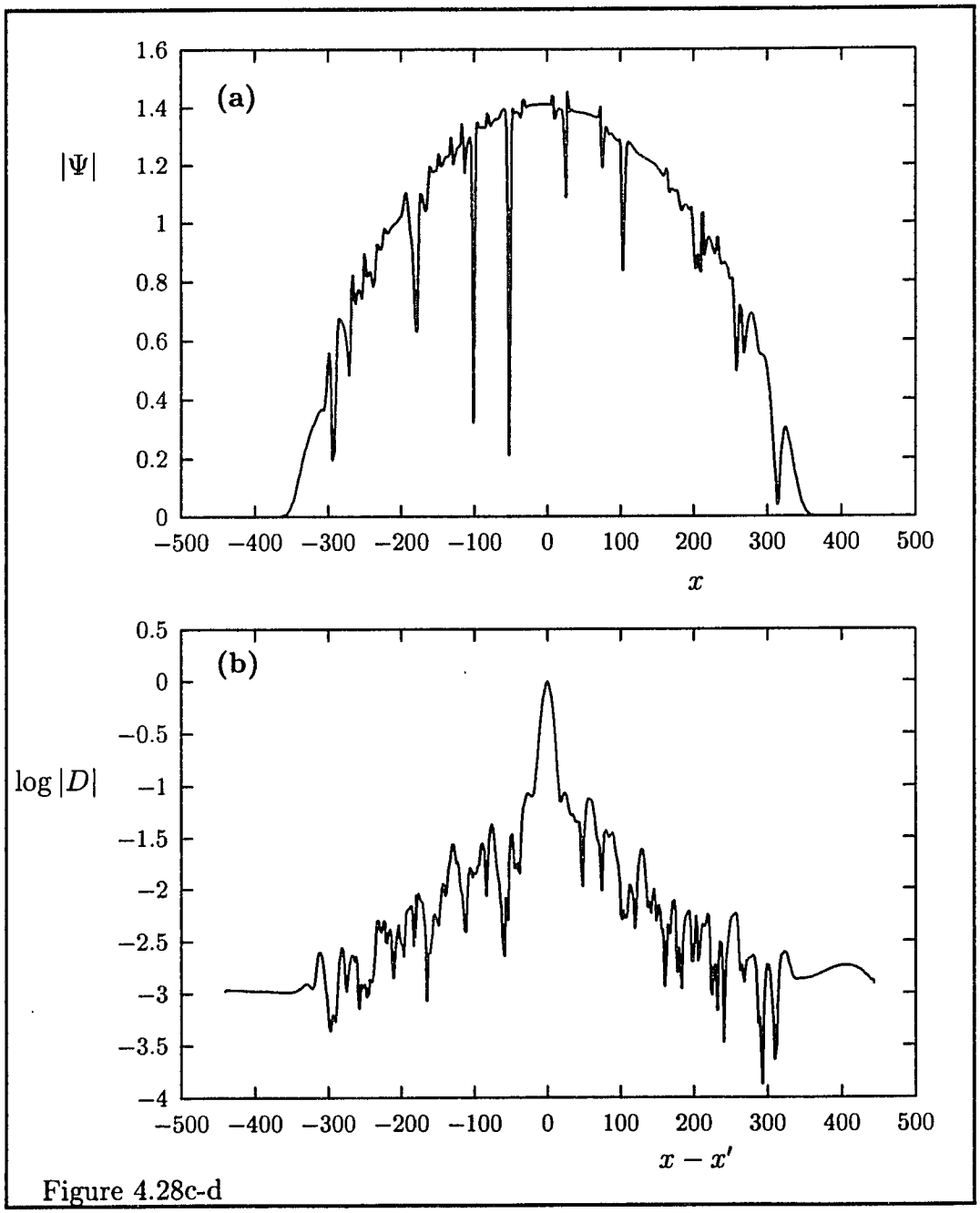

Figure 4.28c-d

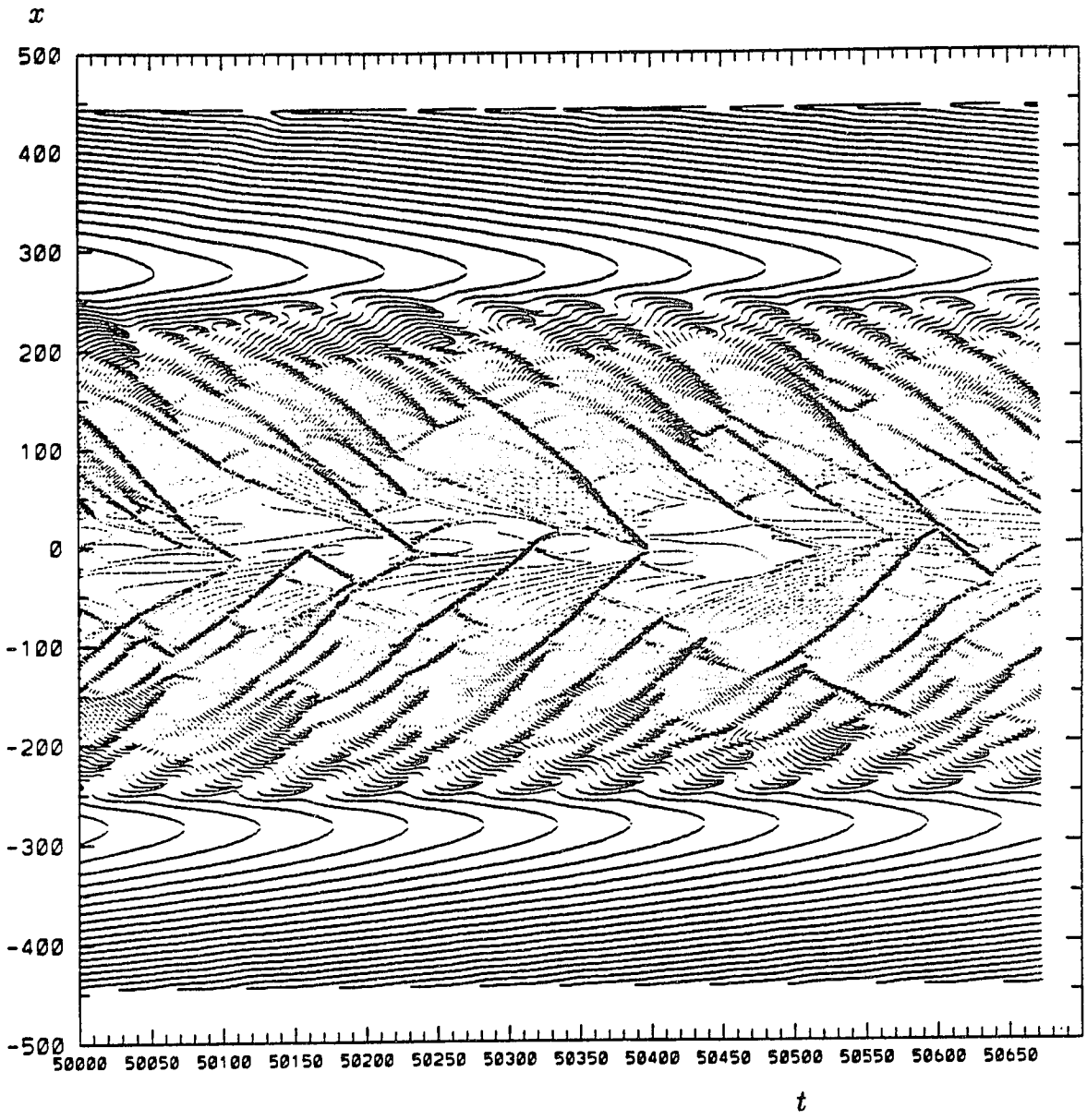

Figure 4.29

Figure 4.29: The lines $Re\Psi = 0$ and $Im\Psi = 0$ for the situation where the behaviour shows spatio-temporal intermittency, $\Sigma_0 = 2$.

4.3 Phase-locked pulses, forced solutions.

We will now discuss solutions of the CGLE with the space dependent growth rate given by (4.25) and (4.26) and non-zero harmonic external forcing. We will consider three types of spatial forcing shapes; a Gaussian forcing given by

$$F(x) = F_0 e^{-k^2|\Lambda|^{-1}x^2}, \tag{4.32}$$

a plane wave forcing given by

$$F(x) = F_0 e^{iq|\Lambda|^{-1/2}x}, \tag{4.33}$$

and finally a constant forcing

$$F(x) = F_0. \tag{4.34}$$

The variable x is again the dimensionless length, $x \in (-\pi, \pi)$. Further, because of the periodic boundary conditions it has to be arranged such that $q|\Lambda|^{-1/2}$ is an integer number. Otherwise we might create behaviour that would be recognized as a size effect, but is infact present because of the discontinuity of the forcing at the system boundary.

The first question we will address is : how much forcing does one minimally need, given c_2, c_3, Σ_0 and K, to create a phase-locked state with

frequency ω around the resonance frequency, for the different forcing types (4.32), (4.33) and (4.34) ? An answer to this question is given in tables (4.3) and (4.4) for the parameter choices $\omega = -4$, $c_2 = -1$, $c_3 = 1$, $\Sigma_0 = 4$, and $K = 0.3$, 0.03 and 0.003.

The phase-locked states $\Psi_L(x,t) = \phi_L(x)e^{i\omega t}$ follow from equation (4.23) with $\phi \to \phi_L$ and $\mu_1 \to -\delta_{k,k'} + \Sigma_{k-k'}$. Numerical details of the solution method are given in appendix C. The stability of the phase-locked states folows from $det(S) = 0$ and $\max(Re(p(k))) < 0$, where S is given by (4.20) with the obvious substitutions.

The tables (4.3) and (4.4) illustrate the following behaviour, which I found typical having looked at more parameter choices. For small systems (K sufficiently large, width of growth rate sufficiently small), the minimium required forcing remains of reasonable order and does not depend much on its precise width in case of a Gaussian forcing. For intermediate size and large systems the minimum required forcing in case of a Gaussian forcing takes on exorbitantly large values as the forcing width becomes of the order of a few times smaller than the growth rate width. As the forcing width increases the minimum forcing takes on reasonable values again and doesn't depend much on its width, compare the results obtained for $k \approx K$ and $k = 0$. Finally,

K	k	$F_{0,min}$
0.3	1.0	6.79
	0.5	3.57
	0.333	3.01
	0	2.39
0.03	0.1	$1.62\ 10^5$
	0.05	28.0
	0.0333	6.66
	0	2.88
0.003	0.01	$1.81\ 10^5$
	0.005	31
	0.00333	6.21
	0	2.83

Table 4.3: Minimum forcing strength required to create a phase-locked state for the parameter choices as shown in the table and $c_2 = -1$, $c_3 = 1$, $\Sigma_0 = 4$, $\omega = -4$. The constant forcing is represented by the $k = 0$ fields.

K	q	$F_{0,min}$
0.03	0.035	2.89
	0.173	3.0
	0.346	3.22
	0.693	3.95

Table 4.4: Minimum forcing strength required to create a phase-locked state in an intermediate size system with a plane wave forcing for the parameter choices as shown in the table and $c_2 = -1$, $c_3 = 1$, $\Sigma_0 = 4$, $\omega = -4$.

we observe that the divergence of the minimum required forcing does not occur for the plane wave forcing. The minimum forcing in this case does infact depends only slightly on the wavelength of the plane wave and is of the same order of magnitude as for a constant forcing, or Gaussian forcing with a width comparable to the width of the growth rate.

Do the above results lead us to conclude that the precise shape of the forcing has little influence on the minimally requiered forcing for a locked-in state, provided the forcing is not much more localized then the growth rate, this is of course not true for the shape of the locked-in state. One finds that the shape of the locked-in state more or less follows the shape of the forcing

in the regions where $\mu_1 < 0$ and is puls shaped in the localized region where $\mu_1 > 0$. A localized forcing gives a locked-in state which is pulse shaped and vanishes exponentially or faster as $x \to \pm\infty$. A constant forcing gives a pulse shaped solution superposed on a constant, $|\Psi| \to c$ as $x \to \pm\infty$, while a plane wave forcing results in a pulse shape where $\mu_1 > 0$ and a plane wave with the same wave number as the forcing for $x \to \pm\infty$.

We will conclude this chapter with a discussion of the phase diagram of the externally forced CGLE for the different forcing types mentioned previously. The phase diagram now involves quite a number of parameters, c_2, c_3, Σ_0, K, F_0, ω and k or q. One may hope that for some of them a discusion in terms of different classes of the phase diagram is a useful approach. We have seen in chapter 3 that this for instance was possible for the LE as far as the parameter c_3 was concerned. My impressions are from results obtained for various parameter choices, and also from results to be discussed in the next chapter, that besides the parameters F_0, ω and the parameter K, which is not a candidate for the above mentioned simplified approach since it determines the size of the system, the parameters c_2, c_3, Σ_0 and even k or q seem to be good candidates. Our discussion here will not involve the complete phase diagram.

We will confine our discussion to the behaviour in the F_0-ω plane of the phase diagram, for a Gaussian forcing and a plane wave forcing type. We will discuss two situations with a Gaussian forcing, one for a small system with $K = 0.3$ and and one for a intermediate size system with $K = 0.03$. The forcing width will be in both cases equal to the growth rate width; $k = K$ in both cases. This last choice might appear to be somewhat exceptional but this is however not true. One observation in this direction is that the shape of the lock-in region in the F_0-ω plane does not change much qualitatively when the width of the forcing is varied [42], provided that it is not a number of times less than the width of the growth rate. Furthermore, from some simulations performed with a uniform forcing, I find the behaviour outside the lock-in region simular as for a Gaussian forcing with $k = K$. This last observation will also be illustrated by the third situation we will discuss below, which is for an intermediate size system with $K = 0.03$ and a plane wave forcing with a wavelength which is about five time smaller than the growth rate width $q \approx 5K$.

For the results that will that will follow the remaining parameters are $c_2 = -1$, $c_3 = 1$ and $\Sigma_0 = 4$. The lock-in region again does not change much qualitatively when these parameters are varied. Unforced stationary

pulse solutions become in general available as one increases the product c_2c_3 (taking also its sign into account) and decreases Σ_0 [42]. As for the change in behaviour outside the lock-in region when the parameters c_2, c_3 and Σ_0 are changed; one certainly can come to a few guesses by looking at the results we will discuss and the ones obtained previously for the unforced system. They will however be little more than that, so we will refrain from doing so.

Having oriented ourselves somewhat concerning the parameter choices made, we will now discuss the actual results for the three situations mentioned.

Like for the situation with constant growth rate, phase locked pulses were observed for all parameter choices and suffuciently large F_0. The lock-in region in the F_0-ω plane was obtained by computing for a set of ω values, the minimum value of F_0 for which the phase-locked state exists and is stable. The ω resolution used is $0.1 \sim 0.5$, while the accuracy in the minimum F_0 is 0.01.

Figure 4.30: (Next page) The F_0-ω plane of the phase diagram for the CGLE for a small system with a Gaussian forcing with $k = K = 0.3$. Phase locking occurs in **L** and **L1**. In region **QP** a two frequency quasi-periodic state exist. Temporal chaos and three frequency quasi-periodic motion is observed in **C1** and **C2**. Note also the outlines of the bistable region for the phase-locked states.

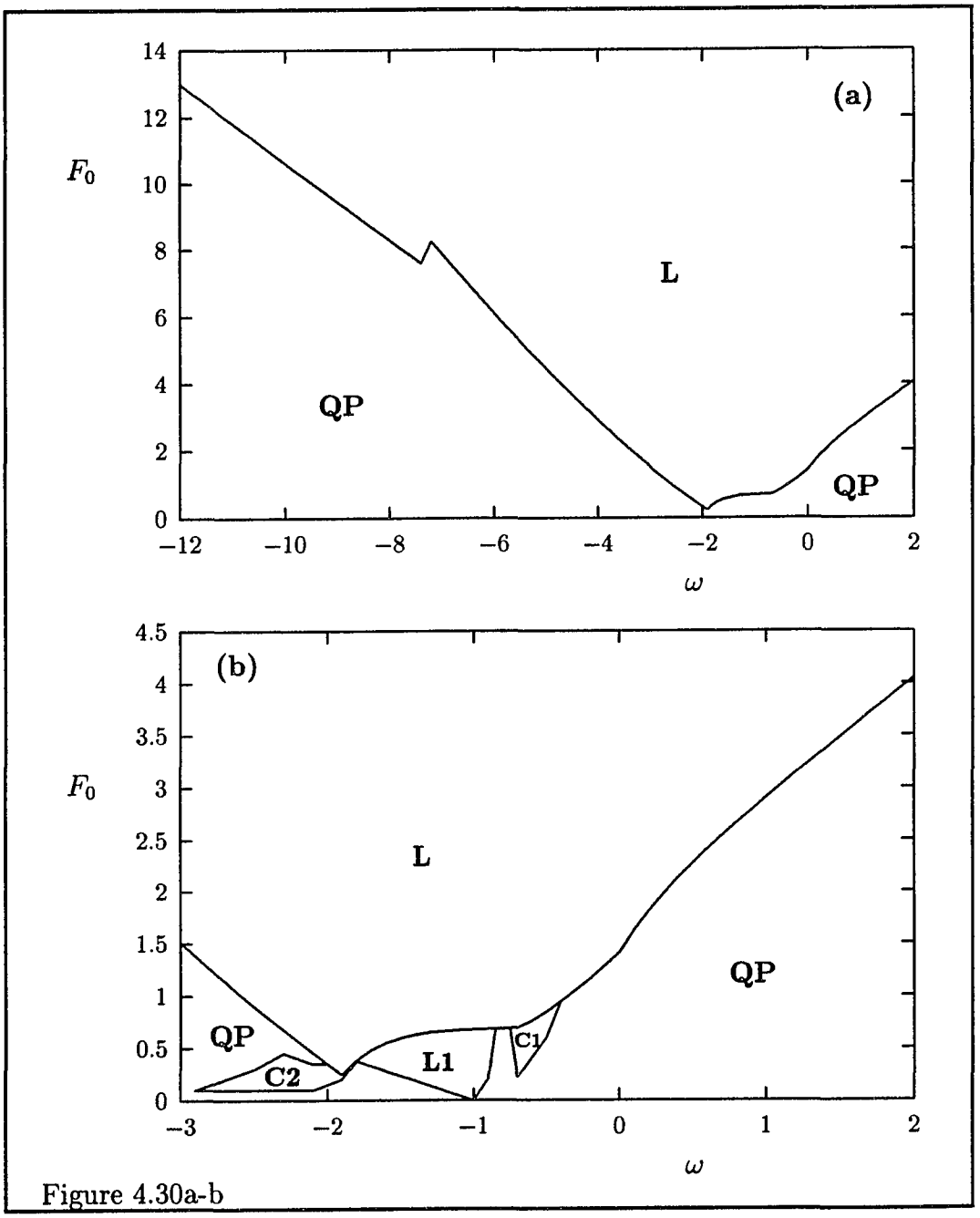

Figure 4.30a-b

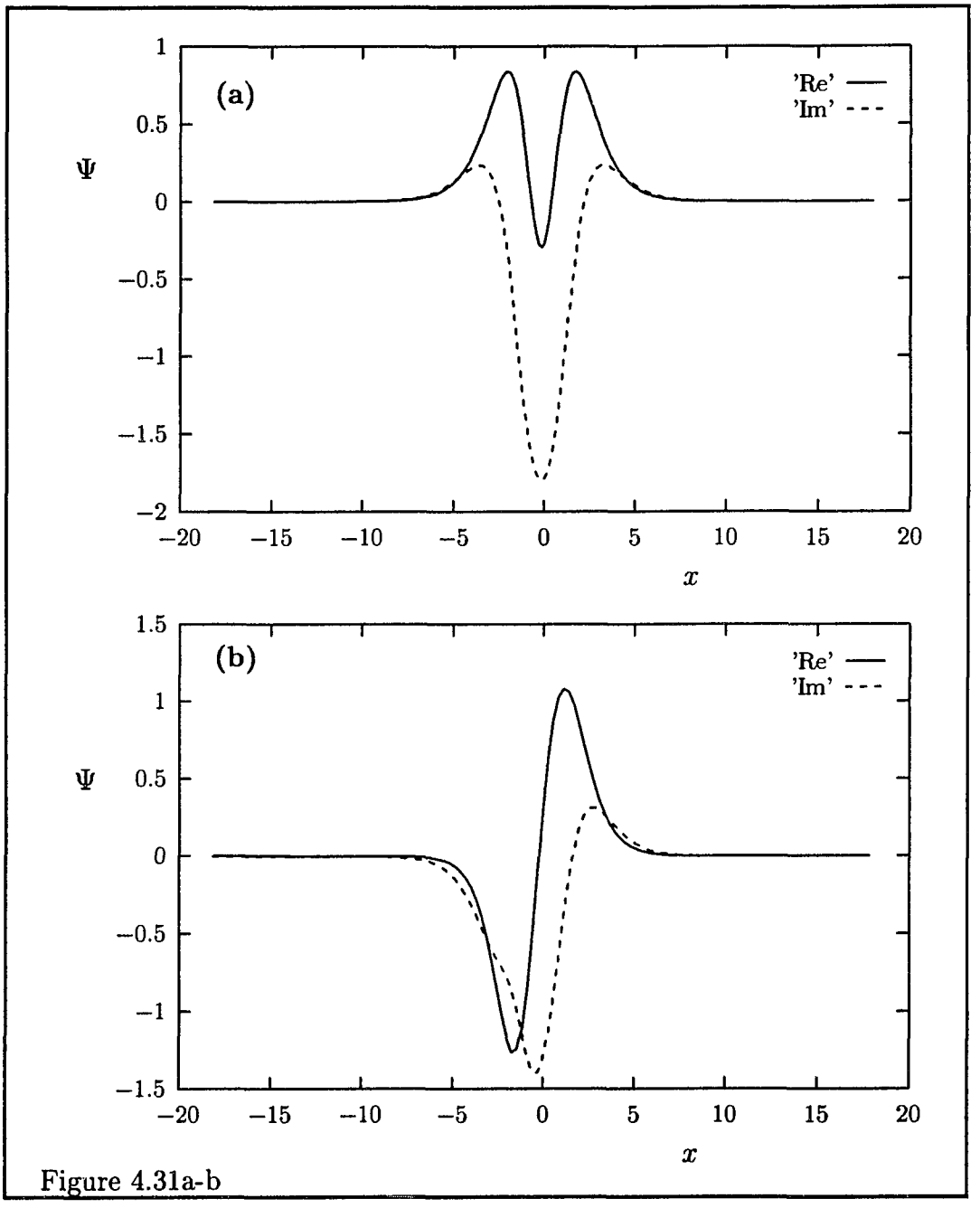

Figure 4.31a-b

Figure 4.31: Snapshots of phase-locked pulses in **L** (a) and **L1** (b). Note the lack of symmetry in panel (b).

Figure 4.32: (Next page) A solution in **C1** for $F_0 = 0.65$ and $\omega = -0.7$. Shown are (a) the power spectrum of $Re(e^{-i\omega t}\Psi(0,t))$, (b) the temporal correlation function $C(0,t,t')$, (c) The spatial correlation function $D(0,x')$, and (d) a snapshot of Ψ.

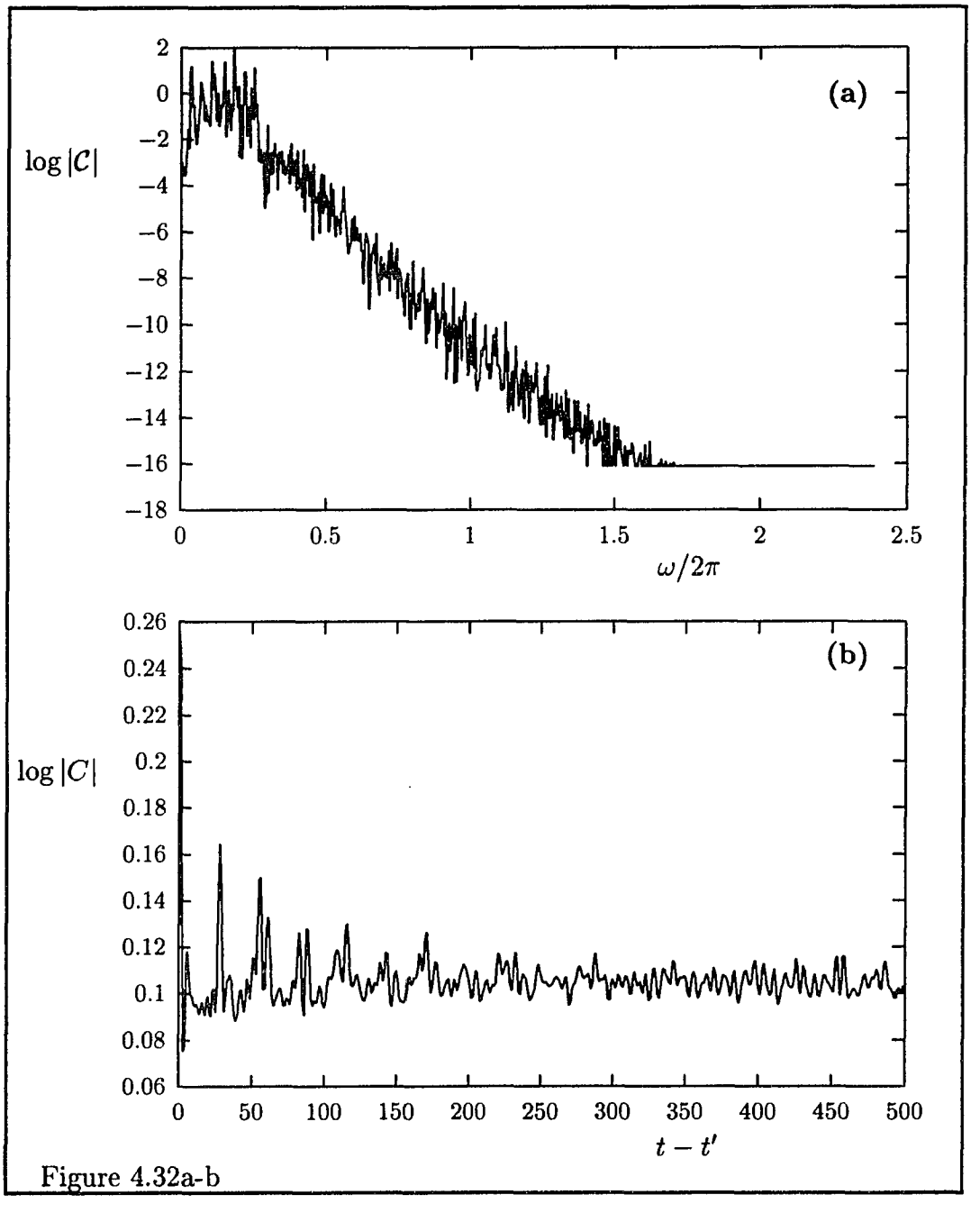

Figure 4.32a-b

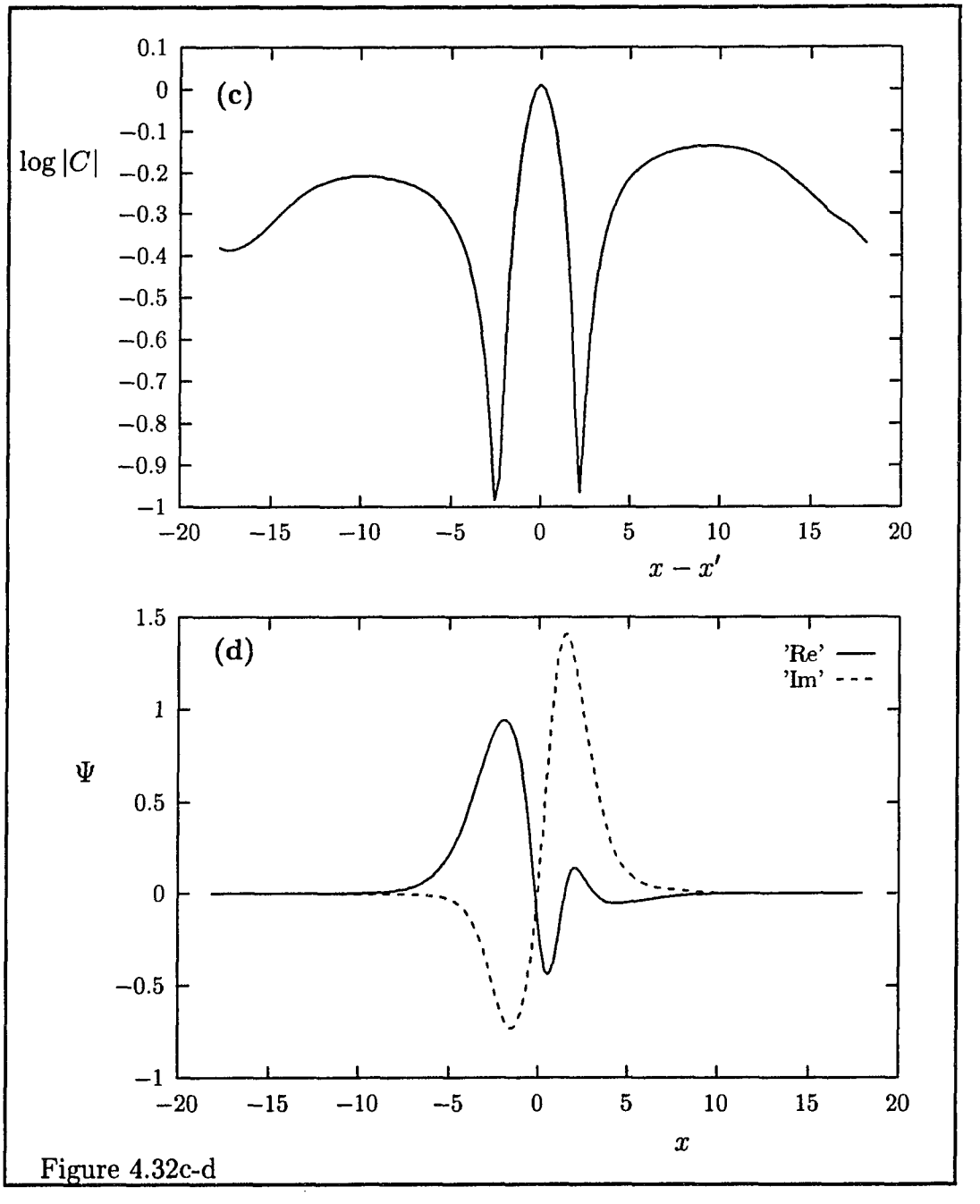

Figure 4.32c-d

Figure 4.33: (Next page) A solution in **C2** for $F_0 = 0.15$ and $\omega = -2.1$. Shown are (a) the power spectrum of $Re(e^{-i\omega t}\Psi(0,t))$, (b) the temporal correlation function $C(0,t,t')$, (c) The spatial correlation function $D(0,x')$, and (d) a snapshot of Ψ.

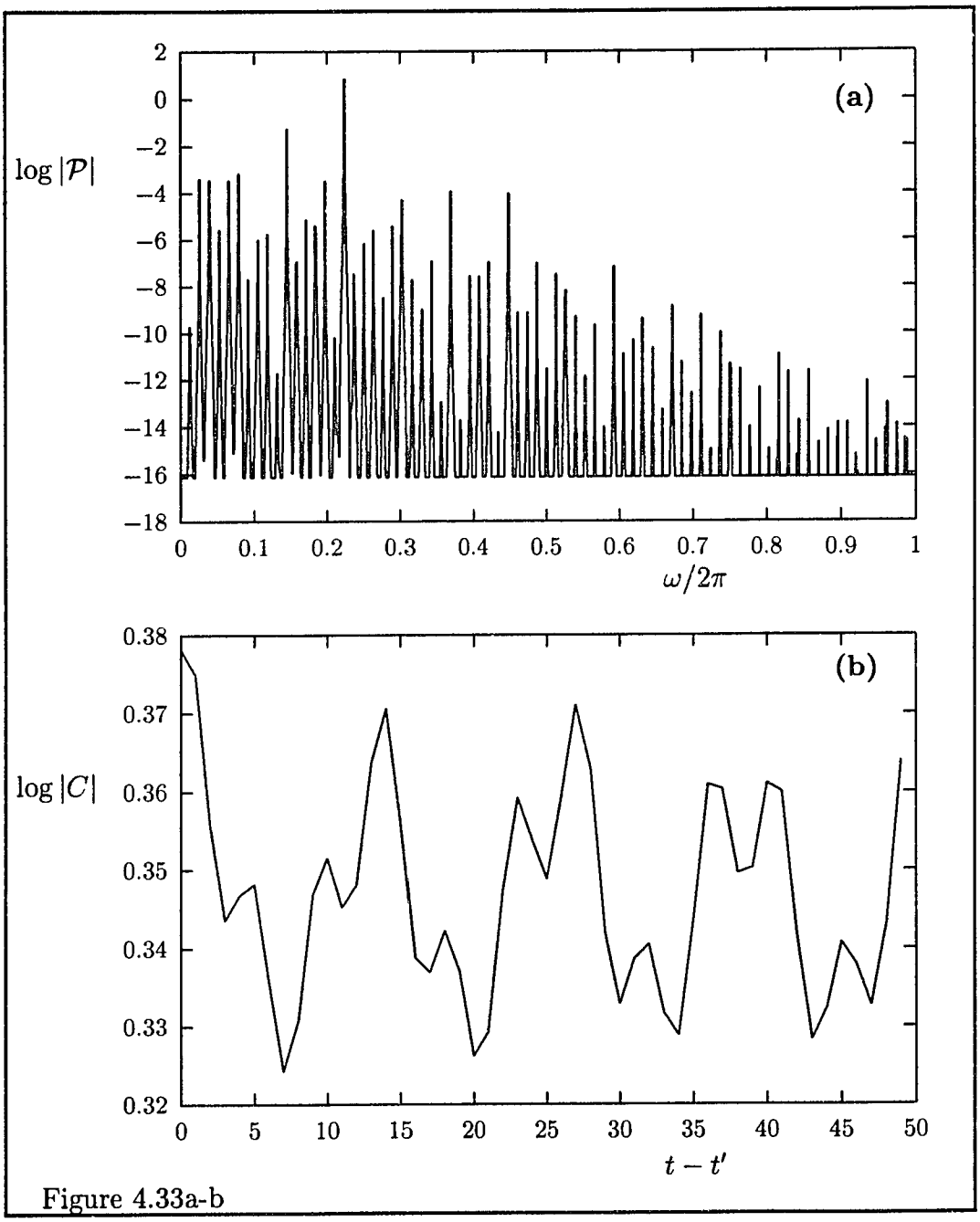

Figure 4.33a-b

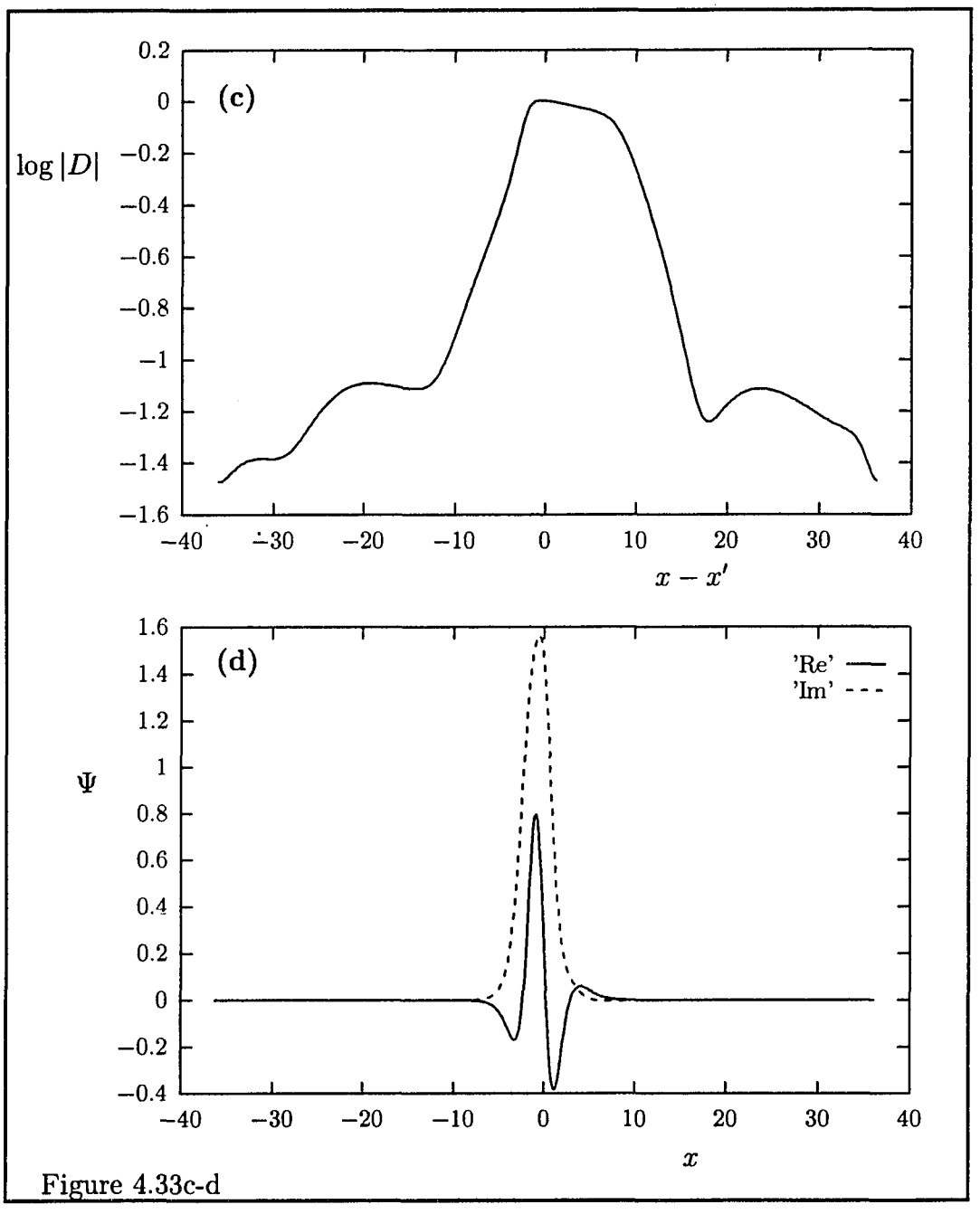

Figure 4.33c-d

Figure 4.34: (Next page) The lines $Re\Psi(x,t) = 0$ and $\Im\Psi(x,t) = 0$ for a small system with a Gaussian forcing. The pictures are for a solution in region **QP** (two frequency quasi-periodic solution) (a) and region **C2** (three frequency quasi-periodic solution) (b).

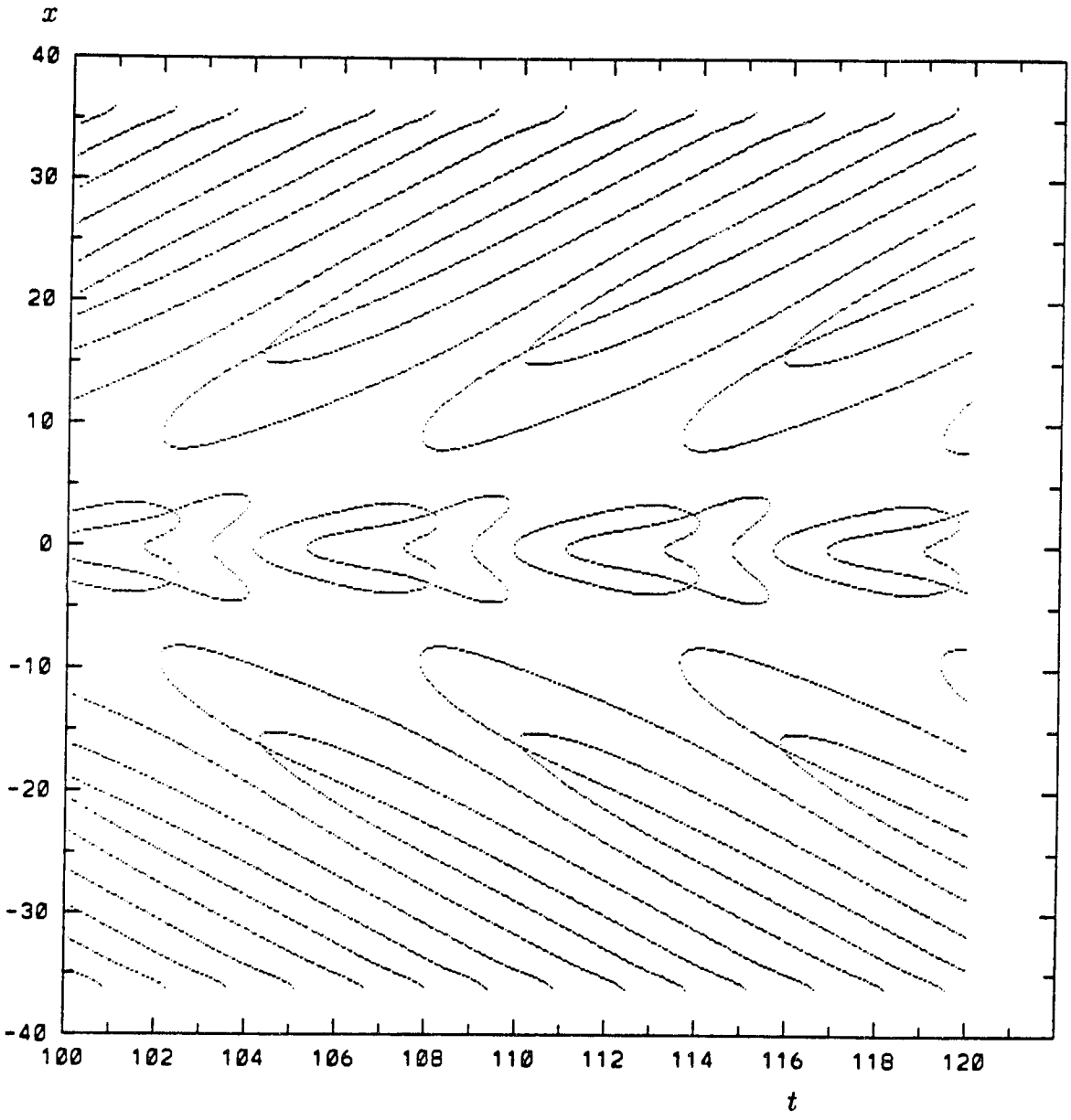
x
40
30
20
10
0
-10
-20
-30
-40
100
102
104
106
108
110
112
114
116
118
120
t

Figure 4.34a

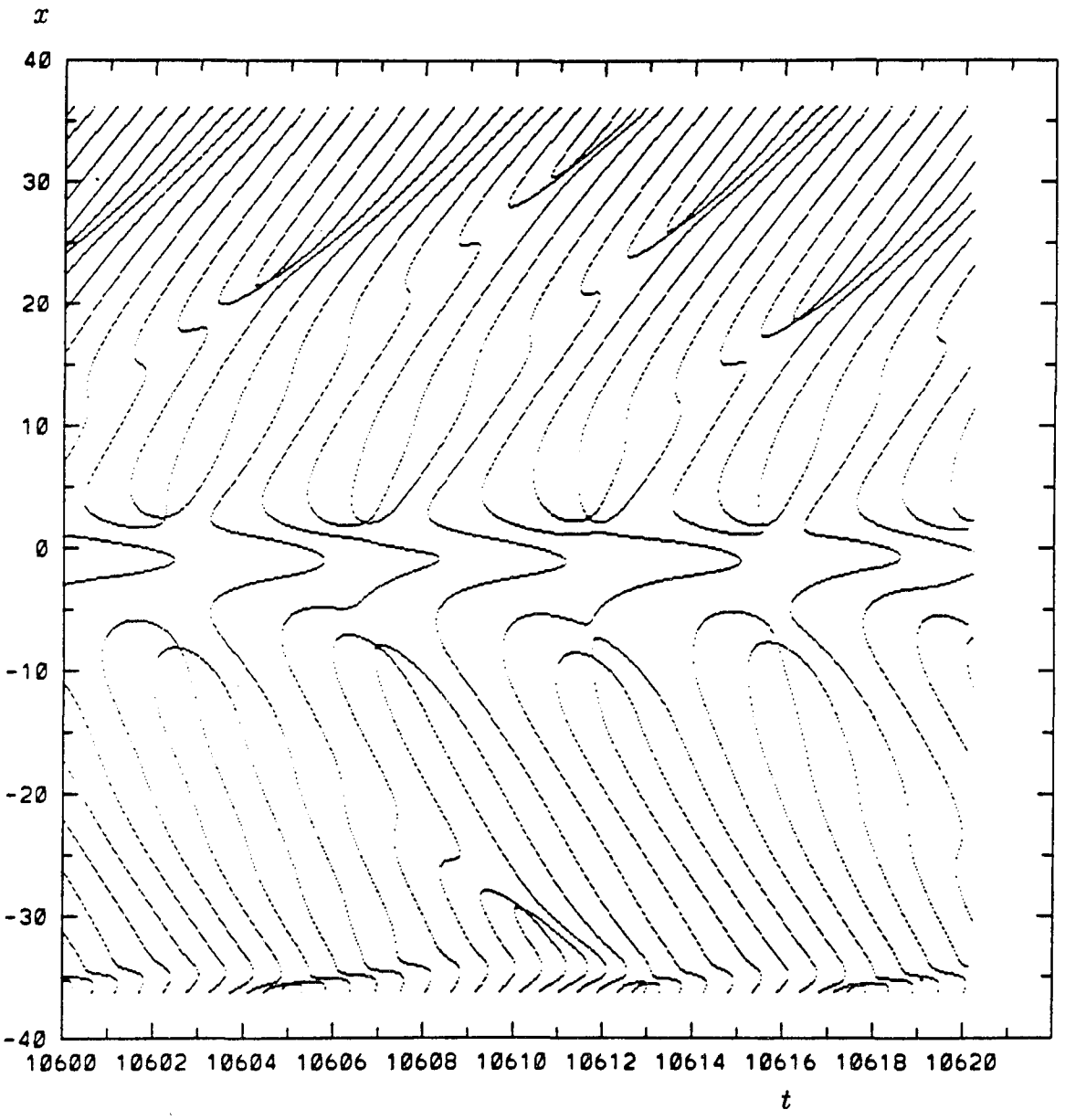
x
40
30
20
10
0
-10
-20
-30
-40
10600 10602 10604 10606 10608 10610 10612 10614 10616 10618 10620
t

Figure 4.34b

4.0.1 Small systems with a Gaussian forcing.

As a representative small system we take again a system with $K = 0.3$. In figure 4.30 the F_0-ω plane of the phase diagram is shown for a Gaussian forcing with $k = K$, the other parameter values are as mentioned. In agreement with results obtained previously [42] the shape of the lock-in region (region **L**) shows a remarkable simmularity with the lock-in region for the harmonically forced LE (chapter 3). We will also observe it for the plane wave forcing. From this we may conclude that the nonlocal effects in the CGLE, introduced by the dispersion term, are of minor influence as far as the lock-in behaviour is concerned. As we shall see, quite the opposite is true for the behaviour outside the lock-in region. The similarity with the LE is also of course not always as presise as in the present case, where even the bistable region is recovered. Some plots of lock-in sates are shown in figure 4.31. Note that the lock-in states in region **L** are spatially symmetric; $\Psi_L(x,t) = \Psi_L(-x,t)$. Going from region **L** to region **L1**, the lock-in state bifurcates via a parity breaking bifurcation to a new lock-in state which is not symmetric. We observed a similar phenomenon in the unforced equation.

Outside **L** and **L1** the dominant behaviour one observes is quasi-periodicity

in time with two incommensurate frequenties, region **QP**. If we write the solutions of the forced equation in the form

$$\Psi(x,t) = e^{i\omega t}\phi(x,t), \tag{4.35}$$

then $\phi(x,t)$ is periodic in t for solutions in region **QP**. There are however small regions here and there within the region **QP**, in which the behaviour becomes more complicated. One observes three frequency quasi-periodic behaviour in time and also temporal chaos. Somewhat larger sized regions of this kind are **C1** and **C2** in figure 4.30. There are however certainly more regions (not shown in the figure) in **QP** in which the behaviour differs from the dominant two frequency quasi-periodic behaviour. The solutions in region **C1** show temporal chaos, see figure 4.32. In region **C2** three frequency quasi-periodic behaviour is possible as well as temporal chaos, see figure 4.33.

Defects occur in all states observed outside **L** and **L1**. For the states in **QP** the defects occur at fixed positions periodically in time as is obvious from (4.35). Size effects are present, they do however not contribute to defect creation and no defects occur at or close to the boundaries for sufficiently large system length. Some x-t plots showing the lines $Re(\Psi(x,t)) = 0$ and $Im(\Psi(x,t)) = 0$ are shown in figure 4.34.

The two frequency quasi-periodic behaviour in the region **QP** is another similarity with the LE. Furthermore, by global inspection one observes just two different types of bifurcations between the region **L** and **QP**, which show characteristic features similar to the Hopf and saddlenode bifurcations observed in the LE. More precisely, for one type of bifurcation one observes, going from **QP** to **L**, a vanishing of the oscillatory part of the periodic function $\phi(x,t)$ in (4.35), which is typical for a Hopf bifurcation. For the other bifurcation one observes a divergence of the period of $\phi(x,t)$, which is typical for a saddlenode bifurcation.

In the next situation we will discuss is for an intermediate size system when the forcing type is again Gaussian with the same width as the growth rate. The other parameters are unchanged.

4.0.2 Intermediate size systems with Gaussian forcing.

As a representative intermediate size sytem we take again a system with $K = 0.03$. The forcing width of the Gaussian forcing is again equal to the growth rate width, $k = K$. The F_0-ω plane of the phase diagram is shown in figure 4.35. The lock-in region is again indicated with **L** and is of similar

shape as observed for a small system, with this difference that the bistable region is not present. Some plots of lock-in states are shown in figure 4.36. Note that they are spatially symmetric. There are no defects present in the lock-in states.

Solutions outside the lock-in region typically allow for a number of spatial regions to be distinguished in which the behaviour shows qualitatively different features. We have encountered this also in the unforced system for $K = 0.03$ and $K = 0.003$. However, in the forced system the phenomenon is richer and there is usually a greater variety in the behaviour.

One observes for instance solutions that show quasi-periodic behaviour in time in certain regions of space while they are locked-in in others. An other example are solutions that show quasi-periodic behaviour in certain spatial regions, temporal chaos in others and lock-in behaviour in yet again other spatial regions. There are some properties which hold for all solutions outside the lock-in region. First, the locations of the various regions in space are always symmetric with repect to the origin. Second, all solutions outside the lock-in region always have regions at the edges of the system in which the motion is locked-in. They are similar to the shoulders observed in $|\Psi|^2$ for the unforced system. There is an important difference however; in the

outer regions in the unforced system, the behaviour is still complex and certainly not stationary, whereas in the forced system the behaviour in the outer regions is truly locked-in.

Below the dashed line in figure 4.35, in the region labeled **C**, the behaviour shows at least temporal chaos in one or more spatial regions, which may become spatio-temporal chaos as the forcing strength F_0 decreases. Recall that the unforced state for $\Sigma_0 = 4$ has a central region in space in which spatio-temporal chaos occurs. Solutions in the region in between the dashed line and the solid line in figure 4.35, the region labeled **QP**, may have different spatial regions in which the behaviour is locked-in, periodic or quasi-periodic in time, but not chaotic.

Unlike in the small system, where if one leaves the lock-in region the solutions are not spatially symmetric and show defects, the situation here is not so straight forward. The parity breaking does not necessarily occur immediately as one leaves **L**, in fact in most cases it does not. However, for all situations covered by figure 4.35 it does occur somewhere in region **QP**, that is, in between the solid and the dashed line. Similar statements are true for the first occurrence of defects, as one leaves region **L**. The solutions usually do not immediately have defects. Particularly for forcing frequenties

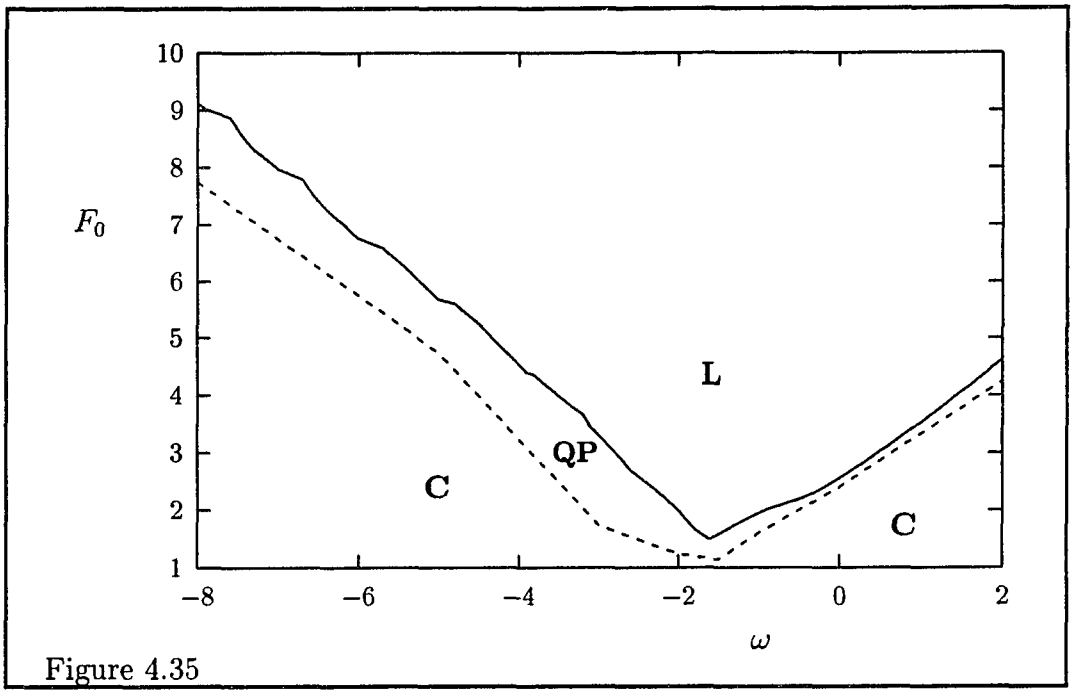

Figure 4.35

Figure 4.35: The F_0-ω plane of the phase diagram for the CGLE for an intermediate size system, with Gaussian forcing with $k = K = 0.03$. Phase locking occurs in **L**. In region **QP** quasi-periodic motion occurs at least in one spatial region but chaotic behaviour is not present. Chaotic behaviour occurs in region **C**.

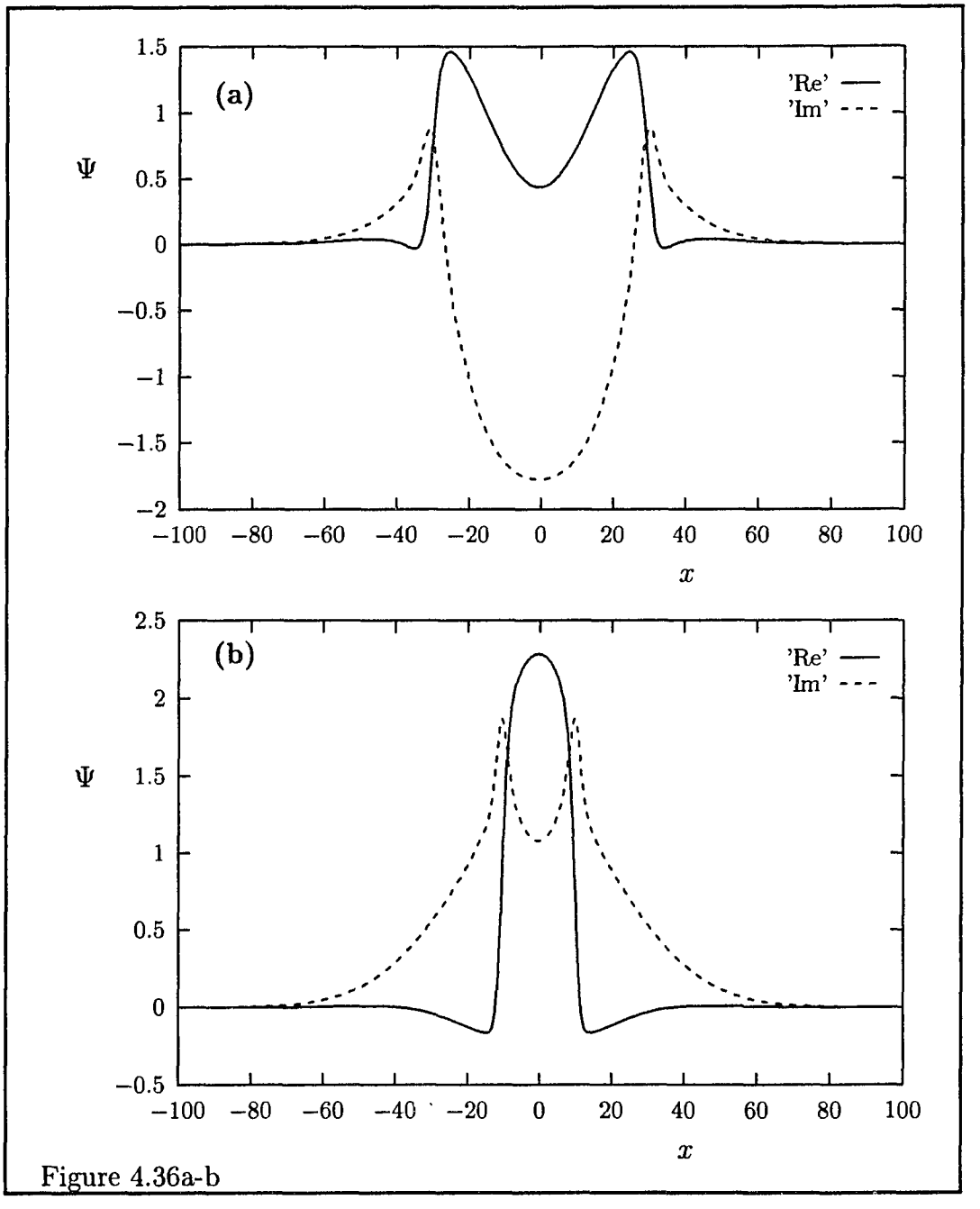

Figure 4.36a-b

Figure 4.36: Phase-locked states for $F_0 = 2.5$, $\omega = -2$ (a) and $F_0 = 9.5$, $\omega = -8$ (b). Note that the states are symmetric.

Figure 4.37: (Next page) The spatial envelop of some solutions in region **QP** close to resonance for $\omega = -2$, (a) $F_0 = 1.9$, (b) $F_0 = 1.5$. Defects occur in the last case but not for $F_0 = 1.9$. In (c) (next page) the temporal behaviour of $\phi(-30, t)$ is shown. A snapshot of $\phi(x, t)$ for $F_0 = 1.5$, $\omega = -2$ is shown in (d), note the symmetry.

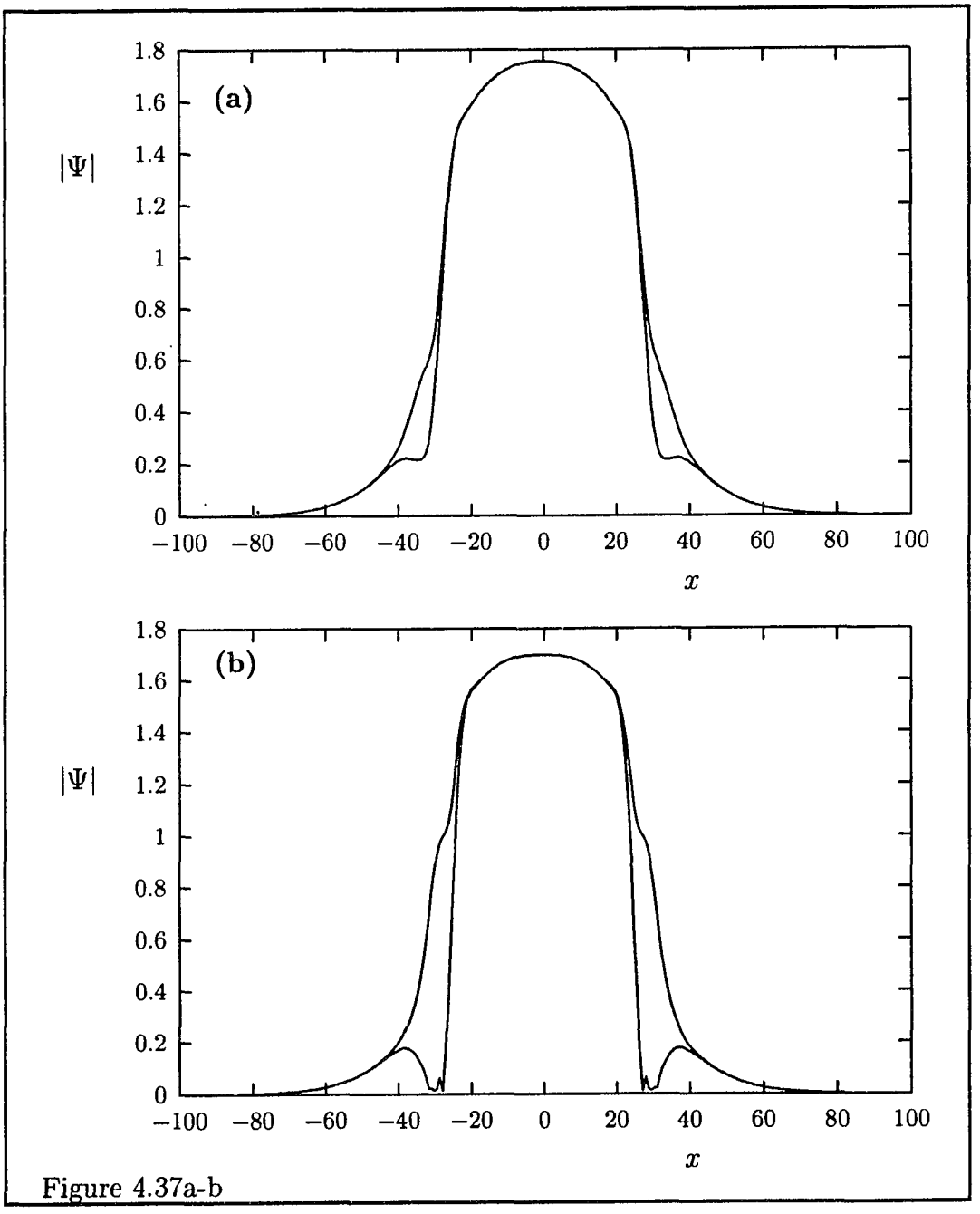

Figure 4.37a-b

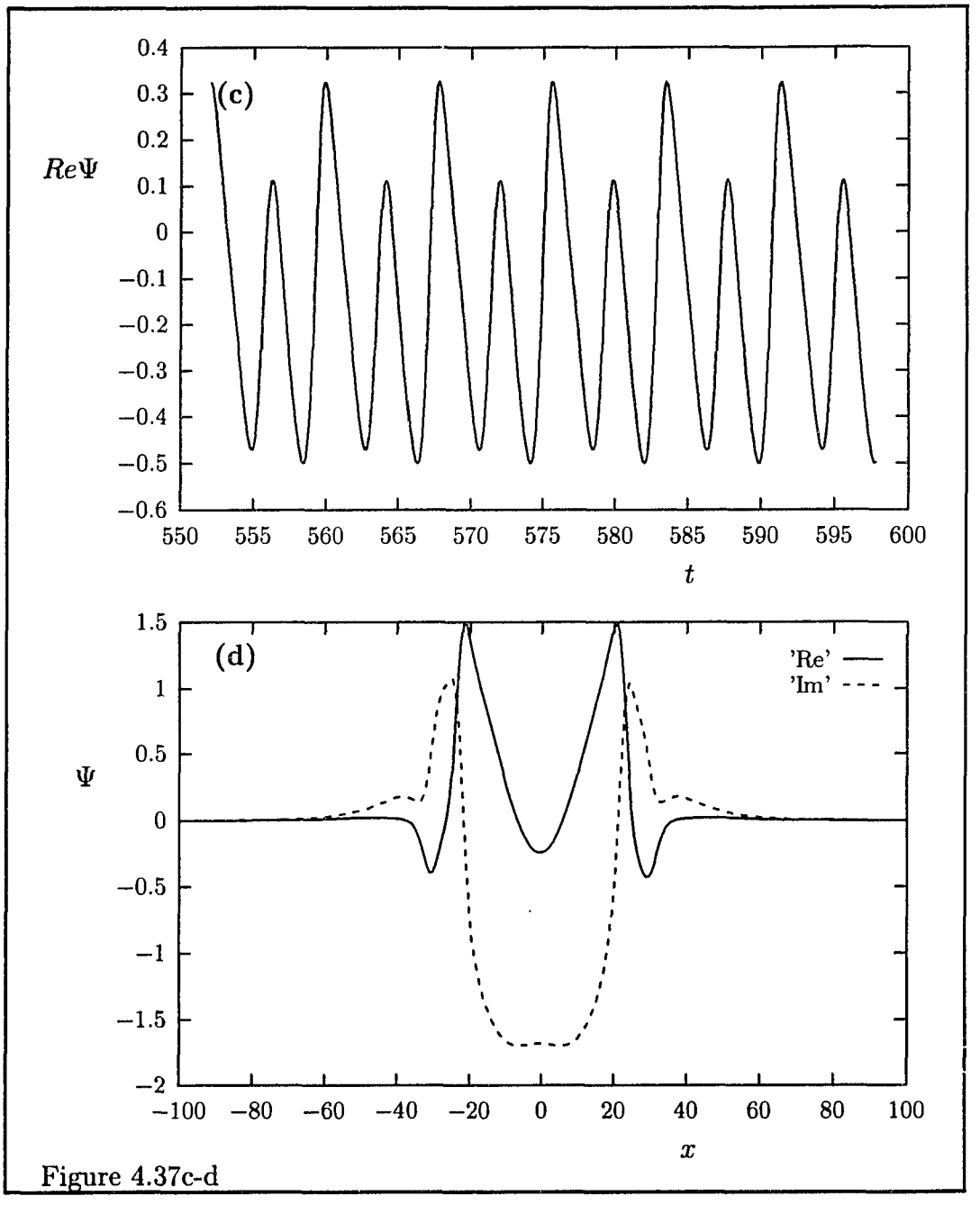

Figure 4.37c-d

Figure 4.38: (Next page) Snapshot of $\Psi(x,t)$ (a) and the spatial envelop of $|\Psi(x,t)|$ (b) for $F_0 = 1$, $\omega = -2$. Next pages: Time behaviour of this solution at $x = 0$ (c), power spectrum of $Re(e^{-i\omega t}\Psi(-38,t))$ (d), the temporal correlation function $C(-38,t,t')$ (e), the spatial correlation function $D(0,x')$ (f) and the defect distribution function $d(x)$ (g). Note that size effects do not lead to defect creation.

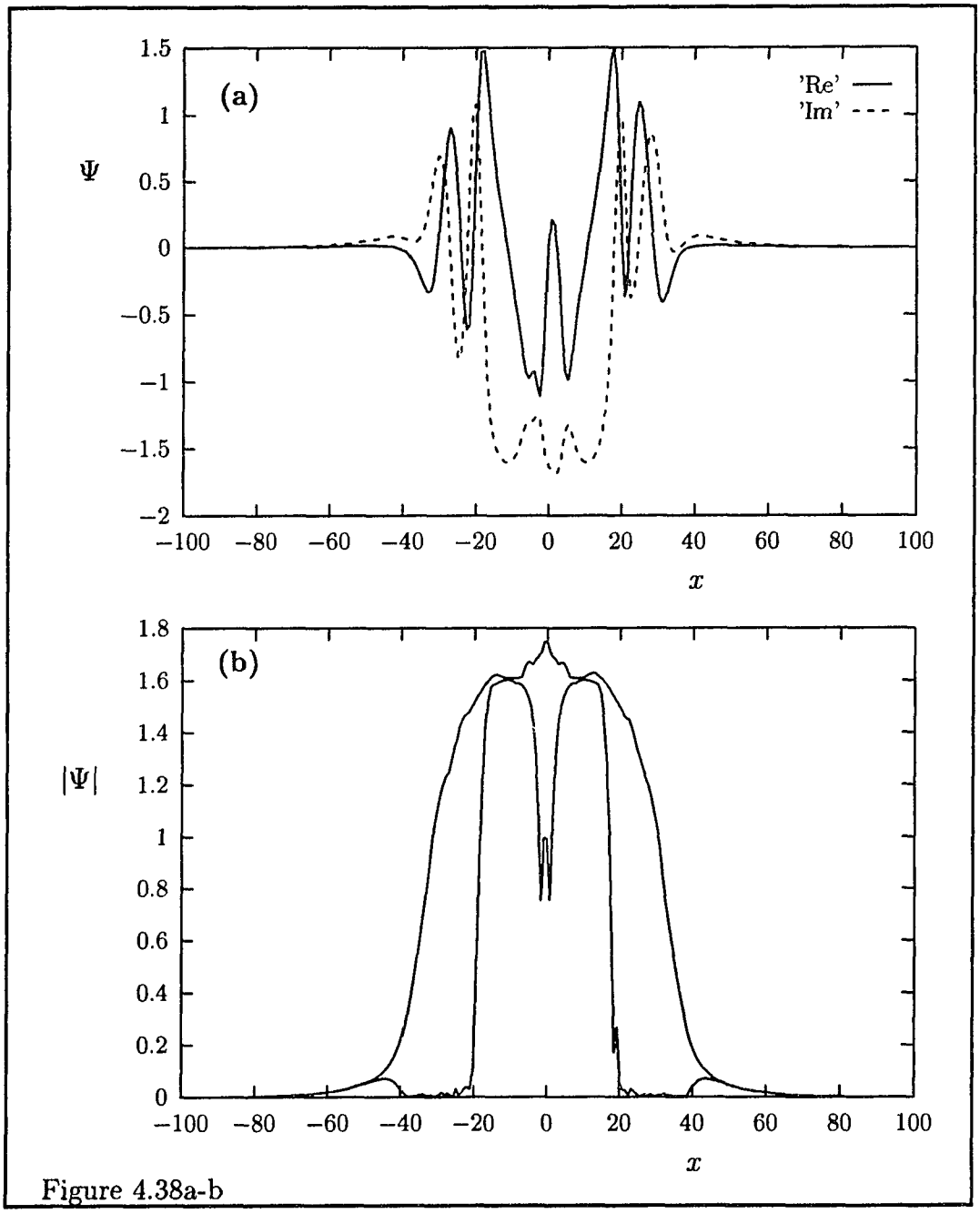

Figure 4.38a-b

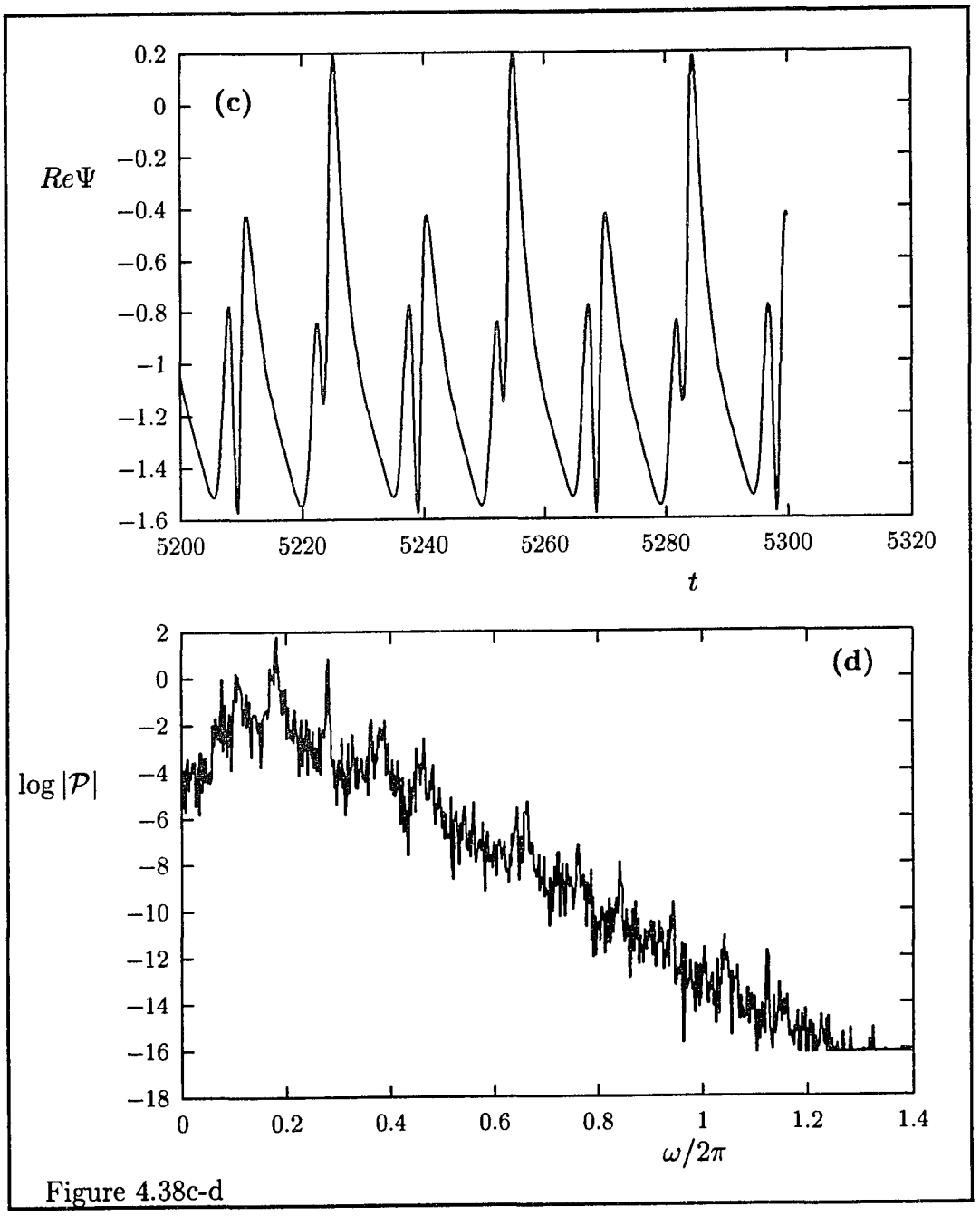

Figure 4.38c-d

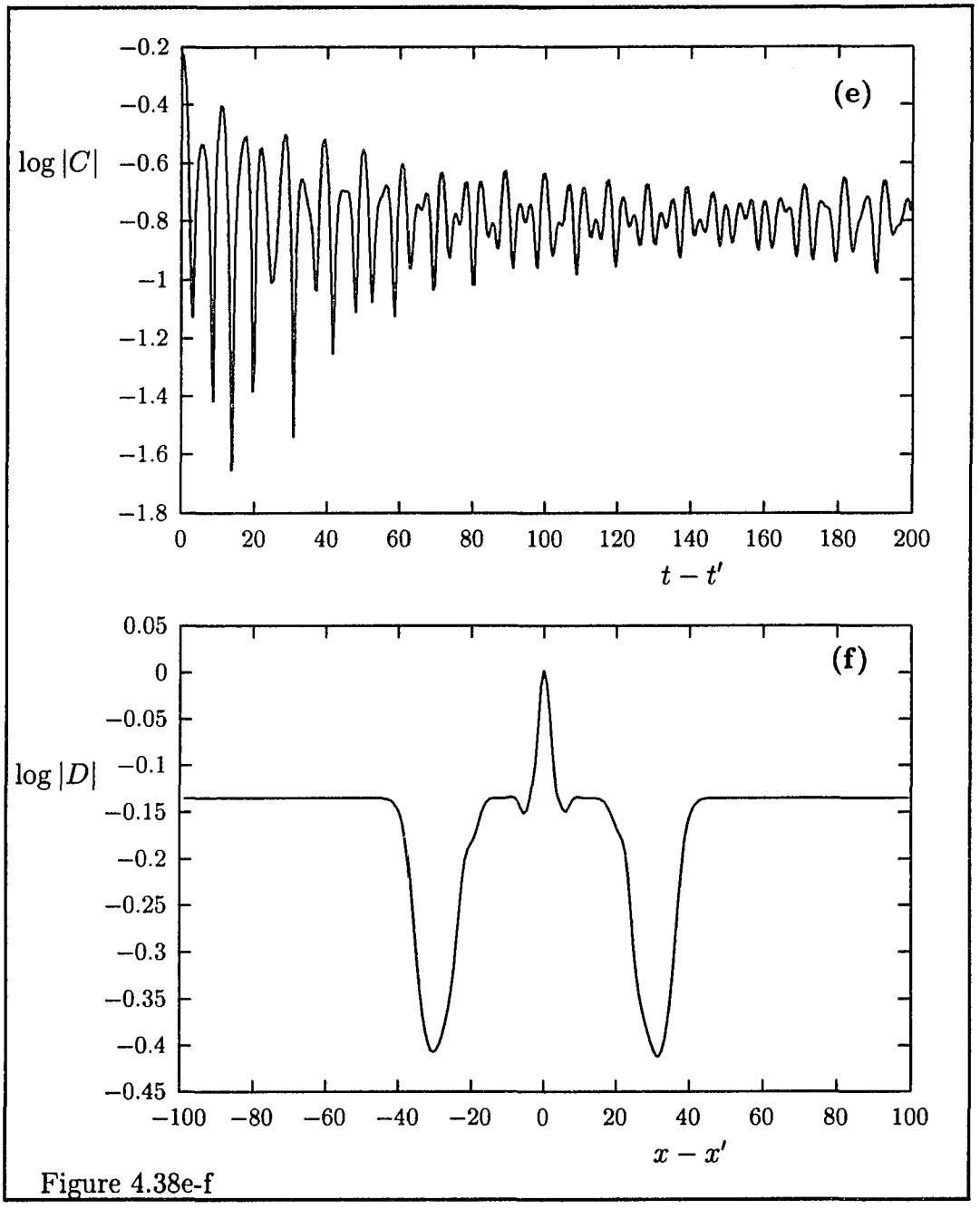

Figure 4.38e-f

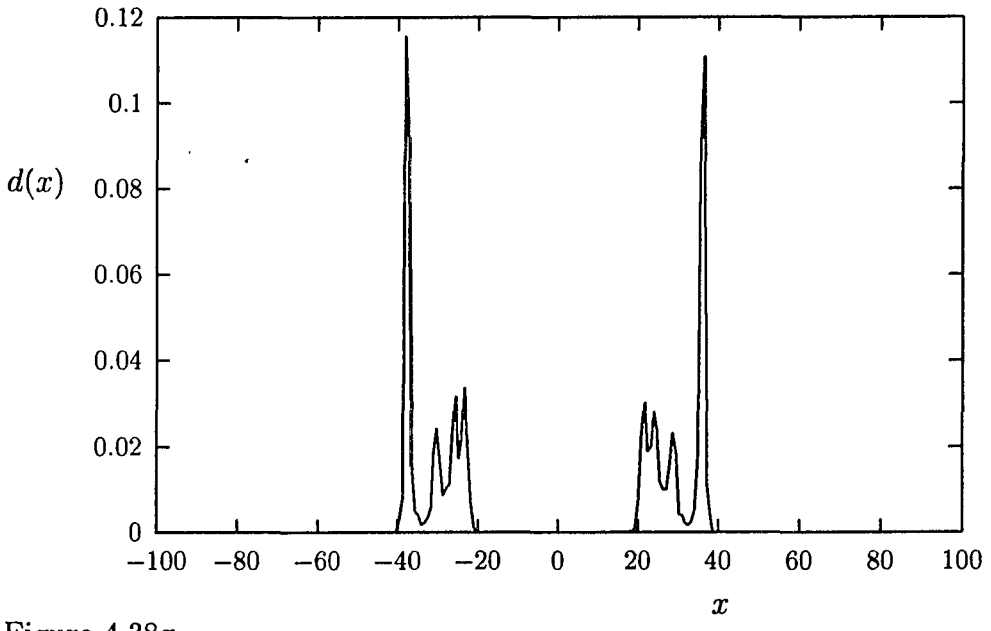

Figure 4.38g

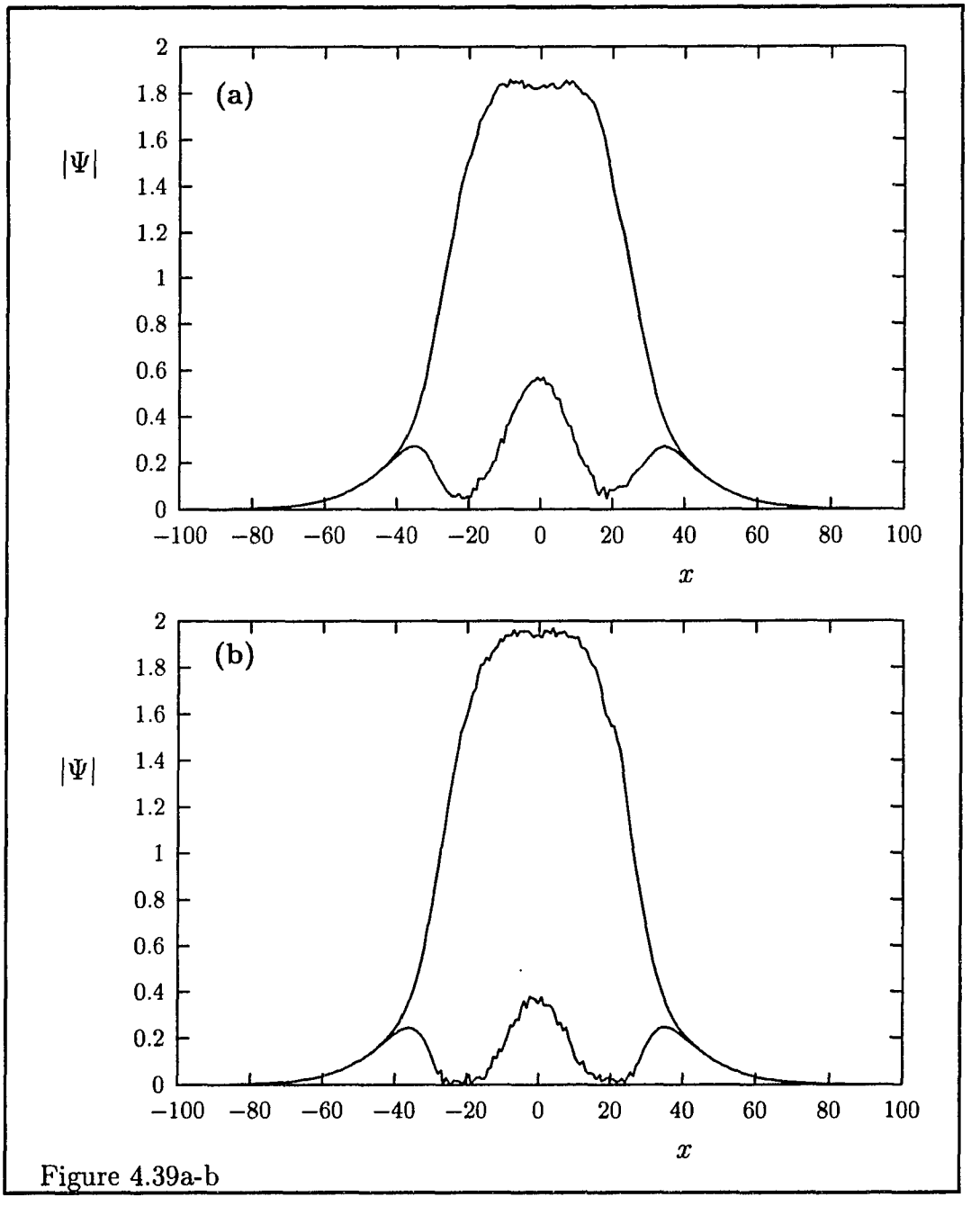

Figure 4.39a-b

Figure 4.39: Spatial envelop of $|\Psi(x,t)|$ for $\omega = -8$, $F_0 = 7.75$ (a), $F_0 = 7.5$ (b) and for $\omega = 2$, $F_0 = 4.5$ (c), $F_0 = 4.2$ (d).

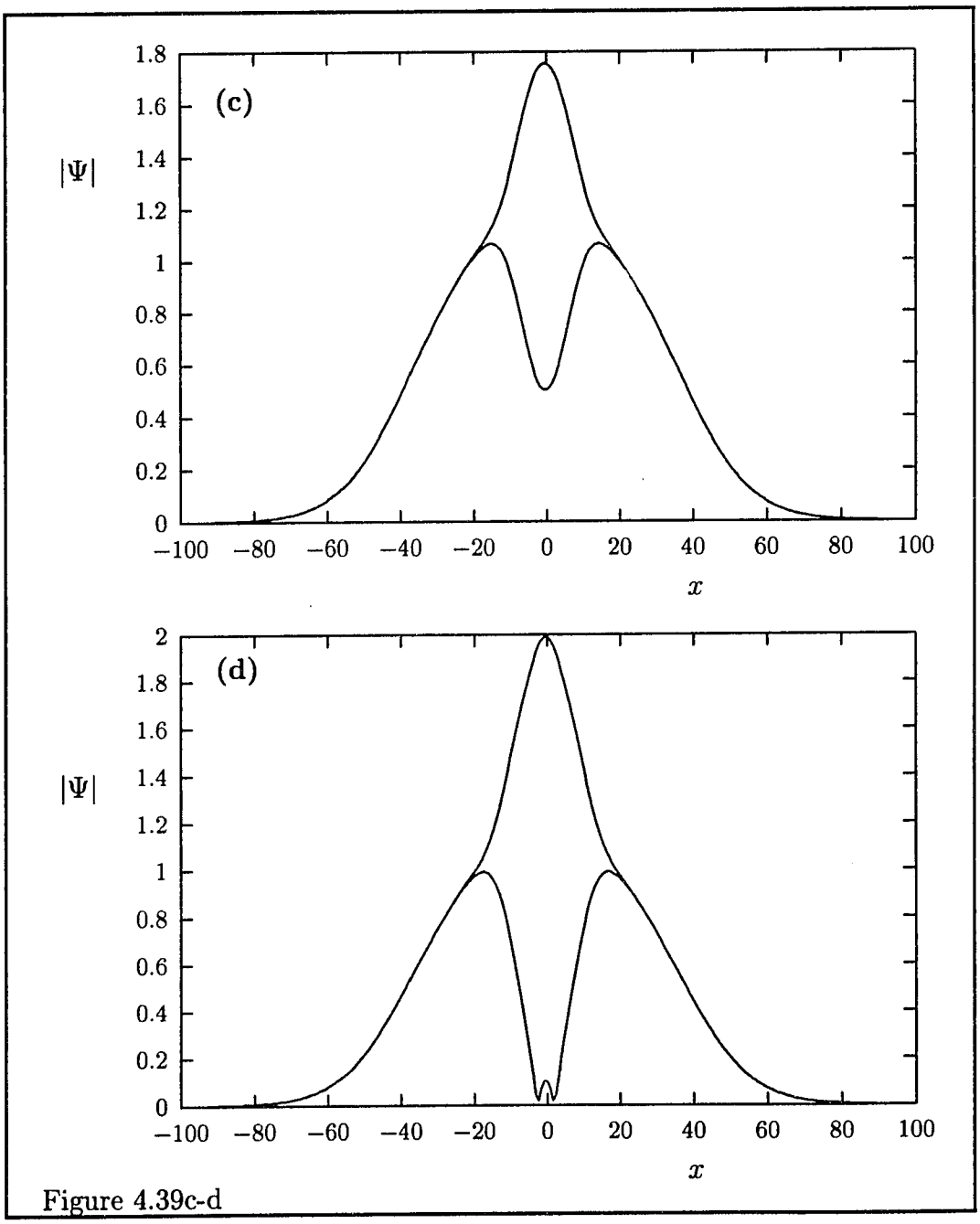

Figure 4.39c-d

Figure 4.40: (Next page) Snapshot (a) of the forced pulse solution for $F_0 = 7.75$ and $\omega = -8$, compare figure 4.39a. Further pictures shown are the spatial correlation function $D(0, x')$ (b), the power spectrum of $Re(e^{-i\omega t}\Psi(0,t))$ (c) and the temporal correlation function $D(0, x')$ (d) for this solution.

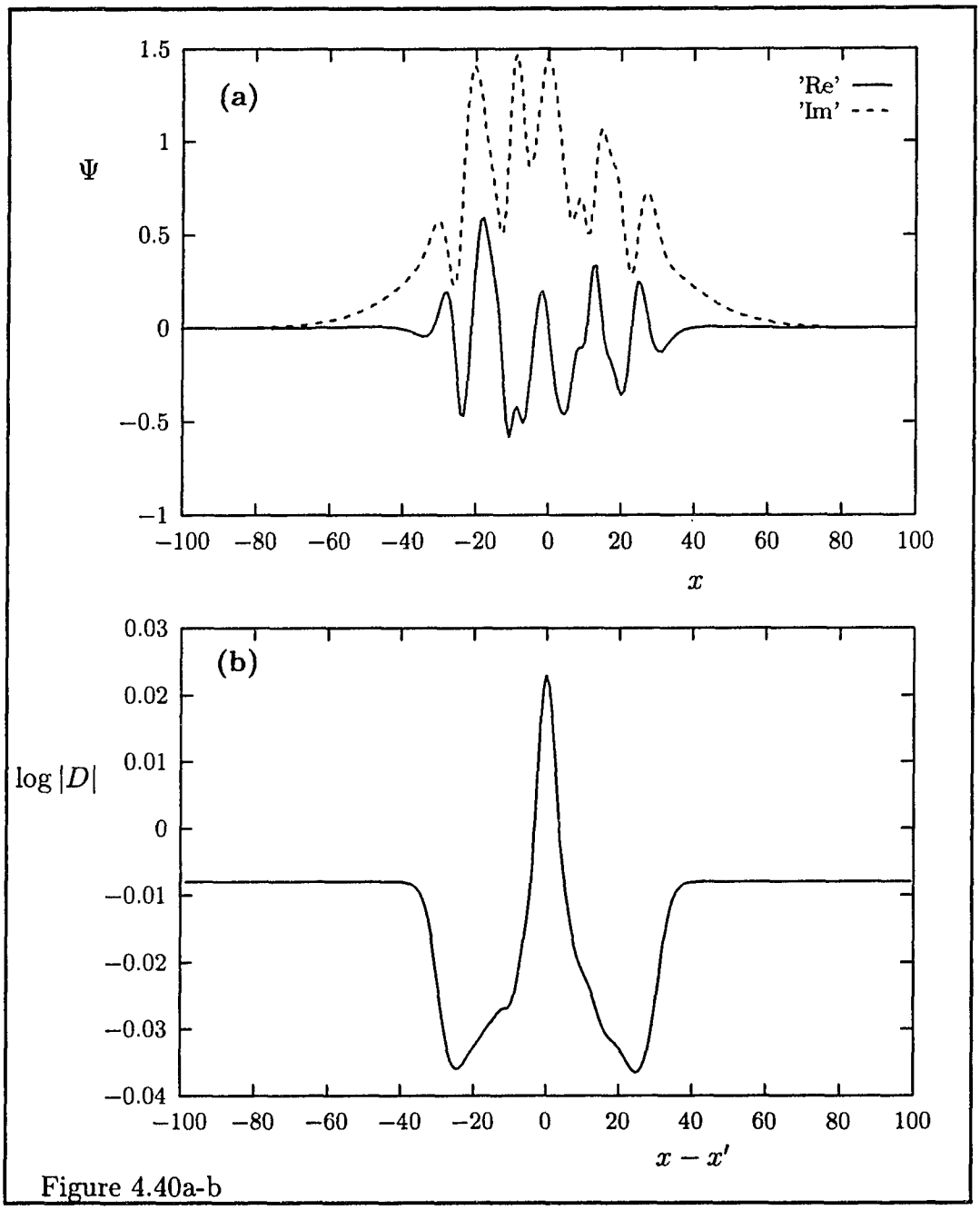

Figure 4.40a-b

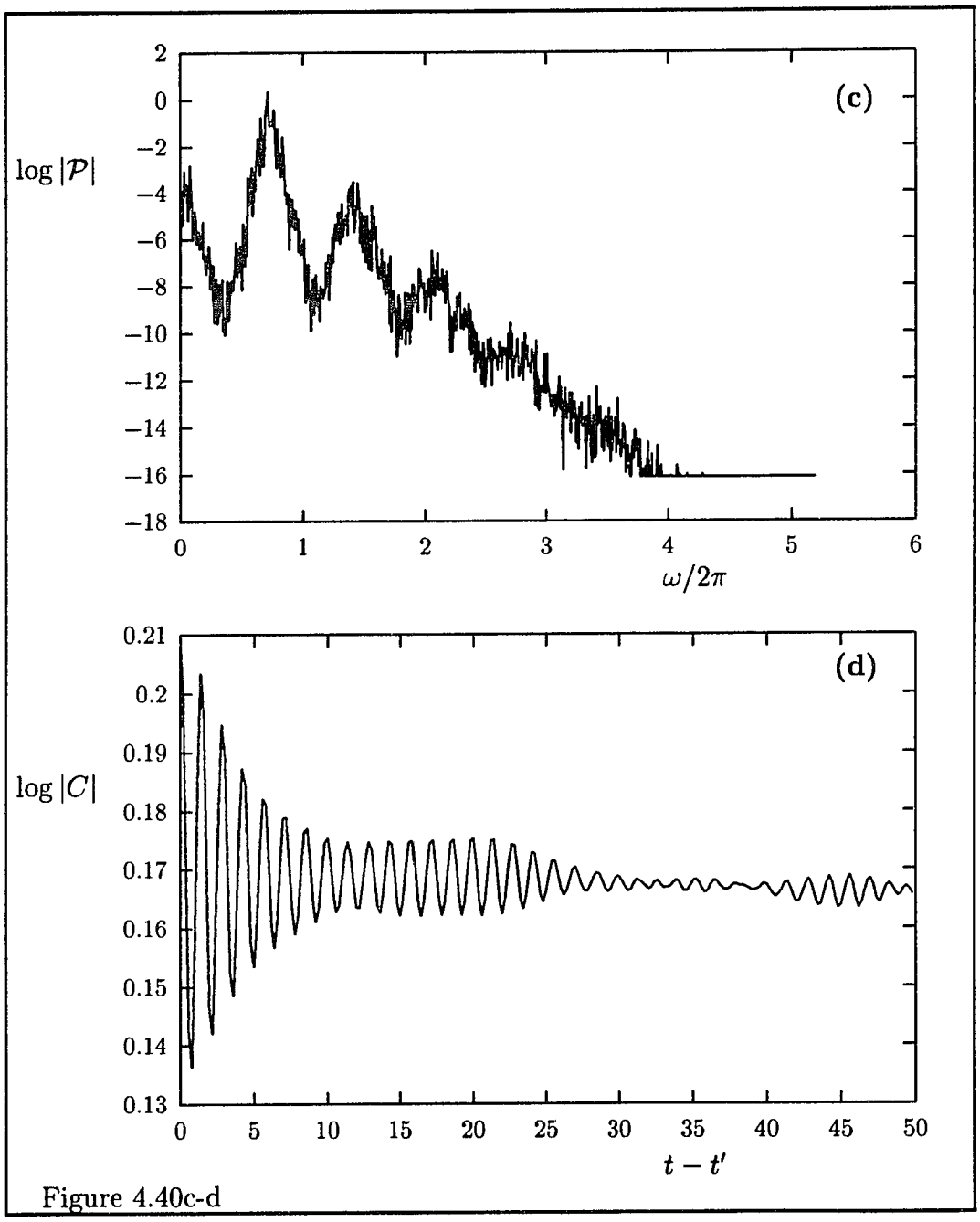

Figure 4.40c-d

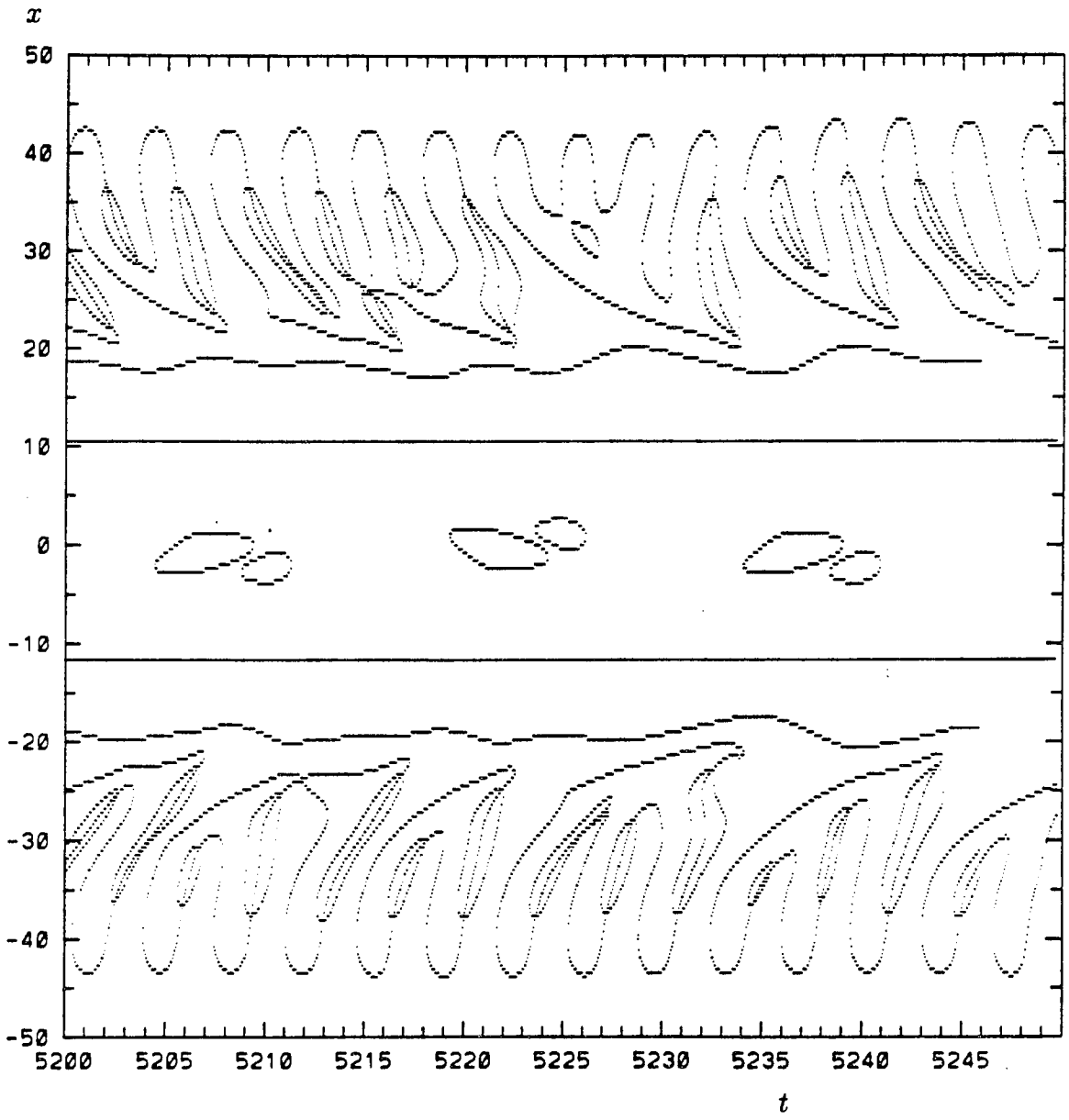

Figure 4.41a

Figure 4.41: Plots of the lines $Re\Psi = 0$ and $Im\Psi = 0$ for $F_0 = 1$, $\omega = -2$ (a) and $F_0 = 7.75$, $\omega = -8$ (b).

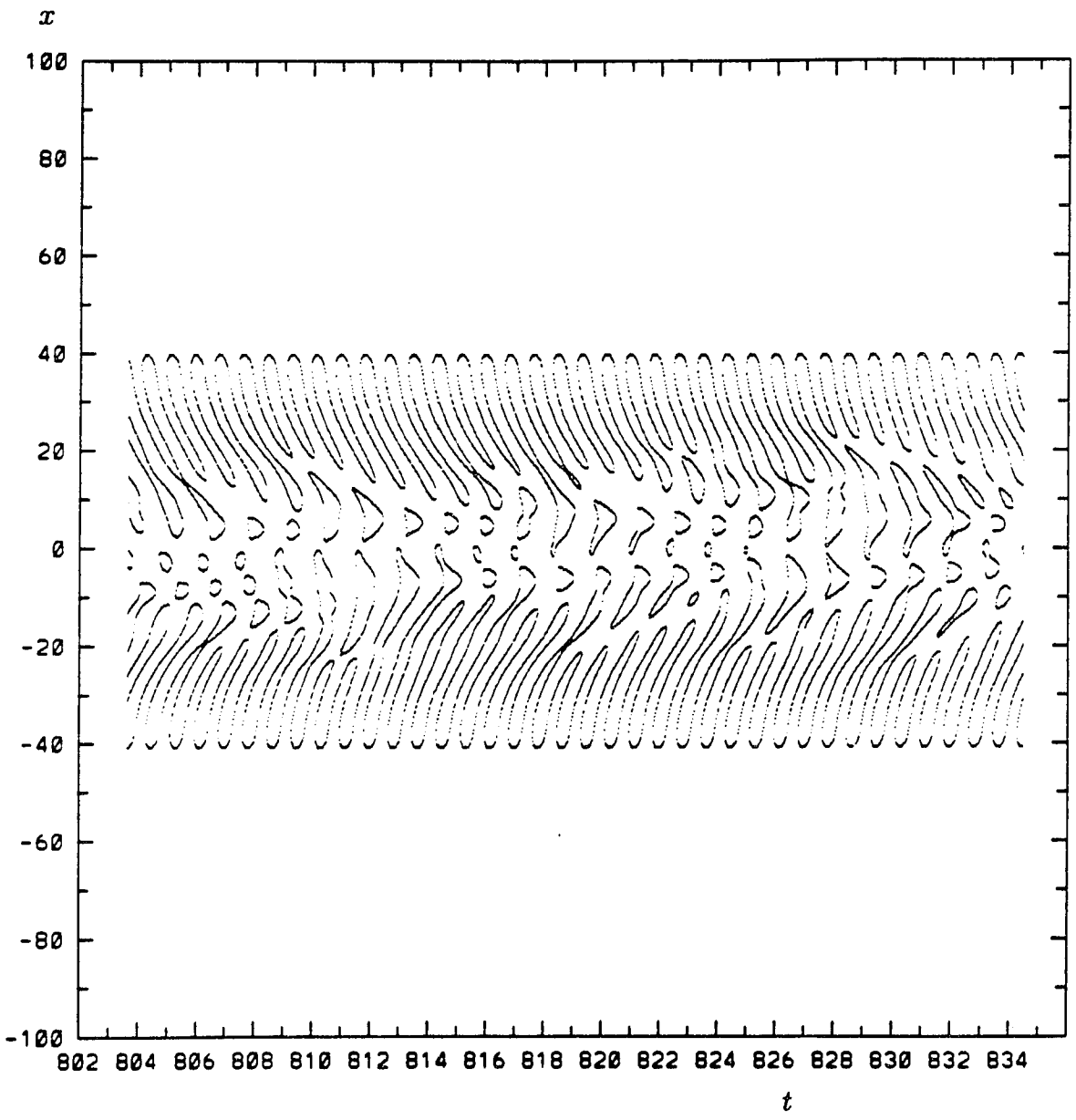
x
100
80
60
40
20
0
-20
-40
-60
-80
-100
802 804 806 808 810 812 814 816 818 820 822 824 826 828 830 832 834
t

Figure 4.41b

well away from the resonance frequency $\bar{\omega}$ for which the minimum required forcing for lock-in is minimum (in this case $\bar{\omega} \approx -1.5$).

For forcing frequenties in the viscinity of $\bar{\omega}$, say in the order of a few times $\bar{\omega}$, defects occur well before one enters region **C** and usually before the parity breaking occurs. Here therefore it is no exception, to observe spatially symmetric states which show quasi-periodic behaviour in time, with or without defects. See figure 4.37. This was not possible in the situations we discussed for the unforced system, neither in the previously discussed forced system. It is also here that one observes the more exotic behaviour. For instance if one moves down into the region **C**, then initially states occur with spatial regions in which the behaviour is quasi-periodic, while in other spatial regions the behaviour shows temporal chaos, and of course there are the always present regions at the edges of the system in which there is lock-in behaviour. Furthermore, the indication is also that there exists a very small spatial region, or perhaps just a single point, in between the region in which the behaviour is chaotic and the one in which it is quasi-periodic, in which the behaviour is locked-in. In any case, the temporal oscillations in $|\Psi|^2$ become very small in magnitude here, I observed oscillations with amplitudes less than 10^{-6}. Going further down one observes a transition to

amplitude chaos in the central region (see also the unforced system). Some pictures of the behaviour just described are shown in figure 4.38.

When the forcing frequency is further away from $\bar{\omega}$ the first occurrence of defects (as one moves down from region **L**) takes place closer to the dashed line bordering region **C** and even below it. The situation for the occurrence of the parity breaking and the occurrence of defects is here in fact quite the inverse of what is obseved when ω is in the vicinity of $\bar{\omega}$. Just below the forcing strength for which the parity breaking bifurcation occurs, one observes nonsymmetric quasi-periodic states without defects, again something that was not possible in the unforced system and in the previously discussed forced system. As one moves further down in region **QP** the spatial behaviour of the solutions can become quite complex before the presence of defects is observed for the first time, figure 4.39. Infact, the bifurcation after which defects are present may occur after passing the dashed line, that is after the onset of chaos. Phase-chaos is characterized by the absence of defects. Therefore, also given the complexity of the spatial behaviour of the solutions in the region where there is temporal chaos, the results suggest that phase-chaotic states exist for negative frequenties right below the dashed line for ω well away from $\bar{\omega}$. See figure 4.40.

As in the previous case, size effects have no influence on the occurence of defects. The regions at the edges of the system in which the motion is locked-in are therefore truly defectless, see also the defect distribution function in figure 4.38g. Some plots of the lines $Re(\Psi(x,t)) = 0$ and $Im(\Psi(x,t)) = 0$ in the x-t plane are shown in figure 4.41.

In the third and last situation we will discuss the system is again an intermediate size system but now the forcing is a plane wave forcing. The other parameters are unchanged.

4.0.3 Intermediate size systems with a plane wave forcing.

In the simulations $q|\Lambda|^{-1/2}$ is kept at an integer value as mentioned earlier. As we will see this situation will show similarities with the previous case for which the forcing was Gaussian, which is an illustration of the statement made earlier that the precise shape of the forcing is not all that important for certain properties. There are of course also differences.

The F_0-ω plane of the phase diagram for this situation is shown in figure 4.42. The region labeled **L** is again the lock-in region, in which stable phase-

locked states exist. For some pictures of phase-locked states see figure 4.43. The phase-locked states are defectless and of course not symmetric. Bistable regions for phase-locked states are not observed.

As in the previous case, for solutions outside **L** usually different spatial regions can be distinguished in which the behaviour shows qualitative differences. Below the dashed line in figure 4.40, in region **C**, there are one or more of such regions in which the behaviour shows al least temporal chaos. In region **QP** the behaviour is at most quasi-periodic in time but not chaotic.

A qualitative difference with respect to a Gaussian forcing is that with the plane wave forcing the parity symmetry is not present. It is also not recoverable via a simple transformation as was the case for the time isotropy. A parity breaking bifurcation is therefore of course not observed. Note also that for the phase-locked states the inversion symmetry is also not recovered in $|\Psi|$. Furthermore, the different spatial regions observed in solutions outside **L** are not located symmetrically with repect to the origin.

All solutions outside **L** have again in common that at both system edges spatial regions occur, in which there is lock-in behaviour, that is, they behave in time as $e^{i\omega t}$. Further outward in these regions ($x \to \pm\infty$ in the extended system) the solution more and more approaches a plane wave shape with the

same wave number as the forcing.

The more exotic behaviour is again observed for frequenties around the resonance frequency, in this case $\bar{\omega} \approx -2$. One observes solutions that show lock-in or quasi-periodic behaviour in certain parts of space while in other parts they show temporal or spatio-temporal chaos. See figure 4.44 for some illustrations. The defect distribution function for a solution in this region is shown in figure 4.45.

For frequenties further away from $\bar{\omega}$ on the negative side, the first defects occur (as one decreases F_0) well below the dashed line. Therefore the conditions for phase-chaos would be even more favourable then for a Gaussian forcing, were it not that the region in which defectless temporal chaotic behaviour occurs turns out to be too small for the frequenties covered in figure 4.42 to observe spatial disorder. See figure 4.46 for results for $\omega = -8$. We can of course not rule out the possibility of phase-chaos for larger negative frequenties.

For frequenties further away from $\bar{\omega}$ on the positive side, the first defects occur a little below the solid line and certainly well before entering region **C**. The defects in region **QP** occur at fixed points and periodically in time, see figure 4.47.

Finally it is interesting to observe the difference in response to a left and right traveling plane wave forcing. Let us denote a solution of (4.2) for a plane wave forcing characterized by q and ω as $\Psi_{q,\omega}(x,t)$. Then obviously it is so that $\Psi_{q,\omega}(x,t) = \Psi_{-q,\omega}(-x,t)$. Thus the responses to a left and to a right traveling wave are identical in this case. This is what one naively expects from equation (4.2) since there is no obvious preference for left or right in the unforced equation. The left-right invariance is however not present for all plane wave forcings. As one observes from equation (4.2), there is no apparent relation between $\Psi_{q,\omega}(x,t)$ and $\Psi_{q,-\omega}(x,t)$, although these solutions are the responses to a to the left and to the right traveling wave respectively. Infact, from the observed behaviour in the F_0-ω plane of the phase diagram, we know that $\Psi_{q,\omega}$ and $\Psi_{q,-\omega}$ are n general very different solutions. We observe therefore a dynamical breaking of the left-right symmetry, that is , the forced equation has a sense of left and right which is of a dynamical origin. From the results of chapter 3 for the LE, it follows that the unsymmetric behaviour in the F_0-ω plane as function of ω is present for all $c_3 \neq 0$. One may expect the left-right symmetry breaking therefore to occur for all values of Σ_0, and not just to be caused by the the fact that in the present case with $\Sigma_0 = 4$ the unforced stable state is nonsymmetric in space.

This concludes our discussion of pulse solutions of the CGLE with a spatially dependent growth rate. In the next chapter we will return to the supercritical CGLE with constant growth rate and we will discuss the phase diagram in the presence of a plane wave forcing.

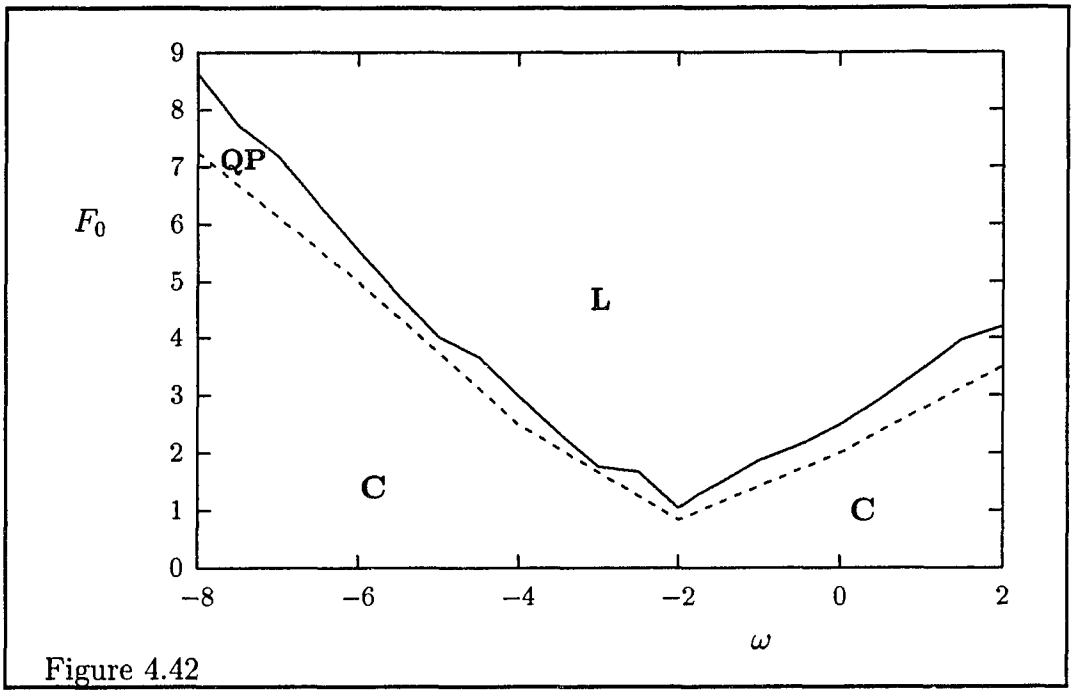

Figure 4.42

Figure 4.42: The F_0-ω plane of the phase diagram for the CGLE in an intermediate size system with plane wave forcing and Gaussian growth rate with $q = 0.173$, $K = 0.03$. Phase locking occurs in **L**. In region **QP** quasi-periodic motion occurs at least in one spatial region but chaotic behaviour is not present. Chaotic behaviour occurs in region **C**.

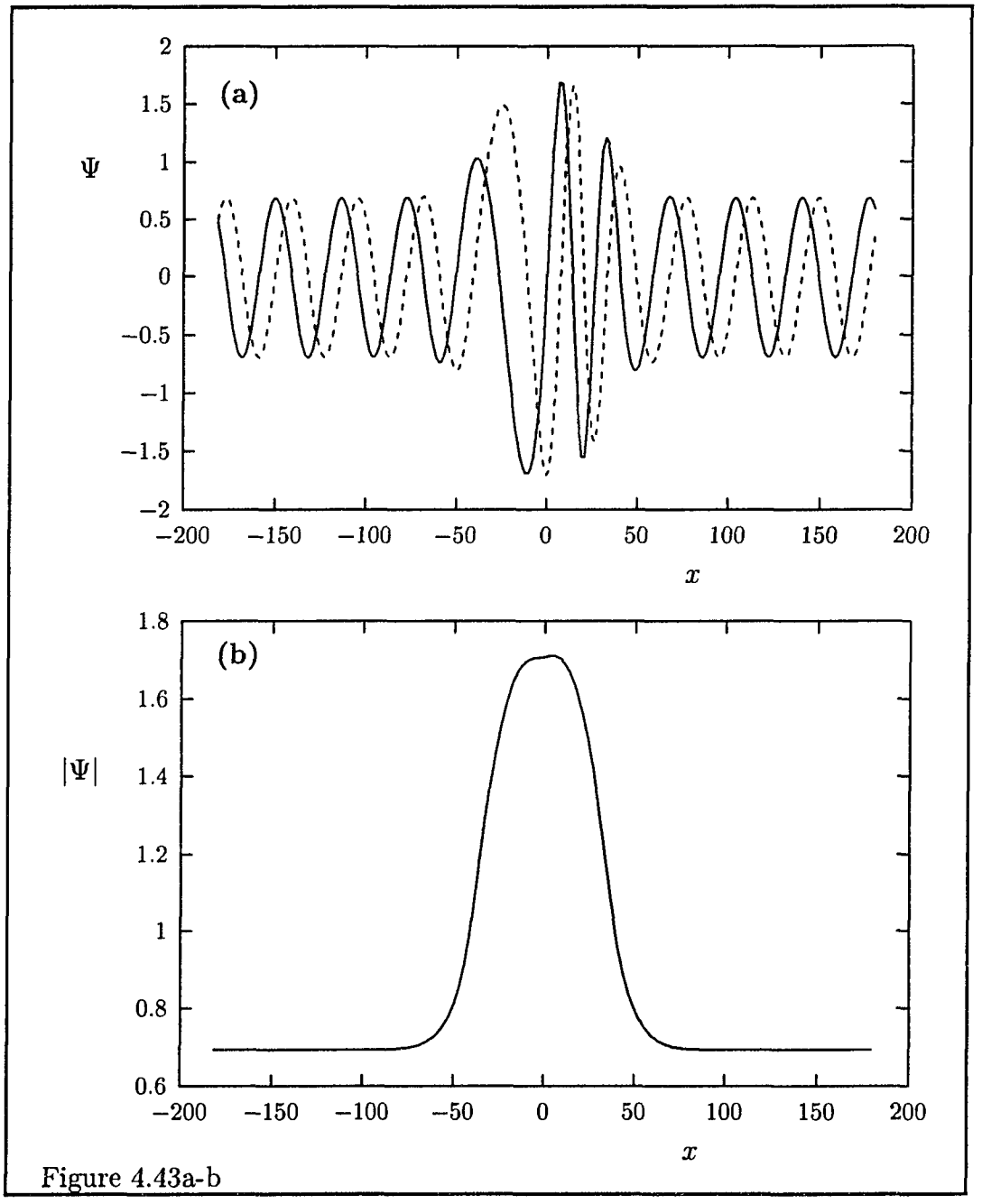

Figure 4.43a-b

Figure 4.43: Snapshots of some lock-in states in region **L**, for $F_0 = 1.5$, $\omega = -2$ (a,b) and for $F_0 = 5$, $\omega = 2$ (c,d). Note the absense of spatial symmetry, particularly in $|\Psi(x,t)|$, panels (b) and (d).

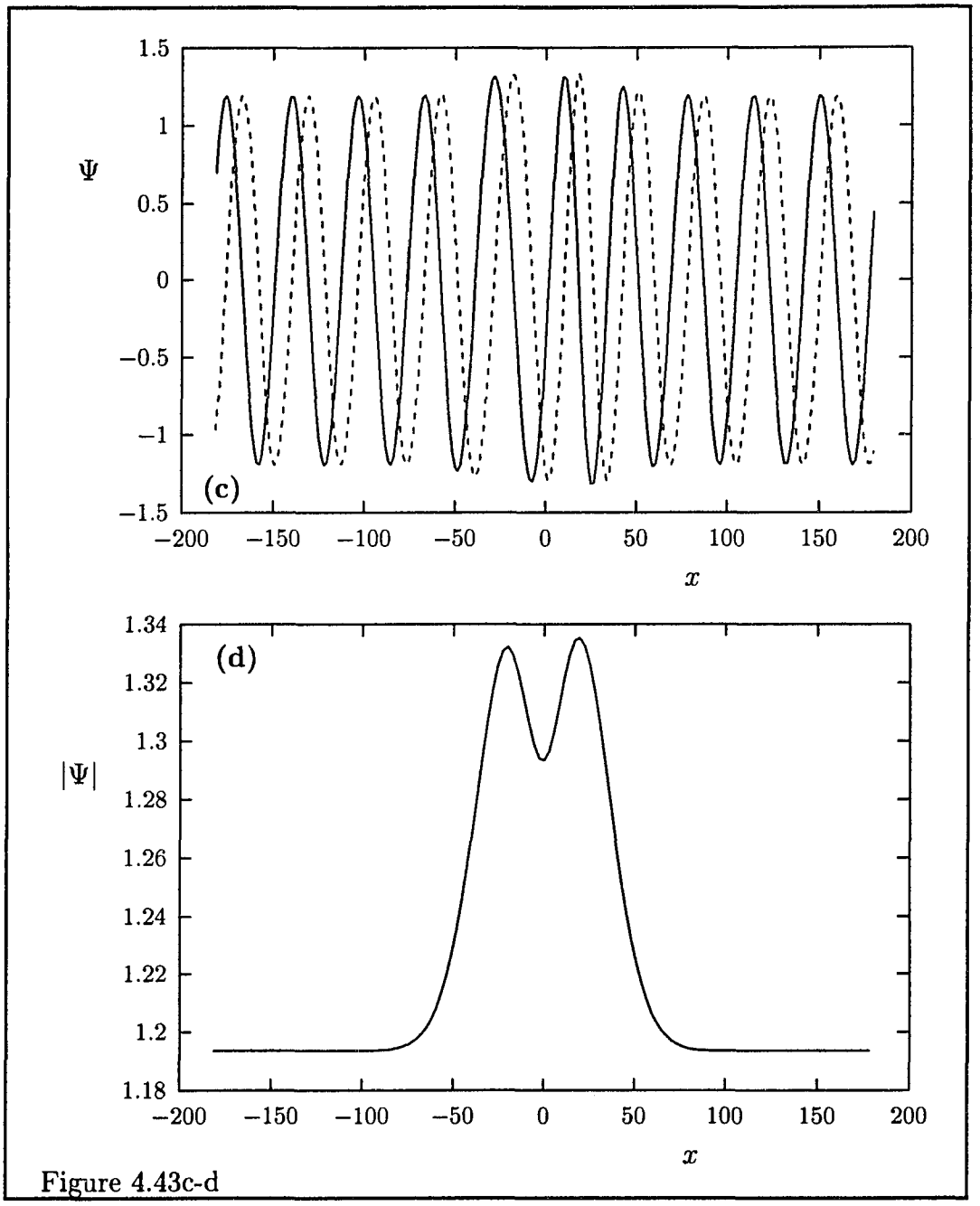

Figure 4.43c-d

Figure 4.44: (Next page) Some pictures of the behaviour close to resonance outside **L**. The spatial envelop of the pulse solution for $\omega = -2$ and $F_0 = 0.9$ (a), $F_0 = 0.8$ (b). Further are shown for the last solution a snapshot (c), the power spectrum of $Re(e^{-i\omega t}\Psi(x,t))$ in $x = 0$ (d) and in $x = 35$ (e), the time behaviour of $Re(e^{-i\omega t}\Psi(-25,t))$ (f), the correlations function $C(0,t,t')$ (g), and $C(35,t,t')$ (h), and the correlation functions $D(0,x')$ (i) and $D(85,x')$ (j).

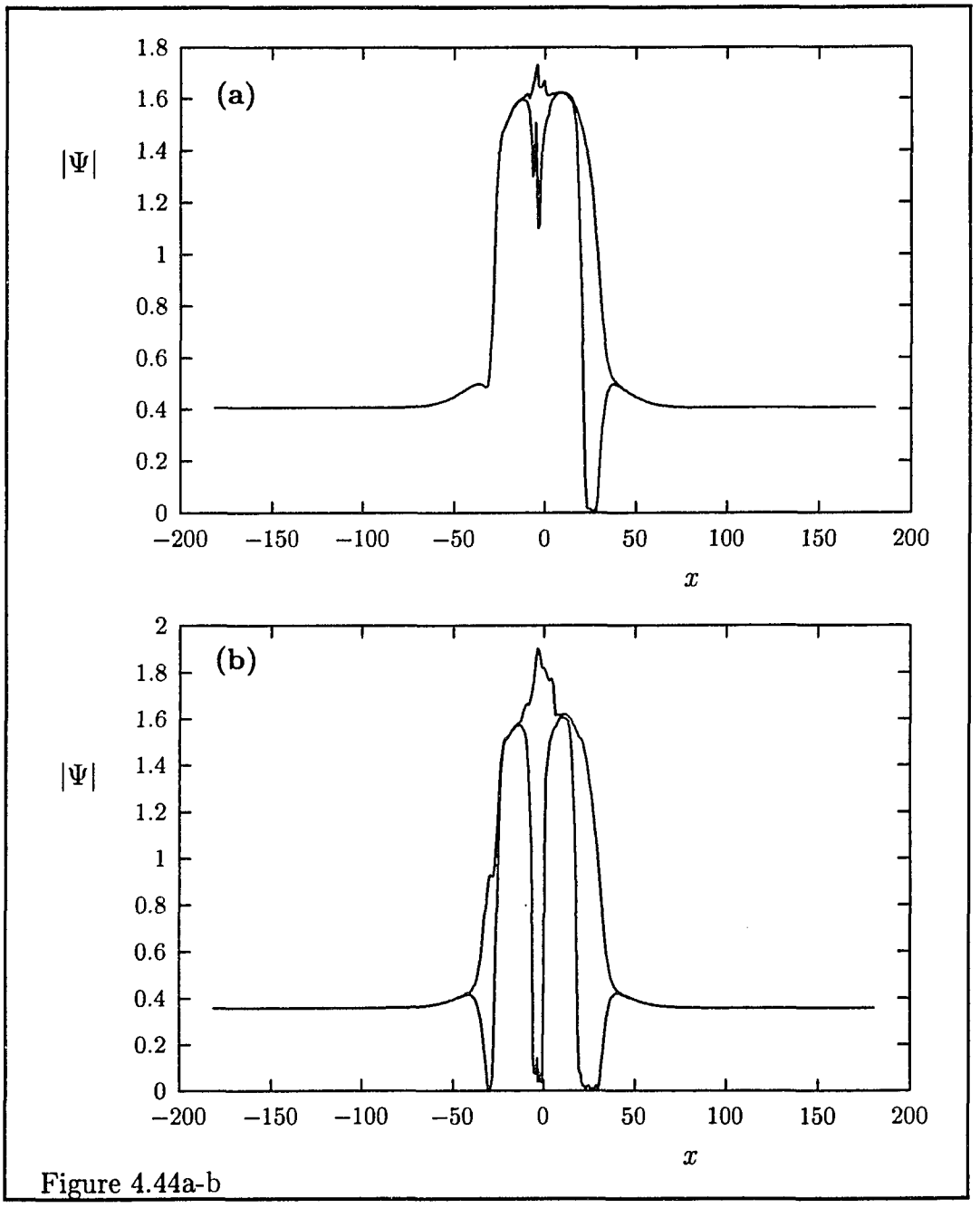

Figure 4.44a-b

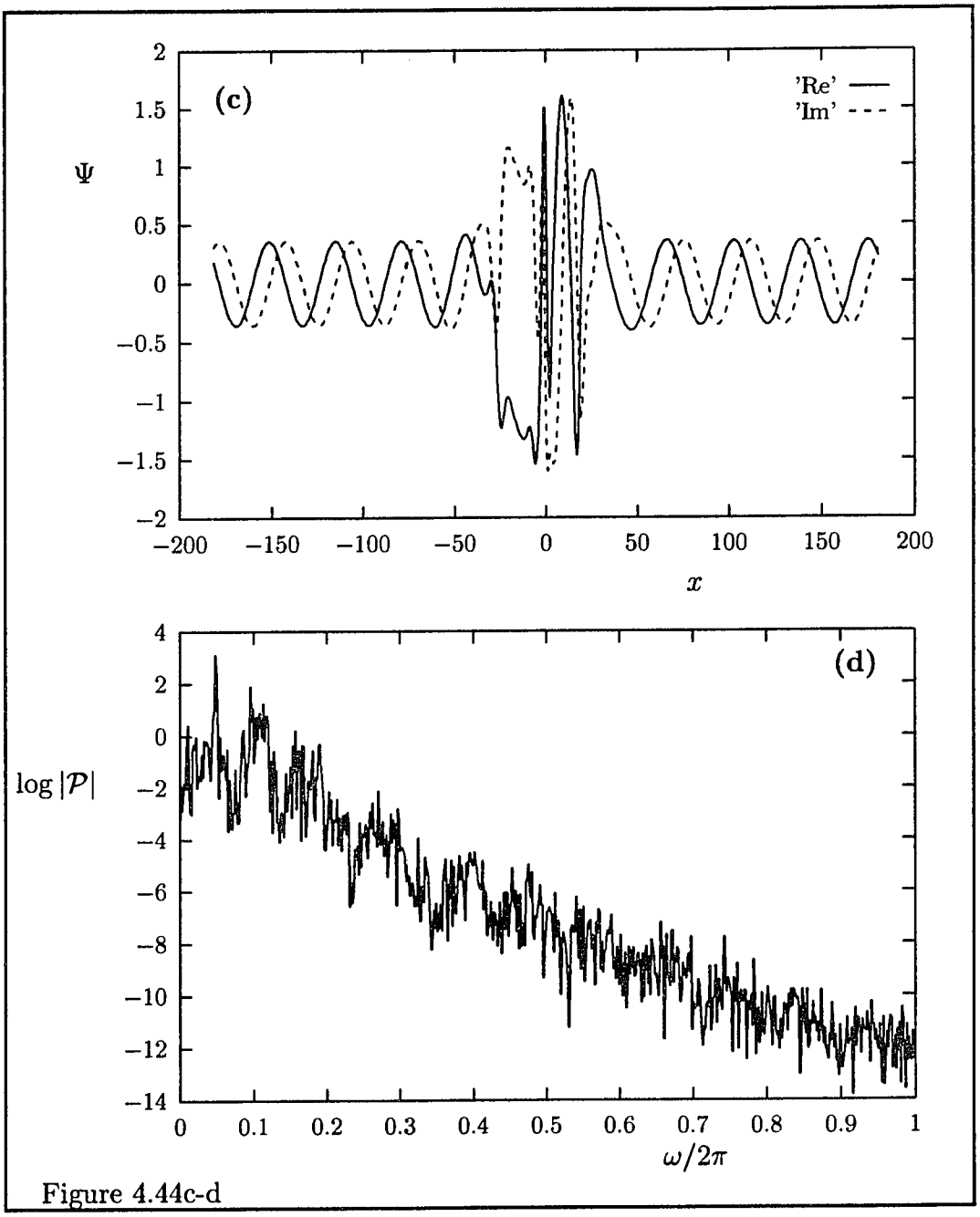

Figure 4.44c-d

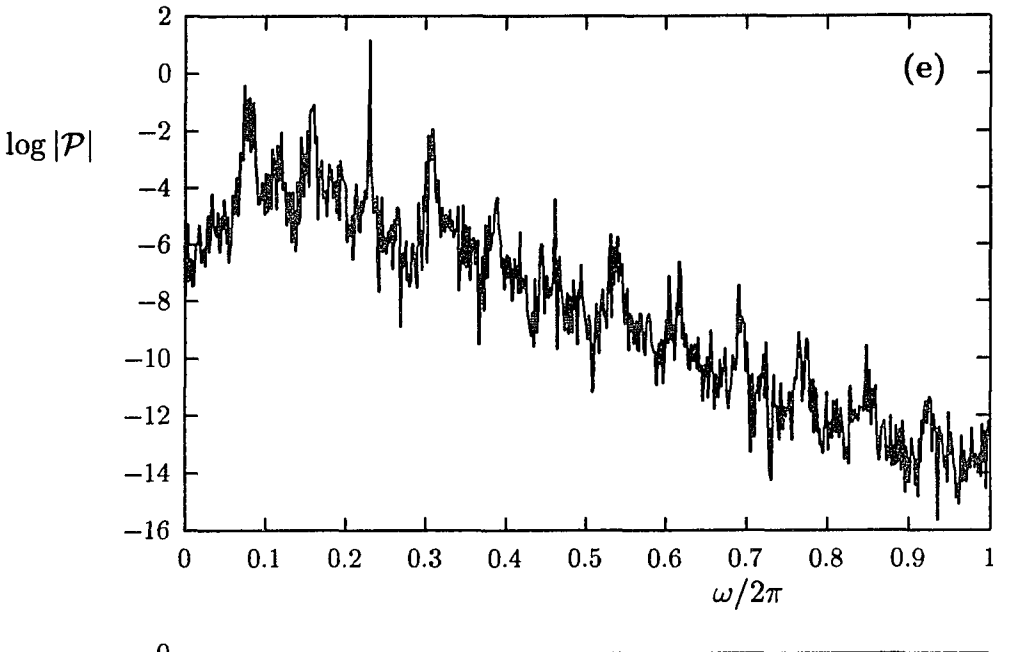

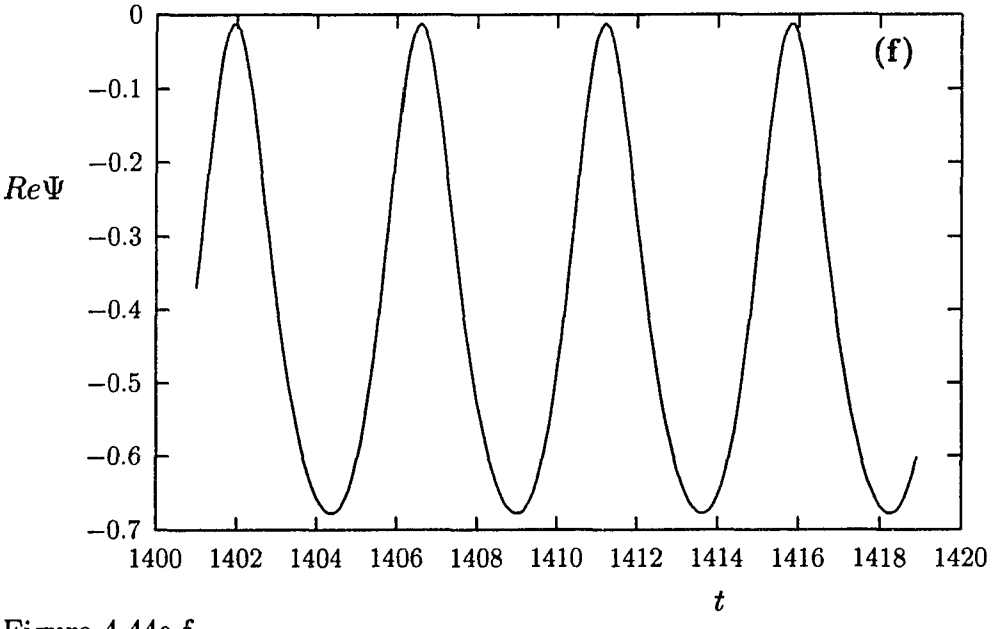

Figure 4.44e-f

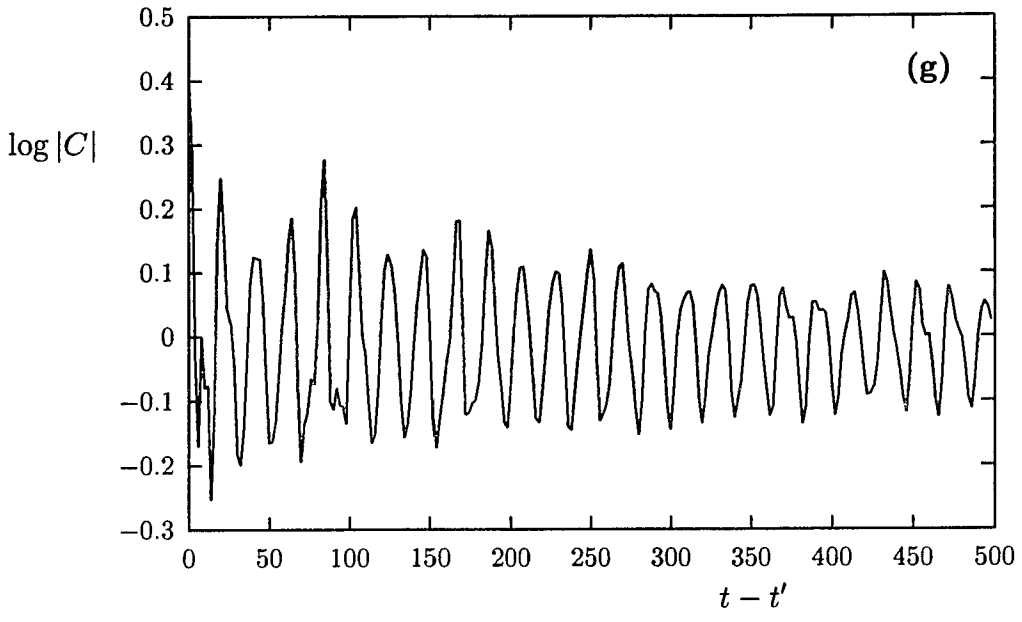

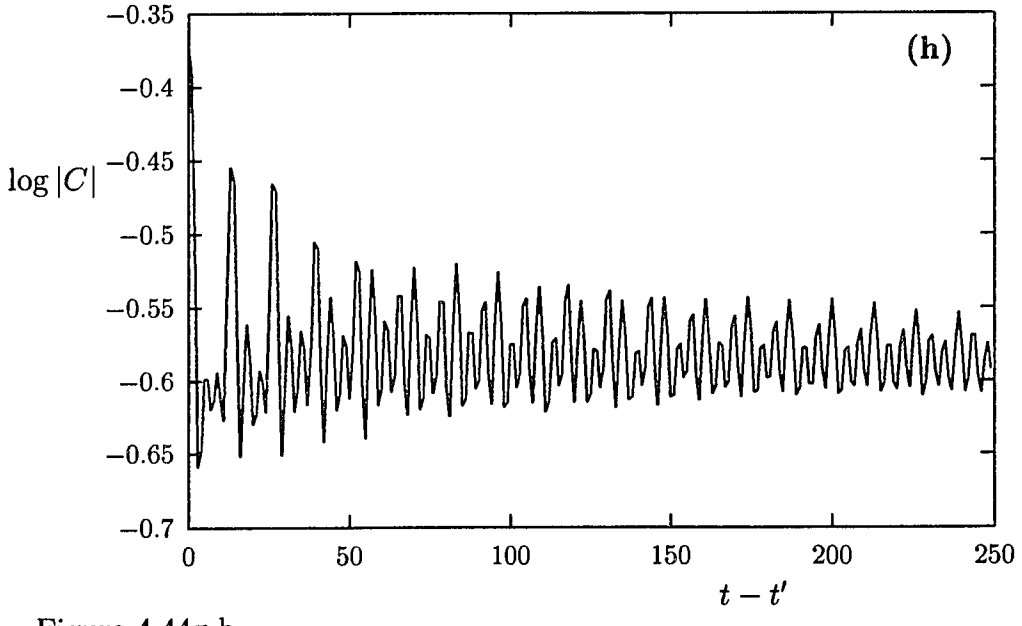

Figure 4.44g-h

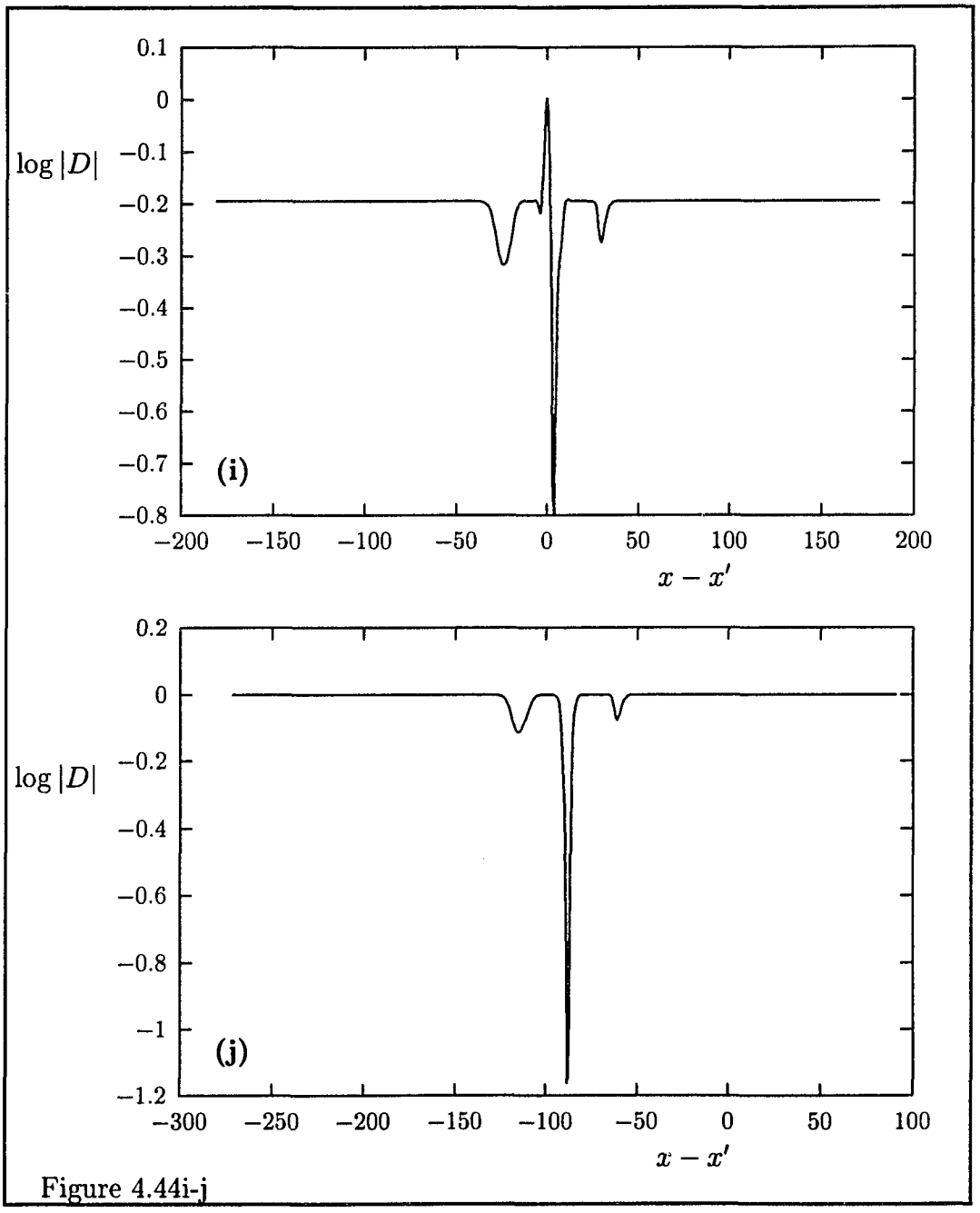

Figure 4.44i-j

Figure 4.45: (Next page) The defect distribution function $d(x)$ for $\omega = -2$ and $F_0 = 0.8$, compare figure 4.44b. The two peaks on the left correspond to defects occurring in a region in which the motion is quasi-periodic, the defects occur here at fixed positions (two) periodically in time. The distribution function in the chaotic regions is shown more detailed in panel (b).

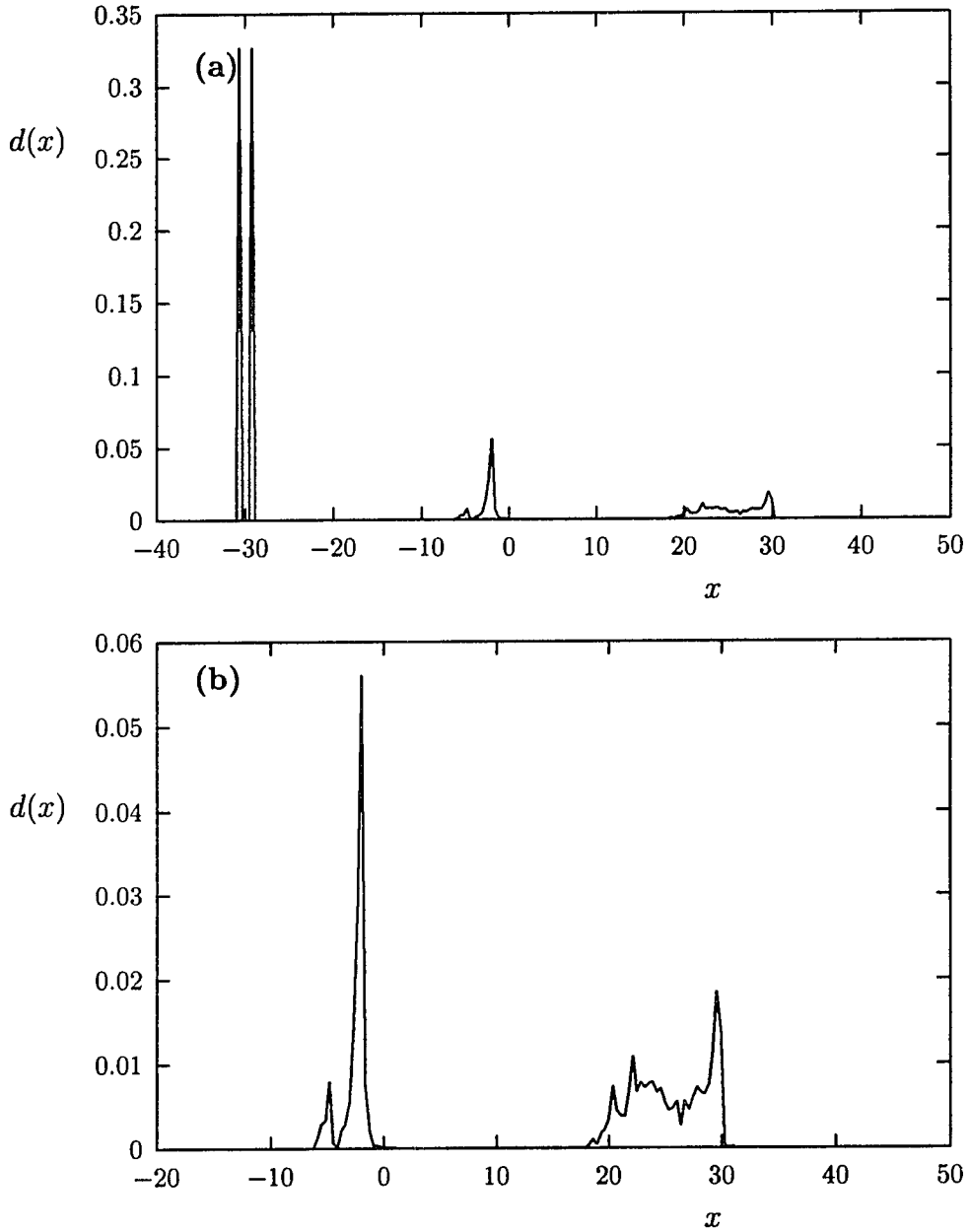

Figure 4.45a-b

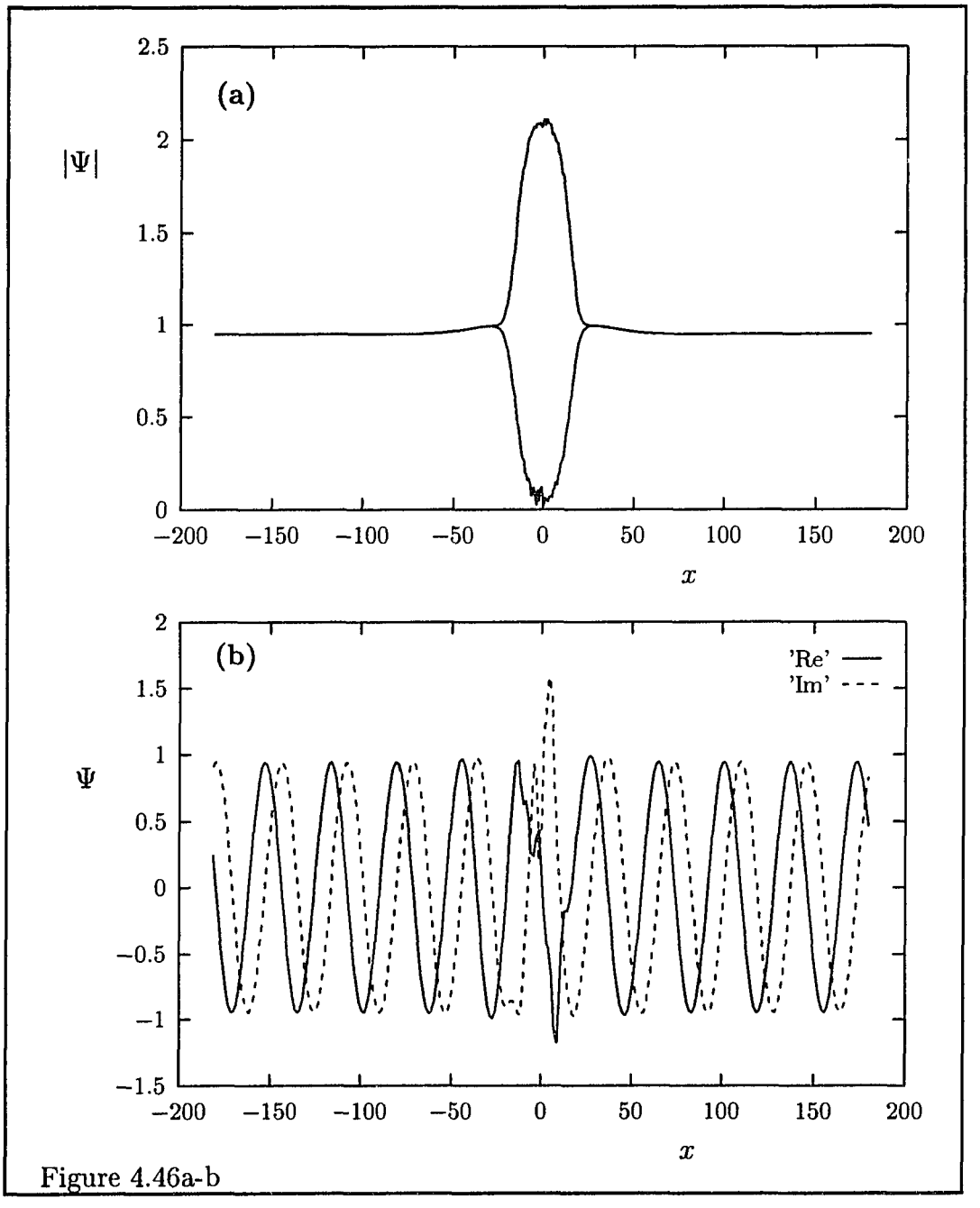

Figure 4.46a-b

Figure 4.46: A solution in region **C** well away from resonance for $\omega = -8$ and $F_0 = 7$. Temporal chaotic behaviour exists in the central region, this region is too small for spatial disorder to develope.

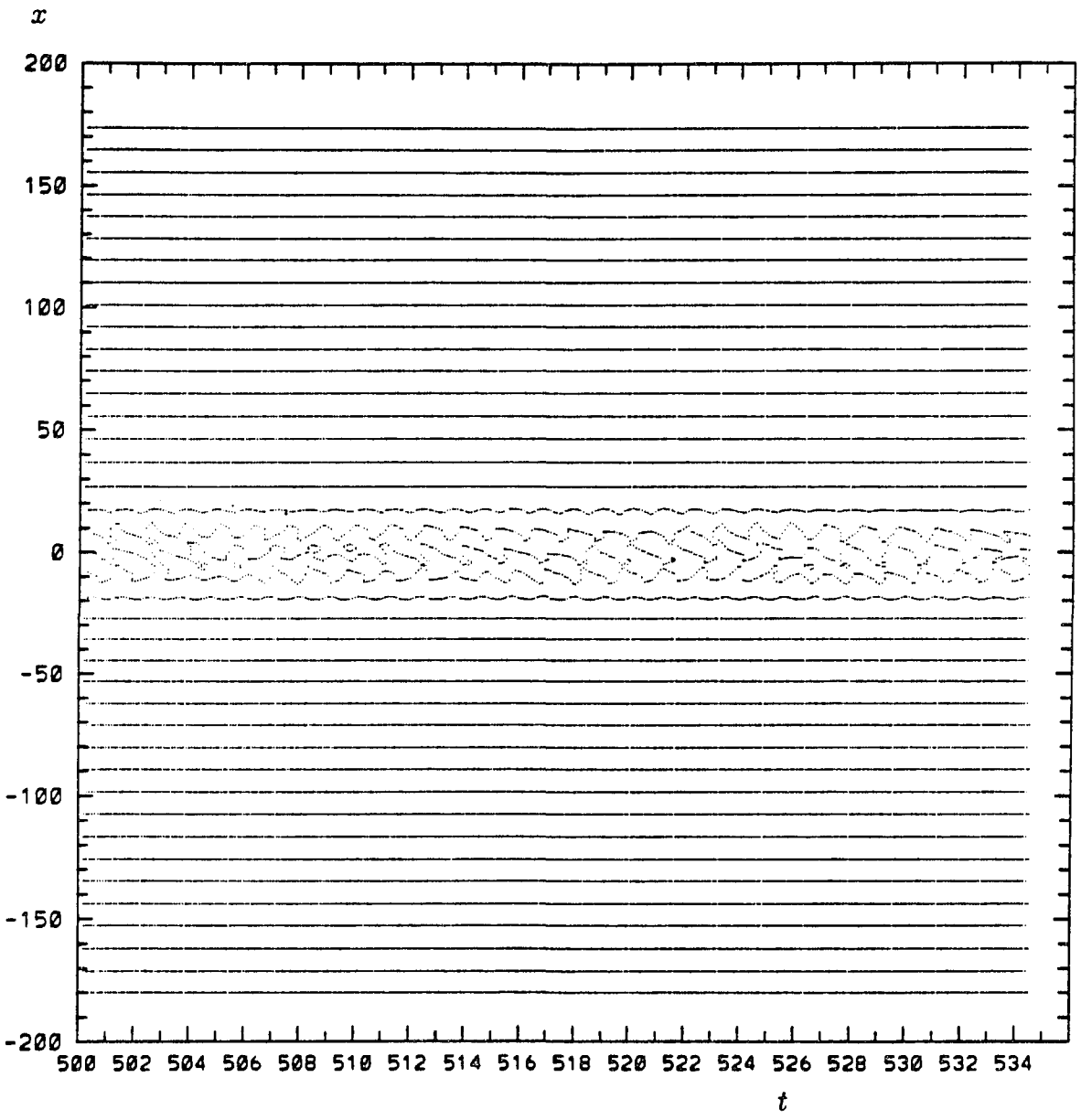

Figure 4.47a

Figure 4.47: Plots of the lines $Re\Psi = 0$ and $Im\Psi = 0$ for $F_0 = 0.8$, $\omega = -2$ (a) and $F_0 = 7$, $\omega = -8$ (b).

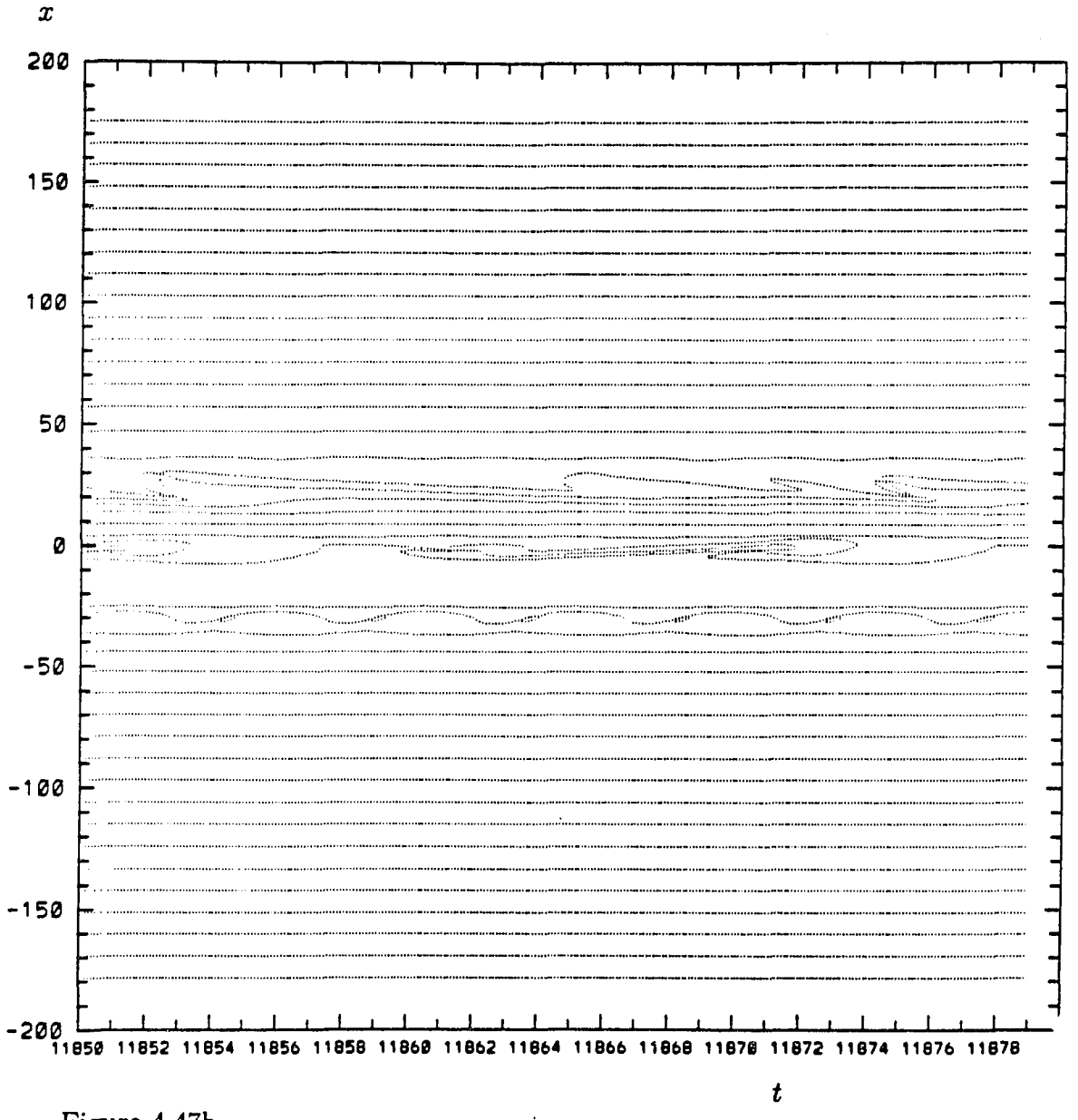
x
200
150
100
50
0
-50
-100
-150
-200
11850 11852 11854 11856 11858 11860 11862 11864 11866 11868 11870 11872 11874 11876 11878
t

Figure 4.47b

Chapter 5

Solutions for a plane wave forcing.

In this chapter we will return to the CGLE with constant linear growth rate. We will confine ourselves to the supercritical case. The forcing we will consider is of a plane wave form,

$$F(x,t) = F_0 e^{iKx+i\omega t}. \tag{5.1}$$

For this type of forcing it is useful to make the transformation

$$\Psi(x,t) = e^{iKx+i\omega t}\phi(x,t) \tag{5.2}$$

and study the behaviour of ϕ rather than that of Ψ. After proper rescaling (chapter 1) the general equation for ϕ then becomes

$$\left[\frac{\partial}{\partial t} - 1 + i\omega - \Lambda(1+ic_2)\left(\frac{\partial}{\partial x} + iK\right)^2 + (1+ic_3)|\phi|^2\right]\phi = F_0, \qquad (5.3)$$

where F_0 may be taken real without loss of generality. The parameter Λ is again the cut-off parameter

$$\Lambda = \frac{(2\pi)^2 Re(\lambda)}{l^2|Re(\sigma)|}. \qquad (5.4)$$

In this chapter we will not confine ourselves to the extended system only but we will include results for finite size systems as well. We therefore define the length l occurring in (5.4) to be equal to be equal to the system lenghth for finite size systems and to be equal to the wave length of the forcing for extended systems. We will impose periodic boundary conditions for finite size systems,

$$\Psi(x+l,t) = \Psi(x,t). \qquad (5.5)$$

For the extended system we will also use periodic boundary conditions in an actual simulation, but of course the system length has to be taken much larger than the wavelength of the forcing l. In order to avoid effects caused by a discontinuity of the forcing at the system boundaries, we take the system

length equal to an integer multiple of l, the periodic boudary condition then becomes

$$\Psi(x + Nl, t) = \Psi(x, t). \tag{5.6}$$

For size systems the dimensional wavenumber of the forcing is necessarily equal to an integer times the the wavenumber of the fundamental mode;

$$K_{dim} = |\Lambda|^{1/2} \left| \frac{Re(\sigma)}{Re(\lambda)} \right|^{1/2} \cdot K, \qquad K = 0, \pm 1, \pm 2, \ldots \tag{5.7}$$

For the extended system the dimensional wavenumber of the forcing may have any real value and it is controlled with the parameter Λ ,the parameter K may have the values ± 1 (left or right propagation). The convergence criterion for the extended system mentioned in the previous chapter, implies here that on has to verify that a result does not depend on N as $N \to \infty$ in order to be valid. The $K = 0$ (spatially uniform forcing) case is of course an exception, in this case the $\Lambda \to 0$ has to be taken. For the finite size system there are two relevant parameters for the external length scale; the system size (Λ) and the modenumber (K). For the extended system there is just one relevant parameter which is the wavelength of the forcing.

In the first section of this chapter we will discuss the phase-locked states and we will derive the shape of their region of stability in the phase diagram.

After that we will look in section 5.2 at the behaviour outside the lock-in region.

5.1 Phase-locked solutions.

With the term phase-locked solutions we will refer to solutions which are plane waves with the same wavenumber and frequency as the forcing. In other words, phase-locked solutions ϕ_L are solutions of (5.3) for which $\partial_x \phi_L = \partial_t \phi_L = 0$;

$$\phi_L(x,t) = \text{constant}. \tag{5.8}$$

Note that this is the only possible 'plane wave' solution of (5.3). Furthermore, there also does not exist any space periodic function consisting of a finite sum of plane waves with the same frequency that solves (5.3).

Recall (chapter 1) that (5.3) has unforced plane wave solutions for which

$$|\phi_L| = \sqrt{1 - K_{dim}^2}, \tag{5.9}$$

with the dispersion relation

$$\omega = -c_2 K_{dim}^2 - c_3(1 - K_{dim}^2) \tag{5.10}$$

Obviously, these solutions do not exist for $K_{dim}^2 > 1$. In the forced system however K_{dim} is not set dynamically but externally by the forcing. The question what solutions occur in the forced system for $K_{dim}^2 > 1$ is therefore all the more interesting. This is one of the things that will be addressed below. In the situation we are considering here, that is below the Benjamin-Feir instability or $1 + c_2 c_3 < 0$, the unforced plane wave solutions are always unstable. Also for $1 + c_2 c_3 > 0$ they become usually unstable well before $K_{dim}^2 = 1$ [28] (see also chapter 1). In our further discussion we wil see how the BF instability behaves in the forced system.

To obtain the linear stability criteria for the forced PW solutions we put

$$\phi(x,t) = \phi_L + \delta\phi(x,t) \tag{5.11}$$

and linearize (5.3) with respect to $\delta\phi$. We obtain

$$\left[\frac{\partial}{\partial t} - 1 + i\omega - \Lambda(1+ic_2)\left(\frac{\partial}{\partial x} + iK\right)^2 + 2(1+ic_3)|\phi_L|^2\right]\delta\phi(x,t)$$

$$+(1+ic_3)\phi_L^2\delta\phi^*(x,t) = 0, \tag{5.12}$$

where ϕ_L follows from

$$\left(i(\omega + c_2\Lambda K^2) - 1 + \Lambda K^2 + (1+ic_3)|\phi_L|^2\right)\phi_L = F_0. \tag{5.13}$$

This last equation is in effect similar to equations (3.5) and (3.6) for the forced LE. It may be rewritten as

$$\left[i\bar{\omega} \mp 1 + (1 + ic_3)|\bar{\phi}_L|^2\right] \bar{\phi}_L = \bar{F}_0, \tag{5.14}$$

where $\phi_L = \bar{\phi}_L \cdot |1 - \Lambda K^2|^{1/2}$, $F_0 = \bar{F}_0 \cdot |1 - \Lambda K^2|^{3/2}$ and $\omega = -c_2 \Lambda K^2 \pm \bar{\omega}(1 - \Lambda K^2)$ and the $+$ $(-)$ sign hold for $\Lambda K^2 < 1$ $(\Lambda K^2 > 1)$. The similarity between (5.14) and the relevant equation for the LE is more obvious. The Hopf bifurcation occurs at $\Lambda K^2 = 1$.

If one performs a stability analyses based on (5.12) and only allows for perturbations which are constant in space to develope, $\partial_x \delta\phi(x,t) = 0$, the results are identical to the results obtained in chapter 3 for the LE. The difference being of course that they are now obtained for the scaled parameters $\bar{F}_0$, $\bar{\omega}$ and $\bar{\phi}_L$. It is straight forward to show that under the same conditions for $\Lambda K^2 > 1$ the forced solutions always exist and are always stable. Also, one shows that bistable regions do not exist in that case. We will see further on that for large ΛK^2 it are infact the perturbations $\delta\phi$ with te same wavenumber as the forcing (solution) that cause the instability. In terms of the original solution Ψ, this are perturbations $\delta\Psi$ which are constant and perturbations with twice the wavenumber of the solution.

Equation (5.12) is solved by putting

$$\delta\phi = a(q)e^{iqx+p(q)t} + b(q)e^{-iqx+p^*(q)t}. \tag{5.15}$$

This gives the following two conditions for stability,

$$-1 + \Lambda(q^2 + K^2) + 2|\phi_L|^2 > 0 \tag{5.16}$$

and

$$\begin{aligned}
&-(\Lambda(q^2+K^2) - 1 + 2|\phi_L|^2)^2 \Big[(\omega + \Lambda c_2(q^2+K^2) + 2c_3|\phi_L|^2)^2 \\
&+(-1 + \Lambda(q^2+K^2) + 2|\phi_L|^2)^2 - (1+c_3^2)|\phi_L|^4 \\
&-4(1+c_2^2)\Lambda^2K^2q^2\Big] \\
&+8(-1 + \Lambda(q^2+K^2) + 2|\phi_L|^2)c_2\Lambda^2K^2q^2(\omega + c_2 + 2(c_3-c_2)|\phi_L|^2) \\
&+4\Lambda^2K^2q^2(\omega + c_2 + 2(c_3-c_2)|\phi_L|^2)^2 < 0
\end{aligned} \tag{5.17}$$

For the finite size system with periodic boundary conditions, the linear stability of a certain lock-in mode given by the integer K, is assured if (5.16) and (5.17) hold for all integer q. For the extended system the linear stability of a lock-in plane wave solution with wavenumber K_{dim} is assured if (5.16) and (5.17) hold for $K^2 = 1$ and all real q. The exception being the case of

a uniform forcing ($K = 0$), in that case (5.16) and (5.17) should hold for all real $Q = \Lambda q^2$.

The condition (5.16) can not hold if $\Lambda < 0$, neither for the extended system nor for the finite size system. In both cases we therefore need for stability

$$\Lambda > 0. \tag{5.18}$$

Condition (5.16) further implies that $2|\phi_L|^2 > 1 - \Lambda K^2$, in other words (see (5.14)) for $0 < \Lambda K^2 < 1$ we need

$$|\bar{\phi}_L|^2 > \frac{1}{2}. \tag{5.19}$$

This is similar to condition (3.8) obtained for the LE. For $\Lambda K^2 > 1$, the inequality (5.16) is trivially true for all q and ϕ_L. In what follows we confine ourselves to the case that $1 + c_2 c_3 < 0$, the case that $1 + c_2 c_3 > 0$ may however also be analyzed in a similar way. Futher we take $c_3 > 0$, which is not a real limitation since the stability conditions for solutions belonging to the parameters $\{\omega, c_3, c_2, F_0\}$ and $\{-\omega, -c_3, -c_2, F_0\}$ are identical, compare (3.14).

The condition (5.17) is a fourth order polynomal in Λ. It does not appear to be factorizable in general when $K \neq 0$. There is one non trivial situation

however for which the stability conditions may be solved analytically. This is for the extended system with a spatially uniform forcing. In this case $K = 0$ and (5.17) effectively reduces to a second order polynomal inequality in the continuous parameter $Q^2 = \Lambda q^2$;

$$\alpha Q^2 + \beta Q + \gamma > 0, \tag{5.20}$$

where

$$\alpha = 1 + c_2^2$$

$$\beta = 2((1 + c_2 c_3)|\phi_L|^2 - 1 + \omega c_2))$$

$$\gamma = (\omega + 2c_2|\phi_L|^2)^2 + (2|\phi_L|^2 - 1)^2 - (1 + c_3^2)|\phi_L|^4. \tag{5.21}$$

For stability we need $\gamma > 0$ and $\beta > 0$ or $\beta^2 < 4\alpha\gamma$. The condition $\beta > 0$ implies $|\phi_L|^2 < f(\omega)$ where

$$f(\omega) = \frac{1 - c_2\omega}{2(1 + c_2 c_3)}. \tag{5.22}$$

Obviously, in the light of condition (5.19), stability on the grounds of $\beta > 0$, $\gamma > 0$ can only occur when $f(\omega) > 1/2$, which implies $\omega < -c_3$. Stability on grounds of $\beta^2 < 4\alpha\gamma$ is possible whenever $|\phi_L|^2 > a_+^2 > 1/2$ or $1/2 < |\phi_L|^2 < a_-^2$ for $R > 0$ and whenever $1/2 < a_+^2 < |\phi_L|^2 < a_-^2$ for $R < 0$, where

$$R = 2[3(c_2^2 + c_3^2) - (1 + c_2^2 c_3^2) - 8c_2 c_3] \tag{5.23}$$

and

$$a_{\pm}^2 = \frac{-4(c_3 - c_2)(\omega + c_2) \pm 2|\omega + c_2|\sqrt{c_2^2 + c_3^2 + 1 + c_2^2 c_3^2}}{R}. \tag{5.24}$$

Finally, we have $R > 0$ for $c_2 < \tilde{c}_-$ or $c_2 > \tilde{c}_+$ if $c_3 < \sqrt{3}$ and $R > 0$ for $\tilde{c}_+ < c_2 < \tilde{c}_-$ if $c_3 > \sqrt{3}$, where

$$\tilde{c}_{\pm} = \frac{4c_3 \pm \sqrt{3}(1 + c_3^2)}{3 - c_3^2}. \tag{5.25}$$

Combining the above results with the results obtained in chapter 3, the conclusion is that the F_0-ω plane of the phase diagram obtained for the forced LE remains basically also valid for the spatially uniformly forced CGLE for extended systems as far as the lock-in region is concerned. There are of course modifications. On the basis of the parameters $\{c_2, c_3\}$ one may distinguish five different classes for the phase diagram. They are given by: (i) $c_3 > \sqrt{3}$, $-c_3 < c_2 < -1/c_3$; (ii) $c_3 > \sqrt{3}$, $\tilde{c}_+ < c_2 < -c_3$; (iii) $c_3 > \sqrt{3}$, $c_2 < \tilde{c}_+$; (iv) $1 < c_3 < \sqrt{3}$ and (v) $0 < c_3 < 1$. We will discuss the different modifications occurring for each of these classes below. The frequenties ω_0 and ω_0' used there are given by

$$\omega_0 = -c_2 - \frac{R/4}{2(c_3 - c_2) + \sqrt{c_3^2 + c_2^2 + 1 + c_2^2 c_3^2}} \tag{5.26}$$

and

$$\omega_0' = \frac{-R/4 - c_2(1+c_2c_3)[2(c_3-c_2)+\sqrt{c_2^2+c_3^2+1+c_2^2c_3^2}\,]}{(1+c_2c_3)[2(c_3-c_2)+\sqrt{c_2^2+c_3^2+1+c_2^2c_3^2}\,]-c_2R/4}. \qquad (5.27)$$

Some realistic pictures of the F_0-ω plane for each of the five classes are shown in figures 5.1 (iv,v) and 5.2 (i,ii,iii).

- Class (i). (Figure 5.2a.) The modification occurs for frequenties $\omega_0' < \omega < \omega_0$. Here stable states exist only with $|\phi_L|^2 > a_+^2$ and $1/2 < |\phi_L|^2 < A_{L-}^2$ where A_{L-} is given by (3.10). The unforced uniform state is unstable but stable uniform states are created with a little forcing at arbitrary frequenties.

- Class (ii). (Figure 5.2b.) Modification occurs at frequenties $\omega < \omega_0$. Here stable states have $|\phi_L|^2 > a_+^2$ or $1/2 < |\phi_L|^2 < A_{L-}^2$. More forcing is needed than in the previous case to create a stable lock-in state. When c_2 approaches $\tilde{c}_+$ the minimum forcing required for lock-in at resonance frequenties diverges, $F_{0,min} \to \infty$.

- Class (iii). (Figure 5.2c.) The lock-in region for the LE is modified all frequenties. Stable lock-in states exist only with $\omega < \omega_-$ where ω_- is given by (3.12), and have $1/2 < |\phi_L|^2 < A_{L-}^2$. Lock-in is not

possible for $\omega > \omega_-$, in particular, lock-in is not possible for resonance frequenties (around $-c_3$). Moreover, lock-in for $\omega < \omega_-$ is only possible for forcing strenths within a certain bounded interval.

- Class (iv). (Figure 5.1a.) Modification occurs for $\omega_0' < \omega < \omega_0$. The stable lock-in states have $|\phi_L|^2 > a_+^2$ or $1/2 < |\phi_L|^2 < A_{L-}^2$. The bistable region is cut (reduced in size) and is cut heavily as c_2 increases. Lock-in around resonance becomes possible with little forcing if c_2 is small. The minimum forcing required for lock-in around resonance increases when c_2 increases but does not diverge for finite c_2.

- Class (v). (Figure 5.1b.) As the previous case but with this difference that the bistable region is not cut. Lock-in states around resonance remain possible with little forcing, even as $c_2 \to -\infty$.

This concludes our discussion of the lock-in region for extended system with a spatially uniform forcing. When the system is of finite size, things become even for a spatially uniform forcing much more complicated. The reason for this is that, although the stability conditions are still second order polynomals in Λ, one now besides the results just obtained also has to verify if a certain perturbation that is causing the instability is indeed possible in

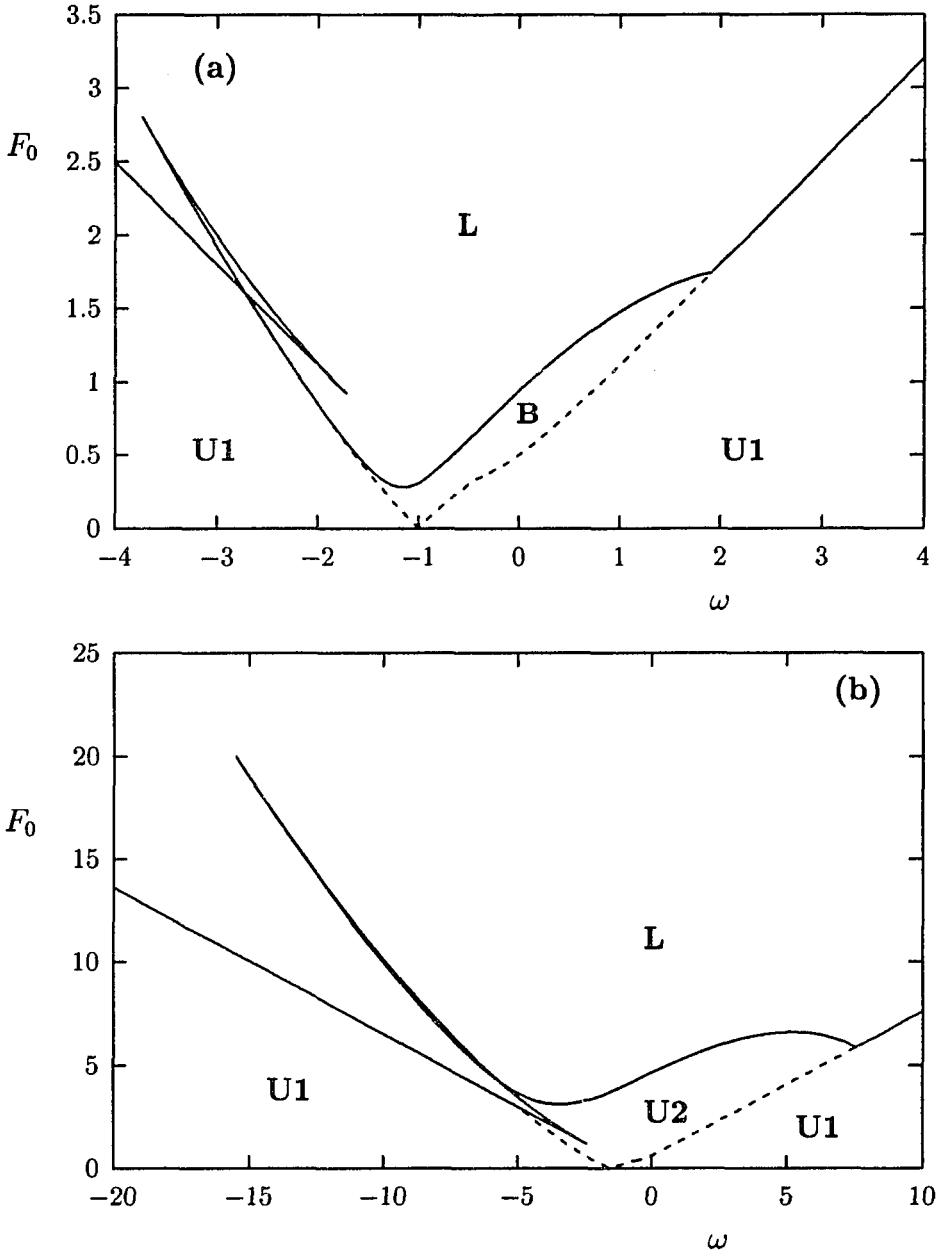

Figure 5.1a-b

Figure 5.1: The F_0-ω plane of the phase diagram for extended systems with $K = 0$ for systems of classes (iv) (panel b) and (v) (panel a). The parameters are (a) $c_2 = -4$, $c_3 = 1$ and (b) $c_2 = -10$, $c_3 = 1.5$.

Figure 5.2: (Next page) The F_0-ω plane of the phase diagram for extended systems with $K = 0$ for systems in the classes (i), (ii) and (iii), respectively shown in panels a-c. The parameters are (a) $c_2 = -1.9$, $c_3 = 2$; (b) $c_2 = -4$, $c_3 = 2$; and (c) $c_2 = -20$, $c_3 = 2$. In panel (d) the frequenties $\tilde{c}_\pm$ are shown as function of c_3.

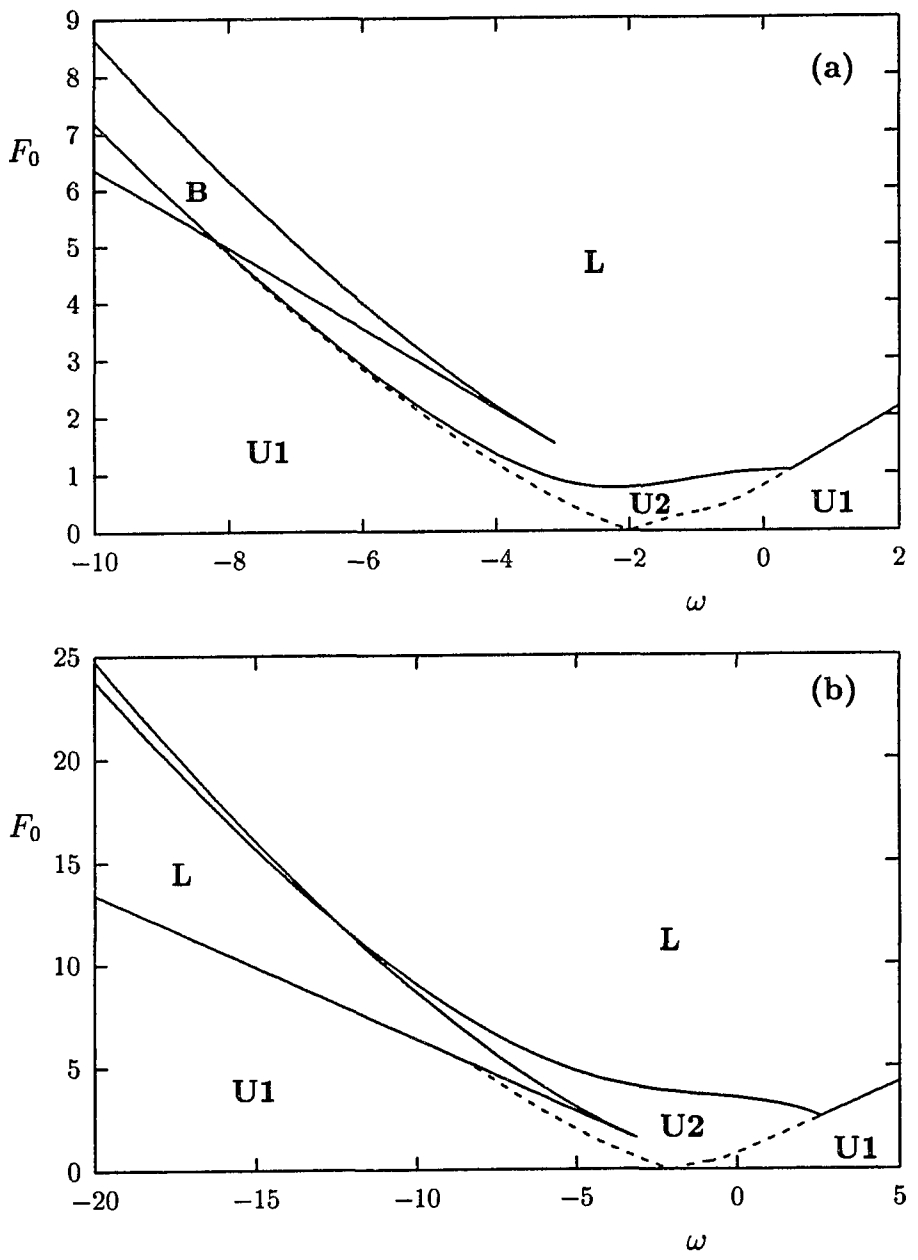

Figure 5.2a-b

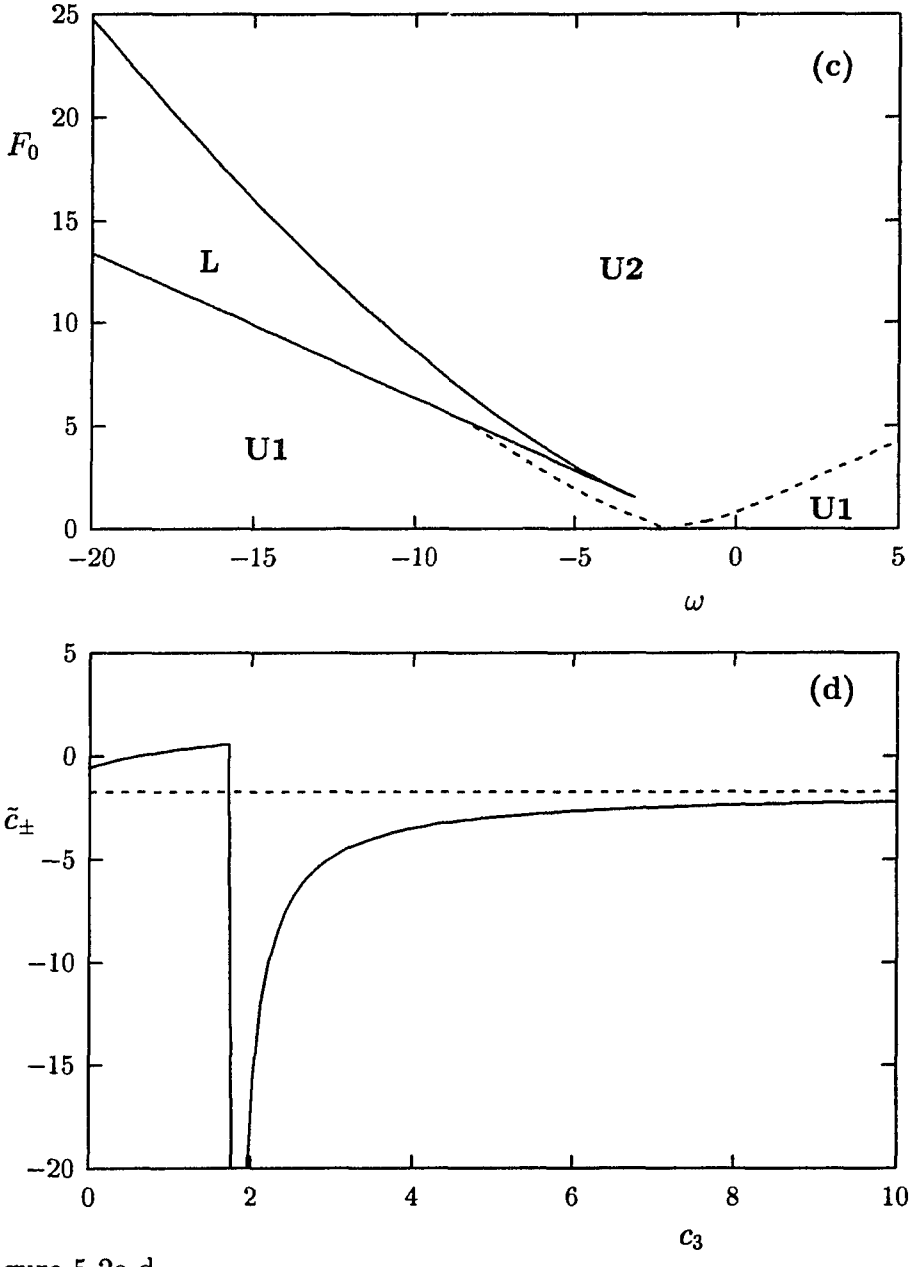
(c)
F_0
25
20
15
10
5
0
L
U2
U1
U1
−20
−15
−10
−5
0
5
ω
(d)
$\tilde{c}_\pm$
5
0
−5
−10
−15
−20
0
2
4
6
8
10
c_3

Figure 5.2c-d

a finite size system. This is expresed in the fact that the stability conditions need only hold for integer q. It is obvious that in the regions marked **U1** in figures 5.1 and 5.2 that systems lengths exist for which the unstable perturbations are not possible, resulting in stable lock-in states in these regions. In region **U2** this is impossible because of the violation of (5.19) by a $q = 0$ perturbation. Here therefore spatially uniform states will be unstable for all system lengths. Some pictures of the shape of the lock-in region in the F_0-Λ plane of the phase diagram are shown in figure 5.3. The edge of the lock-in region consists for all cases except (iii) of an infinite series of wedges, starting at around $\Lambda = 1$ and decreasing in size as $\Lambda \to 0$. For case (iii) the wedges are of infinite size and become sharper as $\Lambda \to 0$. The small amplitude states present in the bistable region remian stable for all values of Λ and create bistable regions also in the F_0-Λ plane. Finally, one makes a not too surprising but important observation from figure 5.3, which is also provable analytically. This is that for large Λ (small systems) one recovers the lock-in region of the forced LE. To prove this, we deduce from (5.20) that the dangerous perturbation for large Λ is the $q = 0$ perturbation. For that perturbation however (5.20) reduces precisely to the inequality (3.9), which together with $|\phi_L|^2 > 1/2$ determined the lock-in region of the LE, which

proves our observation. From figure 5.3 we see that "large" Λ infact means $\Lambda \sim 1-2$ for all cases except (iii) where the the lock-in region of the LE will only be recovered in the limit $\Lambda \to \infty$.

For the $K \neq 0$ cases the lock-in region in the F_0-Λ plane were obtained with some numerical help. The roots of (5.18) were obtained using a standard algorithm. After this the lock-in region was constructed using (5.19) and (5.14). A few analytic results may be derived which are helpful in this construction. First, one observes that the relations used to construct the lock-in region become independent of K as $\Lambda \to 0$. This means that the results for $K = 0$ have to be recovered for $K \neq 0$ in the limit of small Λ. Second, for large ΛK^2 the instability is caused by perturbations with wavenumber $q^2 = K^2$, for which the coefficient of Λ^4 vanishes. The stability in that case is determined by the coefficient of Λ^3 which for $q^2 = K^2$ reduces to $-16K^6(1 + c_2^2)(-1 + 2|\phi_L|^2)$. Hence the only stability criterion for large ΛK^2 simply becomes

$$|\phi_L|^2 > \frac{1}{2}. \tag{5.28}$$

Recall that the condition (5.16) is trivially satisfied when $\Lambda K^2 > 1$, so that the result (5.28) is not something already implied by (5.16). Furthermore,

Figure 5.3: (Next page) Some typical lock-in regions in the F_0-Λ plane for finite size systems with $K = 0$. The parameters are (a) $c_2 = -4$, $c_3 = 2$, $\omega = -2$; (b) $c_2 = -4$, $c_3 = 2$, $\omega = +2$; (c) $c_2 = -4$, $c_3 = 2$, $\omega = -7$; and (d) $c_2 = -20$, $c_3 = 2$, $\omega = 0$.

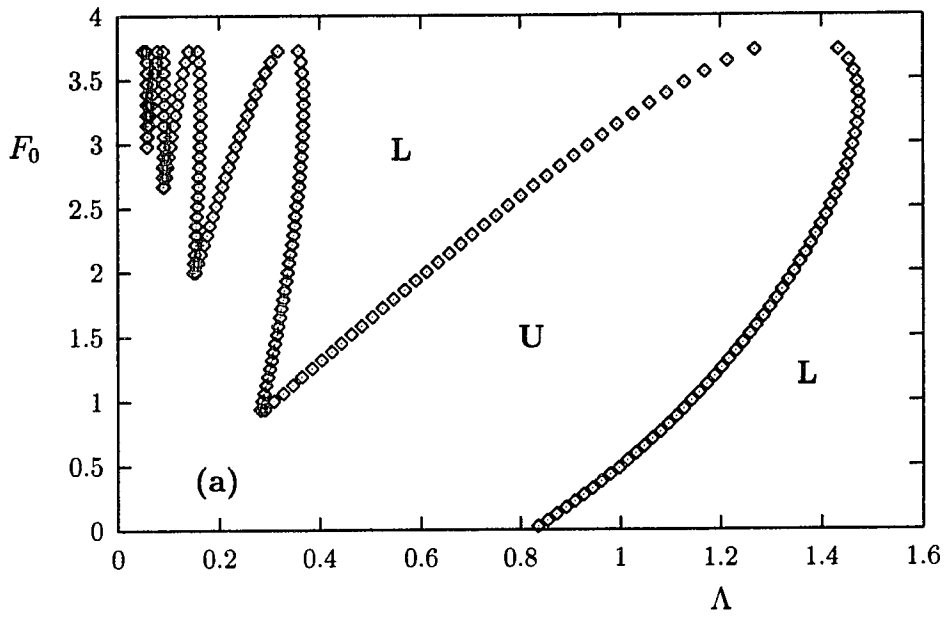
F_0
4
3.5
3
2.5
2
1.5
1
0.5
0
L
U
L
(a)
0
0.2
0.4
0.6
0.8
1
1.2
1.4
1.6
Λ

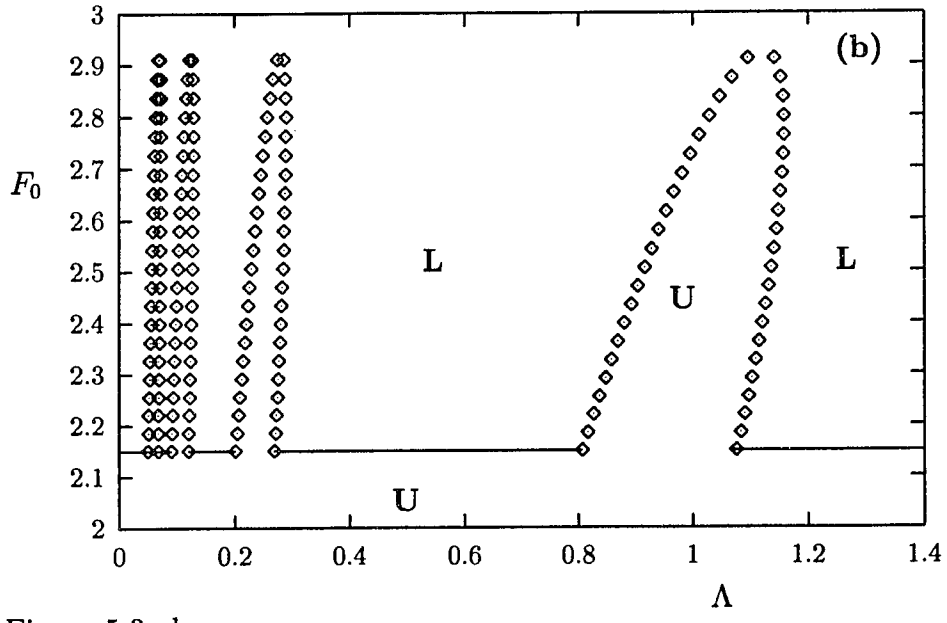
F_0
3
2.9
2.8
2.7
2.6
2.5
2.4
2.3
2.2
2.1
2
(b)
L
U
L
U
0
0.2
0.4
0.6
0.8
1
1.2
1.4
Λ

Figure 5.3a-b

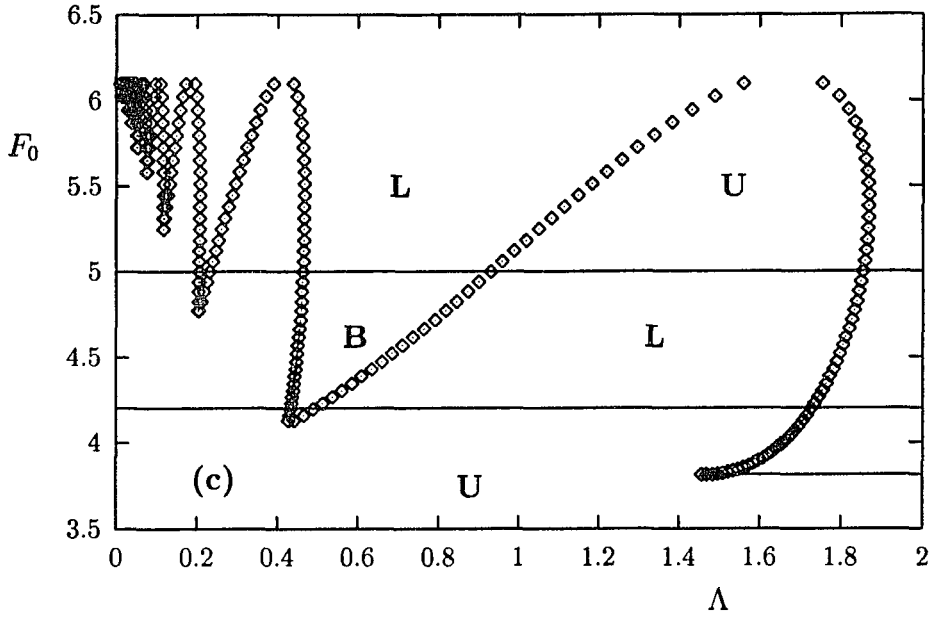
6.5
6
5.5
5
4.5
4
3.5
F_0
L
U
B
L
(c)
U
0
0.2
0.4
0.6
0.8
1
1.2
1.4
1.6
1.8
2
Λ

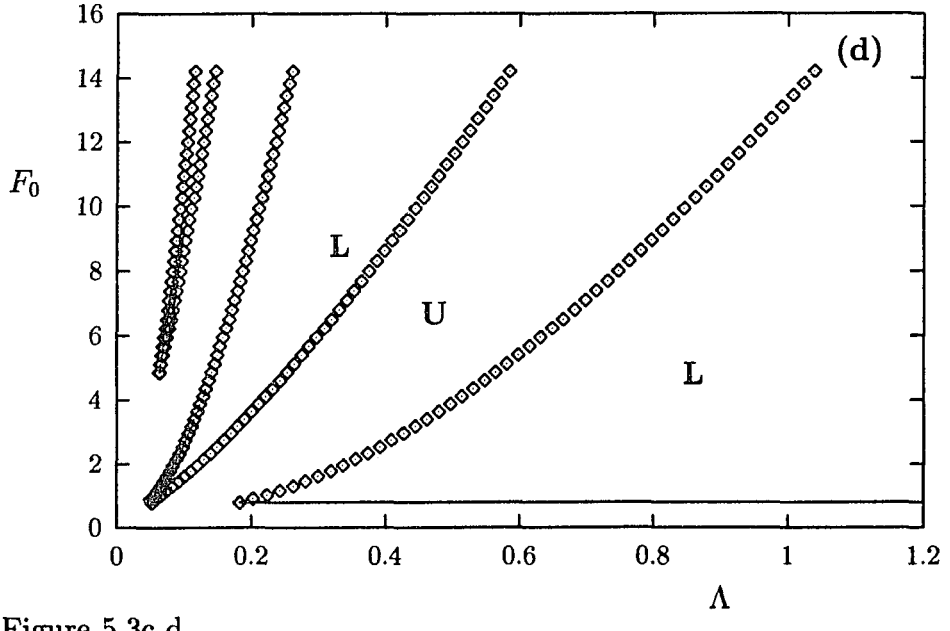
16
14
12
10
8
6
4
2
0
F_0
(d)
L
U
L
0
0.2
0.4
0.6
0.8
1
1.2
Λ

Figure 5.3c-d

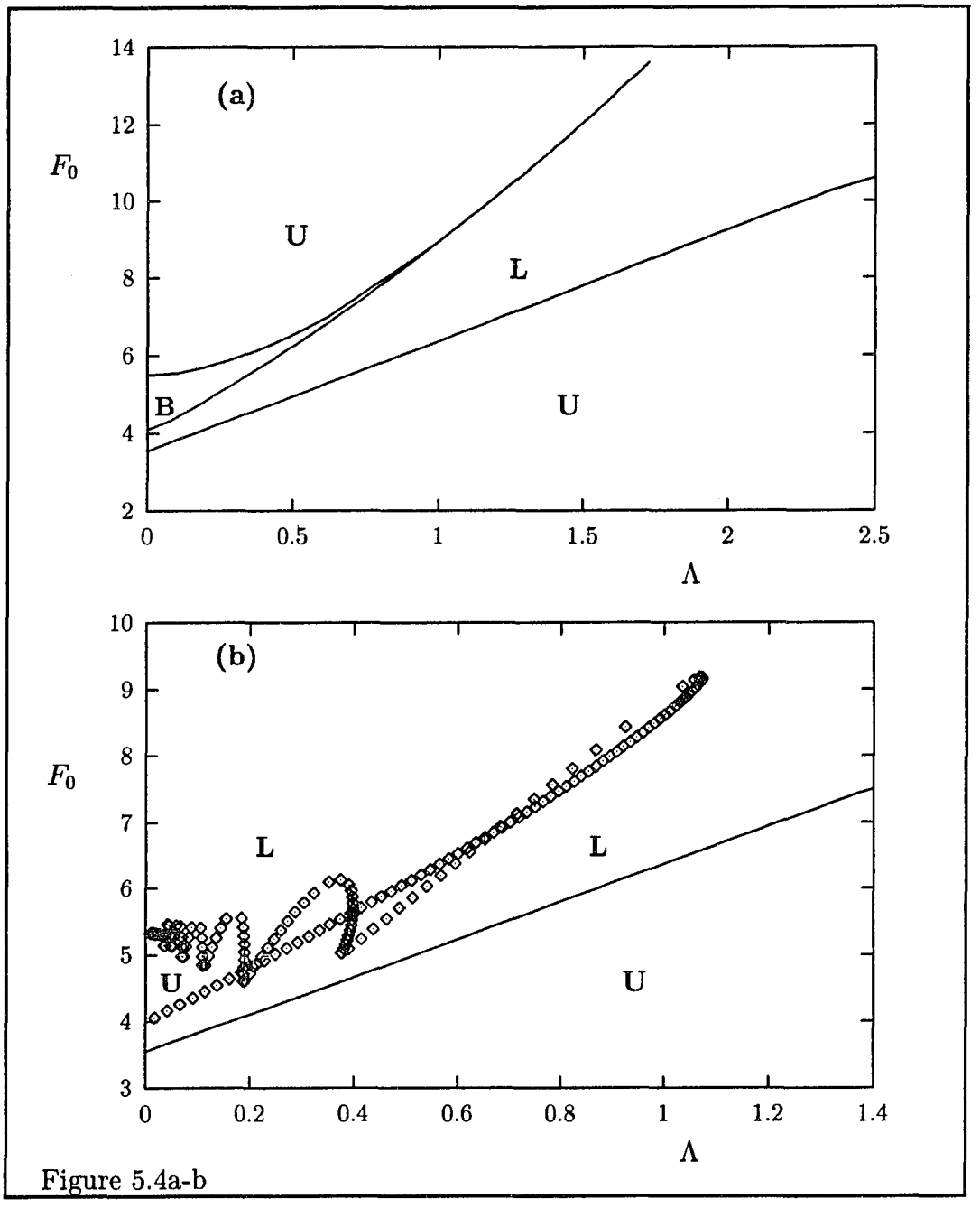

Figure 5.4a-b

Figure 5.4: The lock-in region in the F_0-Λ plane for $c_2 = -4$, $c_3 = 2$ and $\omega = -6$ for (a) the extended system and (b) (c) (d) the finite size system for the $K = 1$, $K = 2$ and $K = 3$ modes respectively.

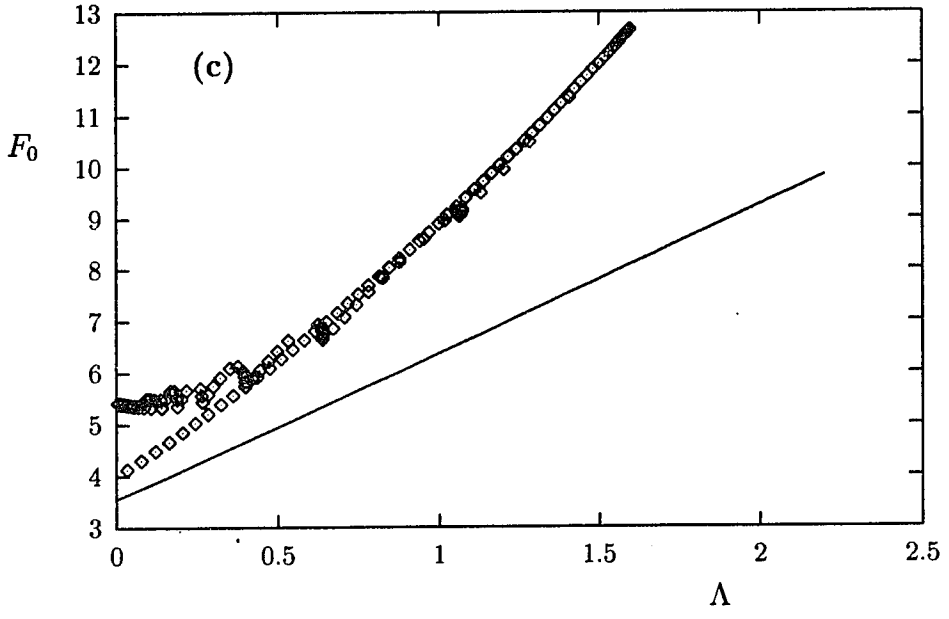
(c)
F_0
13
12
11
10
9
8
7
6
5
4
3
0
0.5
1
1.5
2
2.5
Λ

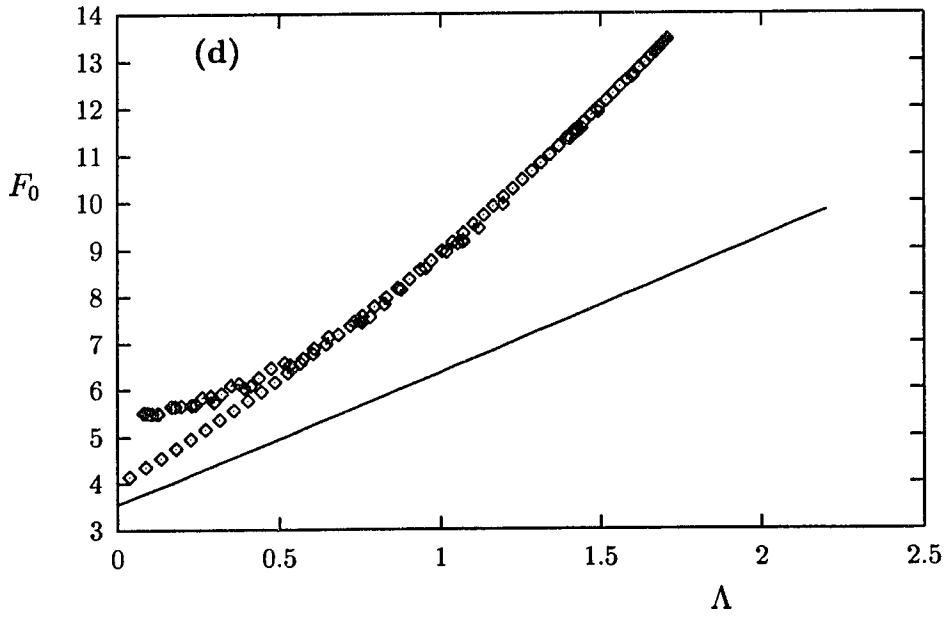
(d)
F_0
14
13
12
11
10
9
8
7
6
5
4
3
0
0.5
1
1.5
2
2.5
Λ

Figure 5.4c-d

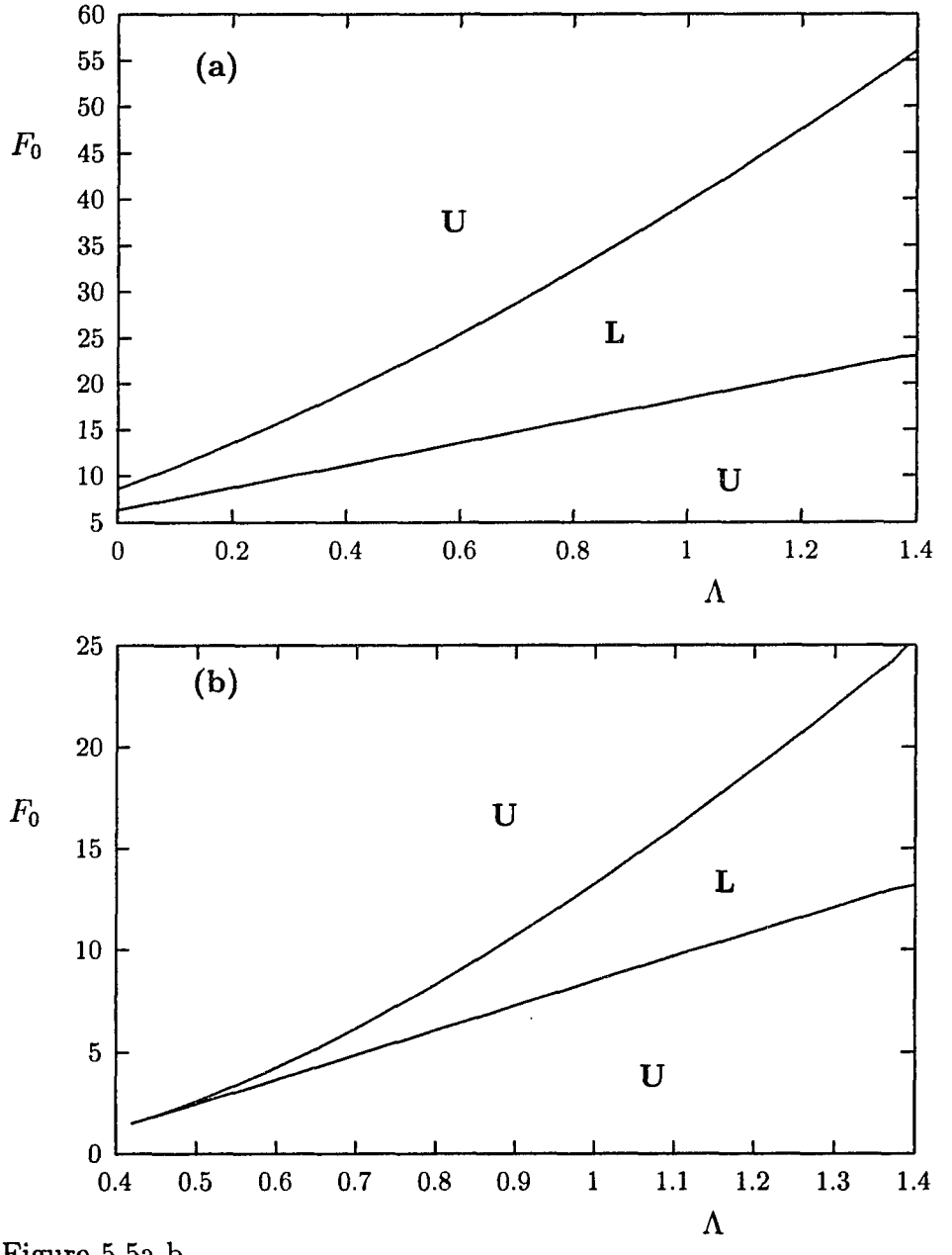

Figure 5.5a-b

Figure 5.5: The lock-in region in the F_0-Λ plane for $c_2 = -20$, $c_3 = 2$ in the extended system for $\omega = -10$ (a), $\omega = +4$ (b) and in the finite size system for the $K = 1$ mode for $\omega = -10$ (c) and $\omega = +4$ (d).

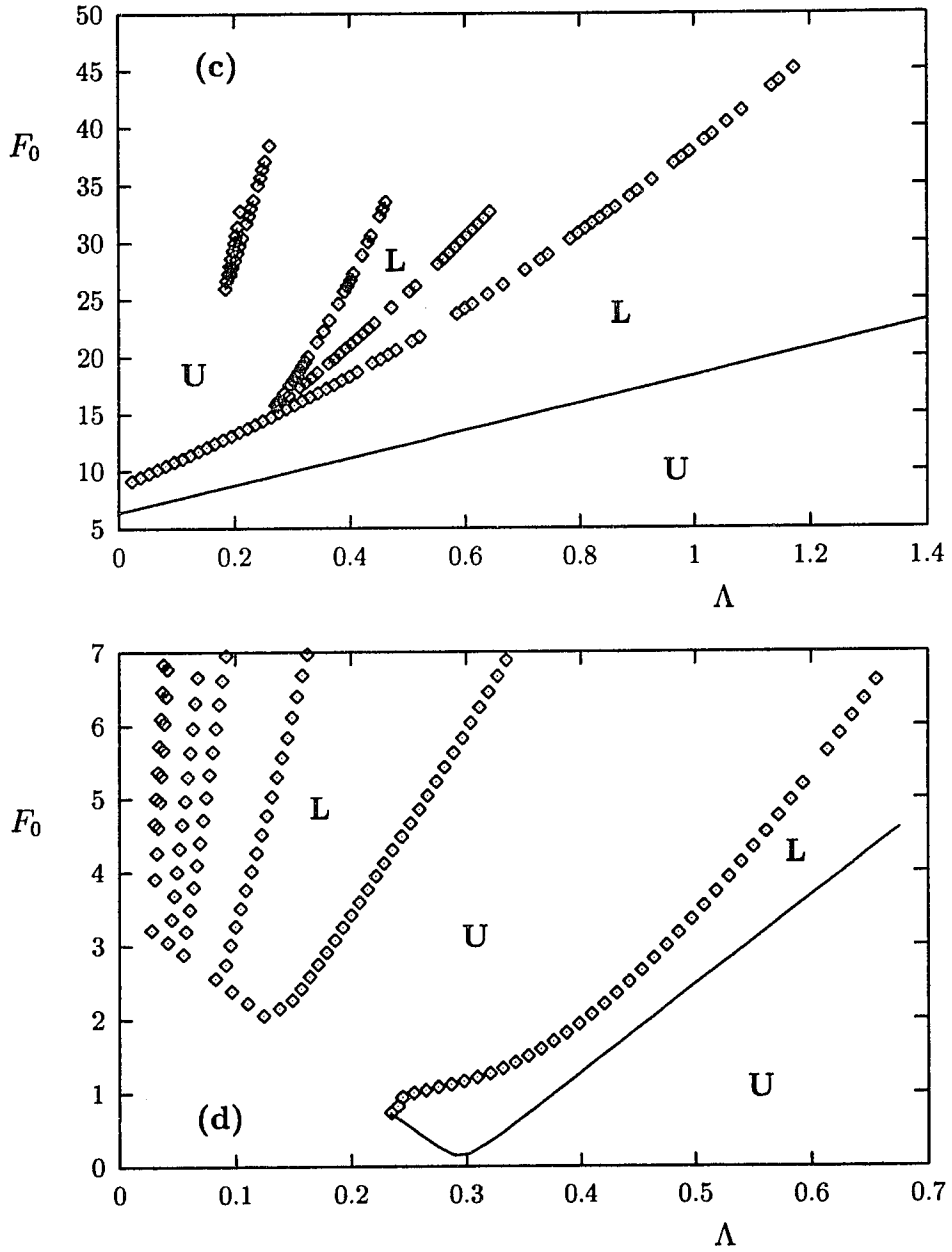
(c)
F_0
50
45
40
35
30
25
20
15
10
5
0
0.2
0.4
0.6
0.8
1
1.2
1.4
Λ
L
L
U
U
(d)
F_0
7
6
5
4
3
2
1
0
0
0.1
0.2
0.3
0.4
0.5
0.6
0.7
Λ
L
L
U
U

Figure 5.5c-d

Figure 5.6: (Next page) The lock-in region in the F_0-Λ plane for the $K = 1$ mode in a finite size system with $c_2 = -4$, $c_3 = 1$ and $\omega = -1$ (a), $\omega = -2.3$ (b) and for the extended system with the same parameters c_2 and c_3 and $\omega = -1$ (c), $\omega = -2.3$ (d) and $\omega = 3$ (e).

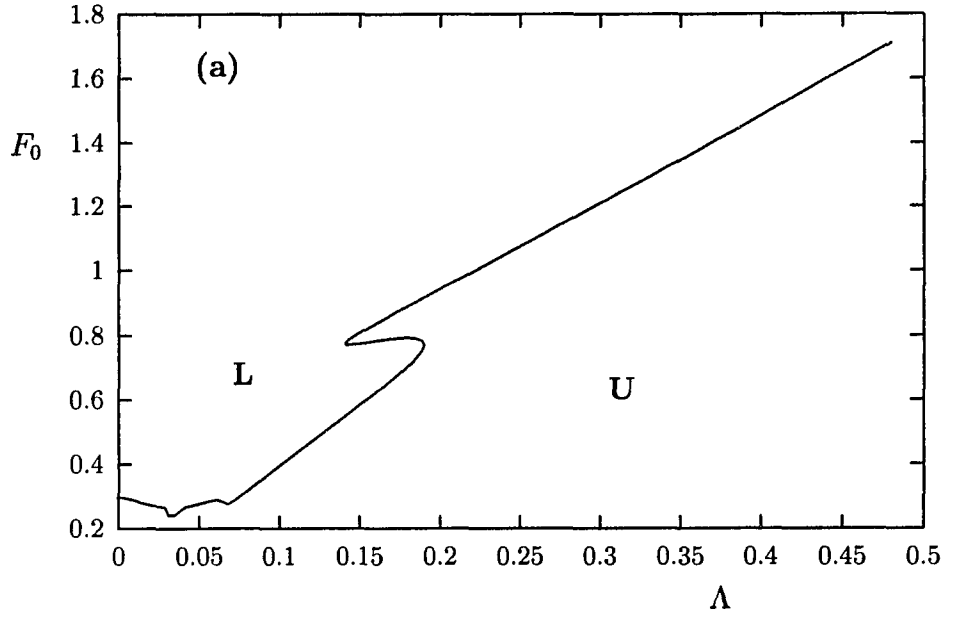
(a)
F_0
1.8
1.6
1.4
1.2
1
0.8
0.6
0.4
0.2
L
U
0
0.05
0.1
0.15
0.2
0.25
0.3
0.35
0.4
0.45
0.5
Λ

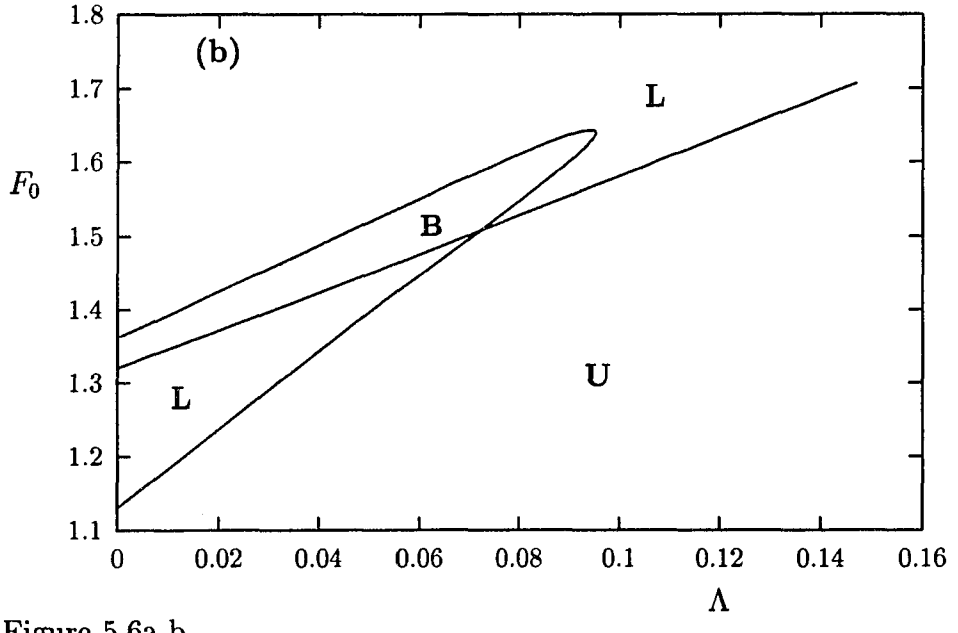
(b)
F_0
1.8
1.7
1.6
1.5
1.4
1.3
1.2
1.1
L
B
L
U
0
0.02
0.04
0.06
0.08
0.1
0.12
0.14
0.16
Λ

Figure 5.6a-b

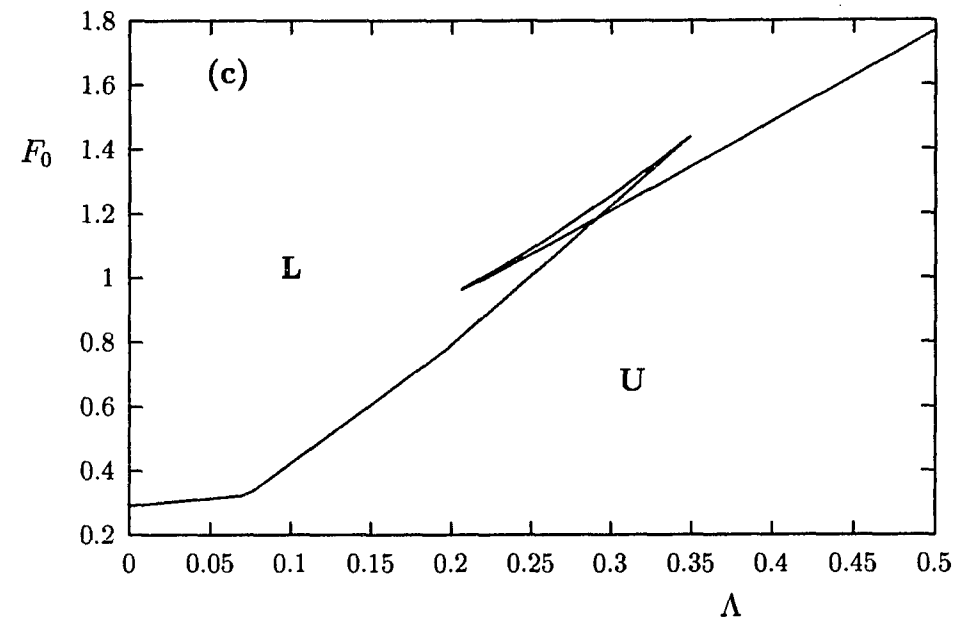

Figure 5.6c-d

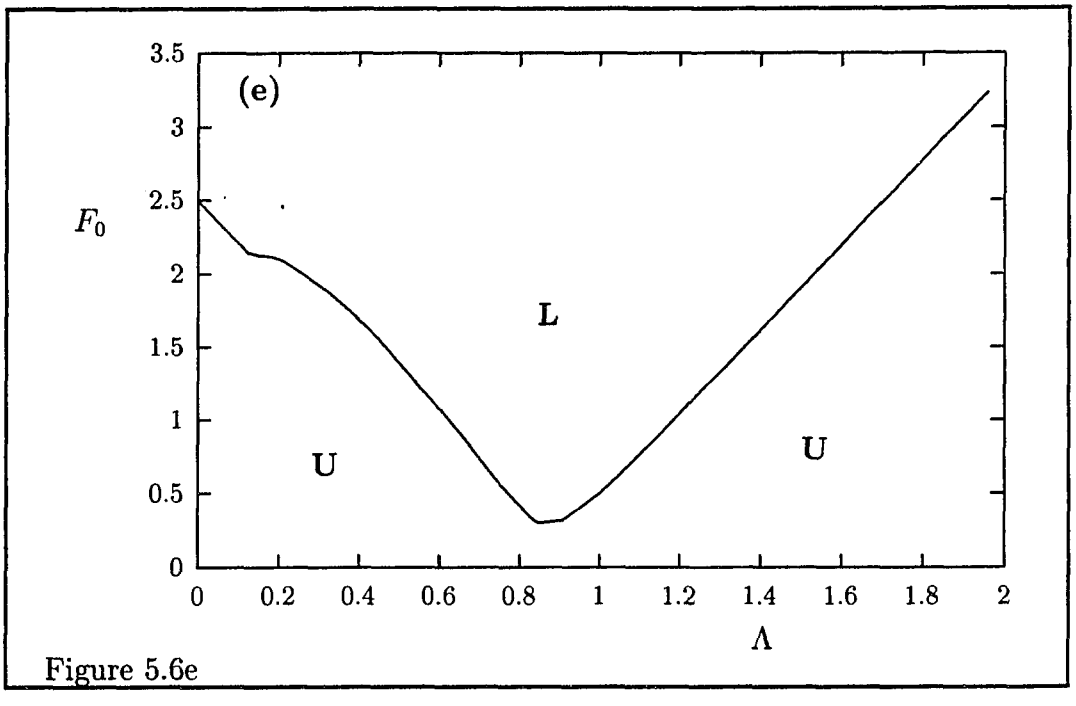

Figure 5.6e

note also that (5.28) differs from condition (5.19) present or $\Lambda K^2 < 1$ in the sense that (5.28) puts a condition on $|\phi_L|$ rather than on $|\bar{\phi}_L|$.

Some representative pictures of the lock-in regions are shown in figures 5.4 to 5.6. The first observation one makes is that the wedges present for small Λ in the finite size system case, gradually disappear as the wavenumber K increases. The wedges are not present for the extended system. One finds that the results for a finite size system rapidly aproach that of the extended system (same forcing wavelength) as the modenumber increases. For $K \geq 5$ there is usually already no visible difference anymore.

We observe from figure 5.6e that resonance also occurs as the wavenumber of the forcing is varied, similar to frequency resonance. One expects this to occur at Λ values compatible with the unforced dispersion relation,

$$\Lambda_{res} = \frac{\omega + c_3}{K^2(c_3 - c_2)}. \tag{5.29}$$

Figure 5.6e is in good agreement with this, and also in general one finds good agreement. Note that (5.29) also explains that resonance is not observed for $\omega < c_3$ if $1 + c_2 c_3 < 0$. However, (5.29) only makes sense if $\omega < -c_2$, since unforced plane wave solutions do not exist if $\Lambda K^2 > 1$. It therefore does not completely explain resonance occurring for $\Lambda > K^{-2}$ ($\Lambda > 1$ in the extended

system) which one actually does observe for certain parameter choices.

In figure 5.5 the lock-in region is shown for a system from the most unstable class, class (iii). Note that all the wedges have disappeared in the extended system except the most right one, in which infact also still some resonance is observable. Further we observe that although spatially uniform states are impossible for $\omega > \omega_-$ in the extended system, forced plane wave states of sufficiently small wavelength become possible for sufficiently large forcing. The forcing also has an upper bound. The situation is a litlle better for $\omega < \omega_-$: does the forcing still have an upper and lower bound, lock-in plane wave solutions are now possible with all wavelengths.

The lock-in region for a system of class (v) is shown in figure 5.6. Comparing the reults for the extended system with the lock-in region in the F_0-ω-$\Lambda = 0$ plane, we discover that the bistable region in the complete three dimensional parameter space infact has the shape of a ring segment, more or less centered around the $\omega = -c_3$, $\Lambda = 0$ axis.

From the results presented we see that the BF instability in extended systems has basically the same nature in forced systems as in unforced systems, in the sense that stable plane waves exist only with wavenumbers $K^2_{dim} < K^2_{max}$. For systems of class (iii) the situation is a little more com-

plicated. Here there is also a maximum wavelength with which plane waves (forced) can exist, $K^2_{min} < K^2_{dim} < K^2_{max}$

We also see that the classifications made as function of the parameters c_2 and c_3 for the case that $K = 0$ is quite effective in general. By looking at the lock-in region in the F_0-Λ plane for a few values of ω, and comparing this with the $\Lambda = 0$ result, one obtains a reasonable picture of the full shape of the lock-in region in the $\{F_0, \omega, \Lambda\}$ parameter space. This shape is qualitatively the same within each class.

Some differences between the classes infact disappear as Λ is increased. For large Λ one may effectively reduce the number of classes again to three as for the $\Lambda = 0$ situation. Unlike the $K = 0$ case, where one recovers the lock-in region of the LE for large Λ, this is not so for the $K \neq 0$ case. The classification is infact quite different from that of the LE. The first catagory of systems appearing for large Λ is the ones for which $c_3 > \sqrt{3}$, $\tilde{c}_+ < c_2 < -1/c_3$. The lock-in region in the F_0-ω plane is bounded by the line $F_0(\omega, |\phi|^2 = 1/2)$. A bistable region is present for negative ω. Large Λ here infact means $\Lambda \sim 1 - 2$. The second catagory of systems is the ones for which $c_3 > \sqrt{3}$, $c_2 < \tilde{c}_+$. Here the lock-in region region in the F_0-ω plane is bouded by the line $F_0(\omega, |\phi|^2 = 1/2)$ from below. No stable regions are

present. There is however for any finite Λ also an upper bound which only disappears in the limit $\Lambda \to \infty$ for $\omega < \omega_-$ and which eliminates the lock-in region for $\omega > \omega_-$ in that limit. The third class of systems are systems with $c_3 < \sqrt{3}$. Here at large Λ the lock-in region in the F_0-ω plane is simply bounded by the line $F_0(\omega, |\phi|^2 = 1/2)$ for all frequenties. No bistable region appears. For any c_2, large Λ infact means $\Lambda \sim 1 - 2$.

An important unexpected observation we make is that the difference as far as the lock-in region is concerned, between the finite size and the extended system is eliminated as Λ becomes larger, that is, as the system length of the finite size system becomes shorter! The explaination of this is that it is the $q = K$ perturbation that causes the instability at large Λ, and this perturbation is of of course always allowed in the finite size system.

Finally, we have seen a little earlier that in the hypothetical case in which one only allows $q = 0$ perturbations ($K \neq 0$), the system shows a Hopf bifurcation at $\Lambda K^2 = 1$. For $\Lambda K^2 > 1$ phase locked states are always stable, no bistable regions occur. For $\Lambda K^2 < 1$ the lock-in region of the LE is recovered, all be it in the rescaled parameters $\bar{F}_0$ and $\bar{\omega}$ which are themselves functions of Λ. Although our results show that a bifurcation of this kind does (as expected) not occur if one allows perturbations with $q \neq 0$, it's presence

does however explain the fact that we observe the transition to "large Λ" behaviour in systems of catagories (i), (ii), (iv) and (v) at Λ values around 1.

This concludes our discussion of the lock-in behaviour. In the next section we will look at the behaviour outside the lock-in region.

5.2 Not phase-locked solutions.

In this section we will discuss solutions of the CGLE with a plane wave forcing for parameter values F_0, ω and Λ outside the lock-in region. We will again rely solely on results obtained by numerical integration of the equation. The linear stability analyses for the phase locked states is of course still of use to explain certain properties of a solution, especially when we are close to the lock-in region.

For the integration of the equation a Split Step Fourier method was used []. In this method one splits up the equation in two parts, each of which can be integrated analytically. In each time step both integrals are computed, using the result of one as input for the other. This method was shown in [] to give good and fast results for the nonlinear Schrödinger equation. It also

works also well for the CGLE with constant coefficients. For further details see appendix C.4.

The results we will discuss are for the extended system, we will not consider the finite size system in this section. It is interesting to look at an example of "correct behaviour" as we take the limit for infinite system size ($L \to \infty$). Let us consider the situation that the solution is chaotic in time and disordered in space (spatio-temporal chaos), as is the case for the unforced solutions ($1 + c_2 c_3 < 0$). For large enough systems, the boundary conditions are not expected to be of influence on the solutions, in particular also not on the characteristic length scale(s) present in a solution. Therefore if one computes the quantity

$$<< \phi(x,t) >>=< \frac{1}{L} \int_0^L dx \phi(x,t) >, \tag{5.30}$$

where $< \cdot >$ denotes the time average (4.31), one expects that $<< \phi >>$ will become independent of the system size for large enough L. We may write

$$<< \phi >>= \sum_n < |\hat{\phi}_L(k_n,t)|^2 >, \tag{5.31}$$

where $k_n = \frac{2\pi}{L} \cdot n$. Suppose now that we increase the system size with a factor two, $L' = 2L$. Then for large enough L one should have $< |\hat{\phi}_L(k_n,t)|^2 > \approx <$ $|\hat{\phi}_{L'}(2k_n,t)|^2 >$. The sum in (5.34) therefore has twice as many significant

terms when $L' = 2L$. Since the result has to be independent of L one deduces that $< |\hat{\phi}_L(k_n, t)|^2 >$ necessarily scales as $\Lambda^{1/2}$ as $L \to \infty$. A comparision of the spectra $\mathcal{S}(k) = < |\hat{\phi}(k, t)|^2 > \Lambda^{-1/2}$ for two actual unforced solutions for $c_2 = -2.5$, $c_3 = 2$ (amplitude chaos) and for $c_2 = -2.5$, $c_3 = 0.77$ (phase chaos) is shown in figure 5.7. We see that the infinite system limit is reached properly in both cases.

From figure 5.7 we further see that for the case of amplitude chaos the spectra are nearly flat for small k. For larger k values there is exponential decay. The behaviour for small k is typical for spatially disordered solutions with a finite correlation length much smaller then the system size, and it is explained as follows [9]. The Fourier components

$$\hat{\phi}(k, t) = \frac{1}{L} \int_0^L dx \; \phi(x, t) e^{-ikx} \tag{5.32}$$

for small k may be evaluated by deviding the integration interval L into small subintervals much smaller than L but still much larger than the correlation length. The exponential factor may be assumed to be piecewise constant on each interval. A Fourier component thus represent for each t a random walk in the complex plane and from the central limit theorem it then follows that the distribution function of $\hat{\phi}(k)$ will be Gaussian and essentially the same

Figure 5.7: (Next page) The scaled Fourier spectra $\mathcal{S}(k) = < |\hat{\phi}(k,t)|^2 > \cdot\Lambda^{-1/2}$ for a state of amplitude chaos $c_2 = -2.5$, $c_3 = 2$ (a) and for state of phase chaos $c_2 = -2.5$, $c_3 = 0.77$ (b). The number of Fourier components is 102 (solid curve) and 2048 (dashed curve). The cut-off parameters were $\Lambda = 5 \cdot 10^{-4}$ and $\Lambda = 1.25 \cdot 10^{-4}$ (a), and $\Lambda = 2 \cdot 10^{-4}$ and $\Lambda = 5 \cdot 10^{-5}$ (b).

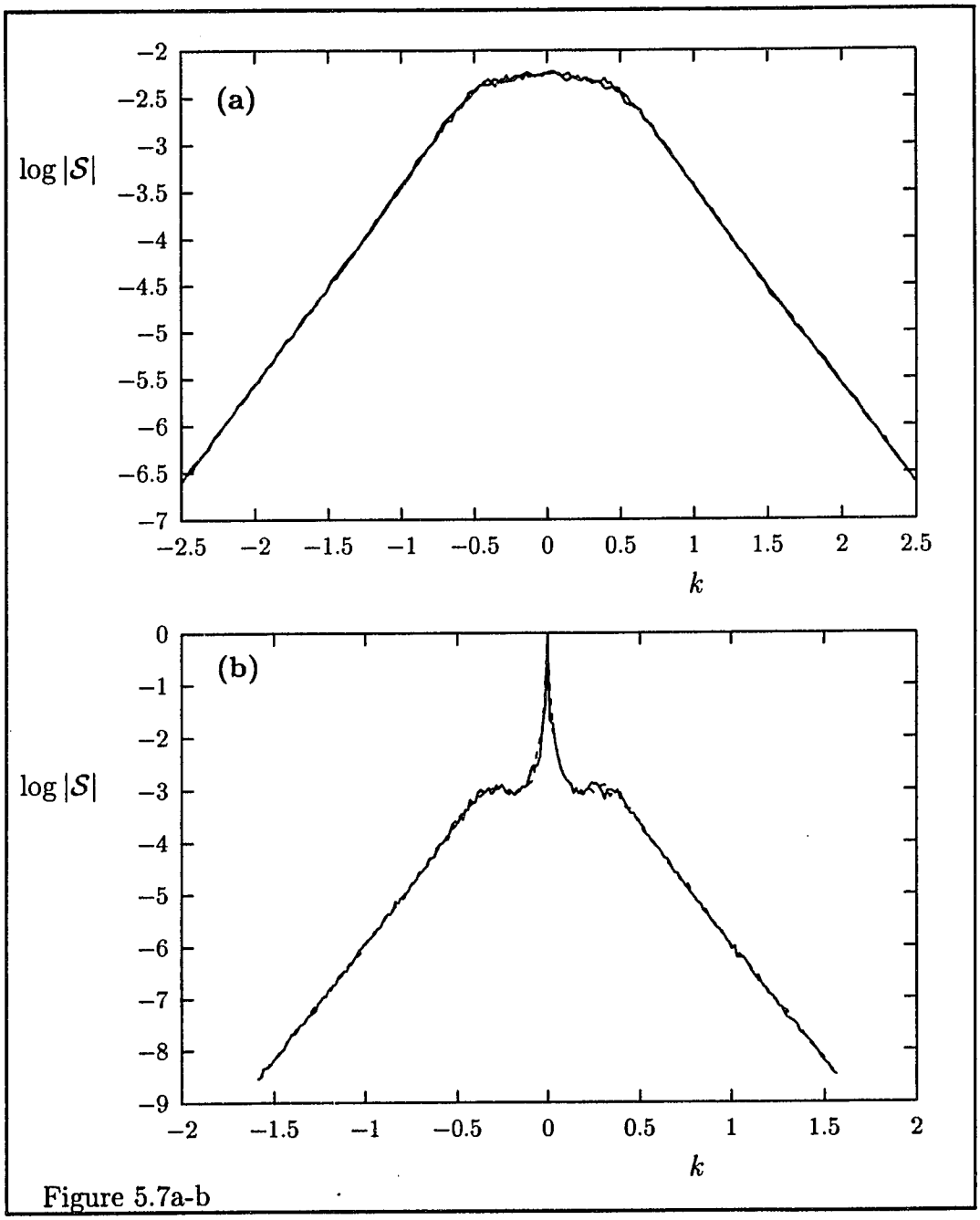
(a)
log |S|
−2
−2.5
−3
−3.5
−4
−4.5
−5
−5.5
−6
−6.5
−7
−2.5 −2 −1.5 −1 −0.5 0 0.5 1 1.5 2 2.5
k
(b)
log |S|
0
−1
−2
−3
−4
−5
−6
−7
−8
−9
−2 −1.5 −1 −0.5 0 0.5 1 1.5 2
k

Figure 5.7a-b

for all k (small k).

The above reasoning breaks down when the solutions display phase chaos, as can also be seen from figure 5.7b. The reason is that the spatial (as well as temporal) correlations are believed to decay less than exponentially in such a solution so that a correlation length does not exist (is infinite). In the results for the forced system we will encounter many other examples for which the ideal situation (amplitude chaos) as discussed above does not apply, we will see other deviations from the simple flat behaviour of $< |\hat{\phi}(k,t)|^2 >$ for small k.

For the analyses of the not phase locked solutions, quantities such as the spatial Fourier components, temporal power spectra, appearence and distribution of defects are evaluated. Information about the spatial and temporal correlations is obtained from computation of the correlation functions $\mathcal{D}(x,x')$ and $\mathcal{C}(t,t')$,

$$\begin{aligned} \mathcal{D}(x,x') &= \mathcal{G}(x,t,x',t), \\ \mathcal{C}(t,t') &= \mathcal{G}(x,t,x,t'), \end{aligned} \tag{5.33}$$

where

$$\mathcal{G}(x,t,x',t') =< \phi^*(x',t')\phi(x,t) > - < \phi^*(x',t') >< \phi(x,t) > . \tag{5.34}$$

This correlation function of course vanish for the phase locked states for

which $\partial_x \phi(x,t) = \partial_t \phi(x,t) = 0$. This somewhat unnatural property does not lead to complications here because of the uniformity of the system, that is, the local lock-in behaviour as observed in the previous chapter does not occur here.

Different definitions of correlation functions are used by different people. Let us therefore discuss some properties of the ones used here with care. Suppose that $\phi(x,t)$ is a regular solution in the sense that is does not show chaos nor disorder. Let $\mathcal{T}_z$ denote a translation in space with a displacement z, then it is of course so that $\mathcal{T}_z \phi(x,t) = \phi(x-z,t)$ is also a solution since the equation is invariant under translations. The solution $\mathcal{T}_z \phi(x,t)$ is obtained by starting with different initial conditions, different from the ones that resulted in $\phi(x,t)$. In the light of this observation we have, when $\{\cdot\}$ denotes the average over initial conditions,

$$\mathcal{T}_{x'}\{\phi^*(x',t')\phi(x,t)\} = \{\phi^*(0,t')\phi(x-x',t)\}. \tag{5.35}$$

If one now believes that in case the solution shows chaotic behaviour in time, the average over initial conditions is identical to the average over time (ergodicity), one has the following property

$$< \phi^*(x',t')\phi(x,t) > = < \phi^*(0,t')\phi(x-x',t) > . \tag{5.36}$$

Since this is now an average over time one may manipulate the time variable in the same way to obtain

$$< \phi^*(x',t')\phi(x,t) > = < \phi^*(0,0)\phi(x-x',t-t') > . \qquad (5.37)$$

The only assumption to arrive at this result has been ergodicity. This seems to be quite reasonable because in actual results obtained by numerical integration one indeed observes the validity of (5.37).

Using property (5.37) we obtain for the Fourier transform of the spatial correlation function

$$\hat{\mathcal{D}}(k) =< \hat{\phi}^*(k,t)\hat{\phi}(k,t) > - < \hat{\phi}^*(k,t) >< \hat{\phi}(k,t) > . \qquad (5.38)$$

This expression is useful since it provides a faster more efficient way to compute the spatial correlation function numerically. In figure 5.8 the results are shown for $\hat{\mathcal{D}}(k)$ obtained from computation of (5.33) and Fourier transformation, and obtained from direct computation of (5.38). Although the averaging time for the first result was 10 times as large as for the second, the first result itself is still much worse. This is understood if one realizes that when taking the Fourier transform before averaging, one implicitely uses the translational invariance of the system and in effect increases the averaging time by a factor equal to the number of Fourier components. In the example

shown the number of Fourier components used was 1024. The same situation occurs in the computation of the temporal correlation function since

$$\mathcal{C}(t-t') = \sum_k \hat{\mathcal{G}}(k, t-t'). \tag{5.39}$$

Finally, in view of the correlation functions used here and there the following observation is important. The Fourier components of

$$\begin{aligned} \mathcal{G}'(x-x', t-t') = &<< (\phi^*(x',t') - << \phi^*(x',t') >>) \\ &\cdot(\phi(x,t) - << \phi(x,t) >>) >> \end{aligned} \tag{5.40}$$

are given by

$$\hat{\mathcal{G}}'(k, t-t') = < \hat{\phi}^*(k,t')\hat{\phi}(k,t) > - < \hat{\phi}^*(k,t') >< \hat{\phi}(k,t) > \delta_{k,0}. \tag{5.41}$$

The correlation function $\mathcal{G}'$ would therefore be identical to $\mathcal{G}$ if $< \phi(k,t) >= 0$ for $k \neq 0$. For small k this will hold for solutions which display amplitude chaos. The situation for intermediate k values or when the solution does not show amplitude chaos is however not clear. Although numerically one finds reasonable agreement between (5.38), (5.39) and (5.41) in most cases, the space averaging is somewhat superfluous and these results are in general not necessarily equal.

We will discuss the behaviour outside the lock-in region for two parameter choices $\{c_2, c_3\}$. The first case we will consider is for $c_2 = -2.5$, $c_3 = 2$. In

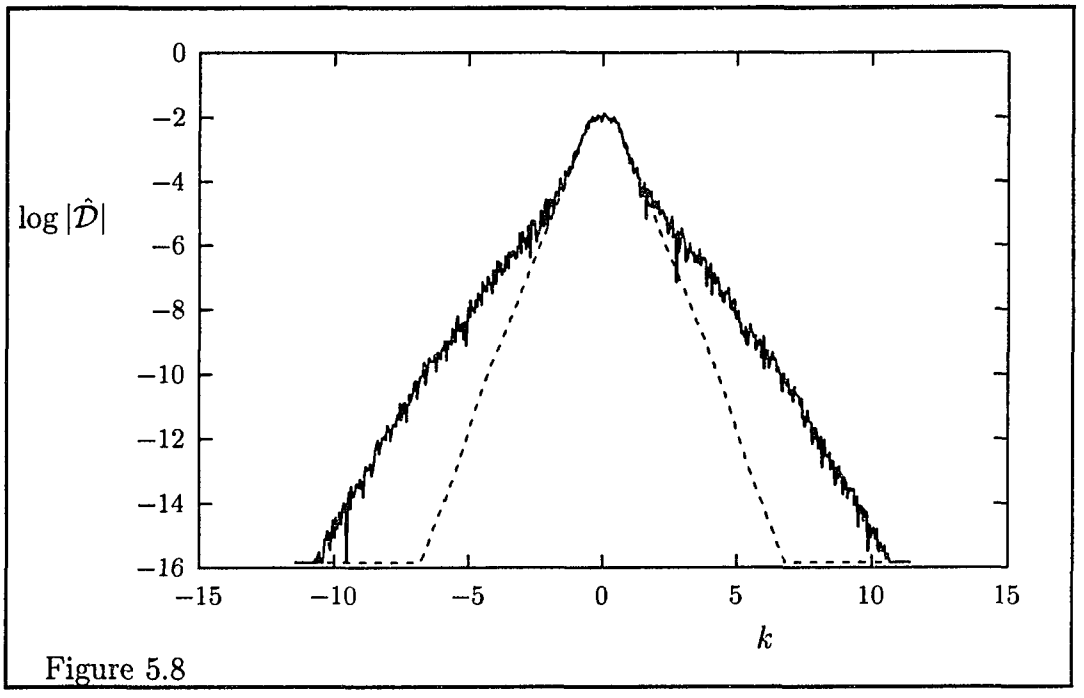

Figure 5.8: The Fourier components $\hat{\mathcal{D}}(k)$ of the spatial correlation function computed directly (dashed curve) and via $\mathcal{D}(x-x')$ (solid curve) for a state of amplitude chaos with $c_2 = -2.5$, $c_3 = 2$. The number of Fourier components used was 1024.

this case the unforced solution shows amplitude chaos. The second situation we will consider is $c_2 = -20$, $c_3 = 2$. The unforced solution in this case also shows amplitude chaos. For this parameter choice however the possibility of phase locked solutions is also severly limited with respect to the first case.

For the initial conditions the unstable phase locked plane wave solution was used, perturbed by a random disturbance,

$$\phi(x,0) = \phi_L + 0.2\phi_L \cdot \nu(x) \tag{5.42}$$

where $\nu(x)$ is a set of random numbers between -0.5 and 0.5. In case there are for a certain forcing amplitude three posible phase locked solutions, the one with the largest modulus was used as initial condition. For the cases tried, the same results were obtained for sufficiently localized initial conditions or with a harmonic (e^{iqx}) disturbance added to ϕ_L of sufficiently large q. The number of Fourier components used was 1024, 2048 or 4096, while the time step size varied from $dt = 0.2$ to $dt = 0.01$. The total integration time was of the order of 10^4 to 10^5, system lengths necessary varied from the order of 10^2 to 10^3. The disapearance of transients, especially the low wave number modes, was checked for a (just) stable phase locked state corresponding to the

ω and Λ value of each case considered. Transients in this way were found to vary but not to survive integration times of 10^4. No apparent contradiction to this has been observed in the actual integration outside the lock-in region.

We will now discuss the observed behaviour for $c_2 = -2.5$, $c_3 = 2$. The lock-in region in F_0-ω-Λ parameter space is for what concerns the relevant parts shown in figure 5.9. First we will look at the situation for $K = 0$ (spatially uniform forcing). We will look at the behaviour as one leaves the lock-in region for three frequency values; at resonance, $\omega = -2$ and well away from resonance, for $\omega = -10$ and $\omega = +2$.

For $\omega = -2$ phase-locked states exist for $F_0 > 1.5$. For $0.61 < F_0 < 1.5$ the solution remains locked-in in time, that is, $\partial_t \phi = 0$. In space however a periodic pattern appears with a period corresponding the wavenumber of the maximally unstable perturbation (perturbation with maximum linear growth rate). See figure 5.10.

At $F_0 = 0.61$ one observes period doubling in space and at the same time $\phi(x,t)$ becomes periodic in time. See figure 5.11. An explaination for the sudden occurrence of the time dependence is not possible from linear stability analyses. One shows analytically that the imaginary part of the growth vanishes for the unstable perturbations. The origin of the time dependence of

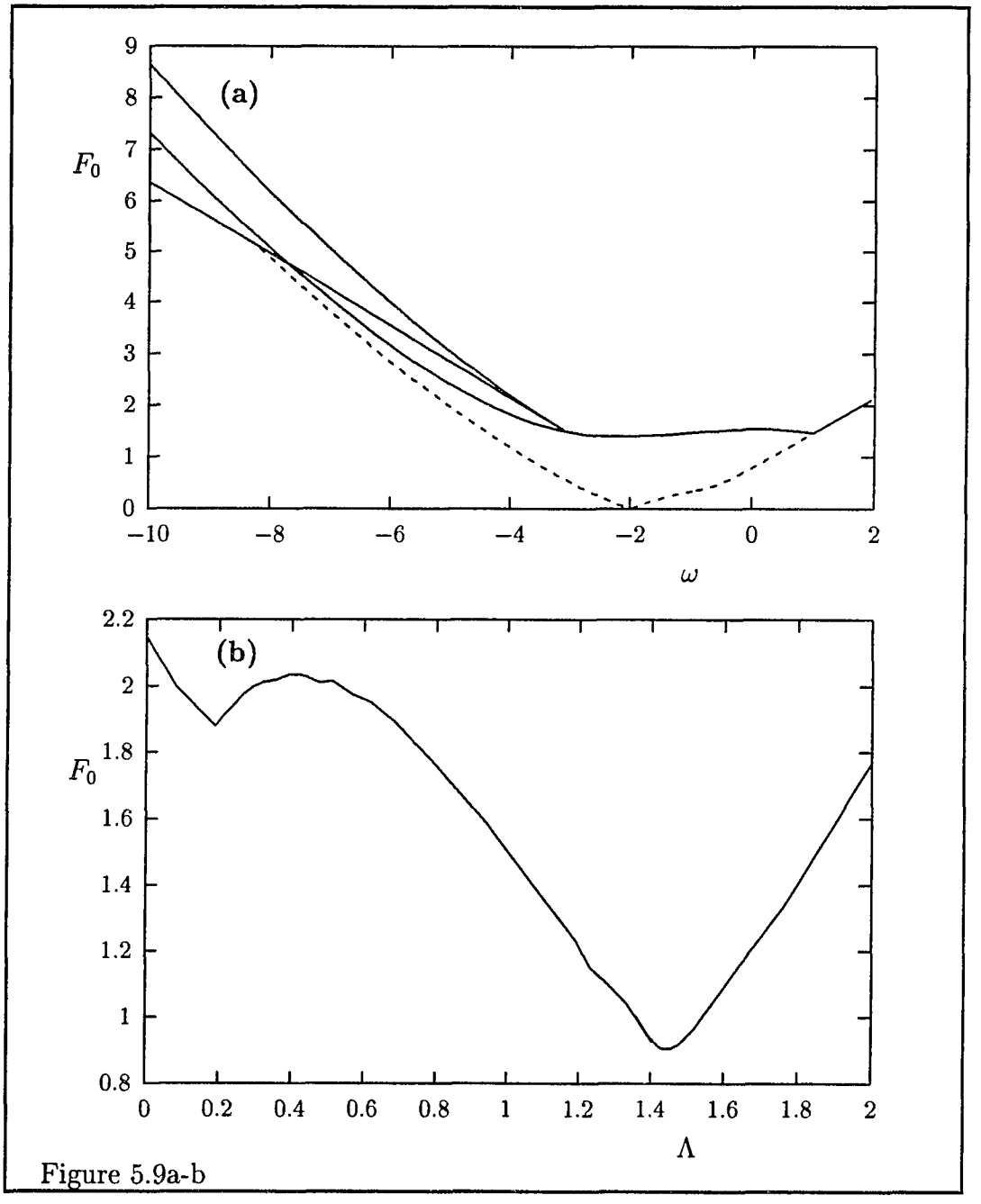

Figure 5.9a-b

Figure 5.9: Some relevant pictures of the lock-in region for an extended system with $c_2 = 2$, $c_3 = -2.5$.

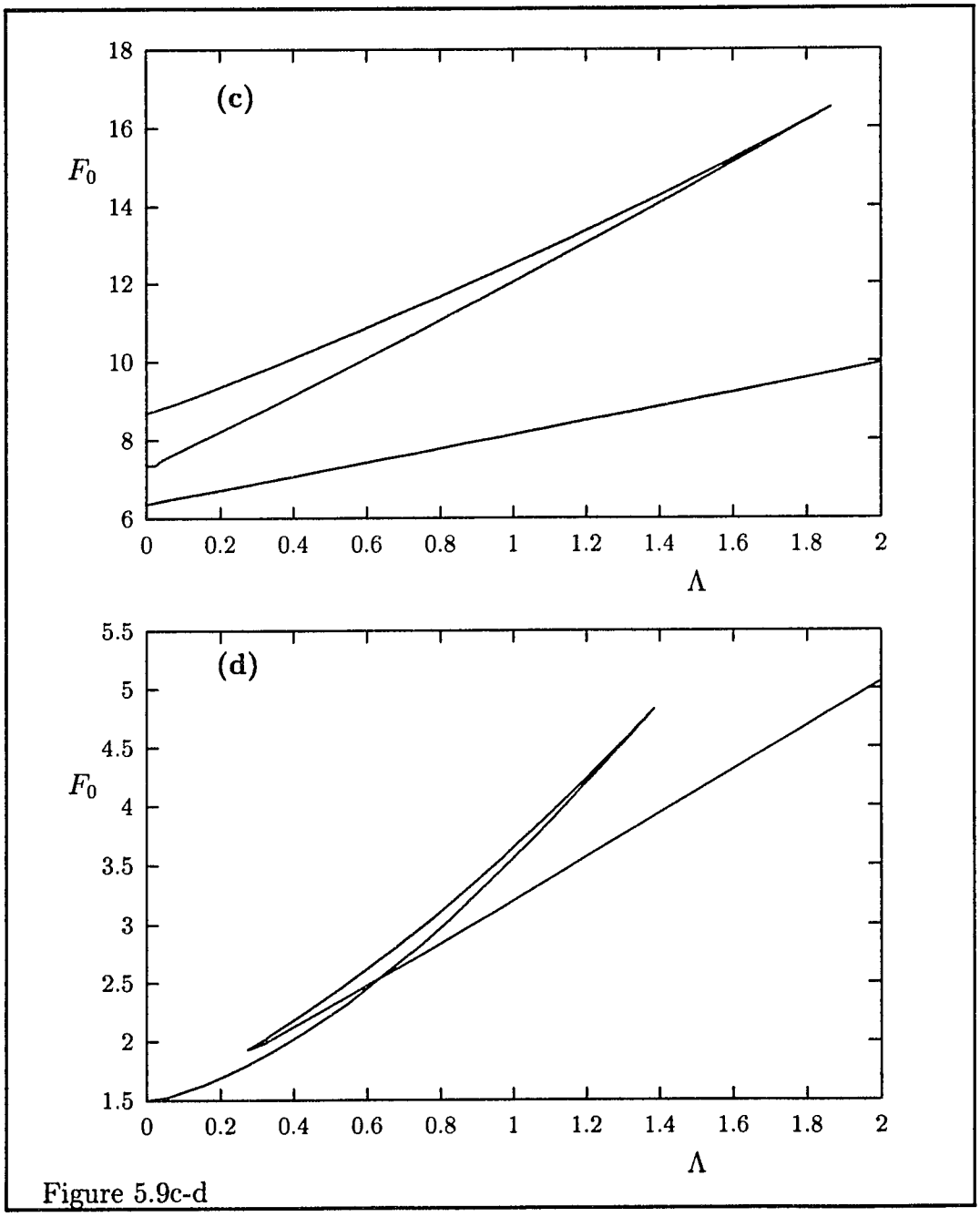
(c)
F_0
18
16
14
12
10
8
6
0
0.2
0.4
0.6
0.8
1
1.2
1.4
1.6
1.8
2
Λ
(d)
F_0
5.5
5
4.5
4
3.5
3
2.5
2
1.5
0
0.2
0.4
0.6
0.8
1
1.2
1.4
1.6
1.8
2
Λ

Figure 5.9c-d

Figure 5.10: (Next page) The spatially periodic pattern (a) observed for $F_0 = 0.65$ and $\omega = -2$, $c_2 = -2.5$, $c_3 = 2$ in the extended system for $K = 0$. The linear growth rate of the corresponding (unstable) lock-in solution is shown in panel (b).

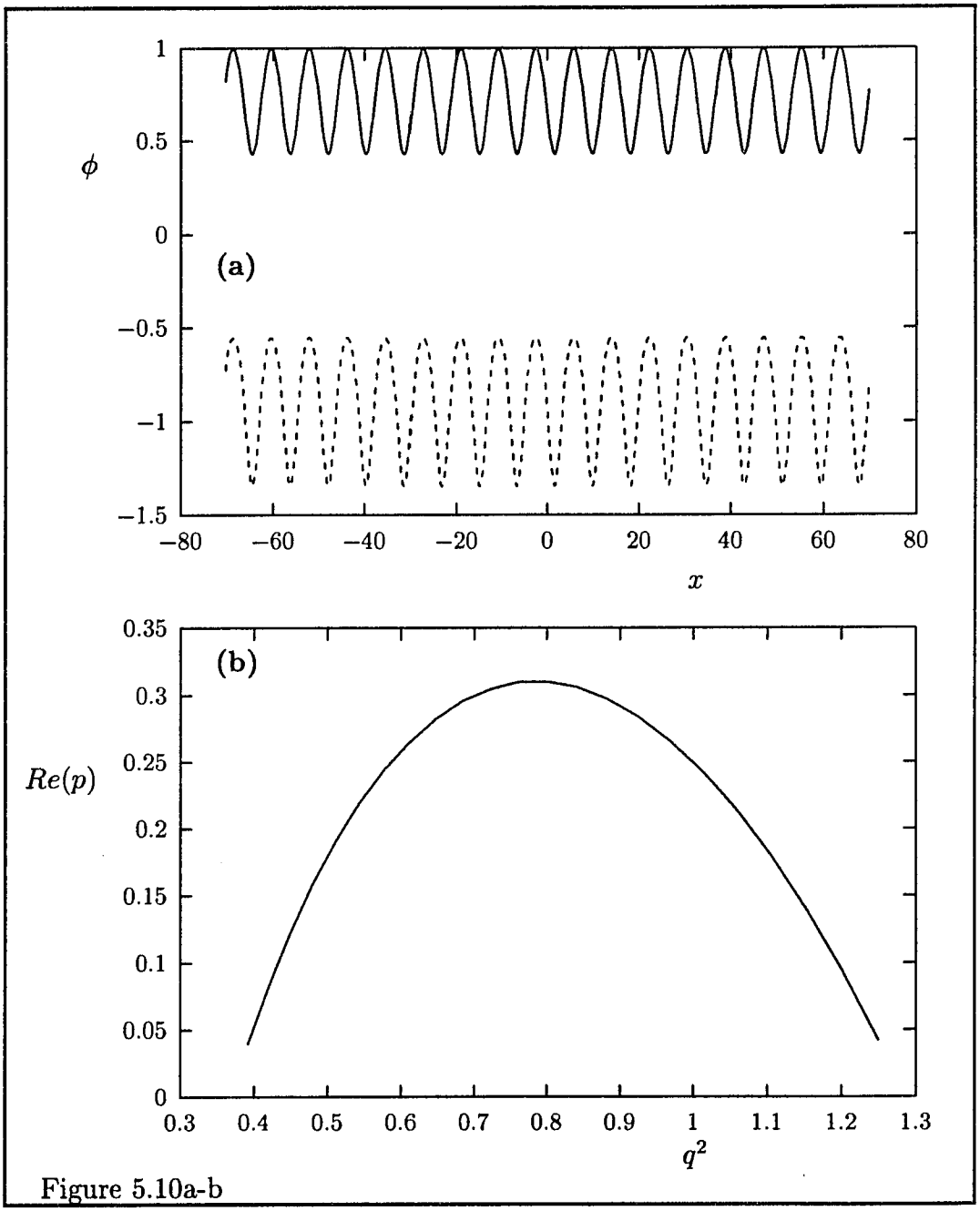

Figure 5.10a-b

$\phi(x,t)$ must therefore lie in nonlinear effects. The same is true for the period doubling; no qualitative change of the linear growth rate of the unstable perturbations as function of their wavenumber occurs.

Some pictures of the behaviour for $0.51 < F_0 < 0.6$ are shown in figure 5.12. The solution $\phi(x,t)$ is now quasi-periodic in time for fixed x with two frequenties. The periodicity in space is also disturbed and the question arises if perhaps quasi-periodicity in space also occurs. Unfortunately, within our formulation of the problem quasi-periodicity in space can strictly speaking not be observed. The two frequenties appearing in the quasi-periodic motion in time are orders of magnitude apart. The Fourier spectrum of the spatial correlation function $\hat{\mathcal{D}}(k)$ shows various peaks, which also at quasi-periodic motion in space. It is also interesting to observe how the coherence of the pattern decreases as the forcing decreases. On a time scale of the order of the highest fudamental frequency occurring in the quasi-periodic motion and on length scales of the order of the smallest length scale ocurring, the pattern appears to be periodic both in space and time. Deviation of periodic behaviour only occurs on the large scales.

For $0.45 < F_0 < 0.5$ the solution $\phi(x,t)$ becomes chaotic in time. The spatial behaviour does not undergo a significant change at $F_0 = 0.5$ but

gradually starts showing (more) long range disorder . Pictures are shown in figure 5.13. There is a clear decay visible of the spatial correlations on the large scale. Provided the spatial quasi-periodicity indeed occurs one observes here thus a transition from quasi-periodicity to spatial disorder. As the forcing drops below 0.5 defects occur for the first time. For F_0 just below 0.5 their appearance in the x-t plane is in the form of clusters which themselves however appear to be randomly distributed over the system. For smaller F_0 the clusters disappear and the defect distribution becomes uniform as one would expect.

For forcing amplitudes below $F_0 = 0.45$ the solutions display spatio-temporal chaos. Initially however the Fourier spectrum of the spatial correlation function shows besides the long range disorder also still some short range order because a small peak occurs (at wavenumber of the maximally unstable perturbations) just before the exponential decay sets in. A similar spectrum is observed for the spatio-temporal chaotic solutions of the Kuramoto-Sivashinski equation [45] [46]. One therefore may expect a description in terms of a phase equation to be still possible here despite the presence of defects. For the unforced solutions, the phase description was shown to break down when defects occur, being the point where the transi-

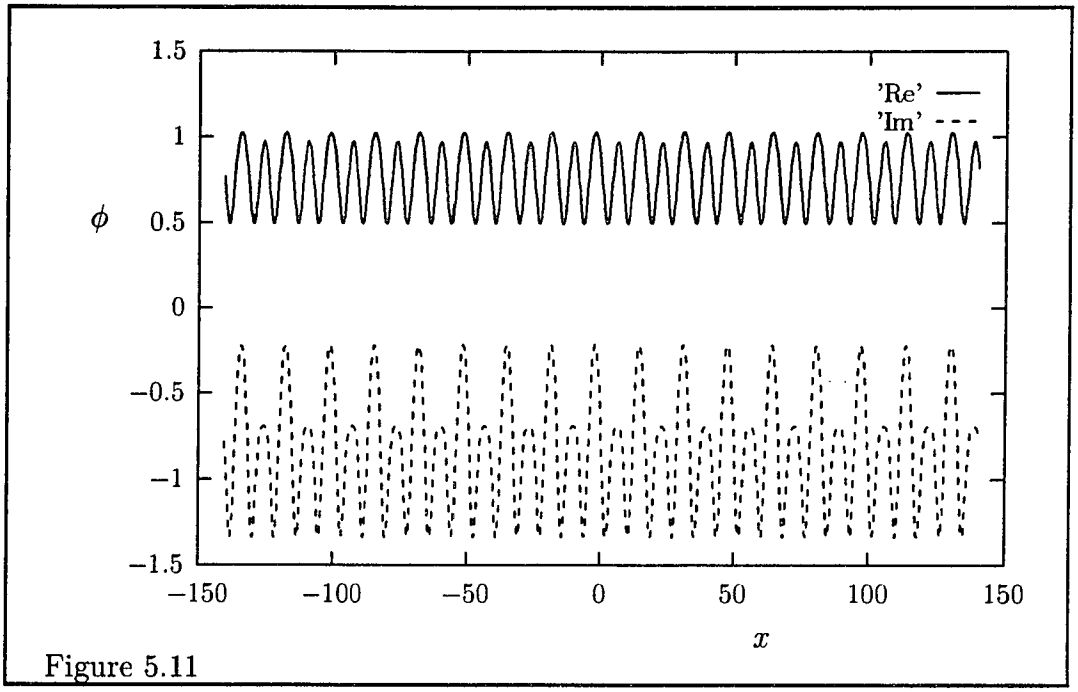

Figure 5.11

Figure 5.11: Pattern observed after period doubling at $F_0 = 0.61$.

tion from phase chaos to amplitude chaos takes place. Our results suggests that this is not the case for the forced solutions. See figure 5.14 for pictures.

Next we will discuss the situation for $K = 0$ and the two frequenties away from resonance. Some results for these frequenties are shown in figure 5.15. A qualitative difference with the situation for frequenties around resonance is that now immediately as one leaves the lock-in region, the linear instability

Figure 5.12: (Next page) Snapshot of $\phi(x,t)$ (a), spatial correlation function $\hat{\mathcal{D}}(k)$ (b) and $\mathcal{D}(x-x')$ (c) and the temporal correlation function $\mathcal{C}(t-t')$ for $c_2 = -2.5$, $c_3 = 2$ and $\omega = -2$, $F_0 = 0.55$ in the extended system with a spatially uniform forcing.

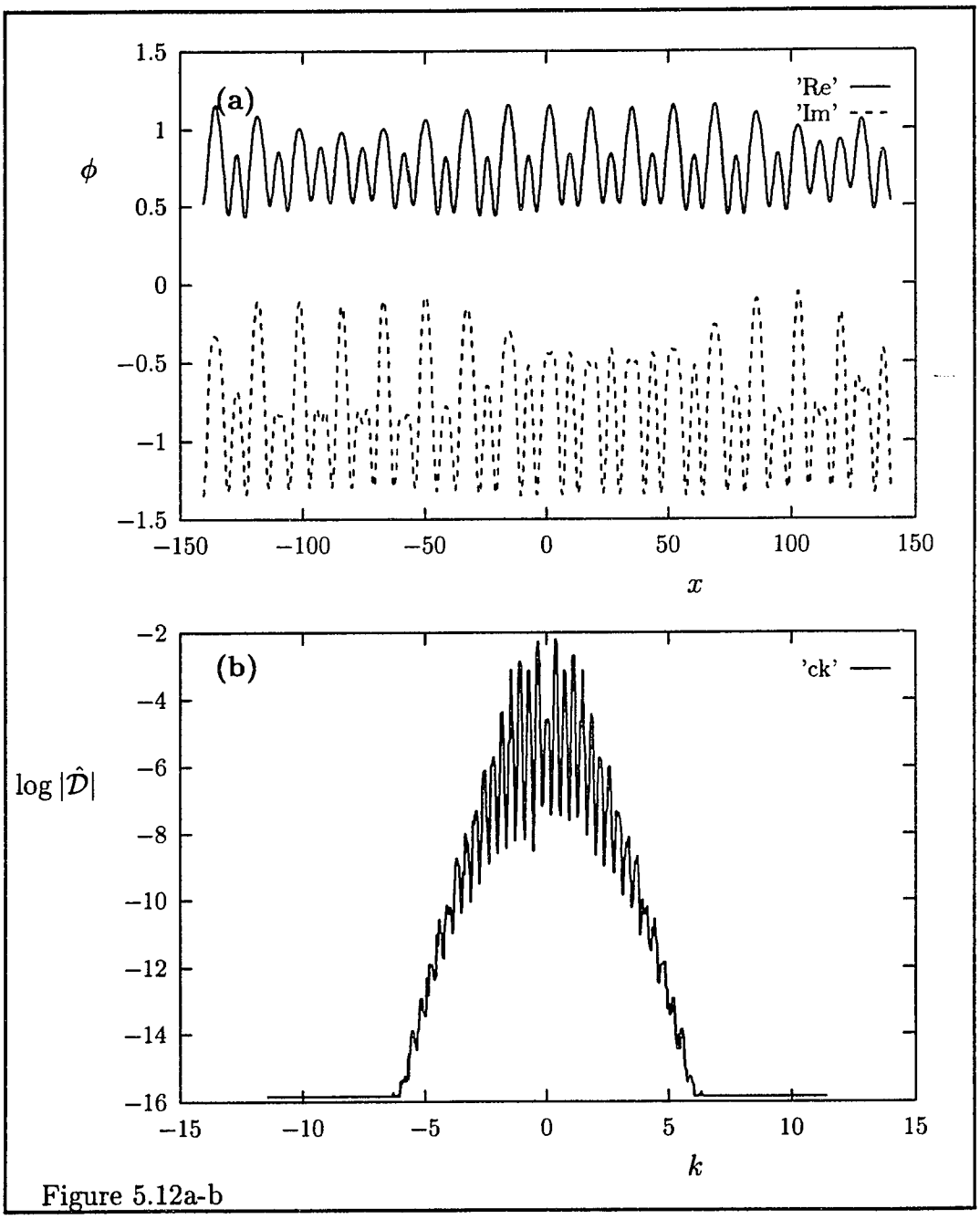

Figure 5.12a-b

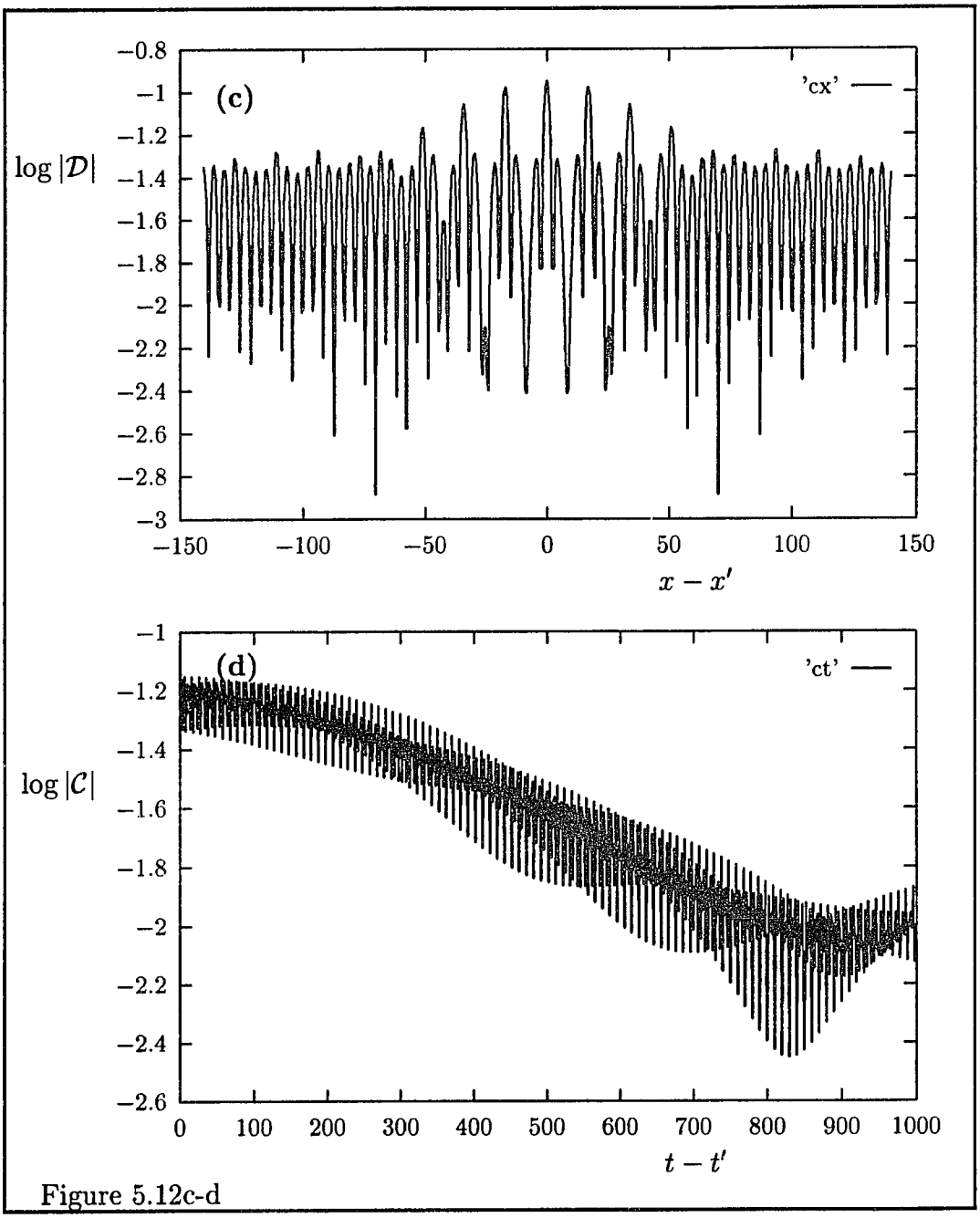

Figure 5.12c-d

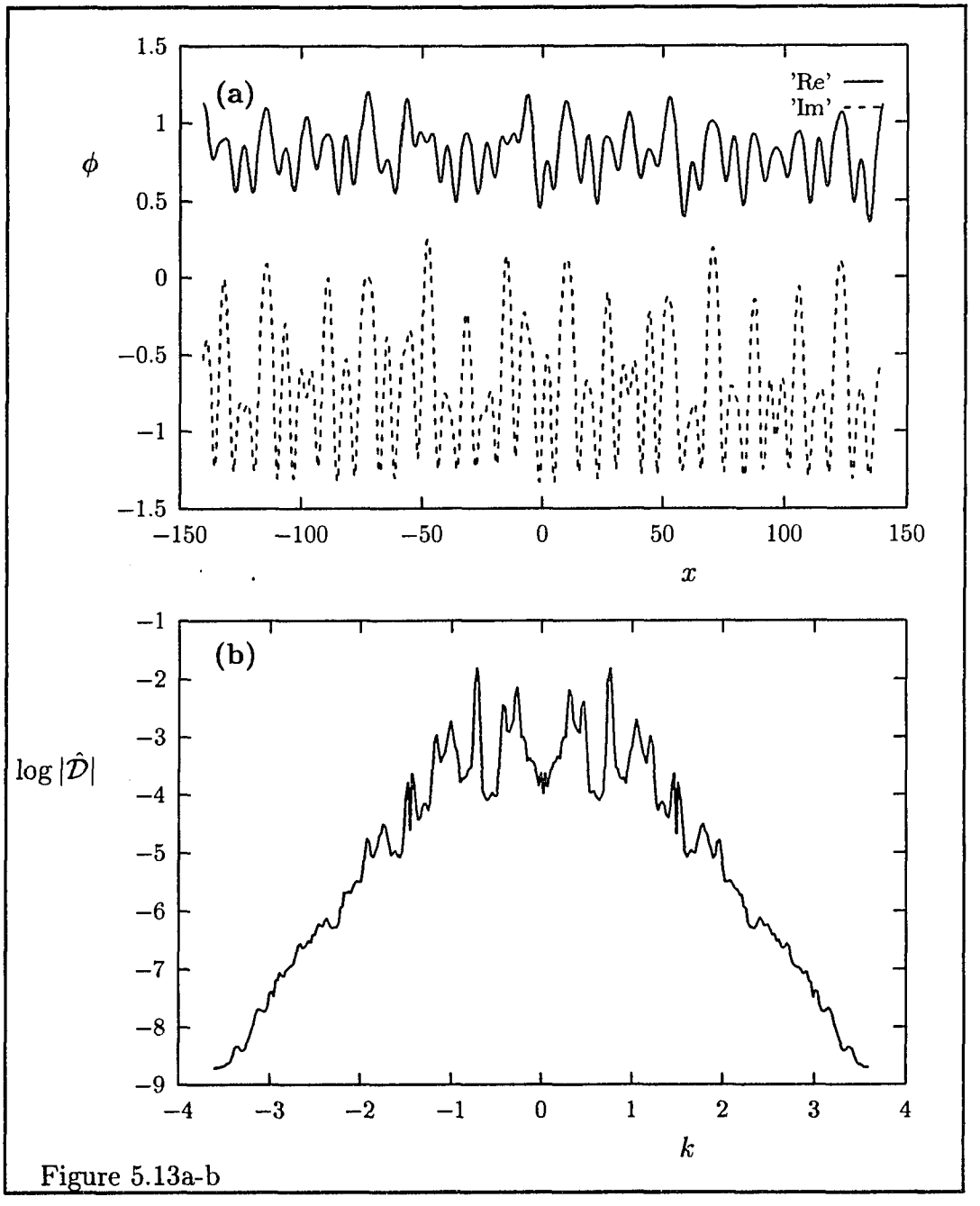

Figure 5.13a-b

Figure 5.13: Snapshot of $\phi(x,t)$ (a), spatial correlation function $\hat{\mathcal{D}}(k)$ (b) and $\mathcal{D}(x-x')$ (c) and the power spectrum of $Re\phi(0,t)$ for $c_2 = -2.5$, $c_3 = 2$ and $\omega = -2$, $F_0 = 0.5$ in the extended system with a spatially uniform forcing.

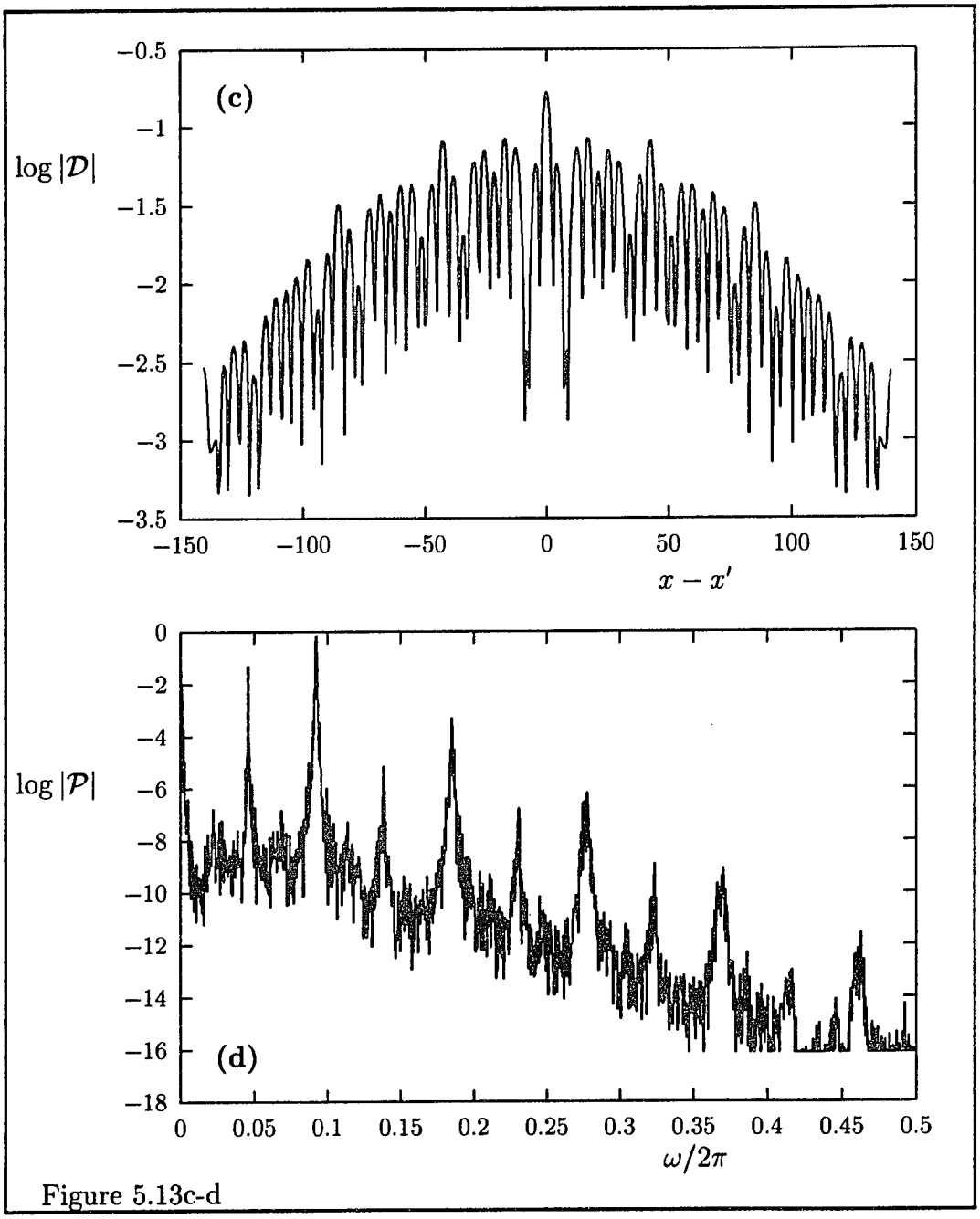

Figure 5.13c-d

Figure 5.14: (Next page) Snapshot of $\phi(x,t)$ (a), spatial correlation function $\hat{\mathcal{D}}(k)$ (b) and $\mathcal{D}(x-x')$ (c) and the temporal correlation function $\mathcal{C}(t-t')$ (d) for $c_2 = -2.5$, $c_3 = 2$ and $\omega = -2$, $F_0 = 0.5$ in the extended system with a spatially uniform forcing. In panel (e) and (f) a snapshot of ϕ and the temporal correlation function are shown respectively for $F_0 = 0.35$.

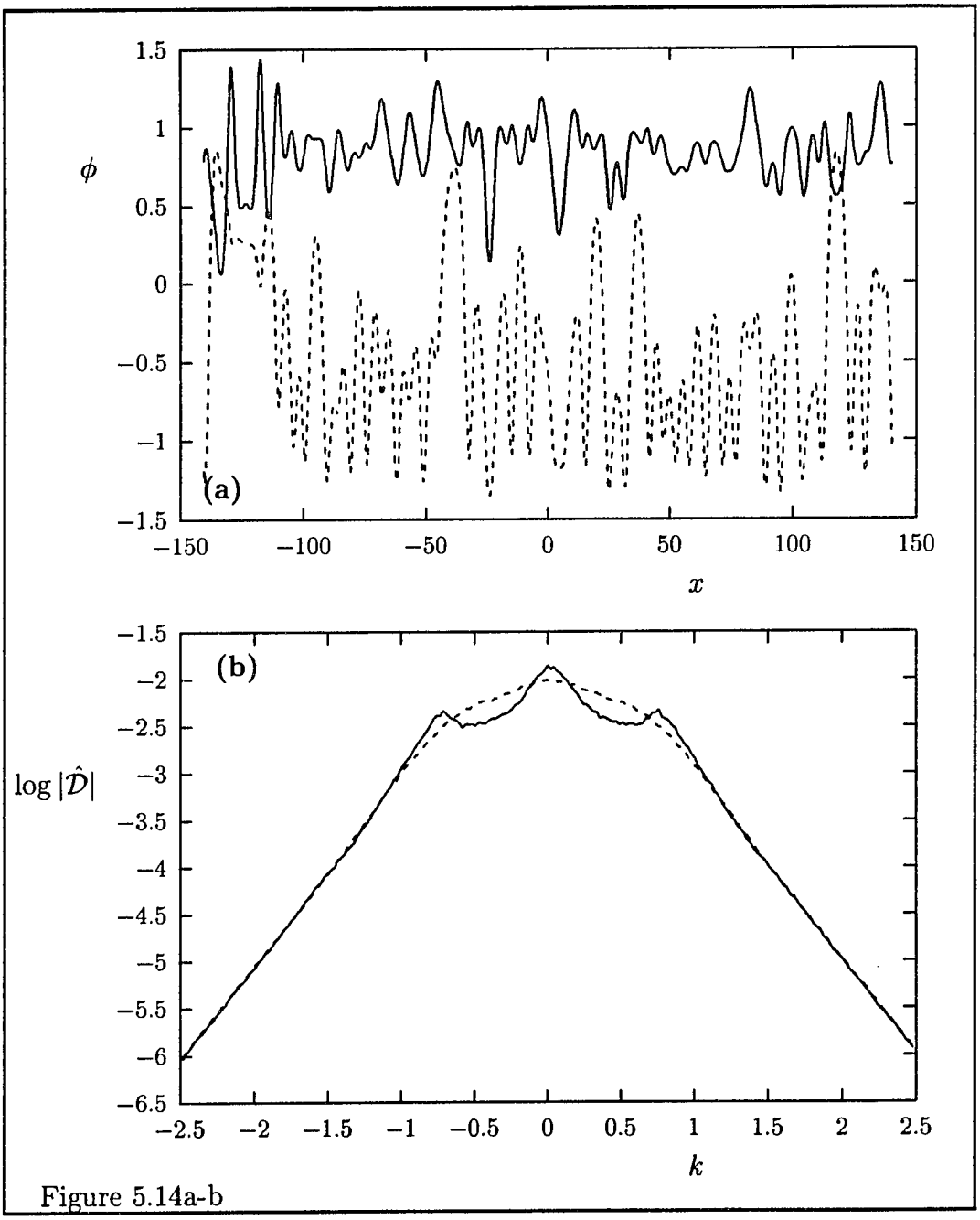

Figure 5.14a-b

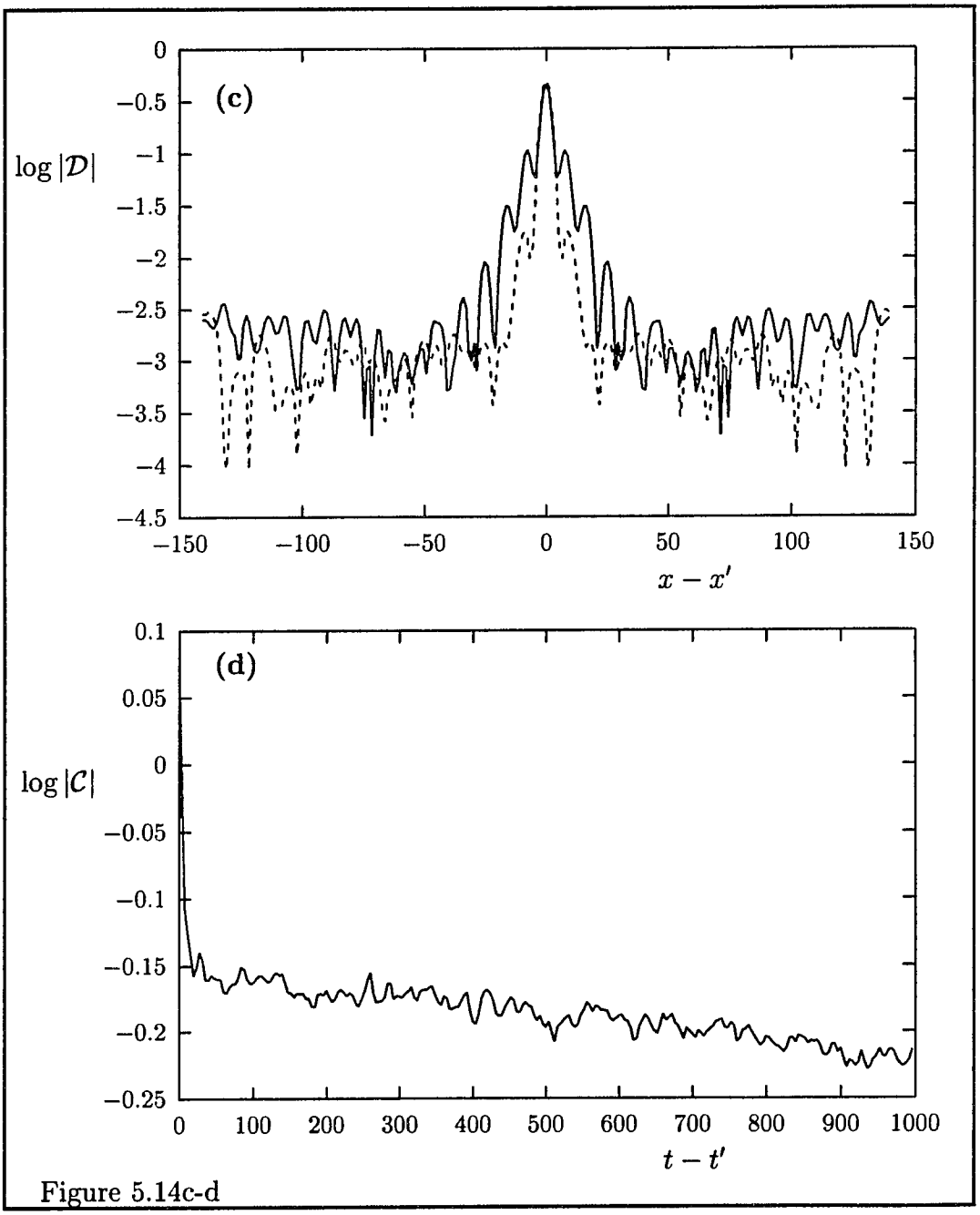

Figure 5.14c-d

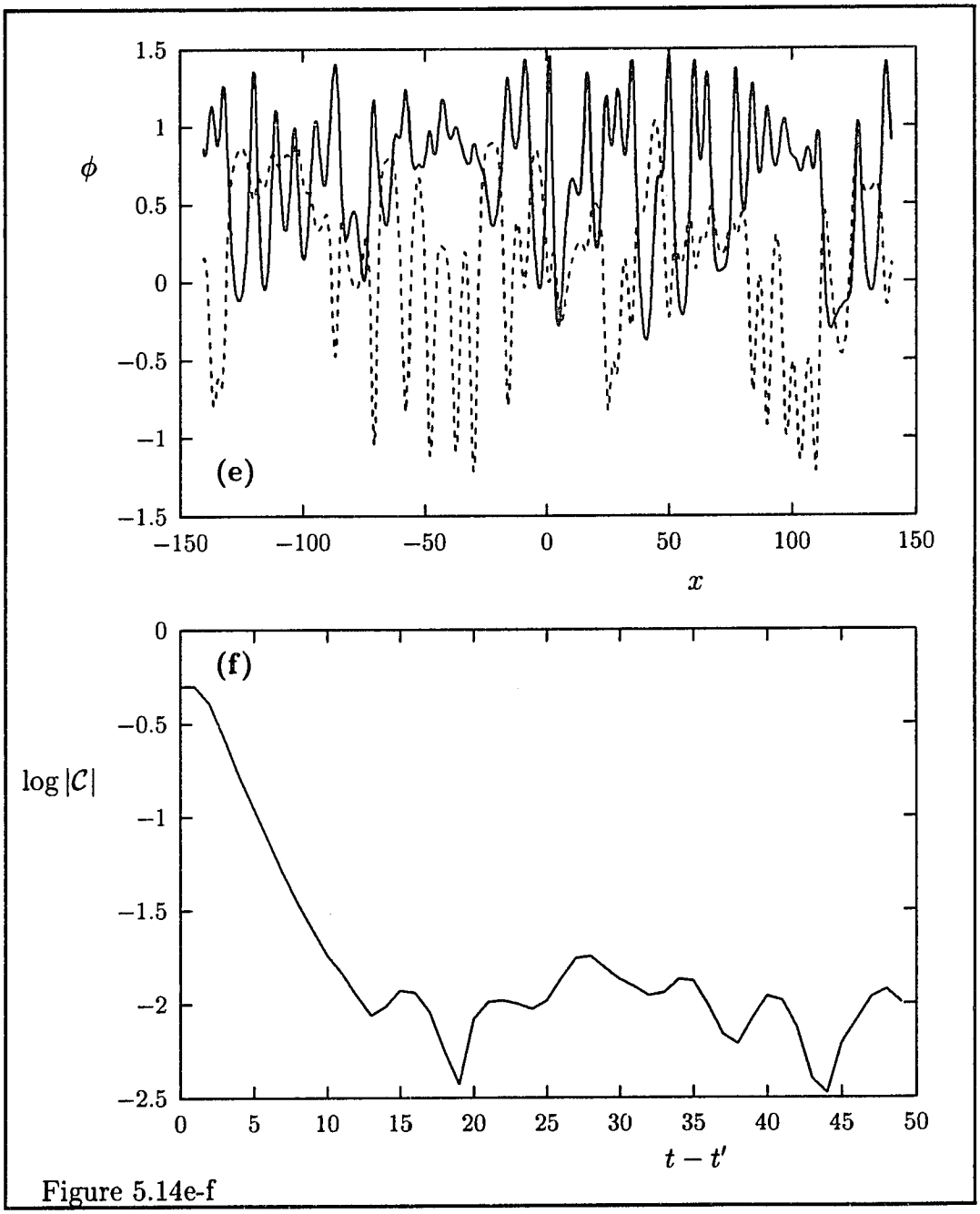

Figure 5.14e-f

occurs for perturbations with small q, including $q = 0$. Right below the lock-in region therefore patterns are observed with a characteristic length close to the system length if one starts with initial conditions which have a harmonic perturbation with a small wavenumber. Most initial conditions of this kind lead to different patterns. For the random initial conditions used here however this complication does not occur, provided it contains Fourier components of much larger wavenumber than the largest wavenumber of the unstable modes. For $\omega = -10$ in that case one observes immediately below the lock-in region spatio-temporal chaos. The Fourier spectrum of the spatial correlation function takes qualitativele the same form as for the unforced solutions as soon as one leaves the lock-in region, there is no gradual change as observed for $\omega = -2$. An important diference with the unforced solution is however that now no defects are present. Strictly speaking here the states therefore should be characterized as phase chaos. However, the behaviour of $\hat{\mathcal{D}}(k)$ is qualitatively very different for phase chaotic solutions. Also the decay of the temporal correlations one observes here is not characteristic for phase chaos, in which case they are believed to decay slower than exponentially. One therefore arrives at the conclusion that it is better to classify these states as amplitude (defect) chaos although no defects are present. Is the presence

of defects a useful criterion for the classification of the unforced chaotic states, it obviously is not for the forced solutions.

One arrives at the same conclusion by observation of the results for $\omega = +2$, figure 5.16, but this time from a different perspective. Here the solutions just outside (but not immediately outside) the lock-in region display spatio-temporal chaos which strictly speaking should be classified as amplitude chaos because defects are present. However, the correlation functions $\mathcal{D}$ and $\mathcal{C}$ show behaviour typical for phase chaos. Also in this case thus, a classification of the forced solutions based on the presence of defects turns out to be unsuitable.

The appearance of two very different length scales in these solutions, also typical for phase chaos in unforced solutions, is more pronounced here then at resonance. It is also reflected by the strong peaks in $\hat{\mathcal{D}}(k)$ and the several harmonics present. Unlike for the unforced case, their explaination is not possible on the basis of linear stability analyses. The maximally unstable perturbation is the $q = 0$ perturbation, which explains the occurrence of the large length scale. As q moves away from zero however, the growth rate gradually decreases and eventually becomes negative beyond a certain wavenumber. The behaviour just explained sets in somewhat below the lock-

in region. The behaviour one observes immediately outside the lock-in region is a state of ordinary phase chaos.

So far our discussion concerned the $K = 0$ case. We will now look at two situations for a real plane wave forcing with $\omega = +2$ and $\omega = -3$. We will not discuss the complete bifurcation sequence as $F_0 \downarrow 0$, but confine ourselves to a description of the behaviour as one leaves the lock-in region. For $\omega = +2$ we will look at the situation for two different wavelengths, $\Lambda = 0.2$ and $\Lambda = 1.5$ (recall that the wavenumber of the forcing is $K_{dim} \sim \sqrt{\Lambda}$). For $\Lambda = 1.5$ some of the results are shown in figure 5.17, we are around the resonance wavelength, just below lock-in. The pattern we observe here looks at a first glance similar to the quasi-periodic patterns obsereved around resonance (frequency) for $K = 0$. Now the spatial oscillations in the pattern are of much larger amplitude, particularly if one looks at $|\phi|$. Another difference is that now defects occur. Although the time series is chaotic for fixed x, there is a dominant presence of a high and a low frequency (two time scales). The defect locations in the x-t plane reveal some structure and on the short time scale defectless regions in space are recognized which coincide with the regions in which the solution is quenched. One wonders if the presence of the long time scale is infact not a size effect; does it occurs because of the

Figure 5.15: (Next page) Snapshot of $\phi(x,t)$ (a), spatial correlation function $\hat{\mathcal{D}}(k)$ (b) and $\mathcal{D}(x-x')$ (c) and the temporal correlation function $\mathcal{C}(t-t')$ (d) for $c_2 = -2.5$, $c_3 = 2$ and $\omega = -10$, $F_0 = 6.05$ in the extended system with a spatially uniform forcing.

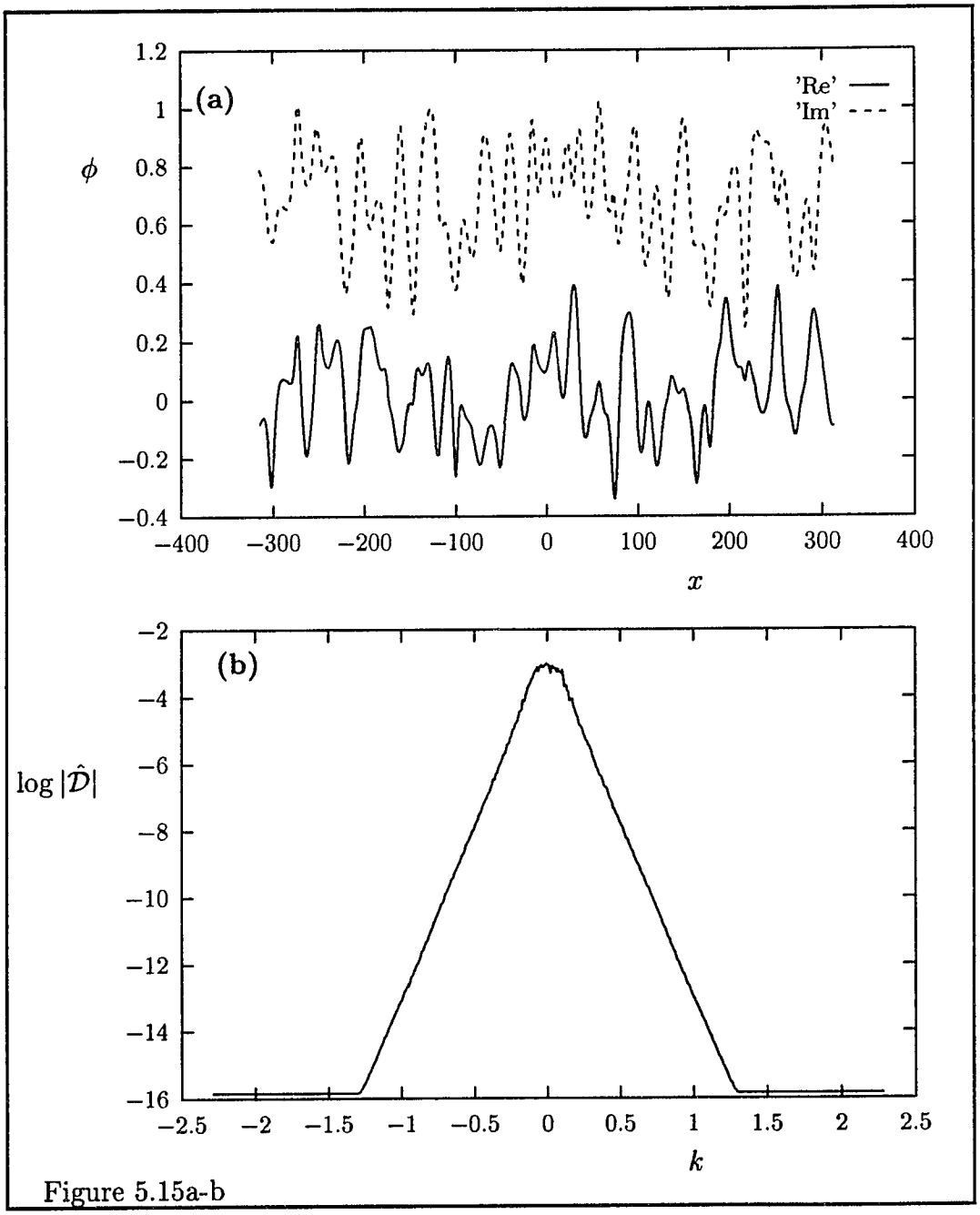

Figure 5.15a-b

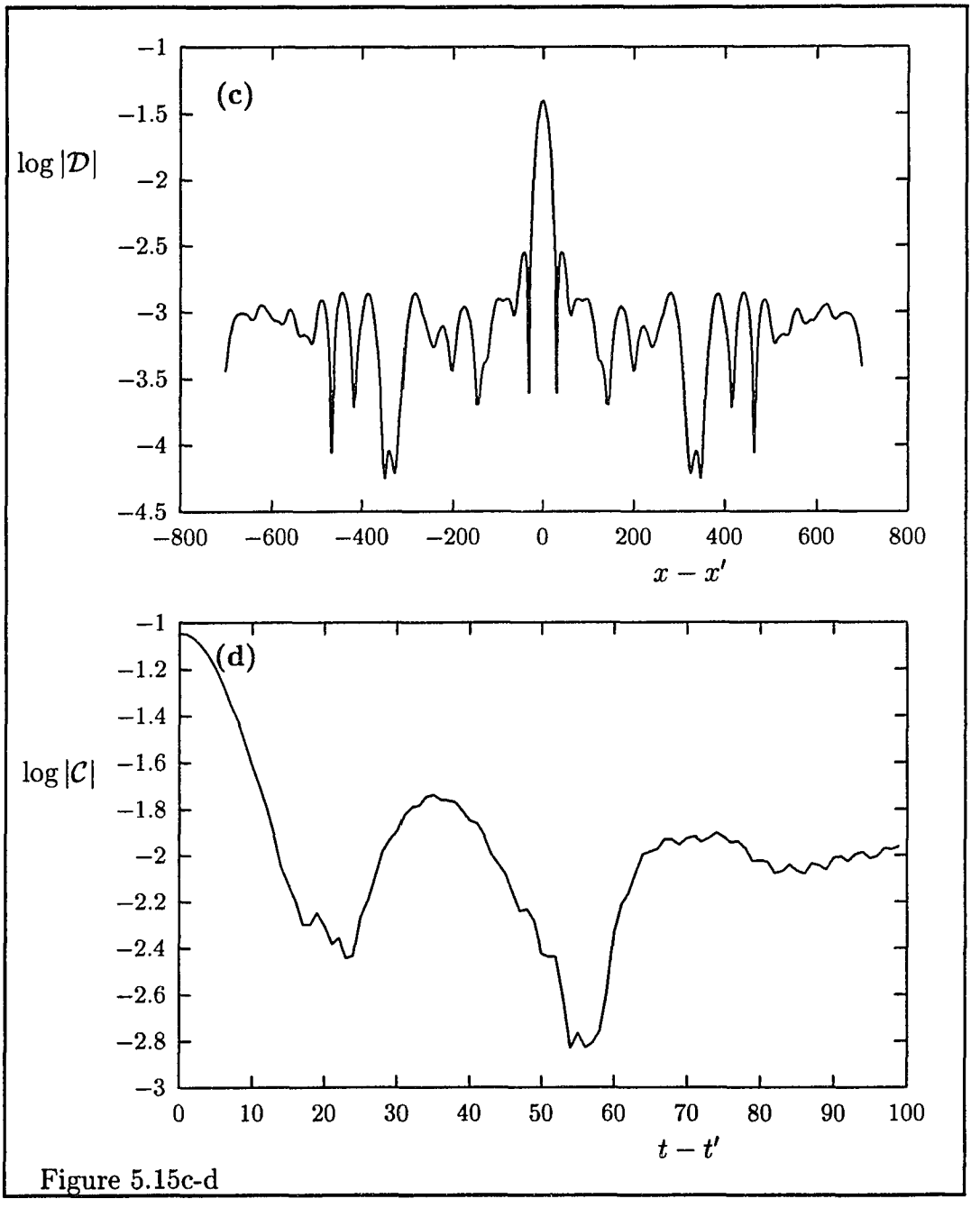

Figure 5.15c-d

Figure 5.16: (Next page) Snapshot of $\phi(x,t)$ (a) (b), a defect (c), the spatial correlation function $\hat{\mathcal{D}}(k)$ (d) and $\mathcal{D}(x-x')$ (e) and the temporal correlation function $\mathcal{C}(t-t')$ (f) for $c_2 = -2.5$, $c_3 = 2$ and $\omega = +2$, $F_0 = 1.95$ in the extended system with a spatially uniform forcing.

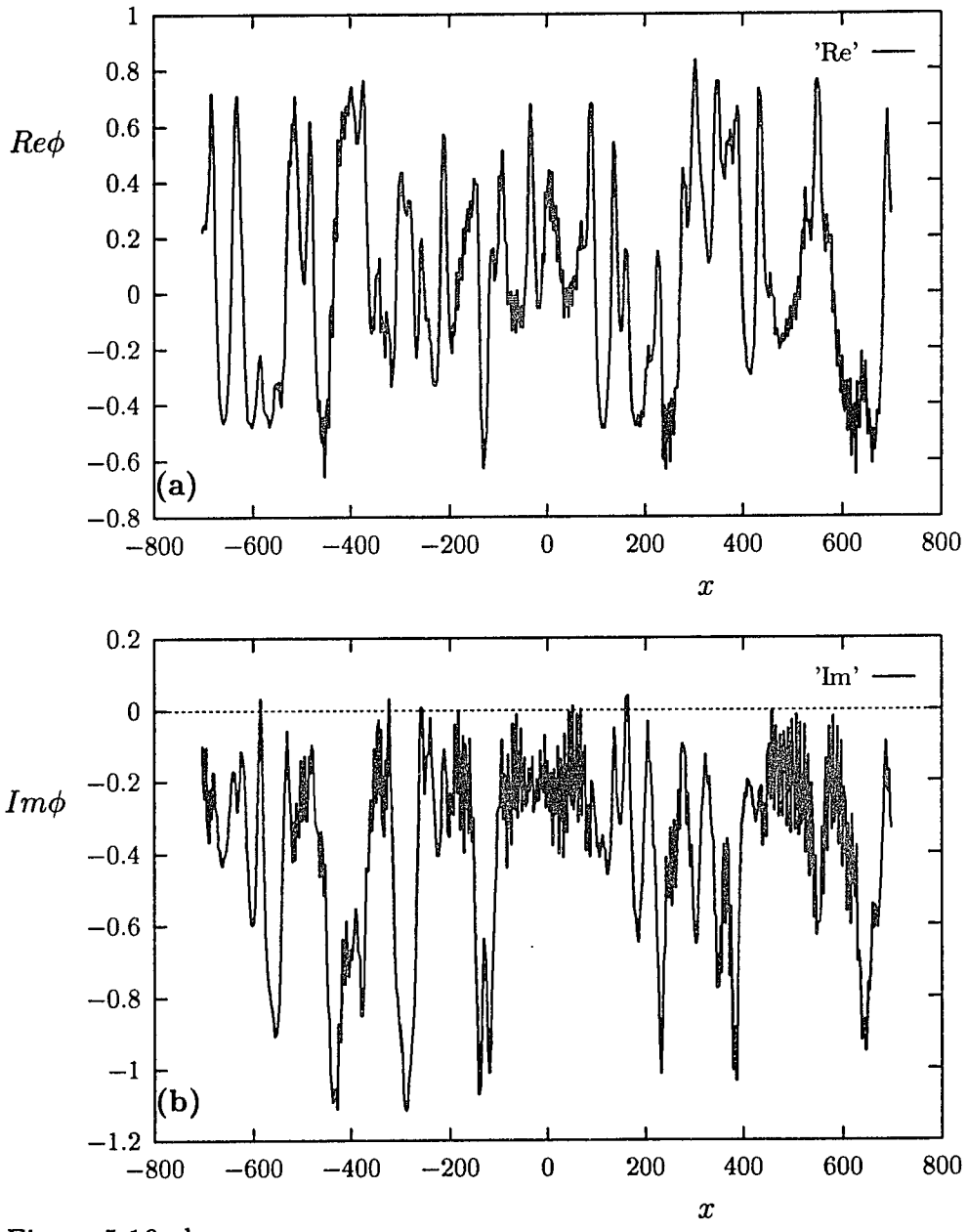

Figure 5.16a-b

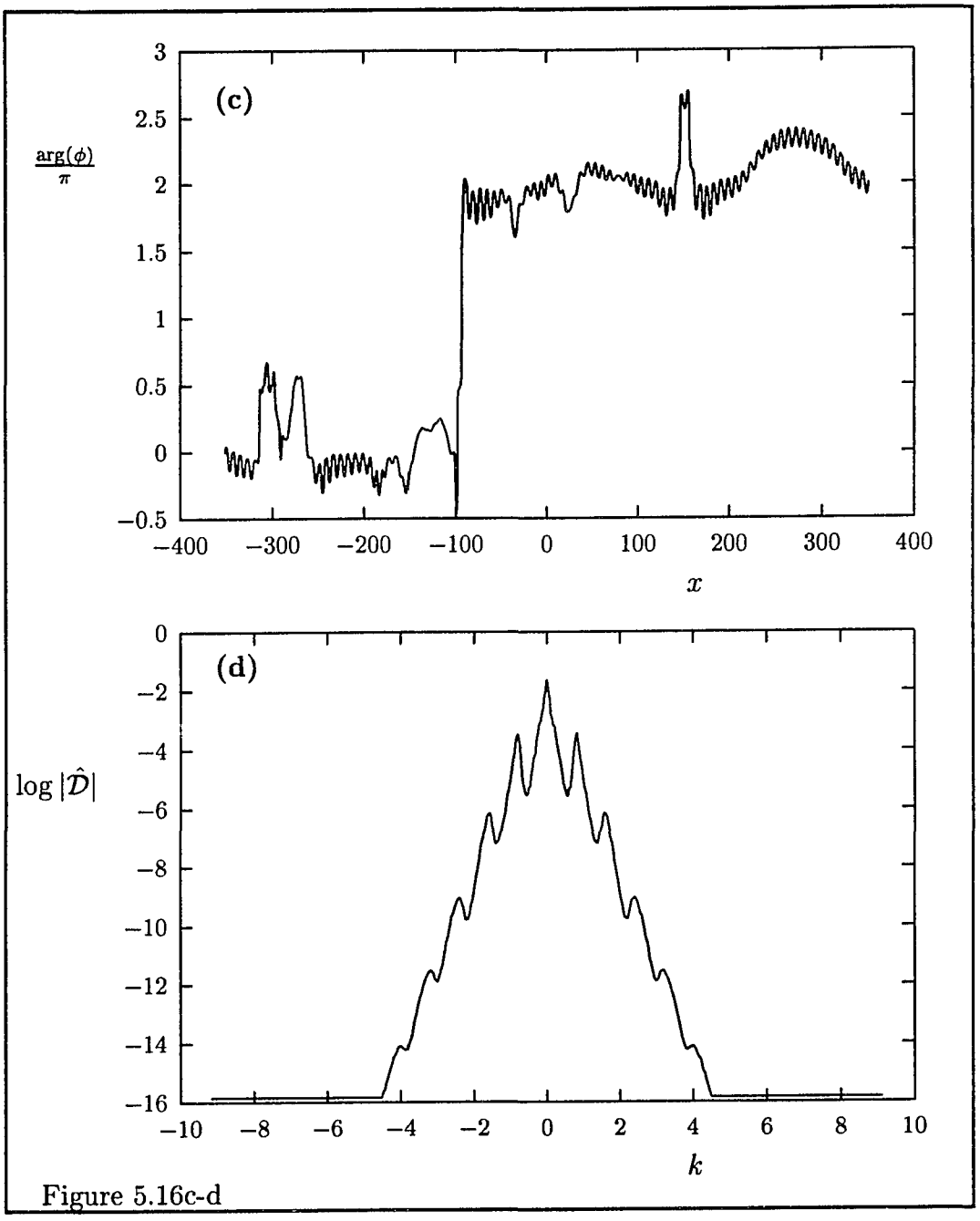

Figure 5.16c-d

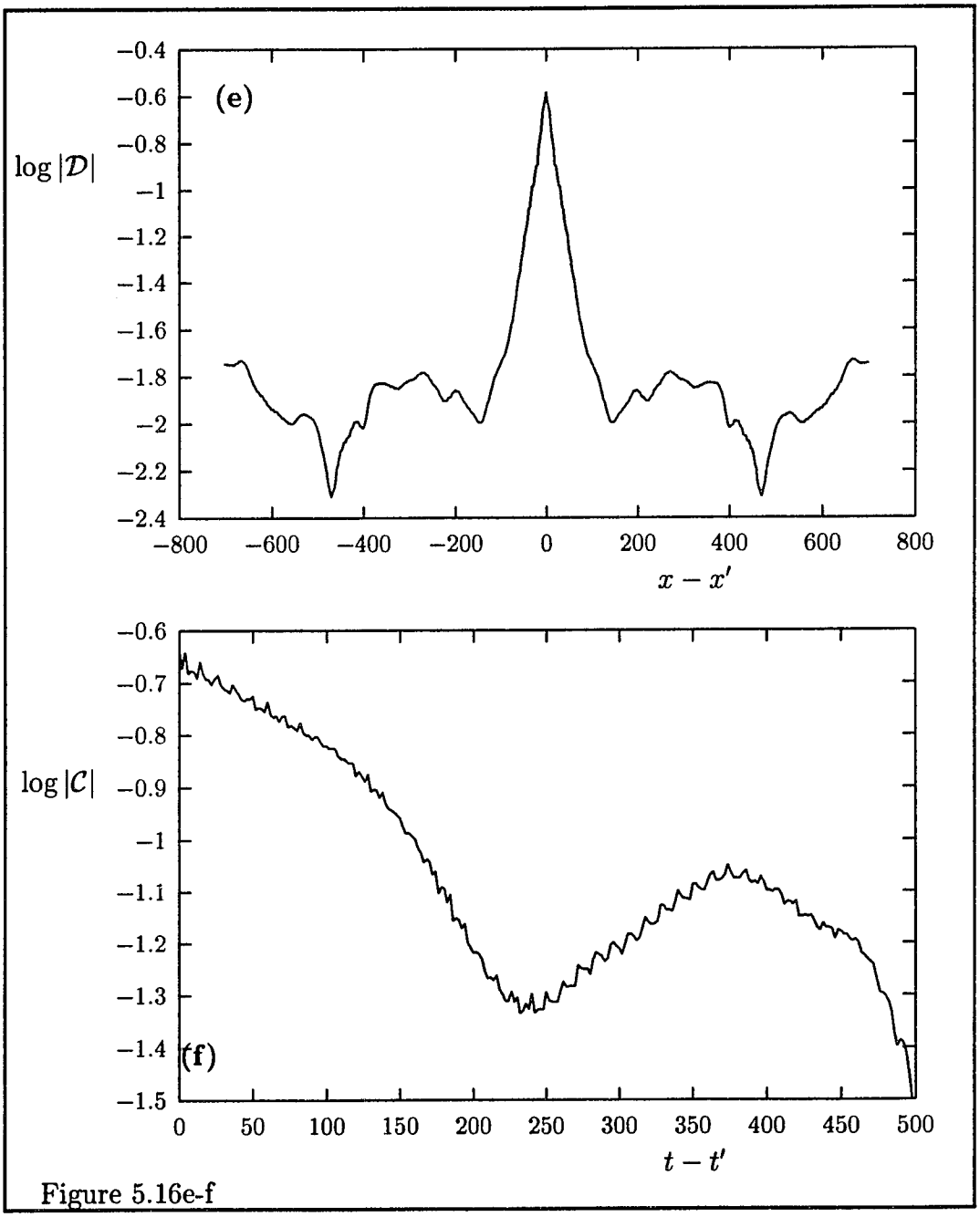

Figure 5.16e-f

boundary conditions ? Although no change is observed when one doubles the system size when the original system length is large enough, some response is observed to to "fine tuning" of the system length.

The Fourier transform of the spatial correlation function is shown in figure 5.17b. Note that unlike for $K = 0$, $\hat{\mathcal{D}}(k)$ is now of course not symmetric in k. The major peak occurs at $k = -K_{dim}$, which in this case happens to be close to the wavenumber of the maximally unstable perturbation. Furthermore, one also does not recover symmetry of $\hat{\mathcal{D}}(k)$ with respect to the $k = -K_{dim}$ axis. This fact may be explained from linear stability analyses. It is most clearly demonstrated if one looks at small perturbations with wavenumber q' of the original solution $\Psi(x,t)$; $\delta\Psi = e^{iKx}\delta\phi \sim e^{iq'x+p'(q')t}$. In general the growth rate $p'(q')$ is not symmetric with respect to q'. This is also true for this particular case. One may expect because of this in general assymetric behaviour of $\hat{\mathcal{D}}(k)$ with respect to $k = -K_{dim}$.

The shape of $\hat{\mathcal{D}}(k)$ again demonstrates significantly more phase chaos in contrast to amplitude chaos, although defects are present. The absence of a peak at $q = 0$ however shows that long range disorder does occur, see also figure 51.7c. A little more similarity with phase chaos is observed in the temporal correlation function.

The situation for a somewhat larger forcing wavelength, $\lambda = 0.2$, is shown in figure 5.18. Right below the lock-in region one observes spatio-temporal chaos. The spatial oscillations in $|\phi|$ are large in amplitude, however no defects are present. The linear growth rate for this case shows two maxima, figure 5.18f,g,h. This fact is clearly recovered in the Fourier spectrum of the spatial correlation function. One observes three different characteristic peaks; two for the wavenumbers of the most unstable perturbations and one for the wavenumber of the forcing. One does not observe significant exponential decay of neither the spatial nor the temporal correlations. The presence of long range disorder is however visible in $\hat{\mathcal{D}}(k)$.

As one decreases F_0 further the rather exceptional behaviour of the linear growth rate quickly disappears. Defects appear and the correlations start showing exponential decay, see figure 5.19. One also observes a smooth behaviour of $\hat{\mathcal{D}}(k)$ already quite similar to the behaviour for the unforced solution. The peak in $\hat{\mathcal{D}}(k)$ present for negative k is located at the negative wavenumber of the forcing, which again is close to the wavenumber of the maximally unstable perturbation for which also a much smaller peak occurs at positive k, no higher harmonics are present.

Finally, rounding of our discussion for the parameter choice $c_2 = -2.5$,

$c_3 = 2$, we will look at a solution for a real plane wave forcing with $\omega = -3$ and $\Lambda = 0.2$. Resonance in wavenumber is not expected here and also not observed, see figure 5.20. The results shown in figure 5.20 are for a solution just below the lock-in region. Unlike the previous case the phase locked solutions are now stable for perturbations with wavelengths of the order of the wavelength of the forcing, resulting in a much more pronounced peak in $\hat{\mathcal{D}}(k)$ at $k = -K_{dim}$. The dominating influence of the forcing is also visible in $\mathcal{D}(x - x')$, which decays somewhat but this saturates for large $|x - x'|$. Also no significant decay is present in the temporal correlation function, defects are however present all be it with much lower density than in the unforced solutions.

This concludes our discussion for the parameter choice $c_2 = -2.5$, $c_3 = 2$. In the remaining part of this section we will briefly look at the behaviour for $c_2 = -20$, $c_3 = 2$ for which the unforced state is severely unstable. Some illustrations of the behaviour are shown in figure 5.21 for a spatially uniform forcing ($K = 0$). One observes directly below the wedge shaped lock-in region already solutions which show similarity with the unforced state (amplitude chaos). This is particularly obvious in the behaviour of $\hat{\mathcal{D}}(k)$. Elsewhere one observes spatially periodic patterns, which show phase locked

Figure 5.17: (Next page) Snapshot of $\phi(x,t)$ (a), spatial correlation function $\hat{\mathcal{D}}(k)$ (b) and $\mathcal{D}(x-x')$ (c) and the temporal correlation function $\mathcal{C}(t-t')$ (d) for $c_2 = -2.5$, $c_3 = 2$ and $\omega = +2$, $F_0 = 0.8$ in the extended system with a plane wave forcing with $\Lambda = 1.5$.

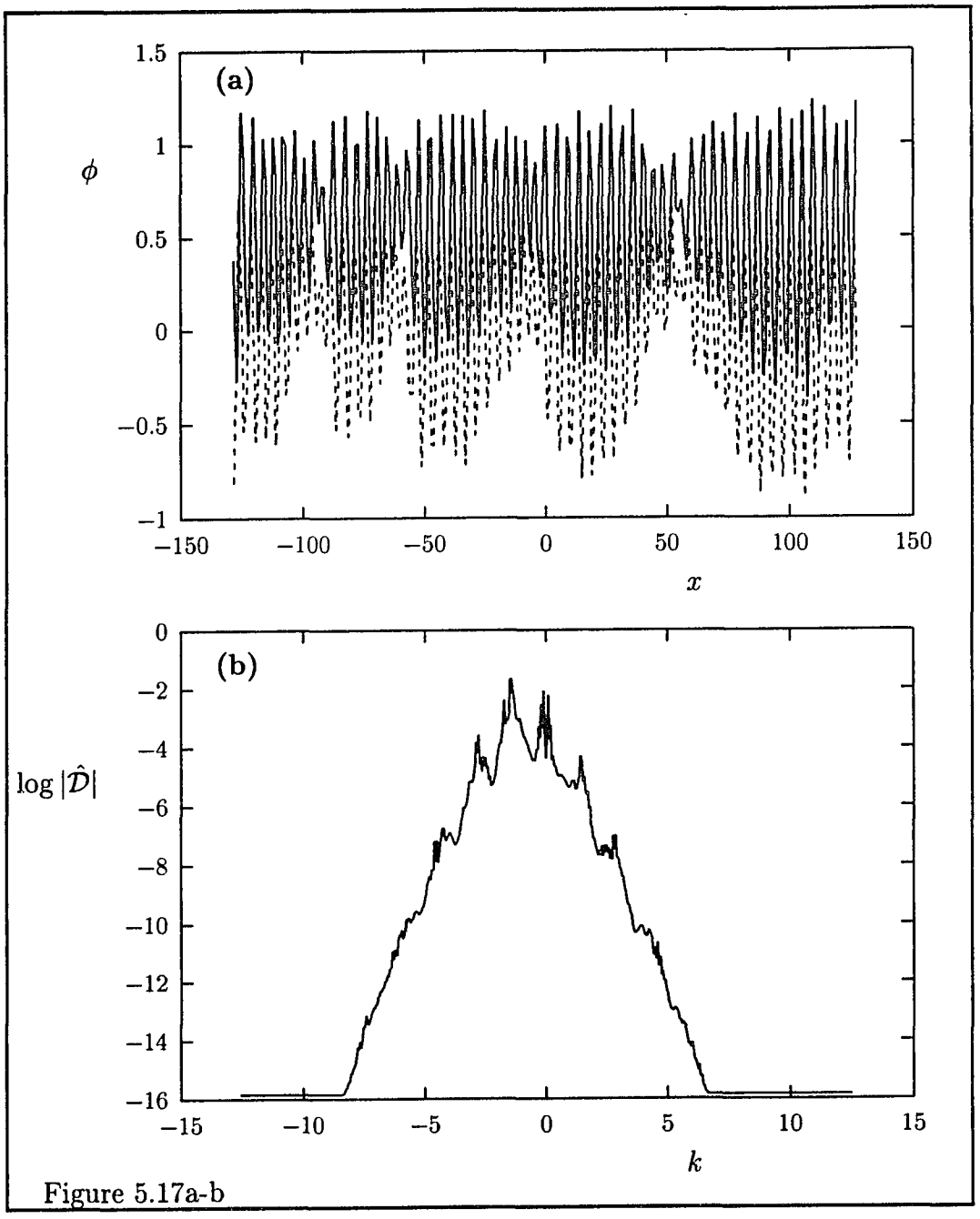

Figure 5.17a-b

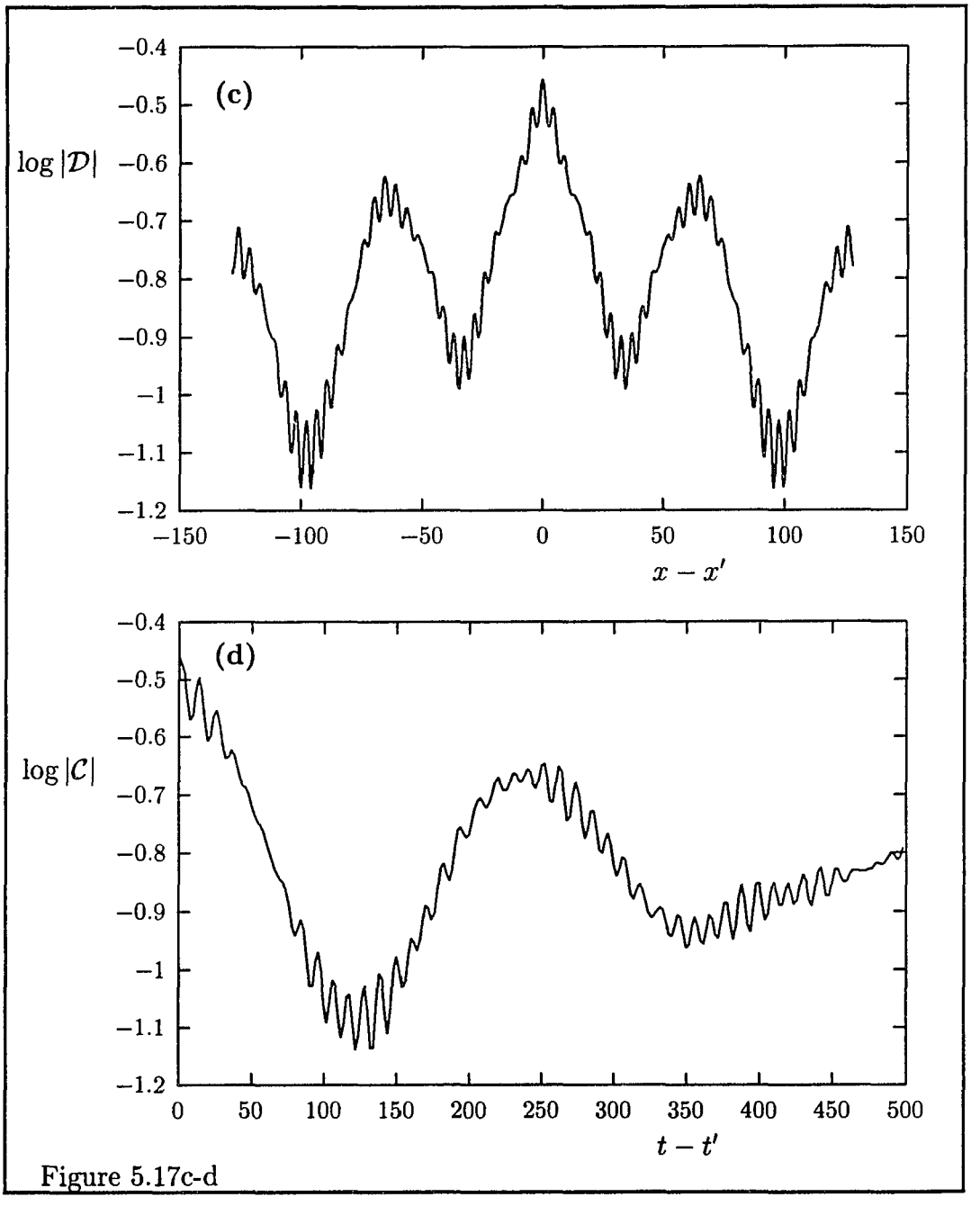

Figure 5.17c-d

Figure 5.18: (Next page) Snapshot of $\phi(x,t)$ (a) (b), spatial correlation function $\hat{\mathcal{D}}(k)$ (c) and $\mathcal{D}(x-x')$ (d), the temporal correlation function $\mathcal{C}(t-t')$ (e) and the linear growth rate (f) (g) (h) for $c_2 = -2.5$, $c_3 = 2$ and $\omega = +2$, $F_0 = 1.8$ in the extended system with a plane wave forcing with $\Lambda = 0.2$.

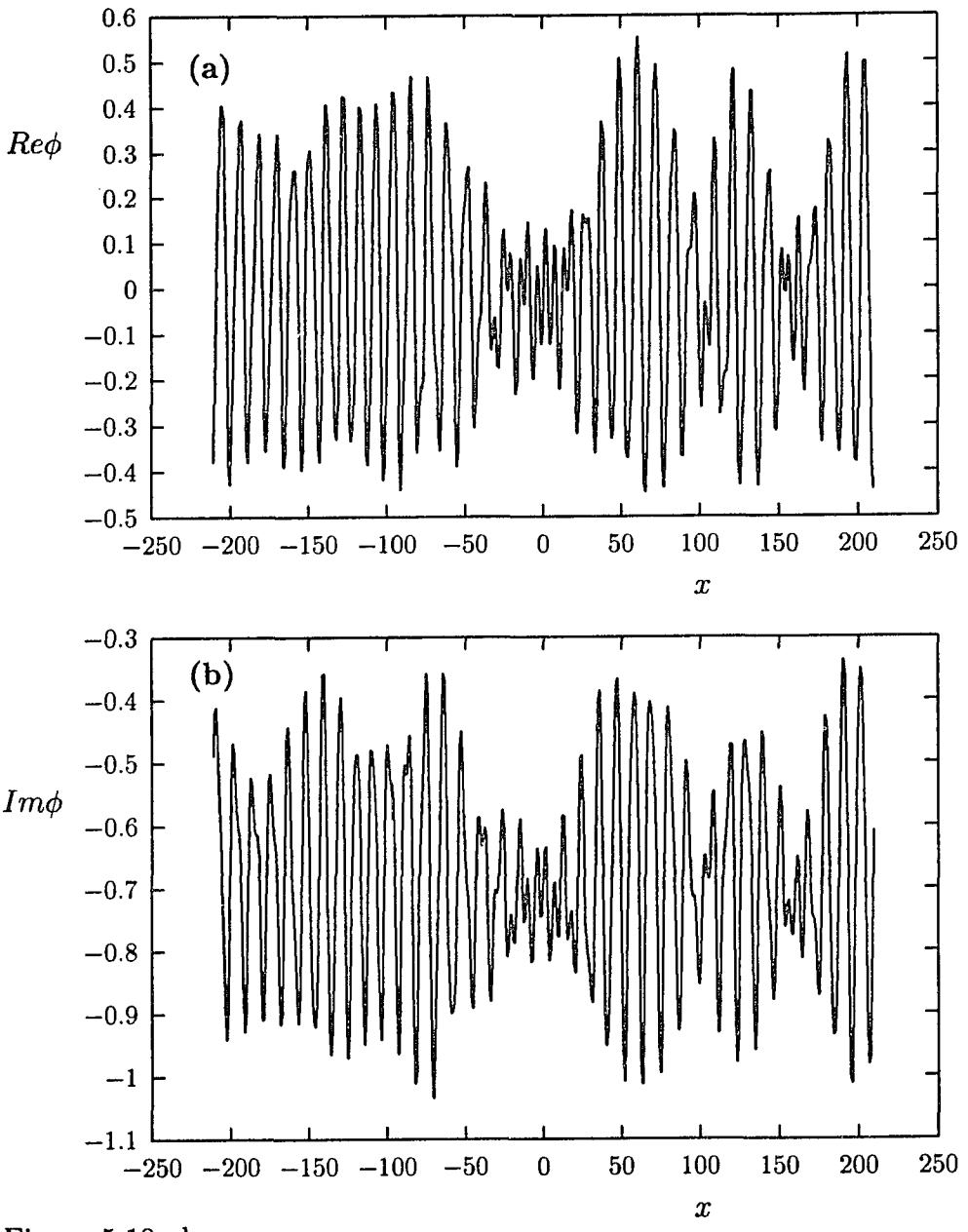

Figure 5.18a-b

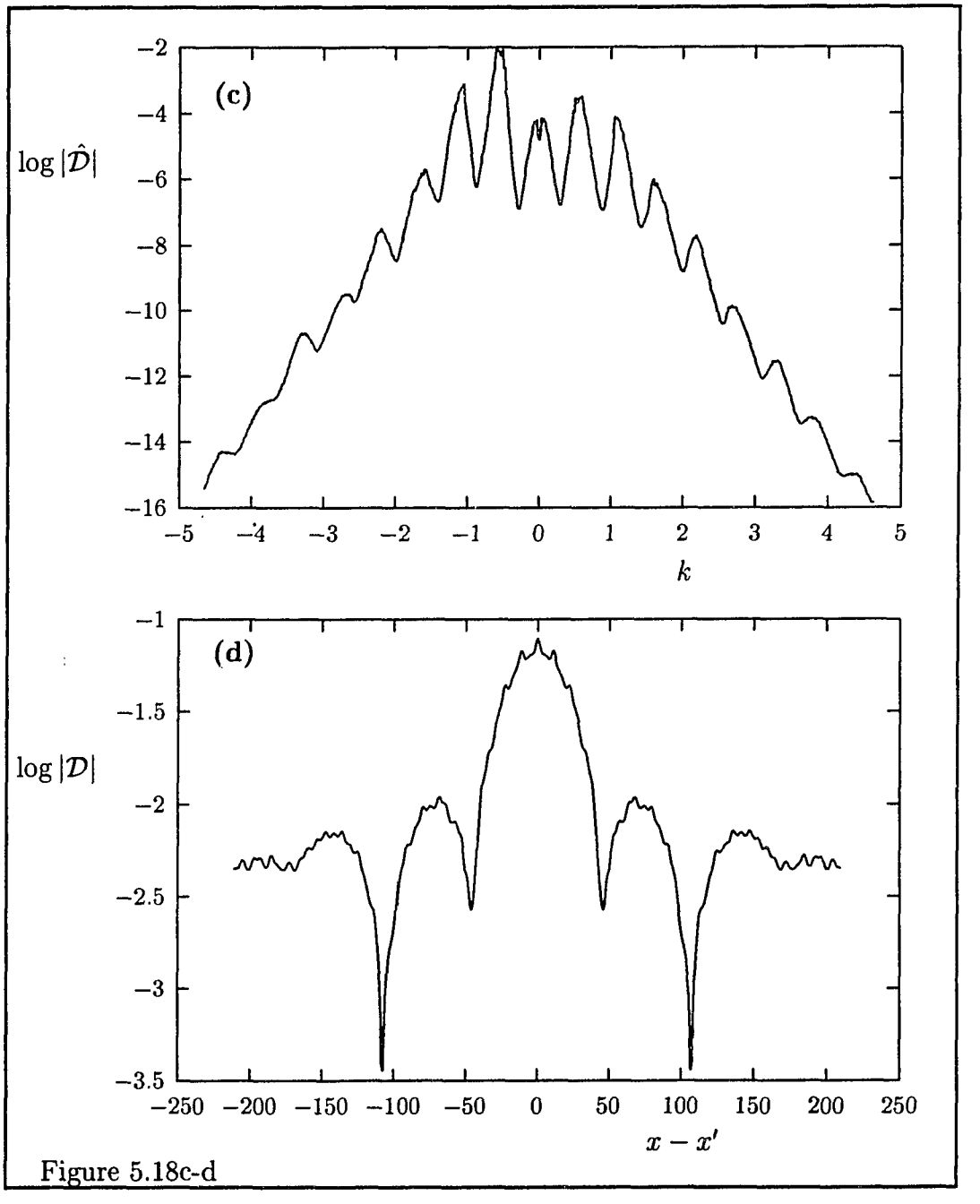

Figure 5.18c-d

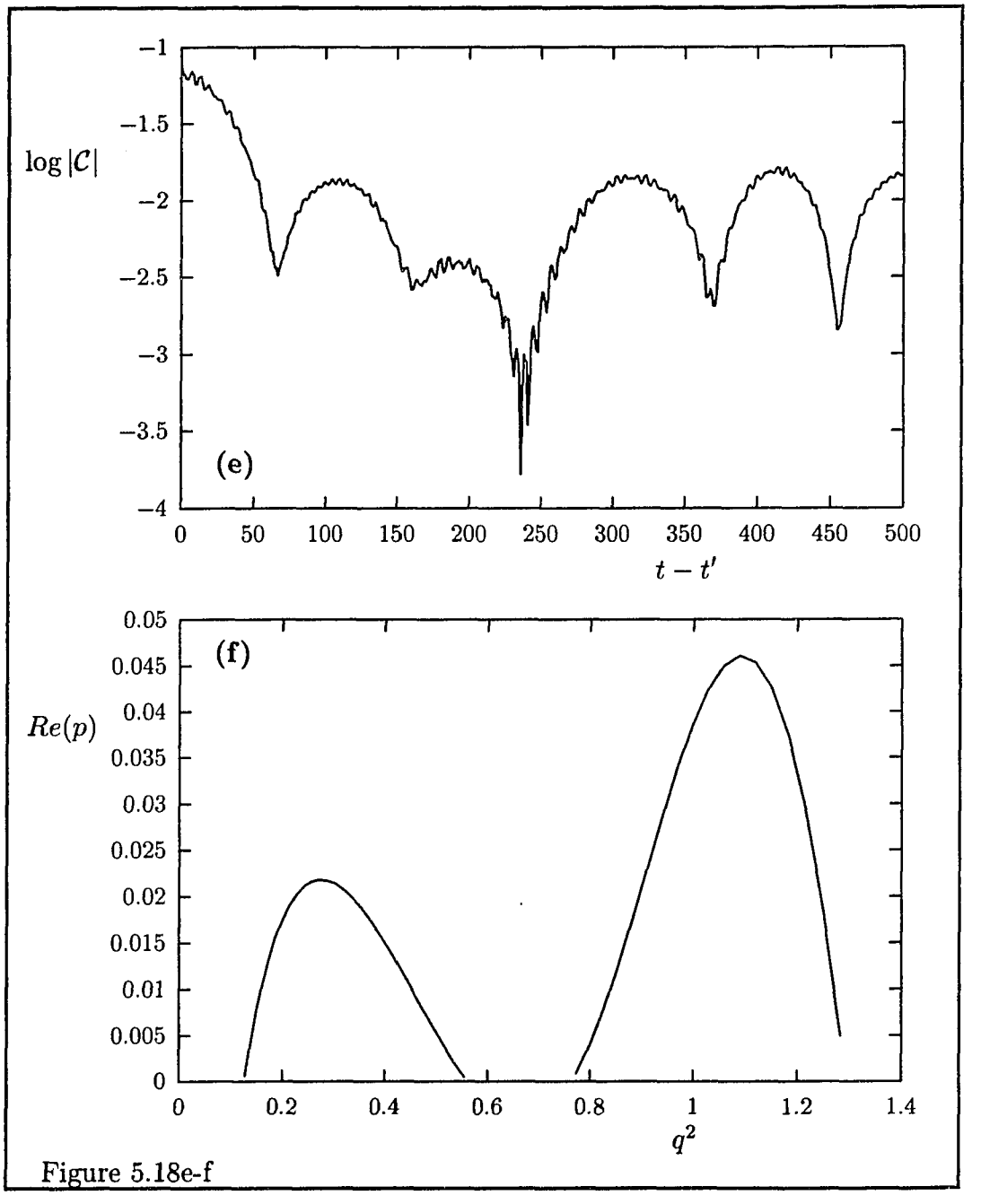

Figure 5.18e-f

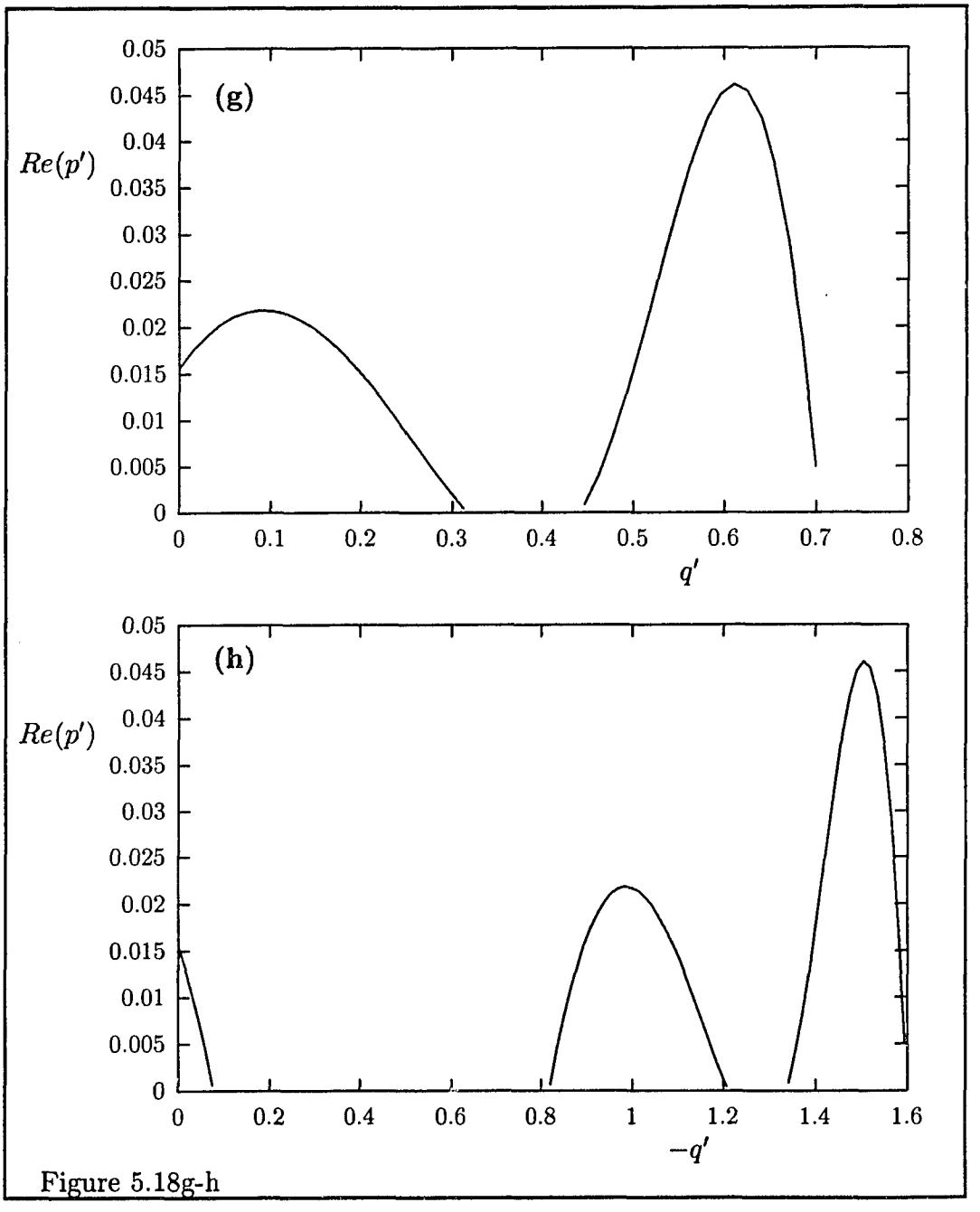

Figure 5.18g-h

Figure 5.19: (Next page) Snapshot of $\phi(x,t)$ (a), spatial correlation function $\hat{\mathcal{D}}(k)$ (b) and $\mathcal{D}(x-x')$ (c) and the temporal correlation function $\mathcal{C}(t-t')$ (d) for $c_2 = -2.5$, $c_3 = 2$ and $\omega = +2$, $F_0 = 1$ in the extended system with a plane wave forcing with $\Lambda = 0.2$.

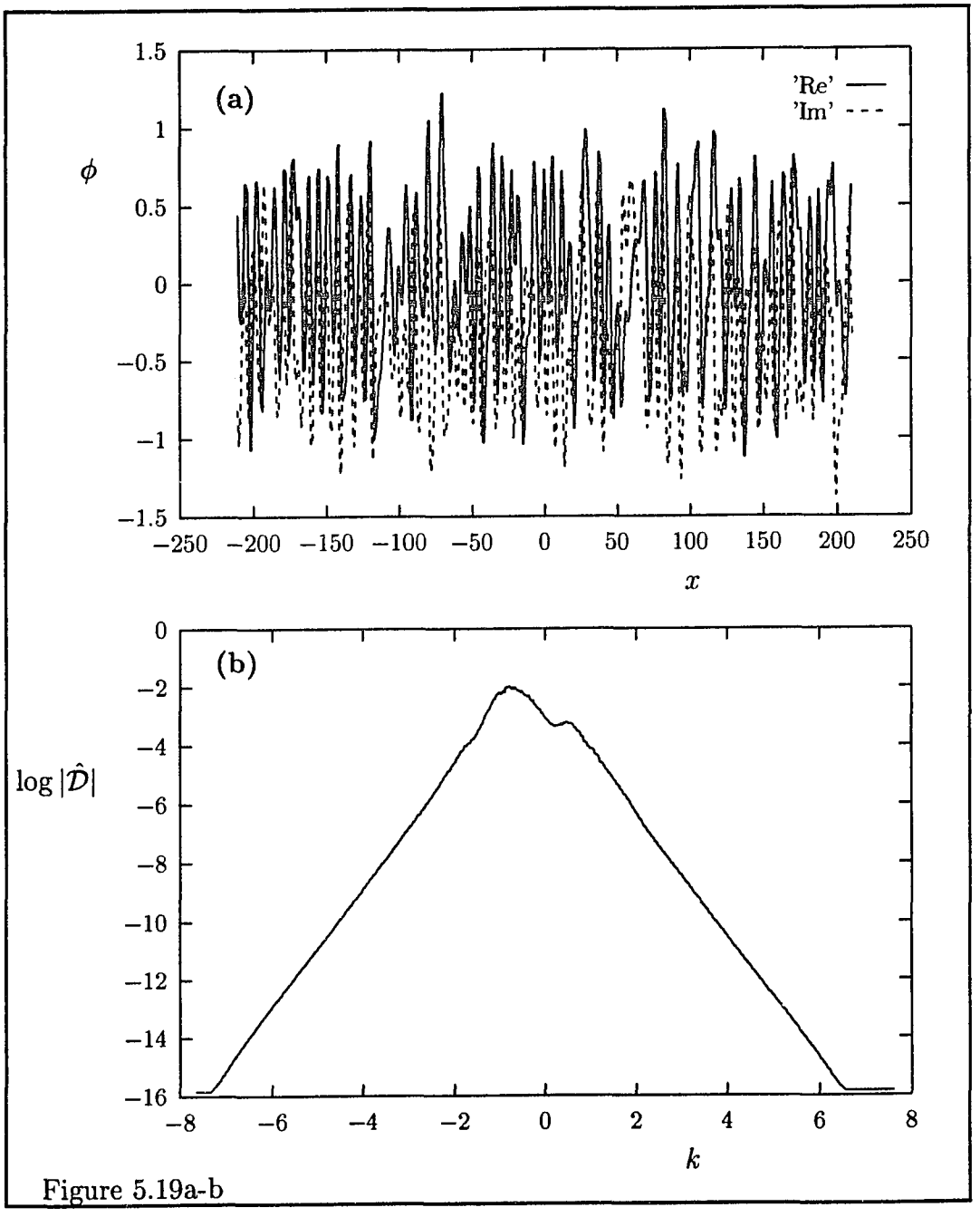

Figure 5.19a-b

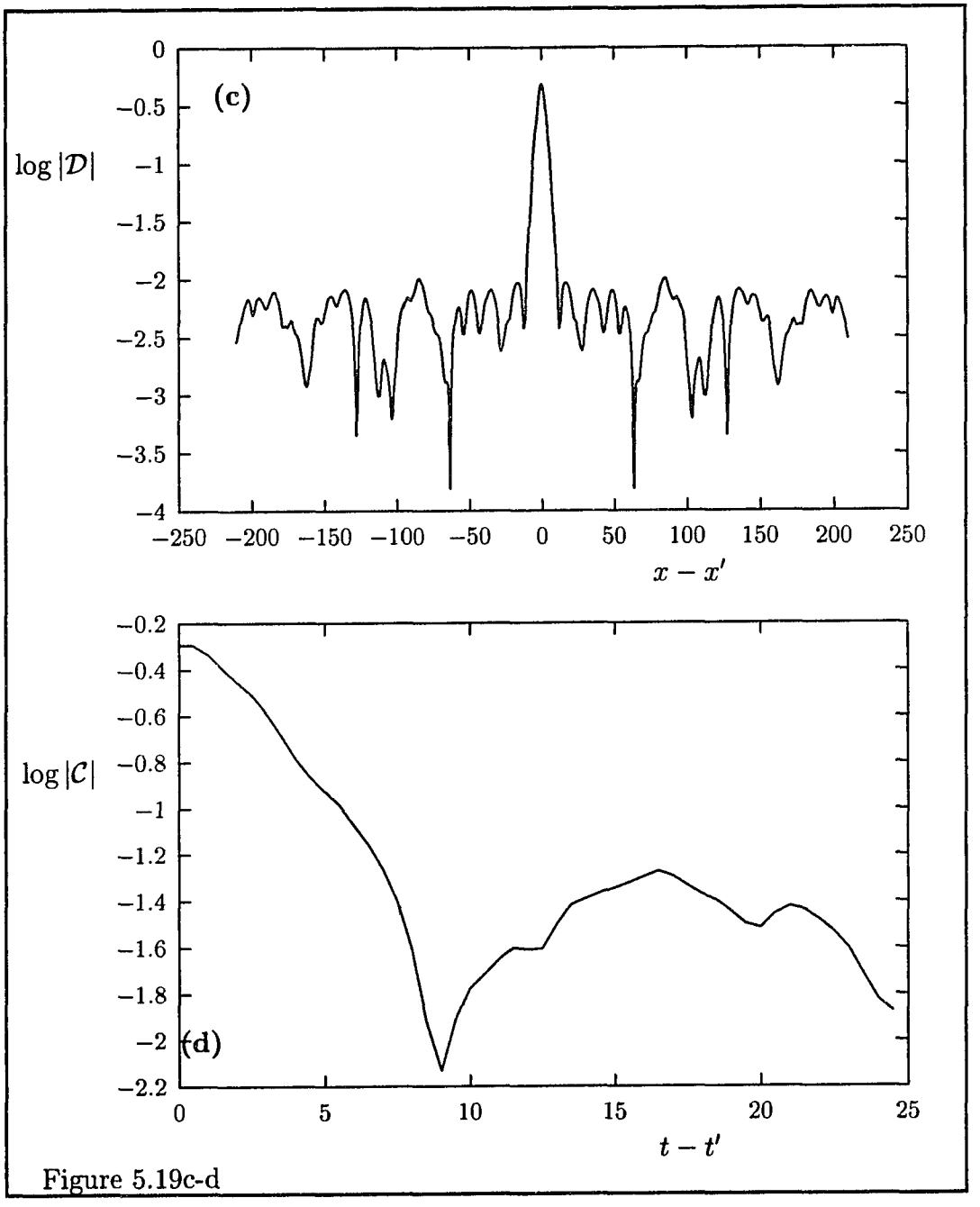

Figure 5.19c-d

Figure 5.20: (Next page) Snapshot of $\phi(x,t)$ (a) (b), spatial correlation function $\hat{\mathcal{D}}(k)$ (c) and the temporal correlation function $\mathcal{C}(t-t')$ (d) for $c_2 = -2.5$, $c_3 = 2$ and $\omega = -3$, $F_0 = 1.5$ in the extended system with a plane wave forcing with $\Lambda = 0.2$.

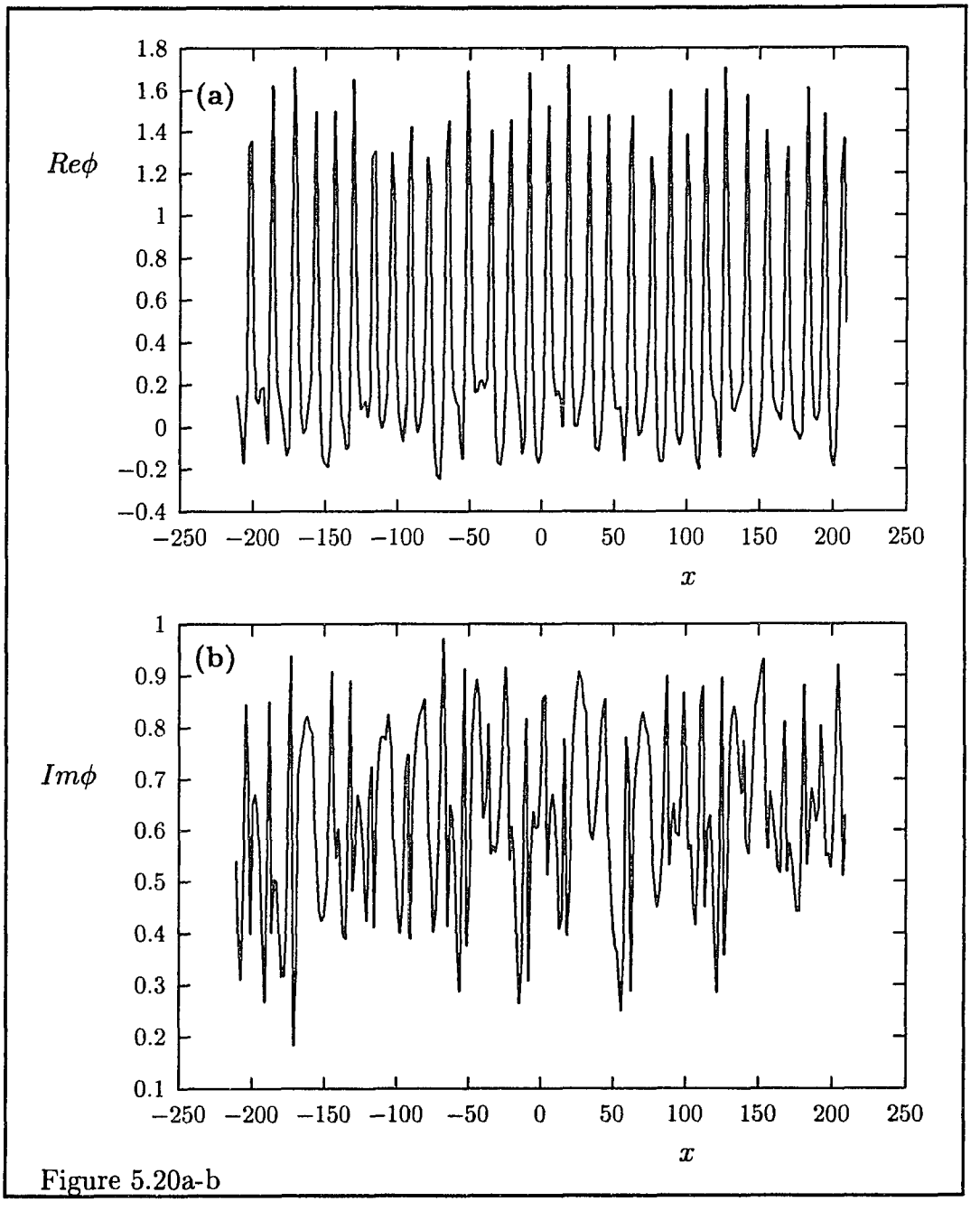

Figure 5.20a-b

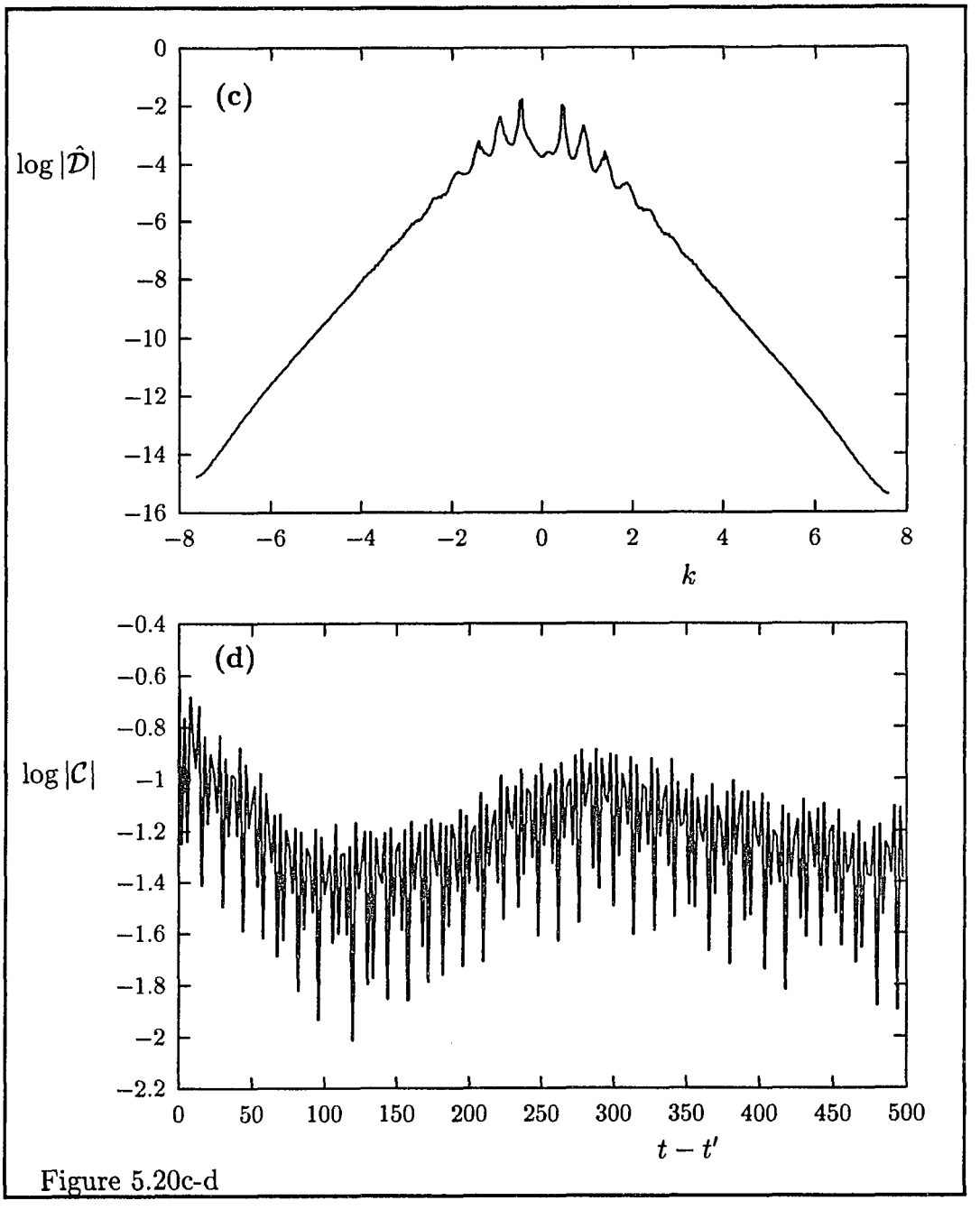

Figure 5.20c-d

($\partial_t \phi = 0$), periodic, quasi-periodic or chaotic behaviour in time. No defects were observed to exist in such states. Spatial period doubling is observed as one decreases F_0, it was not observed to occur more than once for a specific pattern. After this, the spatial behaviour in all cases considered became of a more complex nature. However, for futher decreasing F_0 (but still well above the dashed line below which the $q = 0$ perturbations become unstable) one usually observes the appearance of a new spatially periodic pattern which again sometimes undergoes a period doubling. Summarizing, regions in which spatially periodic patterns exist are separated by regions in which the solutions show spatial disorder.

For a real plane wave forcing some illustrations of the behaviour are shown in figure 5.22. For $\omega = -10$ the wedge shaped lock-in region covers all values of Λ, for $\omega = +2$ lock-in is not possible for $\Lambda < 0.42$, see figure 5.5a-b for an impression. Above the lock-in region for $\omega = -10$ and away or above the lock-in region for $\omega = +2$, one again observes spatially periodic patterns for which much the same can be said as for the patterns observed for $K = 0$. Just below the lock-in region for $\omega = -10$ the spatial correlations show long range disorder, peaks are again observed for the wavenumber of the forcing and the maximally unstable mode. The temporal correlations

also show exponential decay in this case and the solutions are best qualified as amplitude chaos, although no defects are present. For $\omega = +2$ the solutions immediately outside the lock-in region show great similarity with the unforced solution. Defects ocur and the spatial and temoral correlation functions show exponential dacay, $\hat{\mathcal{D}}(k)$ shows an overall smooth behaviour.

In the next chapter a summary will be given of results presented in this work that deserve further study.

Figure 5.21: (Next page) Snapshot of $\phi(x,t)$ (a) (b), spatial correlation function $\hat{\mathcal{D}}(k)$ (c) and the temporal correlation function $C(t-t')$ (d) for $c_2 = -20$, $c_3 = 2$ and $\omega = -10$, $F_0 = 6$ in the extended system with a spatially uniform forcing. Snapshots of ϕ are shown in (e) and (f) for respectively $\omega = +2$, $F_0 = 5$ and $\omega = +2$, $F_0 = 3$ while the other parameters are unchanged.

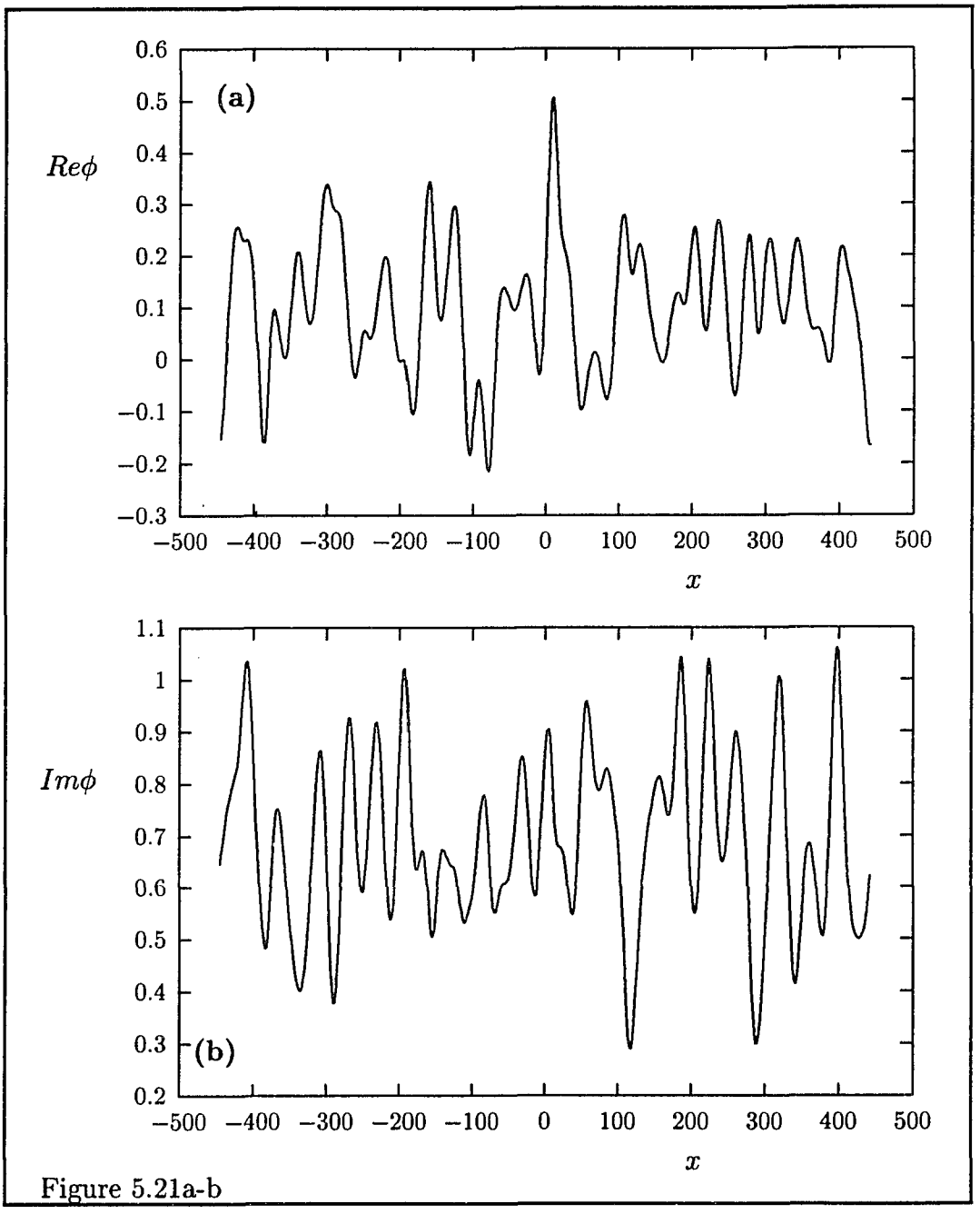

Figure 5.21a-b

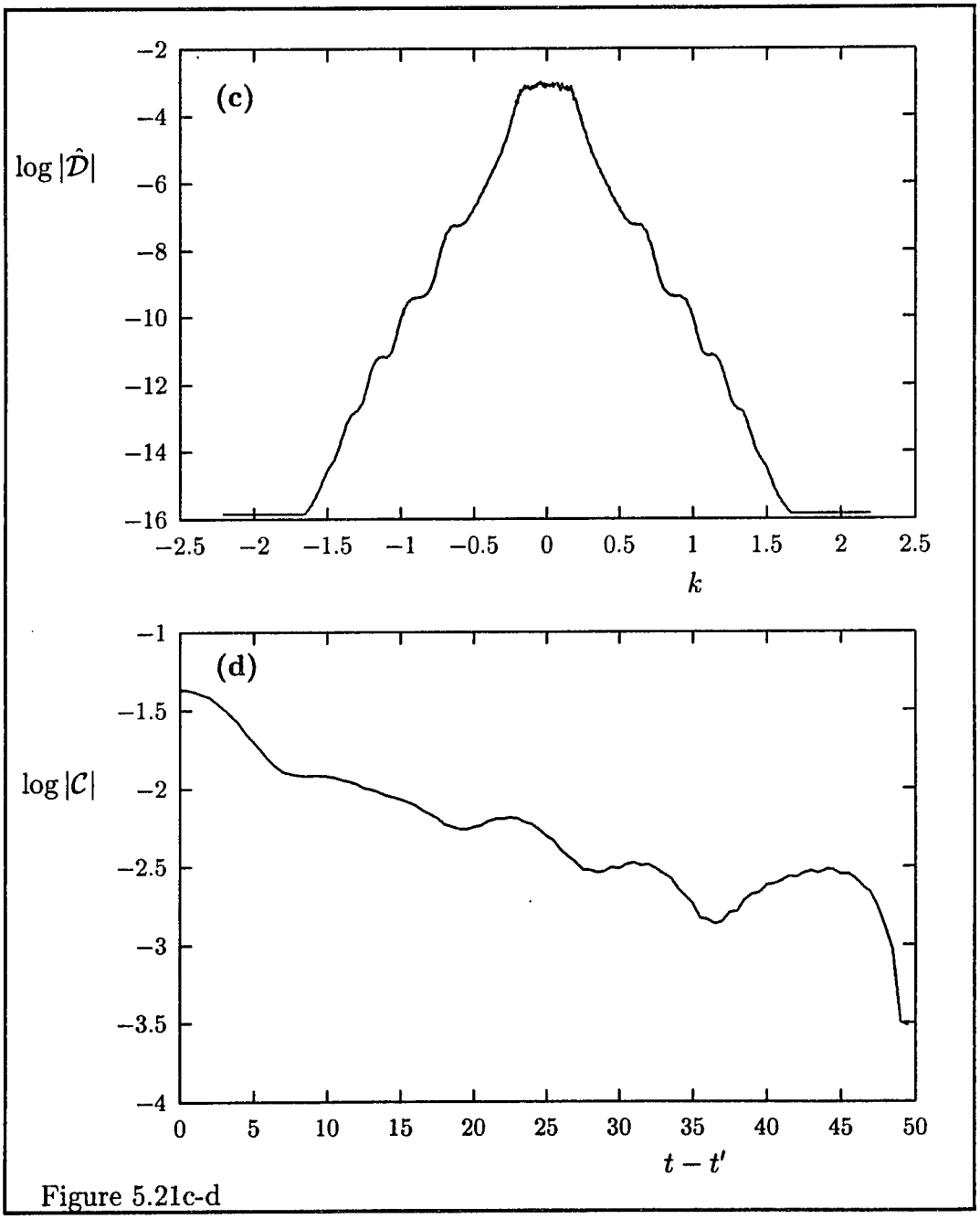

Figure 5.21c-d

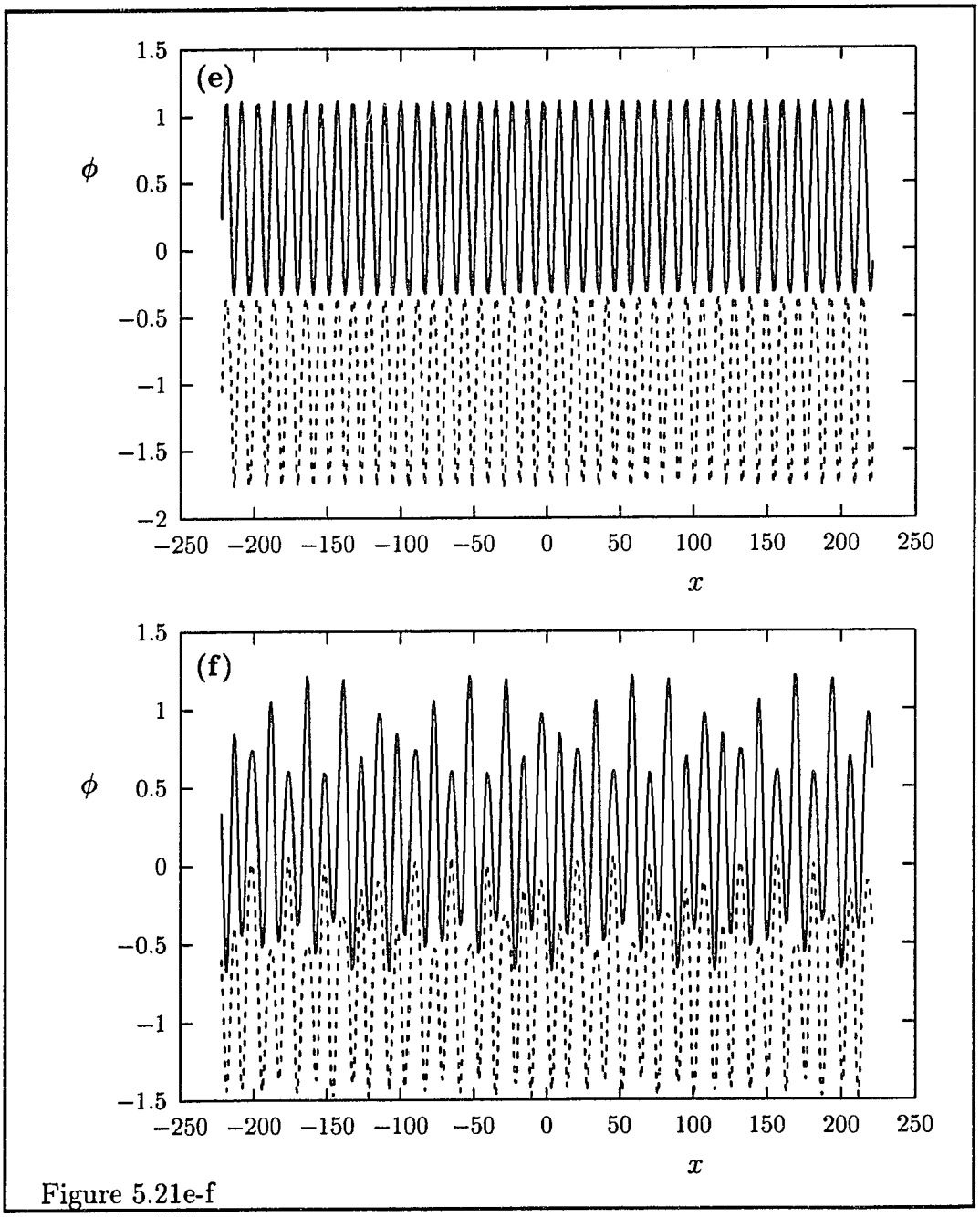

Figure 5.21e-f

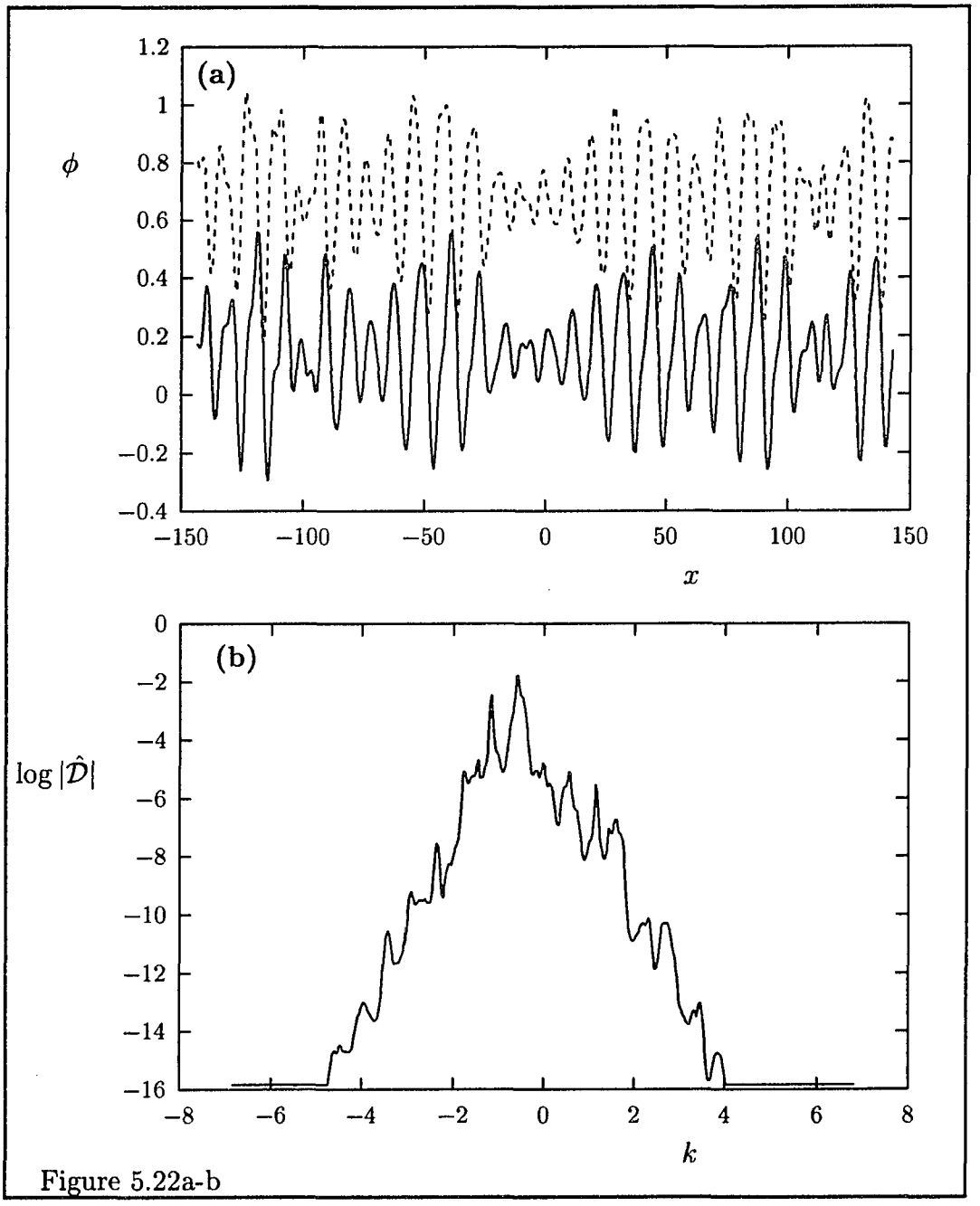

Figure 5.22: Snapshot of $\phi(x,t)$ and spatial correlation function $\hat{\mathcal{D}}(k)$ for $c_2 = -20$, $c_3 = 2$ in the extended system with a plane wave forcing with $\omega = -10$, $\Lambda = 0.3$, $F_0 = 10$ (a) (b) and $\omega = +2$, $\Lambda = 0.5$, $F_0 = 4$ (c) (d).

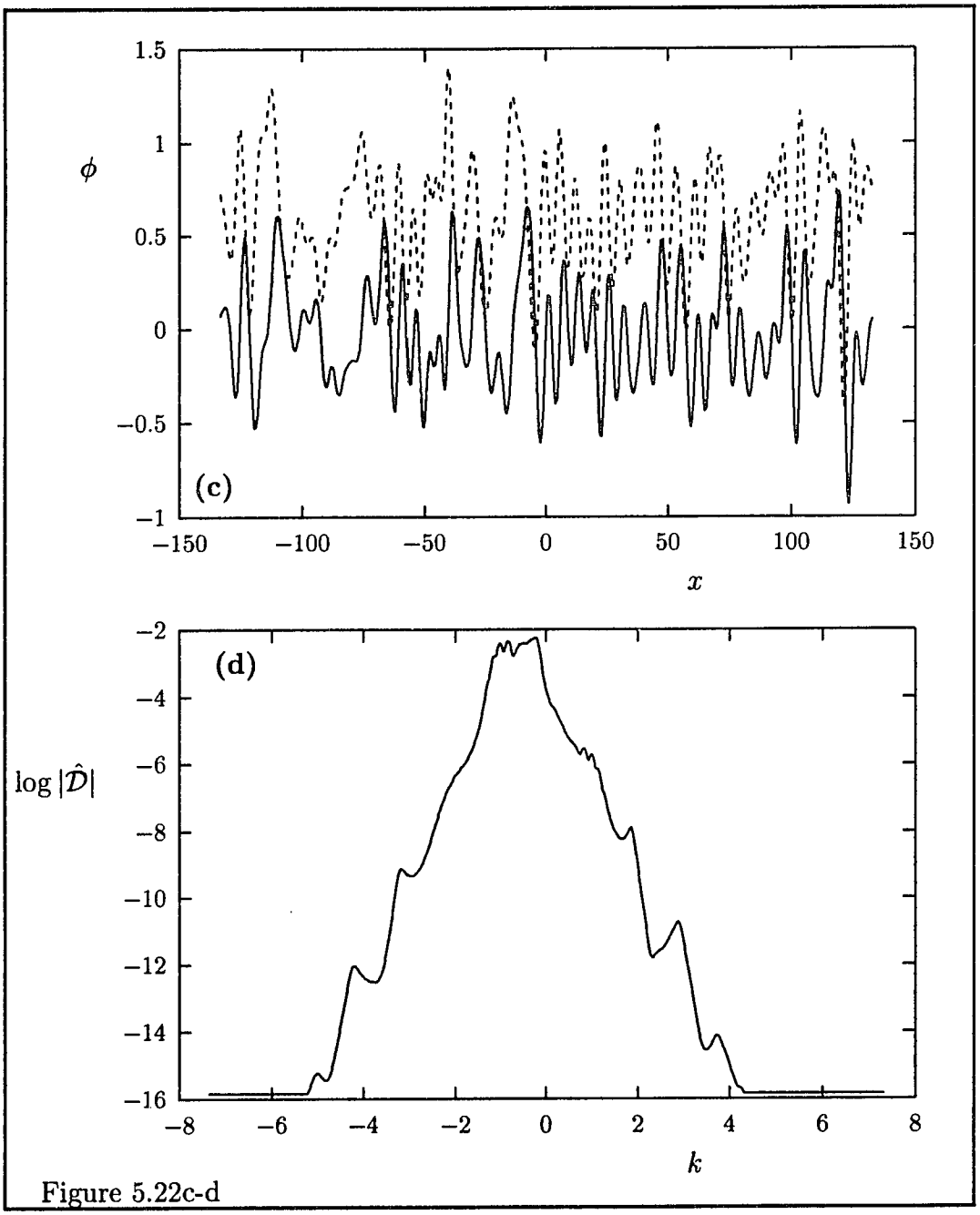

Figure 5.22c-d

Chapter 6

Summary and outlook.

In chapter 3 the phase diagram was obtained for the harmonically forced LE. A classification of the phase diagram based on the value of the natural frequency was given. Stable phase-locked states were shown to exist in all cases for sufficiently large forcing. The possible behaviour other than the lock-in behaviour was scrutinized with care, and it may be said with some confidence that the phase diagram is complete. Outside the stable region for phase-locked states the only stable state is a two frequency quasi-periodic state, of which the analytic form is given by the product of the exponential factor of the forcing and a periodic function. Close to certain parts of the boundary of the lock-in region the quasi-periodic state coexists with a stable

locked-in state.

In chapter 4 the main part of the work concerns the behaviour when the linear growth rate $Re(\sigma)$ is space dependent and of a Gaussian form. Representative examples of a small, intermediate size and large system were discussed. An attempt was made to obtain the bifurcations occurring in these systems as the maximum value of the growth rate (Σ_0) is varied. Initially (small Σ_0), for all system sizes a stationary pulse solution exists, which undergoes a parity breaking bifurcation but remains stationary ($e^{i\omega t}$ time dependence). The examples of the different systems discussed were for fixed parameters $\{c_2, c_3\} = \{-1, 1\}$, which would be precisely at the Benjamin-Feir instability in the spatially uniform system. All systems considered therefore eventually (increasing Σ_0) show a transition to chaotic behaviour.

In small systems, spatial disorder was shown to occur only for very large Σ_0 ($\Sigma_0 > 30$). Except for such large values of Σ_0 the behaviour is chaotic in time but not disorderded in space. The transition to this behaviour from the stationary state takes place via intermittency. A dependence of the temporal behaviour in the intermittent and chaotic regimes on the position in the system was shown to exist. Further analyses is necessary for a more precise description of the parity breaking bifurcation and the intermittency.

In an intermediate size system the behaviour shows qualitative differences in the central region (roughly there where the growth rate is positive) and in the outer regions (roughly there where the growth rate is negative). In the central region a transition to amplitude chaos is shown to occur via quasi-periodic behaviour in time and intermittency. Defects are present as soon as the behaviour becomes quasi-periodic. At the same time in the outer region the motion also becomes chaotic in time, with however one dominant frequency close to the frequency of the stationary puls observed for smaller Σ_0. The solutions decay exponentially in space in the outer regions and their significant size was too small in the example discussed for spatial disorder to occur. Defects do not occur in the outer regions except for the ones that can be contributed to size effects. Interesting for further study are again the parity breaking bifurcation and the intermittency.

Finally, in large unforced systems also a central region and outer regions occur. In the central region a transition to amplitude chaos takes place which is similar to what is observed in intermediate size systems. For larger Σ_0 however, the behaviour shows spatio-temporal intermittency. Two correlation lengths seem to appear, suggesting a state in which spatio-temporal intermittency coexist in the central region with amplitude chaos in its central

part.

A small and an intermediate size system were analyzed in the presence of a Gaussian forcing. The intermediate system was also analyzed for a plane wave forcing. The outlines of the phase diagram were obtained as the forcing strength and amplitude varies. The shape of the lock-in region shows great similarity with that of the LE. For small systems, the similarity also holds for what concerns the dominant behaviour outside the lock-in region, which consists of a quasi-periodic (two frequency) nonsymmetric state. Besides this, small regions exist in the phase diagram in which the behaviour is more complicated, three frequency quasi-periodic motion and temporal chaos are possible.

In the intermediate size system the behaviour for a Gaussian and a plane wave forcing is shown to be similar. Well away from resonance, two spatial regions occur; a central region in which spatio-temporal chaos developes as the forcing strength decreases, and outer regions in which there is lock-in behaviour. For suitably small forcing phase chaos is expected to occur in the central region although this was not verified explicitely. For frequenties around resonance, various spatial regions occur in which the behaviour is qualitatively different. Solutions are shown to exist which show lock-in

behaviour, quasi-periodicity (time) and temporal chaos at the same time in different parts of the system. The size of the spatial regions was too small in the examples considered to observe disorder. Interesting for further study is the change in behaviour as one passes from one region to the other, and of course also the behaviour in the large forced system which has not been addressed here.

In Chapter 5 the supercritical equation with constant coefficients in the presence of a plane wave forcing was analyzed. The lock-in region for plane wave solutions was constructed for finite size systems and extended systems in the Benjamin-Feir unstable regime ($1 + c_2 c_3 < 0$). A classification of the phase diagram in terms of the parameters c_2 and c_3 was shown to be possible. The Benjamin-Feir instability was shown to have the same apearance in the forced system as in the unforced system: for a given sufficiently large forcing, stable plane wave solutions are possible with wave numbers $K^2 < K^2_{max}$. In systems with a severely unstable unforced state however, also a lower limit exists for the wavenumber of stable forced plstable ane wave states; $K^2_{min} < K^2 < K^2_{max}$. A short wavelength regime was shown to exist for which the phase diagram simplifies considerably. This regime is reached in

most cases for finite wave lengths which are of the order of $\left|\frac{Re(\sigma)}{Re(\lambda)}\right|$ to $2\cdot\left|\frac{Re(\sigma)}{Re(\lambda)}\right|$.

The behaviour outside the lock-in region is studied for the extended system for the case that the forced solution shows amplitude chaos. Around resonance, a uniform forcing ($K = 0$) was shown to produce spatially periodic patterns with a period equal to the period of the maximally linearly unstable mode. Period doubling occurs, after which (decreasing forcing amplitude) the behaviour shows more and more long range disorder and eventually amplitude chaos sets in. It was noted that the results suggest that quasi-periodicity in space occurs, although this could not be proven because of the periodic boundary conditions. It was shown that, particularly well away from resonance, classification of the chaotic states in terms of amplitude and phase chaos is not sufficient.

Most interesting for future research is an analyses of the possible transition from spatial quasi-periodicity to spatio-temporal chaos, suggested by the results presented in chapter 5. Also, the behaviour for $K^2 = 1$ as the forcing amplitude decreases to values well away from the lock-in region has not been very extensively analyzed here and may be interesting for further study. The same is true for the situation where the unforced solution shows

phase chaos which has not been addressed here. It must also be mentioned that the CGLE with a plane wave forcing involves quite a large number of possible parameter choices, of which certainly not all relevant ones have been considered in this work.

Finally, it has been clearly demonstrated by the results presented here, that the forced CGLE provides a richer model than the unforced equation with respect to the study of spatio-temporal chaos. Further study of it may contribute to an understanding of this behaviour.

Appendix A

Analyses of the bifurcations of fixed points of the LE.

Here we present the analyses of the bifurcations occurring in the forced LE, given by (3.16) involving the critical points of the equation (local bifurcations).

The linear growth rate $p(\omega, c_3, F_0)$ (eq. (3.7)) for a critical point $u_0(\omega, c_3, F_0)$ is given by

$$p_{1,2} = 1 - 2|u_0|^2 \pm \sqrt{(1 + c_3^2)|u_0|^4 - (\omega + 2c_3|u_0|^2)^2}. \qquad \text{(A.1)}$$

A critical point u_0 is a spiral whenever

$$\begin{aligned} u_2^2 < |u_0|^2 < u_1^2 \qquad & \text{if } c_3^2 < 1/3\,, \\ |u_0|^2 < u_1^2 \text{ or } |u_0|^2 > u_2^2 \quad & \text{if } c_3^2 > 1/3\,, \end{aligned} \tag{A.2}$$

where

$$u_{1,2}^2 = \frac{-2\omega c_3 \pm |\omega|\sqrt{1+c_3^2}}{3c_3^2 - 1}. \tag{A.3}$$

A critical point is a saddle whenever it is not a spiral and

$$(1 - 2|u_0|^2)^2 - (1 + c_3^2)|u_0|^4 + (\omega + 2c_3|u_0|^2)^2 < 0. \tag{A.4}$$

In any other case the critical point u_0 is a node. Spirals or nodes are sinks if $|u_0|^2 > 1/2$.

One immediate observation we make by comparing (A.4) with (3.9) is that the only candidates for saddles occur for $A_{L-}^2 < |u_0|^2 < A_{L+}^2$. This then implies, since A_{L-} and A_{L+} are the extrema of $f_{c_3,\omega}(A_L)$, that there is at most one saddle point, and it rules out the possibility of saddle connections. It is easy to prove that all candidates for saddles are indeed saddles. For $c_3^2 > 1/3$ we have for $\omega < 0$: $u_1^2 \geq A_{L+}^2$, $u_2^2 \leq A_{L-}^2$ and for $\omega > 0$: u_1^2, $u_2^2 < 0$, finally: $\omega_+' < 0$ for all ω. For $c_3^2 < 1/3$ we have $u_1^2 < 0$ and $u_2^2 \leq A_{L-}^2$.

Codimension two bifurcations occur in two points in the phase diagram. For $c_3^2 > 1/3$ they occur in $F_+(\omega_+)$ and $F_-(\omega_-)$, for $c_3^2 < 1/3$ they occur in

$F_-(\omega_+)$ and $F_-(\omega_-)$. In these points many lines come together, on which other bifurcations (codimension one) occur. Careful bookkeeping enables us to construct the complete phase diagram analytically as far as local bifurcations are concerned.

On the basis of the above results we have performed an extensive numerical search for other possible bifurcations, using a Runge-Kutta integration scheme. The result of this search are the bistable regions **B1**, **B2** and **B3** discused in chapter 3. Besides these no other bifurcations were observed.

Appendix B

The periodic solution of the LE in the limit of small forcing.

In this appendix we will show that (3.16) has a stable periodic state $u_P(t)$ with period $T_P = \frac{2\pi}{|\omega+c_3|}$ for $F_0 < d$, where d is some positive constant. We will first show that such a solution $u_P(t)$ exists.

Write

$$u_P(t) = u_0 + g(t) + f(t) \tag{B.1}$$

where u_0 is uniquely determined by

$$[i\omega - 1 + (1 + ic_3)|u_0|^2]u_0 = F_0 \tag{B.2}$$

and $g(t) = \sqrt{1-2|u_0|^2}e^{i\Omega t}$, $\Omega = -(\omega + c_3)$. Then the function $g(t)$ satisfies the equation

$$i\omega g + \frac{dg}{dt} - g + (1 + ic_3)[2|u_0|^2 g + |g|^2 g] = 0 \tag{B.3}$$

and the equation for $f(t)$ becomes

$$(i\omega + \tfrac{d}{dt} - 1)f + (1 + ic_3)[2|u_0|^2 f + u_0^*(g^2 + 2gf + f^2)$$

$$+u_0^2(g^* + f^*) + 2u_0[|g|^2 + g^* f + f^* g + |f|^2] \tag{B.4}$$

$$+2|g|^2 f + g^* f^2 + g^2 f^* + 2g|f|^2 + |f|^2 f] \;=\; 0$$

We now expand $f(t)$ in a Fourier series

$$f(t) = \sum_n e^{i\Omega n t} f_n \,, \tag{B.5}$$

$$f_n = \frac{1}{T_P}\int_0^{T_P} f(t) e^{-i\Omega n t} dt \tag{B.6}$$

and we expand the Fourier components in some small parameter ϵ (to be identified later),

$$f_n = \sum_{i=1}^{\infty} \epsilon^i f_{n,i} \,. \tag{B.7}$$

We have

$$(f^2)_{q,p} = \sum_n \sum_{i=1}^{p-1} f_{n,i} f_{q-n,p-i}(1 - \delta_{p,0})(1 - \delta_{p,1}) \,, \tag{B.8}$$

$$(|f|^2)_{q,p} = \sum_n \sum_{i=1}^{p-1} f_{n,i} f^*_{q+n,p-i} (1-\delta_{p,0})(1-\delta_{p,1}) \,, \tag{B.9}$$

$$(|f|^2 f)_{q,p} = \sum_{n,m} \sum_{i=1}^{p-1} \sum_{j=1}^{p-1} f_{n,i} f^*_{m,j} f_{q+m-n,p-i-j} (1-\delta_{p,0})(1-\delta_{p,1})(1-\delta_{p,2}) \,. \tag{B.10}$$

If we denote $|g| = \alpha$ we have in first order

$$\begin{aligned} &(i\omega + iq\Omega - 1) f_{q,1} \\ &+(1+ic_3)\left[u_0^* \alpha^2 \delta_{q,2} + 2u_0 \alpha^2 \delta_{q,0} + 2\alpha^2 f_{1,q} + \alpha^2 f^*_{1,2-q}\right] \;=\; 0 \,, \end{aligned} \tag{B.11}$$

$$\begin{aligned} &(-i\omega - (2-q)i\Omega - 1) f^*_{2-q,1} \\ &+(1-ic_3)\left[u_0 \alpha^2 \delta_{q,2} + 2u_0^* \alpha^2 \delta_{q,0} + 2\alpha^2 f^*_{1,2-q} + \alpha^2 f_{1,q}\right] \;=\; 0 \,. \end{aligned} \tag{B.12}$$

This is a set of linear equations, written in short

$$\mathcal{M}(q,1) \begin{bmatrix} f_{q,1} \\ \\ f^*_{2-q,1} \end{bmatrix} = \begin{bmatrix} C(q,1) \\ \\ C^*(2-q,1) \end{bmatrix} . \tag{B.13}$$

In general *det* $\mathcal{M}(q,1) \neq 0$ and $C(q,1) = 0$ for all q except $q = 0$ or $q = 2$.

Hence $f_{q,1} = 0$ for $q \neq 0, 2$ and we find

$$f_{0,1} = \frac{-2u_0\alpha^2(1+ic_3)(-i\omega + 2i\Omega - 1 + 2\alpha^2(1-ic_3)) + u_0\alpha^4(1+c_3^2)}{(i\omega - 1 + 2\alpha^2(1+ic_3))(-i\omega + 2i\Omega - 1 + 2\alpha^2(1-ic_3)) - \alpha^4(1+c_3^2)} \,, \tag{B.14}$$

$$f_{2,1} = \frac{-u_0\alpha^4(1-ic_3) - (1-ic_3)\alpha^2 f_{0,1}}{-i\omega + (2-q)i\Omega - 1 + 2\alpha^2(1-ic_3)} \tag{B.15}$$

From this the small parameter appears to be $\epsilon = |u_0|$. We will see later on

that $|u_0|$ is indeed a consistent expansion parameter. Second order gives us

$$\begin{aligned}
&(i\omega + iq\Omega - 1) f_{q,2} \\
&+(1+ic_3)\left[2u_0^*\alpha f_{q-1,1} + u_0^2\alpha\delta_{q,-1} + 2u_0[\alpha f_{q+1,1} + \alpha f^*_{1-q,1}]\right. \\
&\left.+2\alpha^2 f_{q,2} + \alpha\textstyle\sum_n f_{n,1} f_{q-n+1,1} + \alpha^2 f^*_{2-q,2} + 2\alpha\textstyle\sum_n f_{n,1} f^*_{-q+n+1,1}\right] \;=\; 0\,.
\end{aligned} \tag{B.16}$$

This is of the same form as (B.10),

$$\mathcal{M}(q,2)\begin{bmatrix} f_{q,2} \\ f^*_{2-q,2} \end{bmatrix} = \begin{bmatrix} C(q,2) \\ C^*(2-q,2) \end{bmatrix}, \tag{B.17}$$

moreover, the matrix $\mathcal{M}(q,2)$ is identical to $\mathcal{M}(q,1)$:

$$\mathcal{M}(q,2) = \mathcal{M}(q,1)\,. \tag{B.18}$$

Since in general $det\ \mathcal{M}(q,1) \neq 0$ and $C(q,2) = 0$ for $q \neq 1,-1,3$ we have that $f_{q,2} = 0$ for $q \neq 1,-1,3$. Further we observe that $f_{1,2}$ couples with itself while $f_{-1,2}$ couples with $f_{3,2}$, the constants $C(q,2)$ depend on results obtained in first order.

In p^{th} order we obtain

$$(i\omega + iq\Omega - 1) f_{q,p}$$

$$+(1+ic_3)\left[2|u_0|^2 f_{q,p-2} + u_0^* \alpha^2 \delta_{q,2}\delta_{p,1} + 2u_0^* \alpha f_{q-1,p-1}\right.$$

$$+u_0^* \textstyle\sum_n \sum_{i=1}^{p-2} f_{n,i} f_{q-n,p-1-i} + u_0^2 \alpha \delta_{q,-1}\delta_{p,2} + u_0^2 f^*_{q,p-2}$$

$$+2u_0[\alpha^2 \delta_{q,0}\delta_{p,1} + \alpha f_{q+1,p-1} + \alpha f_{1-q,p-1} + \textstyle\sum_n \sum_{i=1}^{p-2} f_{n,i} f^*_{q+n,p-1-i}]$$

$$+2\alpha^2 f_{q,p} + \alpha \textstyle\sum_n \sum_{i=1}^{p-1} f_{n,i} f_{q+1-n,p-i} + \alpha^2 f^*_{2-q,p}$$

$$\left.+2\alpha \textstyle\sum_n \sum_{i=1}^{p-1} f_{n,i} f^*_{q+n-1,p-i} + \sum_{n,m} \sum_{i=1}^{p-2} \sum_{j=1}^{p-2} f_{n,i} f^*_{m,j} f_{q+m-n,p-i-j}\right] \;=\; 0\,. \tag{B.19}$$

From this equation we first of all observe that $\epsilon = |u_0|$ is a consistent expansion parameter. The equation is again of the form

$$\mathcal{M}(q,p) \begin{bmatrix} f_{q,p} \\ f^*_{2-q,p} \end{bmatrix} = \begin{bmatrix} C(q,p) \\ C^*(2-q,p) \end{bmatrix}, \tag{B.20}$$

where $C(q,p)$ is determined by results obtained in previous orders and

$$\mathcal{M}(q,p) = \mathcal{M}(q,1)\,. \tag{B.21}$$

So in general $det\ \mathcal{M}(q,p) \neq 0$ and (B.15) has a unique solution. There always exists a $\delta_1 > 0$ such that the expansion is uniform convergent for $|u_0| < \delta_1$. This completes the proof of the existence of the periodic solution $u_P(t)$ for $F_0 < d_1$, where d_1 is some positive constant.

To test the linear stability of $u_P(t)$ we write $u_P(t) = u_0 + G(t)$, that is $G(t) = g(t) + f(t)$. This yields an autonomous equation for $G(t)$ which is simply given by (B.3) if we replace $g(t) \to G(t)$. Linearization, $G(t) \to G(t) + \delta G(t)$, then gives an equation for $\delta G(t)$ of the form

$$\frac{d}{dt}\begin{bmatrix} \delta G \\ \delta G^* \end{bmatrix} = \mathcal{A}(G, G^*)\begin{bmatrix} \delta G \\ \delta G^* \end{bmatrix}, \tag{B.22}$$

where

$$\mathcal{A}(G, G^*) = \begin{bmatrix} 1 - i\omega + (1 + ic_3)[2|u_0|^2 + 2u_0^* G + 2u_0 G^* + 2|G|^2] & \\ (u_0^*)^2 + 2u_0^* G^* + (G^*)^2 & \end{bmatrix} \tag{B.23}$$

$$\begin{bmatrix} u_0^2 + 2u_0 G + G^2 \\ 1 + i\omega + (1 - ic_3)[2|u_0|^2 + 2u_0^* G + 2u_0 G^* + 2|G|^2] \end{bmatrix}. \tag{B.24}$$

The characteristic exponents of this equation are $\lambda_1 = 0$ and

$$\lambda_2 = \frac{1}{T_P}\int_0^{T_P} Tr\ \mathcal{A}\ dt\ . \tag{B.25}$$

The criterion for stability of $u_P(t)$ is $\lambda_2 < 0$, up to second order in $|u_0|^2$ we obtain

$$-1 - [-2|u_0|^2 + 4Re(u_0^* f_{0,1}) + 2|f_{0,1}|^2 + 2|f_{2,1}|^2 \tag{B.26}$$

$$+4Re(f_{1,2})(1 - 2|u_0|^2)^{1/2} + \mathcal{O}(|u_0|^4)] \;<\; 0\,.$$

There always exists a $\delta_2 > 0$ so that this inequality is satisfied for $|u_0| < \delta_2$. Hence $u_0(t)$ is stable for $F_0 < d_2$ with d_2 some positive constant. This completes the proof that the periodic solution $u_P(t)$ exists and is stable for $F_0 < d$ with $d = min[d_1, d_2]$.

Appendix C

Numerical details.

In this appendix the essential details behind the numerical methods used in this work will be given. Section **C.1** gives a describtion of the solution method used for equation (4.23). In section **C.2** it will be explained how this same method was used to obtain periodic (time) solutions for arbitrary periodic forcing of equation (3.1). The fast Fourier transform is briefly discussed in section **C.3**. Finally, the Split Step Fourier method is discussed in section **C.4**.

C.1 Phase-locked solutions.

Here we will discuss the numerical solution method of equation (4.23). This equation is an algebraic nonlinear equation in the Fourier components of the solution of the original partial differential equation. To numerically solve it the NAG library routine C05PBF was used. This is an easy to use routine based on a modification of the Powell hybrid method [47]. Under reasonable conditions, this guarantees global convergence for starting points far from the solution and a fast rate of convergence. The Jacobian of the system has to be provided and it is updated by the rank -1 method of Broyden. At the starting point the Jacobian is evaluated, but it is not updated until the rank -1 method fails to give satisfactory progress.

The routine works for real systems with real variables. Let N be the number of Fourier components and $a_i = Re\hat{\phi}_i$ and $a_{i+N} = Im\hat{\phi}_i$, $i = 1, \ldots, N$. For phase locked solutions $\partial_t a_i = 0$ one then has to solve

$$f_m(a_l) = 0, \qquad m, l = 1, \ldots, 2N \tag{C.1}$$

where $f_i = Re(z_i)$, $f_{i+N} = Im(z_i)$, $i = 1, \ldots, N$ and

$$z_i = (i\omega - \mu_1 + k_i^2 \Lambda(1 + ic_2))\hat{\phi}_i$$

$$+\sum_{j=1}^{N}\mu_2(1+ic_3)(|\phi(x)|^2)_{i-j}\hat{\phi}_j - F_i. \tag{C.2}$$

The Jacobian of the system

$$J_{m,l} = \frac{\partial f_m}{\partial a_l} \tag{C.3}$$

is most easily evaluated if one uses

$$\frac{\partial}{\partial a_i} = \frac{\partial}{\partial \hat{\phi}_i} + \frac{\partial}{\partial \hat{\phi}_i^*},$$
$$\frac{\partial}{\partial a_{i+N}} = i\left(\frac{\partial}{\partial \hat{\phi}_i} - \frac{\partial}{\partial \hat{\phi}_i^*}\right). \tag{C.4}$$

Then

$$J_{i,j} = Re(A_{i,j} + B_{i,j})$$
$$J_{i,j+N} = Im(B_{i,j} - A_{i,j})$$
$$J_{i+N,j} = Im(A_{i,j} + B_{i,j})$$
$$J_{i+N,j+N} = Re(A_{i,j} - B_{i,j}), \tag{C.5}$$

where

$$A_{i,j} = (i\omega - \mu_1 + \Lambda(1+ic_2)k_i^2)\delta_{i,j} + 2\mu_2(1+ic_3)(|\phi(x)|^2)_{i-j},$$
$$B_{i,j} = \mu_2(1+ic_3)(\phi^2(x))_{i+j}. \tag{C.6}$$

The linear stability is tested by writing

$$a_m(t) = a_{0,m} + \delta a_m(t) \tag{C.7}$$

where $a_{0,m}$ is a solution of (C.1). Writing $\delta a_m(t) = \delta a_{0,m} e^{is_m t}$ the dispersion relation s_m follows from

$$det(J_{m,n} - s_m \delta_{s,m}) = 0. \tag{C.8}$$

Stability requires $s_m < 0$ for all $m = 1, \ldots, 2N$.

Crucial factors in obtaining a numerical solution of (C.1) are the starting point and the possible vanishing of the Jacobian on the way to or at the actual solution. If the Jacobian vanishes somewhere on the way, the routine will end there without obtaining a solution. Being familiar with the Landau equation ($N = 2$) for which there are usually two such points in which $J = 0$, it is not surprising that by actually doing the computation for $N > 2$ one finds that the vanishing of $J_{m,n}$ is a serious obstacle for obtaining a solution. A simple but effective way of dealing with this problem is to make use of the property that the routine can find solutions far from the starting point. We observe from the LE that stable solutions can always be reached without passing a point where $J = 0$, either from $\Psi = 0$ or for Ψ sufficiently far away from the origin. In some cases both starting points will give a stable solution, corresponding to solutions in the bistable regions in the phase diagram. Assuming that such a property is in some way also true for the

CGLE, the following remedy was used. Whenever the routine stranded at a point where $J = 0$, the distance of the starting point to the origin was increased or the starting point was moved to the origin. This method worked very well, always at least one solution was obtained and bistable regions were found to exist. Not a big effort was made however to try to verify the assumption, that is, it can not be completely ruled out that the CGLE infact has tristable regions or additional bistable regions besides the ones obtained in this way. Finally, the criterion "furher from the origin" is of course rather vague if we have a reasonable number of Fourier components. Good results are obtained by starting with a δ or Gaussian shaped function (in x-space), where the amplitude then is used in the "further from the origin" criterion. Amplitudes used were typically of the order of 3-300. Results obtained in this way show very good convergence properties with the actual error in f_m smaller than 10^{-16} in double precision computations.

In order to minimize the computation time, a pseudo-spectral method combined with a Fast Fourier Transformation was used [39]. This means that the nonlinear terms present in f_m and $J_{m,n}$ are computed precisely as indicated, that is as Fourier transformations of $|\phi(x)|^2\phi(x)$ and $\phi^2(x)$ etc.. Since this, dependent on the convergence, may require many back

and forth transformations, one has to make sure that these back and forth transformations are exact, that is, that no structural rounding errors occur in this way. The FFT therefore has to be done with some care, it will be discussed in section C.3.

C.2 Frequency-locked states of the LE.

We will formulate the method used in chapter 3 for the frequency-locked solutions of the LE (3.1) with arbitrary periodic forcing

$$F(t+T_0) = F(t), \qquad T_0 = 2\pi/\omega_0. \tag{C.9}$$

Suppose a frequency-locked states has a period $T = 2\pi/\omega$, $\omega = \frac{p}{q}\omega_0$. It may then be written as a Fourier series,

$$\Psi_{fl}(t) = \sum_n \hat{\Psi}_{fl,n} e^{in\omega}, \tag{C.10}$$

$$\hat{\Psi}_{fl,n} = \frac{1}{T}\int_0^T \Psi_{fl}(t) e^{-in\omega} dt, \tag{C.11}$$

and the Fourier components satisfy

$$(i\omega m - (1+ic_1))\hat{\Psi}_{fl,m} + (1+ic_3)\sum_n (|\Psi_{fl}(t)|^2)_{m-n}\hat{\Psi}_{fl,n} = \delta_{m,q}F_p. \tag{C.12}$$

This equation is of the form (C.1) and may be solved as discussed in the previous section. The Jacobian is given by (C.4) where now

$$A_{l,m} = (i\omega m - (1 + ic_1))\delta_{l,m} + 2(1 + ic_3)(|\Psi_{fl}(t)|^2)_{l-m} ,$$

$$B_{l,m} = (1 + ic_3)(\Psi^2_{fl}(t))_{l+m}. \qquad \text{(C.13)}$$

Regarding the stability of the frequency-locked states things are not quite as straight forward as previously, due to the fact that the forcing does not have the simple harmonic form. In general, this prevents the transformation of (C.4) into an autonomous equation; the explicite time dependence can not be eliminated in general. The resulting equation for stability has time dependent coefficients with period T,

$$\left[\partial_t - (1 + ic_1) + 2(1 + ic_3)|\Psi_{fl}(t)|^2\right] \delta\Psi(t)$$

$$+(1 + ic_3)\Psi^2_{fl}(t)\delta\Psi^*(t) = 0. \qquad \text{(C.14)}$$

For the characteristic exponents λ_1 and λ_2 of this equation one has

$$\lambda_1 + \lambda_2 = 1 - \frac{2}{T}\int_0^T |\Psi_{fl}(t)|^2 dt \qquad \text{mod} 2\pi i. \qquad \text{(C.15)}$$

A solution $\Psi_{fl}(t)$ is therefore unstable whenever

$$\frac{1}{T}\int_0^T |\Psi_{fl}(t)|^2 dt < \frac{1}{2}. \qquad \text{(C.16)}$$

However, if this inequality does not hold it is not gauranteed that $\Psi_{fl}(t)$ is stable. A general stability analyses on the basis of (C.14) is difficult. Floquet's theorem is available but this does not provide a method to compute the characteristic exponents. The strategy for obtaining the phase diagram shown in figure 3.5 therefore has been, to rule out the stability of most of the frequency-locked states on the basis of (C.16) and to test the stability of the remaining states from a time integration as explained in chapter 3.

C.3 Fast Fourier transformation.

In this appendix it will briefly be shown how a Fast Fourier Transformation is used properly to approximate the Fourier transformation

$$\hat{\Psi}_{k_n} = \frac{1}{L}\int_0^L dx \Psi(x) e^{-ik_n x} \tag{C.17}$$

and its inverse

$$\Psi(x) = \sum_{n=-\infty}^{+\infty} \hat{\Psi}_{k_n} e^{ik_n x}, \tag{C.18}$$

where $k_n = \frac{2\pi}{L} \cdot n$. By a Fast Fourier Transformation of a series $\{f(i)\}_{i=0}^{2N-1}$ we will mean the transformation

$$\hat{f}(n) = \frac{1}{2N}\sum_{j=0}^{2N-1} f(j) e^{-i2\pi nj/2N} \tag{C.19}$$

with its inverse

$$f(j) = \sum_{n=0}^{2N-1} \hat{f}(n) e^{i2\pi nj/2N}. \tag{C.20}$$

Below it will be shown how equations (C.17) and (C.18) may be written properly in the form of (C.19) and (C.20) preserving the exact relation between the original transformation and its inverse. More precisely; unavoidably one introduces errors by discretizing (C.17), however, the point is that this should be the only errors introduced. Once discretized, one should require the back and forth transformations to be exact so no extra (rouding) errors are introduced. This is important for the pseudo-spectral method, where one uses intensively back and forth transformation and rounding errors may build up eventually.

One splits the interval $[0, L]$ into 2N points, $x_i = \frac{L}{2N} \cdot i$, $i = 0, \ldots\ldots, 2N-1$. Denote $\Psi(x_i) = \Psi(i)$ and $\hat{\Psi}_{k_n} = \hat{\Psi}(n)$ and define $\Psi(2N) = \Psi(0)$. The Fourier transformation (C.12) then becomes in approximate discretized form

$$\hat{\Psi}(n) = \frac{1}{2N} \sum_{j=0}^{2N-1} \Psi(j) e^{-i2\pi nj/2N}, \tag{C.21}$$

with exact inverse

$$\Psi(j) = \sum_{n=-N}^{n=+N} \hat{\Psi}(n) e^{i2\pi nj/2N} - \frac{1}{2}[\hat{\Psi}(N) + \hat{\Psi}(-N)](-1)^j. \tag{C.22}$$

However, according to (C.16)

$$\hat{\Psi}(N) = \hat{\Psi}(-N) = \frac{1}{2}\sum_{j=0}^{2N-1} \Psi(j)(-1)^j. \tag{C.23}$$

Therefore if one shifts the summation index in (C.17) one has

$$\Psi(j) = (-1)^j \sum_{n=0}^{2N-1} \hat{\Psi}(n-N)e^{i2\pi jn/2N}. \tag{C.24}$$

Finally then, if one defines

$$\Psi'(j) = (-1)^j \Psi(j), \tag{C.25}$$

relations (C.19) and (C.20) will hold for Ψ' and $\hat{\Psi}'$,

$$\hat{\Psi}'(n) = \frac{1}{2N}\sum_{j=0}^{2N-1} \Psi'(j)e^{-i2\pi nj/2N}, \tag{C.26}$$

$$\Psi'(j) = \sum_{n=0}^{2N-1} \hat{\Psi}'(n)e^{i2\pi nj/2N}. \tag{C.27}$$

C.4 The split step Fourier method.

The method consists here in that one splits up the equation in two parts, each of which can be integrated analytically. In each time step then, the solution is advanced for these parts seperately, using the result of one as input for the other. The method is first order accurate in Δt and all order in Δx and is uncondtionally stable according to linear analyses.

In case of the forced CGLE one has infact two relevant options for separation of the equation and two options for arrangement of the actual intgration. The first is where one advances the solution according to

$$\left[\frac{\partial}{\partial t} + i\omega - 1 + (1 + ic_3)|\Psi|^2\right]\Psi = 0, \tag{C.28}$$

resulting in

$$\Psi_1(x, \Delta t) = \frac{\Psi(x, 0)e^{(1+i\omega)\Delta t}}{[1 + |\Psi(x, 0)|^2(e^{2\Delta t} - 1)]^{(1+ic_3)/2}}, \tag{C.29}$$

after which the solution is advanced acording to

$$\hat{\Psi}(k, \Delta t) = \hat{\Psi}_1(k, \Delta t)e^{-\Lambda(1+ic_2)(k+K)^2\Delta t}$$

$$+ \frac{F_0}{\Lambda(1 + ic_2)(k + K)^2}\left[1 - e^{-\Lambda(1+ic_2)(k+K)^2\Delta t}\right], \tag{C.30}$$

or vice versa.

The second is where one advances the solution according to

$$\left[\frac{\partial}{\partial t} + i\omega + (1 + ic_3)|\Psi|^2\right]\Psi = 0, \tag{C.31}$$

resulting in

$$\Psi_1(x, \Delta t) = \frac{\Psi(x, 0)e^{i\omega\Delta t}}{[1 + 2|\Psi(x, 0)|^2\Delta t]^{(1+ic_3)/2}}, \tag{C.32}$$

after which the solution is advanced acording to

$$\hat{\Psi}(k, \Delta t) = \hat{\Psi}_1(k, \Delta t)e^{(1-\Lambda(1+ic_2)(k+K)^2)\Delta t}$$

$$- \frac{F_0}{1 - \Lambda(1 + ic_2)(k + K)^2} \left[1 - e^{(1-\Lambda(1+ic_2)(k+K)^2)\Delta t}\right], \qquad \text{(C.33)}$$

or vice versa.

All methods were found to provide equal efficienty, the actual method used was the second one mentioned, given by (C.32) and (C.33).

References

1. Ginzburg V. L. and Landau L. D., On the theory of superconductivity, Zh. Eksp. Teor. Fiz., 20, (1950),1064.
2. Negele J. W. and Orland H., Quantum Many-Particle Systems, Addison Wesley, 1987.
3. Huang K. , Statistical Mechanics, John Wiley and Sons, 1987.
4. Newell A. C. and Whitehead J. A., J. Fluid Mech., 38, (1969), 279.
5. Segel L. A., J. Fluid Mech., 38, (1969), 203.
6. Cross M. C., Phys. Fluids, 23, (1980), 1727.
7. Haken H., Advanced Synergetics, Springer-Verlag, Berlin, 1987.
8. Cheng M. and Chang H. C. , Phys. Fluids A, 2, (1990), 8.
9. Hohenberg P C and Shraiman B I, Physica D, 37, (1989), 109.
10. Landau L. D. and Lifshitz E. M., Fluid Mechanics, Oxford, Pergamon, 1959.
11. Doering C. R. , Gibbon J. D., Holm D. D. and Nicolaenko B., Nonlinearity, 1, (1988), 279.
12. Malomed B. A. and Nepomnyashchy A. A., Phys. Rev. A, 42, 10, (1990), 6238.
13. Saarloos van W. and Hohenberg P. C., Phys. Rev. Lett. 64, (1990), 749.
14. Bretherton C. S. and Spiegel E. A., Phys. Lett. A, 96, (1983), 152.
15. Schöpf W. and Kramer L., Phys. Rev. Lett. 66, (1991), 2316.
16. Landman M. J., Studies Appl. Math., 76, (1987), 187.
17. Holmes P., Physica D, 23, (1986), 84.

18. Ben-Jacob E., Brand H. R., Dee G., Kramer L. and Langer J. S., Physica 14D, (1985), 348.

19. Saarloos van W., Hohenberg P. C., Physica D, 56, (1990), 503.

20. Patashinskii A. Z. and Shumilo B. I., Sov. Phys. JETP 50, (1979), 4.

21. Hakim V. and Rappel W. J., Phys. Rev. A, 46, (1992), R7347.

22. Dubois-Violette E., Durand G., Guyon E., Manneville P. and Pieransky P., "Instabilities in nematic liquid crystals", in *Liquid Crystals*, edited by Liebert L., Solid State Phys. Suppl., 14, (1978), 147.

23. Coullet P., Phys. Rev. Lett., 56, (1986), 724.

24. Coullet P. and Huerre P., Physica 23D, (1986), 27.

25. Coullet P. and Emilson K., Physica A, 188, (1992), 190.

26. Benjamin T. B. and Feir J. E., J. Fluid Mech., 27, (1967), 417.

27. Newell A. C., "Lectures in mathematics", AMS, Providence R.I., vol. 15, (1974), 157.

28. Stuart J. T. and DiPrima R. C., Proc. R. Soc. Lond. A, 362, (1978), 27.

29. Cross M. C. and Hohenberg P. C., Rev. mod. Phys., 65, 3, (1993), 851.

30. Moon H. T., Huerre P. and Redekopp L. G., Physica 7D, (1983), 135.

31. Coullet P., Gil L., Lega J., Phys. Rev. Lett., 62, (1989), 1619.

32. Shraiman B. I. , Pumir A., van Saarloos W., Hohenberg P. C., Chaté H. and Holen M., Physica D, 57, (1992), 241.

33. Sakaguchi H., Progr. of Theor. Phys., 84, (1990), 792.

34. Chaté H., Nonlinearity, 7, (1994), 185.

35. Bekki N. and Nozaki K., J. Phys. Soc. Japan, 53, (1984), 1581.

36. Bekki N. and Nozaki K., Phys. Lett., 110A, (1985), 133.

37. Guckenheimer J. and Holmes P., "Nonlinear Oscillations, Dynamical Systems, and Bifurcations of Vector Fields", Springer-Verlag, Berlin, (1983).

38. Pereira N. R. and Stenflo L., Phys. of Fluids, 20, (1977), 10.

39. Fornberg B. and Whitham G. B., Phil. Trans. Roy. Soc., 289, (1978), 373.

40. See for instance: Jenkins G. M. an Watts D. G., "Spectral Analysis and its Applications", Holden-Day, (1968), or Bloomfield P., "Fourier Analysis of Time Series: An Introduction", Wiley, (1976).

41. See for instance: Schuster H. G., "Deterministic Chaos, an Introduction", VCH Verlaggesellschaft mbH, Weinheim, Germany, (1989).

42. Wielaard D. J., Thesis proposal, The City College of New York.

43. Hardin R. H. and Tappert F. D., SIAM Rev. Chronicle, 15, (1973), 423.

44. Taha T. R. and Ablowitz M. J., J. of Comp. Phys., 55, (1984), 203.

45. Kuramoto Y. and Tsuzuki T., Prog. Theor. Phys., 55, (1976), 356; Kuramoto Y., Prog. Theor. Phys., Suppl. 64, (1978), 346; Sivashinski G. I., Acta Astronautica, 6, (1976), 569.

46. Toh S., J. Phys. Soc. Japan, 36, (1987), 949.

47. Powell M. J. D., "A Hybrid Method for Nonlinear Albegraic Equations", in *Numerical Methods for Nonlinear Algebraic Equations*, editor Rabinowitz P., Gordon and Breach, (1970).